CO-DOPING OF COBALT FERRITE WITH TRANSITION METALS AND FABRICATION OF THEIR COMPOSITE/S WITH ZnO/Ag NANOPARTICLES FOR ANTIBACTERIAL ACTIVITIES

Thesis Submitted for the Award of the Degree of

DOCTOR OF PHILOSOPHY

in

Chemistry

By

Shyam Kalia

Registration Number: 41900430

Supervised By

Dr. Nupur Prasad (20362)

Department of Chemistry (Associate Professor)

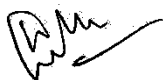**School of Chemical Engineering and Physical Sciences**

Lovely Professional University

LOVELY PROFESSIONAL UNIVERSITY, PUNJAB
2024

DECLARATION

I, hereby declared that the presented work in the thesis entitled "Co-doping of cobalt ferrite with transition metals and fabrication of their composite/s with ZnO/Ag nanoparticles for antibacterial activities" in fulfilment of degree of **Doctor of Philosophy (Ph. D.)** is outcome of research work carried out by me under the supervision of Dr. Nupur Prasad, working as Associate Professor, in the Central Instrumentation Facility, of Lovely Professional University, Punjab, India. In keeping with general practice of reporting scientific observations, due acknowledgements have been made whenever work described here has been based on findings of other investigator. This work has not been submitted in part or full to any other University or Institute for the award of any degree.

(Signature of Scholar)

Name of the scholar: Shyam Kalia

Registration No.: 41900430

Department/school: School of Chemical Engineering and Physical Sciences

Lovely Professional University,

Punjab, India

CERTIFICATE

This is to certify that the work reported in the Ph. D. thesis entitled "Co-doping of cobalt ferrite with transition metals and fabrication of their composite/s with ZnO/Ag nanoparticles for antibacterial activities" submitted in fulfillment of the requirement for the award of degree of **Doctor of Philosophy (Ph.D.)** in the School of Chemical Engineering and Physical Sciences, is a research work carried out by Shyam Kalia, Registration No. 41900430, is bonafide record of his original work carried out under my supervision and that no part of thesis has been submitted for any other degree, diploma or equivalent course.

Nupur Prasad

(Signature of Supervisor)

Name of supervisor: Dr. Nupur Prasad

Designation: Associate Professor

Department/school: Central Instrumentation Facility, Research and Development Cell

University: Lovely Professional University, Phagwara (Punjab), 144411.

Abstract

Cobalt ferrite (CF) has an inverse spinel structure. It has the general formula AB_2O_4, in which A and B are metal cations, whereas O is an (O^{2-}) anion. It exhibits several unique properties, e.g., dielectric, magnetic, optical, and catalytic properties, because of its exceptional molecular shape and hence can be used for various applications. These properties depend upon the distribution of ions between tetrahedral and octahedral sites. Their properties can be altered via doping/substitution. It provides a tool using which CF with desired properties can be synthesised. Several methods have been developed to dope CF, for example, sol-gel, co-precipitation, hydrothermal, and microwave hydrothermal methods, to name but a few. Here, we have synthesised a series of Cu-Ag, Ag-Zn, Cu-Zn, Bi-Ag, and Bi-Zn co-doped CF via the sol-gel route.

These as-prepared samples were characterised using various Advanced Materials' Characterization Techniques. The X-ray diffraction (XRD) technique was used to study the crystalline nature of the samples. The presence of different functional groups in the samples was analysed via Fourier Transform Infrared (FTIR) spectroscopy. The Field Emission Scanning Electron Microscopy (FESEM) technique is used to study the morphology of particles, whereas Energy Dispersive X-ray (EDS) spectroscopy used for elemental analysis of the samples. Vibrating Sample Magnetometer (VSM) was used to study the magnetic properties of the samples. Thermal properties of samples were studied using Differential Scanning Calorimeter (DSC) and Thermogravimetric Analysis (TGA).

XRD results confirmed the formation of simple cubic crystals. The existence of dopants in molecules was also evident from XRD data. The level of doping in the samples of cobalt ferrite nanoparticles (CF-NPs) changes their crystallite sizes and lattice parameters. The ionic size differences between dopant/s ions and host-ions were also responsible for these changes. The position of absorption bands in the infrared spectrum was used for the identification of different chemical components present in the compound. FTIR studies suggested that doping and co-doping did not

disturb the octahedral shape of the spinel. It also shows the minor shift in the absorption bands in doped and co-doped CF-NPs as compared to un-doped CF-NPs.

Co-doping changes the magnetic properties of these materials drastically. Superparamagnetic CF-NPs were formed upon co-doping. It confirmed the change in saturation magnetisation as well as coercivity values. The hysteresis curve of the co-doped sample exhibits high saturation magnetisation and low or negligible coercivity. Zero coercivity is responsible for the change of ferromagnetic CF-NPs into superparamagnetic CF-NPs. The superparamagnetic materials can be used in different biomedical applications, such as gene delivery, drug delivery, Magnetic Resonance Imaging (MRI) and the antibacterial study of samples.

The FESEM images of all the co-doped samples show the presence of agglomerated particles. The Cu-Ag co-doped sample shows the presence of pentagonal-shaped particles with clear edges and surfaces. A few wrinkles can also be observed at the surface of these particles, while the Ag-Zn co-doped sample shows the presence of particles of clear and rounded edges with angular morphology, and the FESEM images of Cu-Zn co-doped CF-NPs show the presence of particles of brick-like shape with rounded edges and angular morphology. The Bi-Ag co-doped sample shows hexagonal-shaped particles with sharp and clear edges, while the images of Bi-Zn co-doped CF-NPs represent particles with rounded and angular edges.

Energy dispersive X-ray (EDS) spectroscopy is used to detect the elemental composition of the samples. It is used for quantitative and qualitative analyses. Elemental mapping identified the presence of elements in the sample, while quantitative analysis was performed to examine the elemental quantities such as atomic percent and weight percent of the sample. EDS is a "semi-qualitative" as well as "semi-quantitative" method of analysis, as it analyses only the surface of the sample.

The thermal properties of the samples were investigated using the Thermogravimetric Analyzer (TGA) and Differential Scanning Calorimeter (DSC) techniques. The results

of TGA demonstrated that all the samples were thermally stable, as no thermal event was observed in any of the samples. The absence of any substantial loss in weight also demonstrates the absence of substantial amounts of impurities in the samples. Although a small, gradual loss in weight was observed in almost all the samples, this might be due to the loss of residual water. Possibilities of loss of absorbed and adsorbed water cannot be evaded. The presence of residual organic substances, e.g., citric acid, which was used as fuel during the reaction, cannot be avoided. The residual nitrate and hydroxyl groups may also be responsible for this observation. Similarly, the results of DSC also did not show any thermal events, showing that there was no change in phase in the given temperature range (room temperature to 440 °C).

Preparation of composites is another way to modify the properties and, hence, applications of the materials. The ZnO/Ag composites of these CF-NPs were also prepared through the mortar-pestle grinding method. The grinding technique is an important aspect of mechanochemical synthesis or reactions. It can be done using a mortar and pestle. The main advantage of the mortar-pestle grinding method is that it does not require sophisticated laboratory infrastructure.

The antibacterial activities of the samples were studied using the Agar disk diffusion method. The antibacterial agents can combat communicable diseases. However, the extensive use of antibiotics created drug-resistant bacteria. This will cause serious health problems in humans. This problem inspired researchers to create novel materials that can combat infectious diseases. Magnetic nanoparticles can play an effective role here to address this issue. These nanoparticles can be used in various biomedical applications, including gene delivery, biosensors, and drug delivery. Apart from this, these particles can also be used for catalysis in the fabrication of optical devices, superconductors, and fuel cells. The composites show better antibacterial activity than the doped and co-doped CF-NPs. The antibacterial activity test was performed using the Agar disk diffusion method. We were used clean filter papers for the creation of circular disks that were used for this purpose. Antibacterial activities were carried out on all the samples, including composites. The formation of clear zones of inhibition confirmed that the samples exhibit antibacterial properties. These

tests were carried out against *Bacillus paranthracis* and *Bacillus nitratireducens*. Co-doping enhanced the antibacterial activity of CF samples. The antibacterial activity in each pair of co-doped samples of CF-NPs increased with an increase in the level of doping. Although all the samples demonstrated their antibacterial activities, the sample co-doped with bismuth and silver showed the best results, i.e., zone with the largest diameter was observed, whereas the composite of co-doped CF-NPs with copper and silver created the largest zone of inhibition.

Acknowledgements

Contents

xii

List of Tables

List of figures

Abbreviations and Symbols

Chapter 1

Introduction

1.1 Background of the project

Magnetic nanoparticles (MNPs) have acknowledged distinct attention since last few years [1]. MNPs show remarkable potential in various applications due to their unique properties. These nanoparticles (NPs) can be used as catalyst, in environmental remediation as well as in biomedicine [2,3]. Generally, the different class of MNPs contains metal, bimetal, and superparamagnetic iron oxide nanoparticles [4]. Ferrite nanoparticles (FNPs) are magnetic in nature [5]. Spinel ferrites (SFs) are iron oxides [6]. The distribution of metal cations among octahedral and tetrahedral sites change their properties [7]. Inverse spinel cobalt ferrite (CF) is one of the classes of spinel ferrites [8,9]. CF is hard magnetic material that shows unique properties like moderate saturation magnetisation, high coercivity, high anisotropy constant, chemical stability, and good insulation [3,10,11]. The magnetic properties of these materials can be changed with change in heat treatment, magnetic annealing, and high compressed pressure [12]. Doping can improve their structural, optical, dielectric, and magnetic properties [13]. Cobalt ferrite nanoparticles (CF-NPs) doped with one or more metal ions can modify their physical, chemical, and antibacterial properties [8,14]. The distinct properties of CF are responsible for their different applications like memory core, in high frequency devices, as a recording media, and in various biomedical fields [15].

Different research groups developed/used different routes of synthesis to synthesise FNPs. These materials can be synthesised via microwave-hydrothermal [6], conventional and microwave combustion [16], sol-gel [17], co-precipitation [18], green synthesis [19], auto-combustion [20], and citrate precursor technique [21] etc. to name but a few. We used the sol-gel method in our work to prepare CF-NPs due to its simplicity. This method yields homogeneous samples of uniform grain sizes and allows the reaction to occur at room temperature [22].

Preparing composites is another way to control the materials' properties [23]. The composite produced small sized particles than by the ingredients that were used to make it. It provides large surface area and exhibits improved properties [24].

The pathogenic microorganism infections are responsible for more deaths than all other causes. They pose a major threat to the health care industry. Antibiotics mostly treat bacterial infections. However, the extensive use of antibiotics created drug-resistant bacteria. This will cause serious health problems in humans. Research on novel and potent antibacterial drugs has evolved as a result of the growing concern over antibiotic-resistant microbes as a health risk [25].

To our knowledge, co-doping of cobalt ferrite with 'silver (I) and copper (II)', 'zinc (II) and silver (I)', 'copper (II) and zinc (II)', 'silver (I) and bismuth (III)', and 'zinc (II) and bismuth (III)', via sol-gel route has not been done yet. The novel ZnO/Ag composites of these CF-NPs were also prepared through mortar-pestle grinding method. Apart from this not much work has been carried out to study the antibacterial activities of magnetic materials.

In this study, a series of 'silver (I) and copper (II)', 'zinc (II) and silver (I)', 'copper (II) and zinc (II)', 'silver (I) and bismuth (III)', and 'zinc (II) and bismuth (III)' co-doped CF-NPs were successfully synthesised by using the sol-gel route. The synthesised un-doped, doped/co-doped CF-NPs were analysed through XRD, FTIR, VSM, FESEM/EDS, TGA and DSC. The antibacterial activities of synthesised CF-NPs and its ZnO/Ag composites analysed here against the bacteriae *Bacillus paranthracis* and *Bacillus nitratireducens* using Agar disk diffusion test.

1.2 Dissertation layout

A brief introduction of the work is presented in Chapter 1. Chapter 2 describes the literature review. Chapter 3 is about the materials and methods used in this work, while Chapter 4 is about the objectives and research gap. Chapters 5 to 9 describe the results and discussions along with the conclusions.

Chapter 2

Literature review

2.1 Introduction

A set of literature has been reviewed to find out the research gap. We also studied several books and book chapters to understand the basic concepts related to it. We have discussed all of them systematically in this chapter to provide a logical and scientific background for our research work.

Several important concepts related to this work are discussed in this chapter; for example, a brief overview of ferrite nanoparticles is given in sec. 2.2. Origin of magnetism in materials (sec. 2.3), classification of magnetic materials (sec. 2.4), classification of ferrites (sec. 2.5), properties of ferrites/cobalt ferrite (sec. 2.6), applications of ferrites/cobalt ferrite (sec. 2.7) are discussed in sections 2.3 to 2.7 respectively. Basic concepts of doping are presented in sec. 2.8. Routes of synthesis of doped ferrites are reviewed briefly in sec. 2.9. Doping of cobalt ferrite nanoparticles (CF-NPs, see sec. 2.10), explanation of routes of synthesis of doped CF-NPs (sec. 2.11), doping of CF-NPs with 3d-series and 4d-series elements of Periodic Table (sec. 2.12), CF-NPs doped with rare earth elements (sec. 2.13), CF-NPs doped with representative elements (sec. 2.14), CF-NPs doped with non-metals (sec. 2.15), CF-NPs doped with more than one element (sec. 2.16), applications of co-doped CF-NPs (sec. 2.17), composites of CF-NPs (sec. 2.18) are described in sections 2.10 to 2.18 respectively. Antibacterial activities are presented in sec. 2.19, and sec. 2.20 concludes the chapter.

2.2 An introduction of ferrite nanoparticles

The term 'nano' stands for number 'nine'. One nano meter is equal to 10^{-9} m. Nanotechnology is an umbrella term. It encompasses science and technology related to synthesis, characterization, and further processing of nanomaterials [26–28]. Nanomaterials can be classified as follows:

- Materials having all dimensions in nanometer-scale are 'Zero-dimensional'

nanomaterials. Example: nanoparticles [29].

- Materials having any one dimension in nanometer-scale are 'One-dimensional' nanomaterials. Example: nanofibers [29].

- Materials having any two of the three dimensions in nanometer-scale are called 'Two-dimensional' nanomaterials. Example: nanosheets [29].

- Materials having more than 100 nm in size are 'Three-dimensional' nanomaterials. Example: nanoflowers, agglomerated nanoparticles[29].

Nanotechnology caught attention with the discovery of fullerene molecule. It is an allotrope of carbon. Sixty carbon atoms are joined together by covalent bonds in fullerene. The structure of this molecule was proposed by Roger Buckminster Fuller. He was an architect as well as a well-known author [26–28]. Here, we have prepared 'ferrite nanoparticles (FNPs)'. Ferrites are oxides of iron [30]. They are magnetic in nature [30,31]. The general formulae of these materials are AB_2O_4, where both 'A' and 'B' are metal cations and 'O' is negatively charged oxide (O^{2-}) ion [32]. Most probably, lodestone (magnetite (Fe_3O_4)) is the first known naturally occurring magnetic material [33,34]. Origin of magnetism in materials is discussed in the following section (see sec. 2.3).

2.3 Origin of magnetism in materials

A charged particle with an angular momentum produces magnetic moment [23]. Atoms of materials also have charged particles viz. protons and electrons [23]. Electrons revolving around nucleus behave like tiny loop of electrical current. Spinning electrons and nucleus also behave like small magnets (see fig. 2.1) [23].
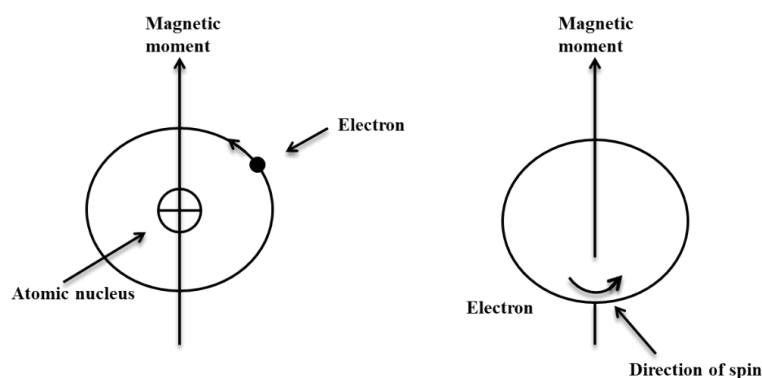
Fig. 2.1 Magnetic moments generated within a material because of
a) motion of electrons in different orbits of atom, b) spin of electrons [23]

These tiny electrical currents are responsible for generation of magnetic field at atomic scale. These electrons also have spin motion along their axis which produces another magnetic moment. Hence, each electron of any material can be considered as a small magnet having permanent spin magnetic moments as well as orbital magnetic moment. The net magnetic moment of an atom is the sum of the magnetic moments of each of the constituent electron, (including both orbital and spin contributions), and considering cancellation of magnetic moments. Nuclear spins can also induce permanent magnetism in materials [23,35]. Magnetic materials are of various types. They are discussed in the following section (sec. 2.4).

2.4 Classification of magnetic materials

These materials are classified according to their properties. The two broad classes are as follows:

(i) Types of magnetic materials based on values of magnetic susceptibilities [36] (see sub-sec. 2.4.1)

(ii) Types of magnetic materials based on values of coercivity and retentivity [35] (see sub-sec. 2.4.2)

2.4.1 Types of magnetic materials based on magnetic susceptibility values

The concept of magnetic susceptibility is described in sub-sec. 2.4.1.1 and the various types of magnetic materials based on it are described in sub-sec. 2.4.1.2.

2.4.1.1 The magnetic susceptibility

The word susceptibility originated from Latin word 'susceptibilis' the meaning of which is 'receptive'. It is the ability of a material to acquire magnetisation when exposed to external magnetic field. It is denoted by χ. Mathematically, it can be expressed by eq^{n}. (2.1),

$$\chi = M/H \dots\dots\dots\dots \text{eq}^{n}. (2.1)$$

Where,

$M =$ Material's magnetisation,

$H =$ Applied magnetic field

The value of magnetic susceptibility shows whether the material is repelled or attracted towards an external magnetic field [23,36].

2.4.1.2 Types of magnetic materials based on values of magnetic susceptibilities

The different class of materials according to the value of susceptibilities is discussed in this subsection. This is reflected in the response of materials when exposed to external magnetic field. It is normally displayed as shown in fig. 2.2.

(a)   **(b)**   **(c)**
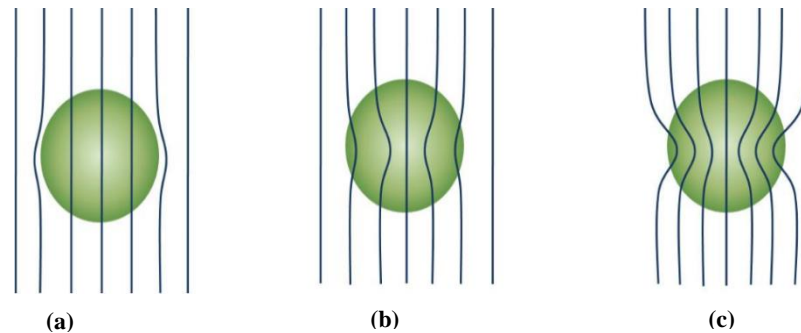
Fig. 2.2: Comparison of attraction of magnetic lines of force in
a) diamagnetic materials, b) paramagnetic materials, and c) ferromagnetic materials [23,37].

These different types of magnetic materials are as follows:

(i) Diamagnetic materials,

(ii) Paramagnetic materials,

(iii) Ferromagnetic materials, and

(vi) Metamagnetic materials [38].

i. *Diamagnetic materials*: The diamagnetic substances have either 'zero' or negative values of magnetic susceptibilities. They are repelled by applied magnetic field and create negative magnetic susceptibility. The magnetic permeability is less than '1'. In simple word we can understand magnetic permeability as the ability of the magnetic lines of force to pass though the material. The shape of magnetic lines of forces flowing around a diamagnetic material can be visualized as shown in fig. 2.2(a). Their net magnetic moment value remains zero. Magnetic moment is a vector quantity which measures the direction and strength of a magnetic field produced by a magnet or any other object. At room temperature alumina, silver, copper, and gold are diamagnetic materials. Benzene and naphthalene are also diamagnetic in nature [23]. A

6

substance shows pure diamagnetic behaviour when their orbital moment is either zero or cancels each other effectively. Their all-electronic spins should be paired as well. Oxygen molecule is an exception [35]. Its magnetic behaviour is explained by Molecular Orbital Theory [39]. It is described in the following paragraph where we discussed paramagnetism. Diamagnetism of materials do not show any significant practical application till date [35].

ii. *Paramagnetic materials:* These substances weakly attract magnetic lines forces. It is diagrammatically shown in fig. 2.2(b).These are the substances having unpaired electrons and hence when they are exposed to magnetic fields their magnetic moments do not cancel out each other completely which results in the form of existence of a resultant magnetic moments of bulk materials which is the resultant of the tiny magnetic moments produced at atomic levels due to the presence of unpaired electron/s [23]. Alloys of titanium, copper, and aluminium show paramagnetic behaviour [38]. As discussed above oxygen molecules also show paramagnetic behaviour which is explained through Molecular Orbital Theory (MOT). The molecular orbitals are pictorially represented in the following figure (see fig. 2.3). Note that, non-bonding orbitals are not shown in fig. 2.3.
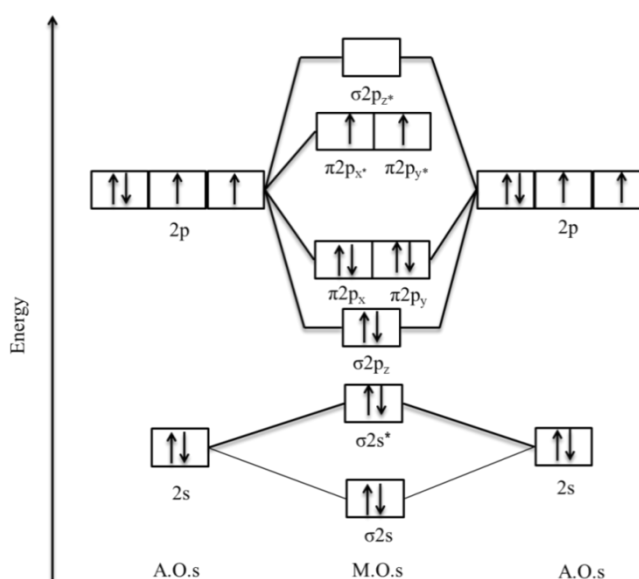
Fig. 2.3: Molecular orbitals of oxygen molecule. Two unpaired electrons can be seen in antibonding orbital which are responsible for paramagnetic behaviour of oxygen molecules [39].

Many materials show paramagnetic behaviour for example gaseous nitric oxide is one of them [40].

iii. *Ferromagnetic materials:* They are permanent magnets. They can retain their magnetic properties in the absence of applied magnetic field [38]. Upon exposure to strong magnetic fields the magnetisation of these materials increases with increasing field strength [23]. They attract magnetic lines of force very strongly which can be depicted graphically as shown in fig. 2.2(c). Ferromagnetic materials contain multiple magnetic domains. These domains reduce the overall magnetic energy of the system which in turn helps the whole system in achieving stability [23]. A ferromagnetic material affects the magnetisation due to the positive interactions of adjoining atomic dipoles. The substructure of these materials composed of magnetic domains with in the grain structure. The regions of aligned dipoles in the materials called domains. In the absence of magnetic field, these domains are randomly oriented in the materials and the net magnetisation becomes zero. The individual magnetic domains are separated through boundaries called Bloch walls. These Bloch walls play an important role in the material. Actually these are the narrow zones where the direction of magnetic moments continuously changes (see fig. 2.4) [23].
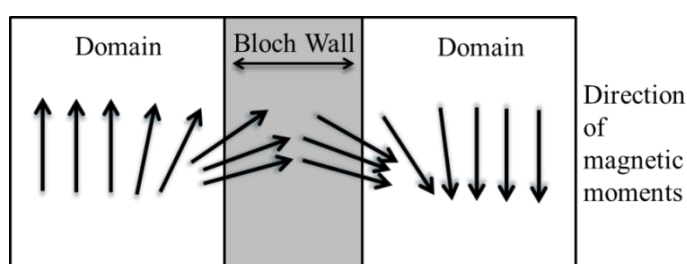
Fig 2.4 The magnetic moments in adjoining atoms change direction continuously across the boundary between domains [23].

When all the domains are properly orientated in the direction of the applied magnetic field, it produces magnetisation [23]. The concept of magnetisation is described in the following paragraph.

Magnetisation: It is a phenomenon where ferromagnetic substances show magnetic behaviour under applied magnetic field. This process also achieves saturation where the magnetisation does not increase any further even if the field strength of the applied field is increased. This process is called saturation magnetisation [23] (see fig. 2.5).
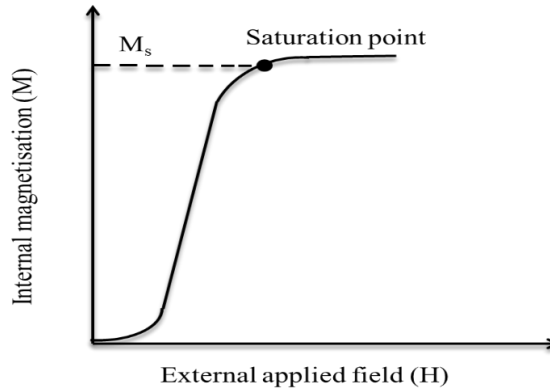
Fig. 2.5 Schematic representation of saturation magnetisation [23].

The magnetic behaviour of these materials also depends upon temperature. It diminishes when they are heated. The thermal agitation breaks the atomic arrangement which in turn changes the alignment of the magnetic moments. Above Curie temperature (T_c, named after Pierre Curie), these materials lose their magnetic behaviour changing from ferromagnetic to paramagnetic materials. Iron, cobalt, and nickel show ferromagnetism [38]. The concept of Curie temperature is described in the following paragraph.
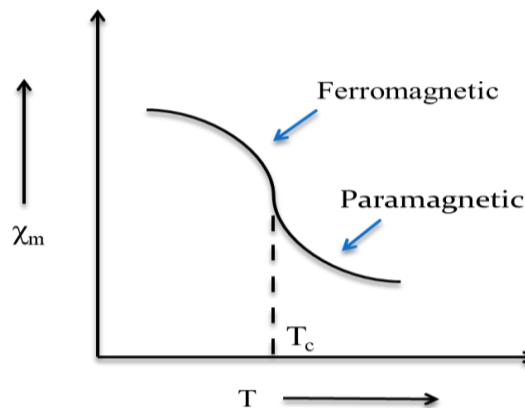
Fig. 2.6 Change in susceptibility with temperature showing Curie Temperature (T_c) [23].

Curie temperature (T_c): The temperature at which the permanent magnet loses its magnetic properties is called Curie temperature. It is denoted by T_C. At Curie temperature a permanent magnetic material starts behaving like a paramagnetic material. The thermal energy added to the system is enough to remove the microscopic magnetic order of permanent magnetic materials and their susceptibilities become minimum [38,41,42]. Above Curie temperature a ferromagnetic substance behaves like a paramagnetic substance (see fig. 2.6) [38,43].

Ferromagnetic materials are further classified as antiferromagnetic materials (see iiia) and ferrimagnetic materials (see iiib).

iiia. Anti-ferromagnetic materials: When these materials are exposed to external magnetic fields the dipoles align with the magnetic field but in opposite direction cancelling each other and no net magnetisation exists. The neighbouring atoms produce magnetic moments in anti-parallel direction. An antiferromagnetic material can be considered as materials where two ferromagnetic lattices are interwoven or penetrated each other in such a way that they cancel each other's magnetic moments. This leads to complete cancellation of magnetic moments they behave like paramagnetic materials. However, antiferromagnetic materials show a temperature dependent magnetic behaviour whereas paramagnetic materials do not show any temperature dependent magnetic behaviour. Curie temperature holds good for ferromagnetic substances while Neel temperature holds good for antiferromagnetic materials [38]. We have discussed Neel temperature in the following paragraph.

Neel temperature (T_N) The temperature above which the antiferromagnetic material loses magnetism is called Neel temperature. It is denoted by T_N. The magnetic susceptibility of antiferromagnetic substances reaches its maximum at this temperature. This behaviour shows that the thermal energy changes the

magnetic arrangement significantly [38,41,42]. Graphically the effect of Neel temperature on magnetic behaviour of material is represented in fig. 2.7 [43].
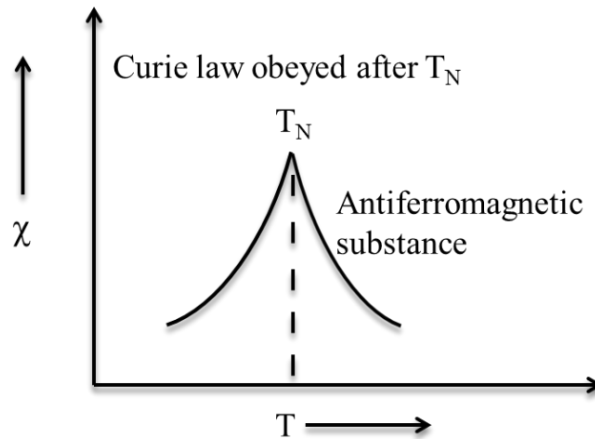
Fig. 2.7 Figure representing effect of Neel temperature on magnetic material [38].

iiib. Ferrimagnetic materials: When these materials are exposed to external magnetic fields the dipoles may or may not align with the magnetic field hence they do not cancel each other completely. A spin moment exists leading to an existence of net magnetisation in the substance. These materials also have different sub-lattices as described in antiferromagnetic substances [38]. The magnetic susceptibilies of these materials are much higher than that of antiferromagnetic materials [38]. These materials strengthen good amplification of the applied field. Ferrites of barium, nickel, cobalt, lead, are ferrimagnetic in character [23,38]. These materials are good insulators and hence they can be used in the fabrication of high frequency transformers [38].

(iv) Meta-magnetic materials: It is a metastable state of magnetic material where the material exists at a very high magnetisation state [38].

The alignment of magnetic moments (magnetic ordering) in different types of magnetic materials (except meta-magnetic materials) is schematically shown in fig. 2.8.
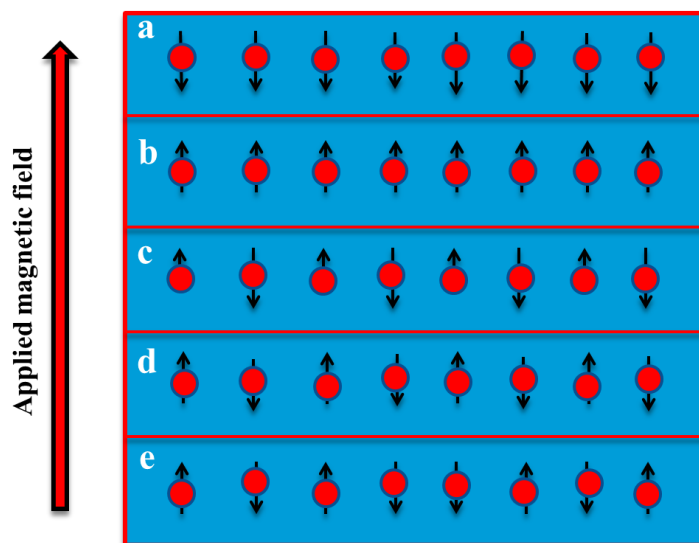
Fig. 2.8 Graphical representation of dipole moments of molecules, when exposed to external magnetic field:
a: diamagnetic,
b: paramagnetic,
c: ferromagnetic,
d: antiferromagnetic,
e: ferrimagnetic [23]*.*

Apart from the above discussed classes of magnetic materials, magnetic materials are also classified based on their behaviour known as 'hysteresis.' See sub-sec. 2.4.2 for a brief explanation of hysteresis and types of magnetic materials based on this.

2.4.2 Types of magnetic materials based on values of coercivity and retentivity

The term 'hysteresis' is coined by Sir James Alfred Ewing [44]. This phenomenon demonstrates the property of a system when output value is not strictly dependent upon the input value [23]. This is explained in the following sub-section (see sub-sec. 2.4.2.1).

2.4.2.1 Explanation of hysteresis in magnetic materials

Magnetic substances like cobalt, nickel, and iron contain magnetic domains (see sub-sec. 2.4.1). The magnetic moments of atoms are arranged in a parallel manner within the domain and are responsible for strong magnetic character in the ferromagnetic materials. In the bulk samples these domains are arranged in the unsystematic manner (not parallel) leading to demagnetisation of whole material. In the presence of

external applied magnetic fields these domains arranged in the systematic manner (parallel) and create strong magnetism in the material.
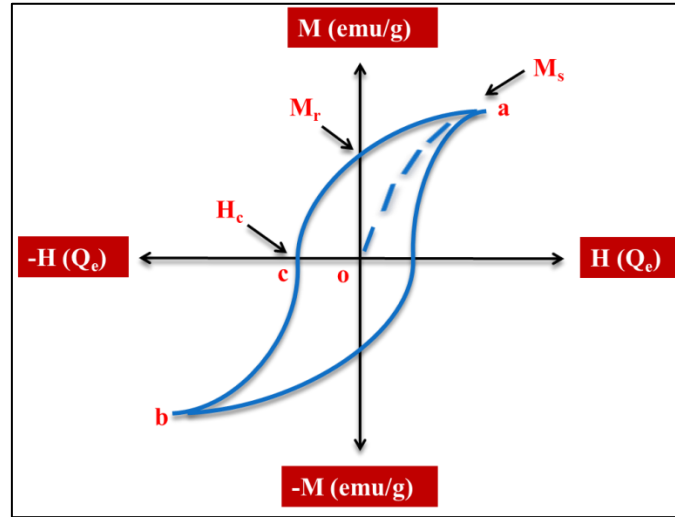
Fig. 2.9 Hysteresis curve for magnetic material where,
H = applied magnetic field strength in Oe, M = magnetisation of the material in emu/g,
M_r = retentivity, H_c = coercivity, M_s = saturation magnetisation [23].

When an external magnetic field (say H_1) is applied on these materials, they acquire strong magnetism. It is due to the parallel alignment of magnetic domains of materials in the presence of external magnetic field. When the magnetic field is removed, the magnetisation of materials does not diminish completely. It is necessary to expose these materials to applied external magnetic field of opposite direction (say $-H_2$) to acquire entire demagnetisation. The lack of ability of these materials to demagnetise themselves entirely upon removal of applied magnetic field is named 'hysteresis.' As term "hysteresis" originated from Greek word "hyst´er¨esis". The meaning of which is "lag" or "delay." This term is coined by Sir J. A. Ewing. According to Ewing, "When there are two quantities M and N such that cyclic variations of N cause cyclic variations of M, then if the changes of M lag behind those of N, we may say that there is hysteresis in the relation of M to N." These words have been used in in this situation. Hence, the reorientation of "magnetic domains" needs some additional energy to attain its original shape. This type of property of material is useful for the fabrication of devices for data storage due to their capacity hold data, sometimes also named as magnetic "memory" or "magnetic history". The ferromagnetic materials like iron oxides and chromium oxides are also used in the fabrication of audio tapes

and computer disks for the storage of their data. Certain ferromagnetic substances permanently reserve their magnetisation known as "permanent magnets." The process of magnetisation and demagnetisation of magnetic materials in the presence of applied magnetic field can be represented in the form of loop called 'hysteresis loop' (see fig. 2.9) [23]. A detailed discussion of the hysteresis curve is shown in fig. 2.9 is presented in the following paragraph.

Magnetisation "M" vs applied magnetic field strength "H" for a magnetic material is drawn here. The applied magnetic field "H" is independent variable and hence plotted on X-axis whereas, magnetisation is dependent variable is and is plotted on Y-axis. The dotted line shows the magnetisation curve. Initially, the "M" value is zero. "M" increases as "H" increases in a non-linear way and it keep on increasing until it reaches a saturation point ("a," as shown in the graph). The behaviour of the material after the applied magnetic field was removed is drawn in the loop-section "a" to "b." It can be seen from the curve that the ferromagnetic material holds a significant "degree of magnetisation" or "remember" the previous state of magnetisation. The amount of "M" retained in the materials after the removal the applied field "H" is called "retentivity." In fig. 2.9, from the origin of the curve to the height "b" on "Y-axis" is retentivity showing that demagnetisation at this stage is only partial. For complete demagnetisation it is required to expose the material in magnetic field of opposite direction. In the curve, the magnitude of the applied magnetic field in the opposite direction is depicted from "origin of the curve" to the point "c." The opposite magnetic direction is depicted on the "Y-axis" with negative direction. This is called "coercivity" [35,36]. The curve also shows the behaviour of these materials in case they will be kept on exposing in an external field in the negative direction. Points "d" and "e" shows the fate of the material when they are exposed to magnetic fields in the opposite directions. Note that, the behaviour of the material shows coercivity and retentivity irrespective of the direction of the applied magnetic fields. Note that ferromagnetic substances show this behaviour prominently [36,45,46]. The different types of magnetic materials based on coercivity and retentivity values are described below in sub-sec. 2.4.2.2 and 2.4.2.3.

2.4.2.2 Soft magnetic materials

These materials have low coercivity and remanence values but they have a high value of relative permeability. Therefore, these materials are used to make electromagnets. The electromagnet has a temporary magnetic effect, essentially a solenoid with a soft magnetic core giving a strong field that can be controlled by varying the current [35].

2.4.2.3 Hard magnetic materials

Hard magnetic materials largely retain their magnetic character even when the external magnetic field is removed. This is reflected in high coercivity and high remanence values [35].

2.5 Classification of ferrites

2.5.1 Based on their crystal structure (see sub-sec. 2.5.1),

2.5.2 Based on their coercivity and retentivity values (see sub-sec. 2.5.2).

2.5.1 Classification of ferrite based on their crystal structure

Ferrites are classified based on their crystal structure [36]. These are listed in Table 2.1 as shown below [36,47].

Table-2.1 Classification of ferrites based on the crystal structure

S. No.	Ferrites	Crystal structure	Composition		Ref.
1.	Spinel	Cubic	$M^{2+}Fe_2^{3+}O_4$ [M = Divalent cations (Cu^{2+}, Mg^{2+}, Ni^{2+}, Co^{2+}, Zn^{2+}) or its combinations]		36,47
2.	Garnet	Cubic	$R^{3+}Fe_5^{3+}O_{12}$ [R = Trivalent cations (Gd^{3+}, Y^{3+})]		36
3.	Hexaferrite	Hexagonal	$AFe_{12}O_{19}$	"M-type"	36
			$AM_2Fe_{16}O_{27}$	"W-type"	
			$AM_2Fe_{23}O_{46}$	"X-type"	
			$A_2M_2Fe_{16}O_{27}$	"Y-type"	
			$A_3M_2Fe_{24}O_{41}$	"Z-type"	
			$A_4M_2Fe_{36}O_{60}$	"U-type"	
			[M = Divalent cations (Cu^{2+}, Mg^{2+}, Ni^{2+}, Co^{2+}, Zn^{2+}) or its combinations]		
4.	Orthoferrite	Orthorhombic	$R^{3+}Fe^{3+}O_3$ [R = Trivalent cations (Lu^{3+}, Y^{3+}, Gd^{3+}, Sm^{3+}, Nd^{3+})]		36

These ferrites are briefly explained in the following sub-sections as:

2.5.1.1 Spinel ferrites

Spinels have the general formula $MgAl_2O_4$. They are ruby red in colour. Spinel ferrites have general formula AB_2O_4 where A and B are divalent and trivalent cations. In this structure Fe_3O_4 crystallised as the general formula of $Fe^{2+}Fe_2^{3+}O_4^{2-}$ in which substitution is possible in Fe sites. This can be diagrammatically shown in fig. 2.10.
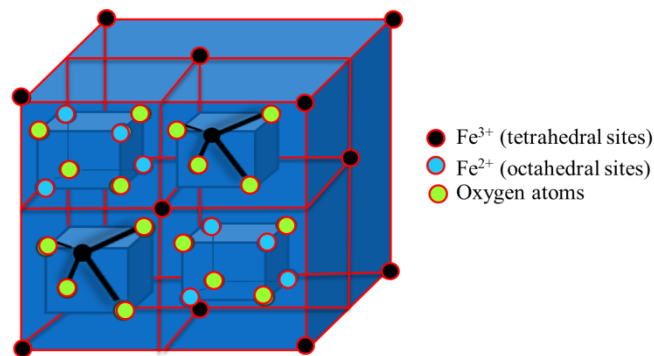
Fig. 2.10 Crystal structure of a general spinel ferrite [48,49].

Substitution is possible by cations of Mn, Co etc. They are named as manganese ferrite and cobalt ferrite, respectively, where the cations occupy 'A' site of the tetrahedral portion of the molecules or it will occupy the 'B' site of octahedral portion of the molecule depending upon oxidation state and the ionic radii of cations. Partial occupancy of both tetrahedral and octahedral sites i.e., $1/8^{th}$ of tetrahedral and ½ of the octahedral sites are occupied. It may be normal or spinel depends upon how cations occupy different interstices. Types of spinel ferrites are presented in Table 2.2.

Table 2.2: Types of spinels based on their crystal structures [4650].

S. no.	Types of spinels	General chemical formula	Structural features	Ref.
1.	Normal	AB_2O_4	A^1 occupy tetrahedral sites. B^2 occupy octahedral sites.	50
2.	Inverse	$(B(AB)O_4)$	A^1 occupy octahedral sites. B^2 equally distributed between tetrahedral and octahedral sites.	50
3.	Mixed	$(A_{1-x}^{2+}B_x^{3+}[A_x^{2+}B_{2-x}^{3+}]O_4^{2-})$, x is degree of inversion	A^1 and B^2 both occupy tetrahedral as well as octahedral sites.	50

1. A: (Mg^{2+}, Cd^{2+}, Cr^{2+}, Cu^{2+}, Mn^{2+}, Fe^{2+}, Co^{2+}, Ni^{2+}, and Zn^{2+})
2. B: (Al^{3+}, Ti^{3+}, Ga^{3+}, In^{3+}, V^{3+}, Cr^{3+}, Ni^{3+}, Fe^{3+}, Co^{3+}, and Mn^{3+})

i.   *Normal spinels:* These spinel's having formula $Me^{2+}[Fe_2^{3+}]O_4^{2-}$ in which all Me^{2+} occupies A site tetrahedral e.g. $Zn^{2+}[Fe^{2+}Fe^{3+}]O_4^{2-}$ (zinc ferrites) and many aluminates such as $MgAl_2O_4$, $FeAl_2O_4$, $CoAl_2O_4$ and a few ferrites such as $CdFe_2O_4$. However, all the Fe^{3+} ions occupy the B site octahedral [46].

ii. *Inverse spinels:* These spinel's having formula $Fe^{3+}[Me^{2+}Fe^{3+}]O_4^{2-}$ in which all Me^{2+} occupies B sites and Fe^{3+} distributed equally between A and B sites e.g. Magnetite Fe_3O_4, $NiFe_2O_4$ and $CoFe_2O_4$. In this structure, ½ of the Fe^{3+} ions occupy the tetrahedral sites and remaining ½ Fe^{3+} and all Me^{2+} ions occupy the octahedral sites [46]. The crystal structure of inverse spinel cobalt ferrite is represented in fig. 2.11 below. Note that the picture (fig. 2.11) is taken from ref. no. 51 where the permission was not required to reproduce the picture.
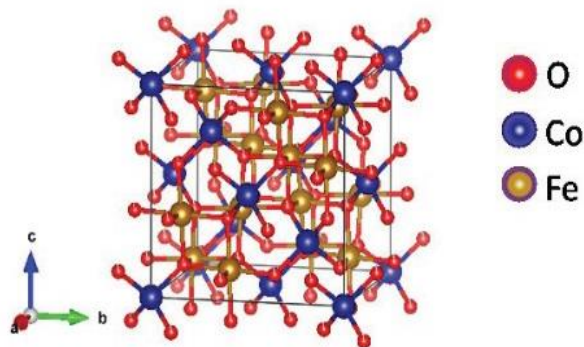
Fig. 2.11 Crystal structure of inverse spinel cobalt ferrite [51].

iii. *Mixed spinels:* The spinel's having formula $Me_{1-y}^{2+}Fe_y^{3+}[Me_y^{2+}Fe_{2-y}^{3+}]O_4^{2-}$, where y is the degree of inversion and cations Me^{2+} and Fe^{3+} occupies A sites and B sites respectively. Despite these structures, few other cubic structures are possible such as perovskite (ABO_3) structure, ReO_3 structure and CsCl structure. Examples of perovskite (ABO_3) are $PbTiO_3$, $BaTiO_3$ etc. [46].

2.5.1.2 Garnets

These are ferrites in which rare-earth ions or transition-metal e.g. Ce^{3+}, Er^{3+}, Tb^{3+}, and Bi^{3+} and others into dodecahedral sites by replacing the Fe^{3+} ions by Ga^{3+}, Al^{3+}, or other metals into tetrahedral sub lattice sites [52].

2.5.1.3 Hexagonal ferrites

These are the ferrites having a hexagonal crystal structure. The main members of the hexagonal ferrite family are as shown below, where Me represents a small 2^+ ion e.g., nickel, cobalt or zinc, and Ba can be substituted by Sr [53].

These ferrites can be further classified as,

i. *M-type:* These are ferrites having formula $BaFe_{12}O_{19}$ (BaM or barium ferrite) where BaM is initially named ferroxdure, other than the spinel ferrite which was called ferroxcube.

ii. *Z-type:* These are ferrites having formula $Ba_3Me_2Fe_{24}O_{41}$ e.g., $Ba_3Co_2Fe_{24}O_{41}$. These are large and complex compounds with formula $Ba_{70}Me_{86}Fe_{444}O_{802}$.

iii. *Y-type:* These are ferrites having formula $Ba_2Me_2Fe_{12}O_{22}$ e.g., $Ba_2Co_2Fe_{12}O_{22}$, or Co_2Y, where Me is a small divalent cation, and the first two to be made were Zn_2Y and Co_2Y.

iv. *W-type:* These are ferrites having formula $BaMe_2Fe_{16}O_{27}$ e.g., $BaCo_2Fe_{16}O_{27}$, or Co_2W, where Me represents a first-row transition metal element one or other divalent cation and the barium substituted by another group two metal.

v. *X-type:* These are ferrites having formula $Ba_2Me_2Fe_{28}O_{46}$ e.g., $Ba_2Co_2Fe_{28}O_{46}$, or Co_2X, where Me represents a divalent first-row transition metal or other divalent Fe^{2+}cation.

vi. *U-type:* These are ferrites having formula $Ba_4Me_2Fe_{36}O_{60}$ e.g. $Ba_4Co_2Fe_{36}O_{60}$, or Co_2U [53].

2.5.1.4 Ortho ferrites

These ferrites having a perovskite structure with formula ABX_3, where A is a cation of large ionic radius of alkaline earth metals or alkaline and most rare earth metals

while B are cations of transition metals of smaller radius and X is anionic species like oxygen [54].

2.5.2 Classification of ferrites based on their coercivity and retentivity values

Ferrites can be classified into two categories based on its coercivity and retentivity values. They are described in the following sub-subsections (see sub-sec. 2.5.2.1 and 2.5.2.2). The shapes of hysteresis loops in these different types of ferrites are shown in fig. 2.12. Although, few authors talked about a third types of ferrite which they referred as semi-hard ferrites which we briefly discussed in sub-sec. 2.5.2.3 [55].
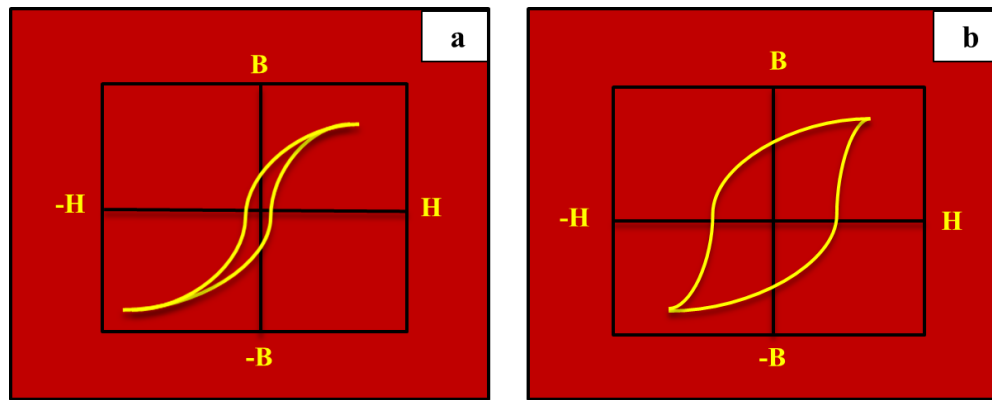
Fig. 2.12 Shape of hysteresis loops in,
a: soft ferrites,
b: hard ferrites [56].

2.5.2.1 Soft ferrites

The hysteresis curve shows that these ferrites have low value of coercivity and remanence (see fig 2.12a). Note that they have a high value of relative permeability. As discussed above in sub-sec. 2.4.2.1 these materials can be used to make electromagnets [33,35,56].

2.5.2.2 Hard ferrites

The shape of hysteresis loops for hard ferrites is depicted in fig. 2.12b. Permanent magnets are made from hard ferrites. Hard ferrites show similar behaviour as hard magnetic materials. They retain magnetic character to a great extent even when the external magnetic field is removed [33,35,56].

2.5.2.3 Semi-hard ferrites

These ferrites are of intermediate coercivity values [57]. Hosni *et al.* considered cobalt ferrite as semi-hard magnetic material [55] (see sub-sec. 2.6.1).

We have co-doped cobalt ferrite with a series of ions. In the next section we will be discussing all the properties of cobalt ferrite in detail (see sec. 2.6). Although, in the above section we have already indicated the magnetic behaviour of this material as far as coercivity and retentivity is concerned.

2.6 Properties of ferrites/cobalt ferrite

Here, we have discussed properties of ferrites with emphasis on the properties of cobalt ferrite as we have synthesised cobalt ferrite co-doped with ions. Ferrites show various properties which are listed below:

(i) Magnetic properties of ferrites/cobalt ferrite (see sub-sec. 2.6.1)

(ii) Electrical properties of ferrites/cobalt ferrite (see sub-sec. 2.6.2)

(iii) Catalytic properties of ferrites/cobalt ferrite (see sub-sec. 2.6.3)

(iv) Optical properties of ferrites/cobalt ferrite (see sub-sec. 2.6.4)

2.6.1 Magnetic properties of ferrites/cobalt ferrite

As discussed in sec. 2.4 and sec 2.5 ferrites are magnetic materials. The different types of ferrites exhibit different crystalline structures as well as different magnetic properties as far as the phenomenon of hysteresis is considered. The crystalline structure of cobalt ferrite is discussed in sub-sec. 2.5.1.1. The magnetic properties of cobalt ferrite based on the shape of hysteresis loop are already described in brief in the sub-sec. 2.5.2.3. Hosni *et al.* classified cobalt ferrite as magnetic materials having semi hard magnetic character [55], whereas Kotnala *et al.* categorised cobalt ferrite as hard magnetic material [36]. Dedi *et al.* categorised cobalt ferrite as a "well-known hard magnetic material with high coercivity and moderate magnetisation", although in the same literature they categorised it as a material with intermediate magnetic material [51].

2.6.2 Dielectric properties of ferrites/cobalt ferrite

Ferrites including cobalt ferrite show dielectric properties. The concept of dielectric properties of materials is discussed in sub-sec. 2.6.2.1 whereas ferrites/cobalt ferrites showing this property as discussed in literature are presented in sub-sec. 2.6.2.2. They are discussed in the following subsections.

2.6.2.1 Concepts related to dielectric properties of materials

The charges present inside a material responds against applied electric field. Yaghmaee *et al.* defined the term 'dielectric' as a "measure of the potential for charge movement inside the material in response to an external electric field" [58]. There are several dielectric materials which we use in everyday life, e.g., distilled water, dry air to name but a few [59]. Mathematically dielectric constant is defined as "the ratio of permittivity to the permittivity of free space" [36]. Permittivity is defined as "the ability of a substance to store electrical energy in an electric field" [36]. Dielectric properties of the material depend upon the formation and movement of the dipoles inside the materials [60]. The term dipole refers to atoms or groups of atoms with an unbalanced charge. In the presence of an applied electric field, they get aligned, which produces polarisation in the material [23]. The polarisation can be categorised as:

i. *Electronic Polarization:* The electronic arrangement or the electron cloud distribution of the atom gets distorted/ changed in the presence of an applied electric field. The electrons/electron cloud concentrate on the side of the nucleus near the positive end of the applied electric field [23].

ii. *Ionic Polarization:* It is observed in ionically bonded materials. When these materials are placed in the applied electric field, the ionic bonds become elastically deformed/ changed. As a result the charge is systematically redistributed within the material. The movement of the cations and anions be influenced by the direction of the applied field, and the induced dipoles produce polarization [23].

iii. *Molecular Polarization:* Certain materials have natural dipoles. In the presence of an applied field, the dipoles rotate and are arranged in the direction of the applied field [23].

Atoms of the substance do not have any intrinsic dipole moment, but they have the capacity to polarize when exposed to magnetic field is called atomic polarizability [61]. Some of the dielectric properties of solids are as follows:

i. *Piezoelectricity:* It is the property of material which shows net dipole moment in the presence of applied electric field [23].

ii. *Pyroelectricity:* Pyroelectricity is the property of material where electric potential is produced at higher temperatures [23].

iii. *Ferroelectricity:* Some of the piezoelectric crystals retain the arrangement of dipoles even in the absence of electric field. They have permanent dipoles. This property is called ferroelectricity. When they are exposed to external electric field, the polarisation changes its direction in reversed order [23].

iv. *Antiferroelectricity:* In this case, the net dipole moment of piezoelectric substances becomes zero [23].

In the following paragraph we have discussed the dielectric property of cobalt ferrite in brief.

2.6.2.2 Dielectric properties of ferrites/cobalt ferrites

Few ferrites including cobalt ferrite shows dielectric properties [62]. This property can be improved by doping, for example chromium doped CF-NPs show improved dielectric properties [63]. Kadam *et al.* doped the CF-NPs with gadolinium ions. They observed an increase in dielectric constant with an increase in gadolinium ion concentrations. The as-prepared samples exhibit excellent dielectric properties [64]. Chakrabarty *et al.* reported that yttrium doping enhances the dielectric character CF-NPs [65]. The as prepared copper-chromium co-doped CF-NPs at different concentrations showed low dielectric loss in a low frequency range. Therefore, these CF-NPs can be used in different electronic applications, such as wireless communication and other electronic devices [66].

2.6.3 Catalytic properties of ferrites/cobalt ferrite

Ferrites, including cobalt ferrite, show catalytic properties [33]. The concept of catalytic properties of materials is discussed in sub-sec. 2.6.3.1 whereas ferrites/cobalt ferrites showing this property as discussed in literature is discussed in sub-sec. 2.6.3.2.

2.6.3.1 Concepts related to catalytic properties of materials

A catalyst alters the rate of a reaction [67]. It lowers the activation energy required to carry out the reaction is called catalysis [68]. The effect of catalyst on the rate of reaction can be graphically shown in the fig. 2.13.
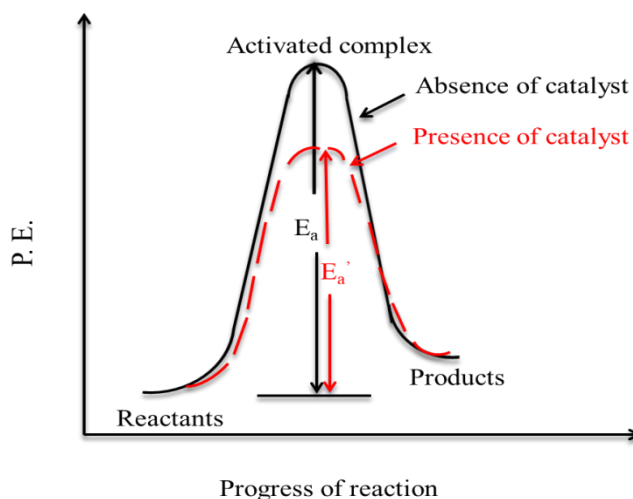
Fig. 2.13 Schematic draw for the effect of catalyst on the rate of reaction [69].

Photo catalysis is the process of using light to speed up or start chemical reactions with the help of a catalyst [70]. Catalytic properties of ferrites/cobalt ferrite are discussed in the following paragraph.

2.6.3.2 Catalytic properties of ferrites/cobalt ferrites

Ferrites show catalytic properties. Several reactions for example, selective oxidation reaction for carbon monoxide, decomposition of alcohols, discolouration of synthetic dyes, and decomposition of hydrogen peroxide can be catalysed using this class of material [68]. Spinel ferrites (MFe_2O_4) containing divalent transition metal ions (M = Fe^{2+}, Ni^{2+}, Cu^{2+}, Zn^{2+}, Co^{2+}) shows catalytic properties. It depends upon the redox nature of substituted ions and distribution of such ions in the tetrahedral as well as octahedral sites of coordination [68]. The spinel oxide (AB_2O_4) powder surface preferably holds octahedral sites. Therefore, its catalytic properties are strongly affected by octahedral cations [68]. Kirankumar *et al.* studied photocatalytic properties of cobalt ferrite. They used this material for the degradation of Congo red [71].

2.6.4 Optical Properties of ferrites/cobalt ferrite

Ferrites including cobalt ferrite show optical properties. The concept of optical properties of materials is discussed in sub-sec. 2.6.4.1 whereas ferrites/cobalt ferrites showing this property as discussed in literature are discussed in sub-sec. 2.6.4.2.

2.6.4.1 Concepts of optical properties of materials

Luminescence is a process of absorption of radiation followed by its emission [72]. It is an optical property of a material [72]. In this process electrons of a material absorbs energy and jump to higher energy state and then return back to their original state to achieve stability (i.e., to a lower energy state). In the return journey they release energy in the form of radiation. This phenomenon is called luminescence [72]. This is explained by Jablonski diagram (see fig. 2.14) [72].
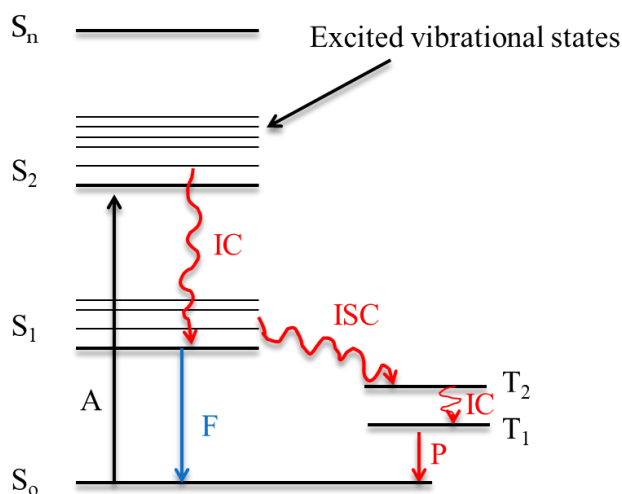
Fig. 2.14 Jablonski diagram presenting the process of photoluminescence where;
IC = internal conversion; ISC = intersystem crossing;
A = absorption; F = fluorescence; P = phosphorescence [72].

This process can be initiated by several ways. The different types of luminescence are categorised based on the different ways of its initiation. For example, when it is initiated by chemicals it is known as chemiluminescence [73], similarly, luminesce initiated by cathode rays or electrons are called cathedoluminescence, and luminesce initiated electrical energy are called electroluminescence [37]. Luminesce initiated by

light or photons are called photoluminescence. This happens mostly by light of ultra-violet region (UV-light) [23,74]. The energy of photon can be calculated by using the Plank's eq^n. (2.2) as;

$$E = h\nu = hc/\lambda \ldots\ldots\ldots\ldots eq^n. (2.2)$$

Where, h = Plank's constant (6.62 x 10^{-34} Js), ν = frequency of radiation ,
c = velocity of light (3 x 10^{-8} m/s) and λ = wavelength of radiation [72].

Metals do not show luminescence [23]. It has been observed in certain ceramics and semiconductors that the energy gap between the valence band and conduction band is such that electrons can easily drop to produce photons of light radiation [23]. The photoluminescent material shows two types of effects. They are fluorescence and phosphorescence. These terms can be discussed in brief as;

i. *Fluorescence:* The transition of electrons from first singlet excited state (S_1) to singlet ground state (S_0) involving emission of photons is called fluorescence. The time required for this process is approximately 10^{-9} sec. to 10^{-4} sec [72].

ii. *Phosphorescence:* The transition of electrons from first triplet excited state (T_1) to singlet ground state (S_0) followed by the emission of photons, is called phosphorescence. This process is also known as delayed fluorescence. Approximately 10^{-4} sec. to 10^{-2} sec is required for the completion of this process [72] .

The interaction of material with photons produces number of optical effects such as absorption, transmission, refraction, reflection, and electronic performance. These phenomena are helpful in understanding the behaviour of materials as well as how these materials can be utilised in number of applications related with critical device that cannot be detected with laser, radar, solar cell, fibre optic devices etc. [23].

2.6.4.2 Optical properties of ferrites/cobalt ferrites

Ferrite materials exhibit optical properties and can be used in optical internet [48]. Doping with different metal ions enhanced their optical properties [13]. Vadivel *et al.* observed that doping of chromium improved the fluorescence properties of CF-NPs. They reported that the doping level of 0.3 at% of chromium gave strong fluorescent emissions [60]. Sumathi *et al.* also reported that the co-doping of CF-NPs with copper and cerium influenced optical properties significantly [75]. Melo *et al.* observed the decrease in optical band gap values with increase in level of doping of nickel ion [76]. Tuning the magnetic, dielectric, optical, and catalytic properties of spinel ferrites make them suitable materials for different applications [13,77]. The different applications of ferrites/cobalt ferrite are discussed in following sec. 2.7.

2.7 Applications of ferrites/cobalt ferrite

Ferrites and cobalt ferrite can be used for numerous applications. A brief discussion about the applications of ferrites/cobalt ferrite is in the following sub-sec. 2.7.1 to 2.7.2.

2.7.1 Applications of ferrites

Ferrite can be used for various applications. These nanoparticles are widely used in audio frequency applications, telecommunication and entertainment applications, EMI applications, microwave devices, magnetic recording appliances e.g. channel filters, magnetic memory cores, wide band transformers, television picture tube yokes, radio and television antennae, magnetic audio tape, floppy disks, hard disks, video cassette tape etc. to name but a few [78]. Ferrites are used as main components in a variety of electronic circuits e.g. voltage-controlled oscillators, low noise amplifiers, impedance matching networks, filters etc. [79]. They can also be used in electronic equipment e.g. computers, scanners, high-speed digital interfaces in notebooks digital cameras etc. [79]. They can be used in phase shifters in which there are two-port components that after changing bias magnetic field provide variable phase shift. It is applied in measurement systems [80]. They are also useful for biotechnological applications. They have several biomedical applications which include therapeutic applications, magnetic resonance imaging (MRI) and hyperthermia [79]. Spinel ferrites are mostly used as

sensing materials. Ferrites are very sensitive towards humidity and gases. It is used as a humidity/gas sensor due to their porosity needed for a humidity sensor [30].

2.7.2 Applications of cobalt ferrites

Cobalt ferrite is spinel in nature [81]. Spinel ferrite has excellent electrical, optical, magnetic and structural properties which can be exploited for various applications [82]. Since we have prepared cobalt ferrite nano particles (CF-NPs) we have discussed its various applications in the following sub-subsections.

2.7.2.1 Biomedical applications

i. *In biosensors:* CF-NPs are widely used in bio sensing applications because of their ability to align themselves with external magnetic field [2].

ii. *For magnetic separation and purification:* These materials can be utilized for magnetic extraction, separation, and purification for pollutants and toxins from environmental and biological samples [2].

iii. *In diagnostic and therapeutic applications*: CF-NPs can be used in diagnostic and therapeutic applications. The magnetic susceptibility of CF-NPs can be used for magnetically targeted drug delivery systems. It can be used for Magnetic Resonance Imaging (MRI) [2].

iv. *Drug delivery:* They can also be used as promising materials for nanocarriers for drug delivery applications with encouraging results and studies that have reached clinical trials in the past decade [2].

v. *Hyperthermia:* Magnetic hyperthermia is a therapeutic method where magnetic nanoparticles are administered at the tumor site. The treatment incorporates application of electromagnetic field (in radiofrequency). CF-NPs are widely used for this application [2].

2.7.2.2 Applications of cobalt ferrite as catalyst

Cobalt ferrite nanoparticles used as a nano catalyst in organic synthesis for many reactions e.g. condensation, oxidation, reduction, coupling and multi-component reactions. Cobalt ferrite nanocatalysts have many advantages like a simple operation, preparation, easy separation, high catalytic activity and ability to reused [83]. CF-NPs

with sizes up to 25 nm used as a catalyst for the oxidation of different alkenes in the presence of tert-butylhydroperoxide (t-BuOOH). The study shows that CF-NPs are an efficient catalyst for the conversion of alkenes to aldehydes or epoxides with good yield. The catalyst isolated with an external magnet and no loss of activity was examined when it reused. The effects of parameters on the oxidation reactions were observed e.g. temperature, nature of oxidant and solvents [84].

People working in "Materials Science and Engineering" try to tailor the properties of materials for desired applications. Doping is widely used to modify the properties of materials [9]. The concept of doping is discussed in the following section (see sec. 2.8).

2.8 The basic concept of doping

The word 'doping' originated from the Afrikaans word "dop,". The term 'dop' stands for small stimulating drink. It is an impurity effect which changes the original structure of the molecule. Generally, it is restricted to very low quantities [85]. Doping is a technique used for modification of solid states properties by addition of small amount of impurity in a base material [85]. The small concentration of dopant changes the conductivity of material. For example, doping of phosphorus into silicon changes into n-type conductor while the doping of boron changed the silicon into p-type conductor [85]. Doping alters the properties of materials hence, materials of desired properties for specific applications can be synthesised using various routes of synthesis. A brief review on routes of synthesis of doped ferrites is discussed in sec. 2.9.

2.9 A brief review on routes of synthesis of doped ferrites

Several rsearch groups worked on doping of ferrites with metal and non–metals [5,86–88]. For example, Ran *et al.* prepared magnetite film doped with Co^{2+} ion to study the influence of doping on magnetic, structural, and valance band structures [87]. Cao *et al.* synthesised sulphur doped coral-like CF-NPs [88]. Sharifianjazi *et al.* published their review paper on doping of the cobalt ferrites with metals [86]. We also published a mini-review on synthesis of ferrites using various parts of plants [5]. A list of doped ferrites

prepared with various metal ions and using different parts of plants is presented in Table 2.3 [9,19,32,89–100]

Table 2.3: Routes of synthesis of ferrites doped with various metal ions and using various parts of plant.

S. No.	Name of ferrite	Routes of synthesis	Ref.
1.	$NiFe_2O_4$	Sol-gel	[94]
2.	$CoFe_2O_4$	Ceramic method	[9]
		Co-precipitation	[9]
		Sol-gel auto-combustion	[9]
		Polyol method	[9]
		Microemulsion	[9]
		Solid state reaction technique	[9]
3.	$ZnFe_2O_4$	Thermal treatment method	[95]
4.	$AgFe_2O_4$	Modified co-precipiation	[96]
5.	$CuFe_2O_4$	Aerosol method	[97]

S. No.	Name of ferrite	Routes of synthesis/ Parts of plants used	Ref.
1.	$CoFe_2O_4$	Self-combustion/ *Ginger* root and *Cardamom* seeds	[98]
		Self-combustion and wet ferritization /*Hibiscus rosa- sinensis* flower and leaf	[19]
2.	$NiFe_2O_4$	Green synthesis/ *Hydrangea paniculata* flower	[99]
		Greener synthesis/*Rosemary* leaves	[100]
		Modified sol-gel /*Aloe- vera* plant	[32]
3.	$ZnFe_2O_4$	Microwave-assisted/ Limonia acidissima juice	[89]
		Co-precipitation/ *Aurantium* flower	[90]
		Green method/*Aegle marmelos* leaves	[91]
		Modified sol-gel /*Aloe-vera* plant	[32]
4.	$CuFe_2O_4$	Microwave heating and modified sol–gel /*Hibiscus rosa-sinensis* leaf	[92]
		Modified sol-gel / *Aloe-vera plant*	[32]
5.	$AgFe_2O_4$	Co-precipitation/ *Amaranthus blitum* leaves	[93]

Since, our work is focussed on synthesis of co-doped cobalt ferrite we have reviewed doping and co-doping of cobalt ferrites in separate sections (see sec 2.12 to 2.16).

2.10 Doping of cobalt ferrite nanoparticles (CF-NPs)

As discussed above in sec. 2.8, doping changes the properties of materials [9] and hence this can be a method to produce materials of tailored properties for desired applications [9]. Hence, several routes of synthesis have been developed for doping of cobalt ferrite [9,50,101]. All the routes of synthesis for doping of ferrites are discussed in sec. 2.11. A small review on doping of CF-NPs with 3d-series and 4d-series elements of Periodic Table is discussed in sec. 2.12. Similarly, doping of CF-NPs with rare-earth elements is discussed in sec. 2.13, whereas doping of CF-NPs with representative elements are discussed in sec. 2.14. The doping of CF-NPs with non-

metal elements is discussed in sec. 2.15 whereas the doping procedures of CF-NPs with more than one element are discussed in sec. 2.16.

2.11 Explanation of routes of synthesis of doped CF-NPs

The methods used for the synthesis of doped cobalt ferrite are discussed in the following sub sections (see sub-sec. 2.11.1 to 2.11.6).

2.11.1 Sol-gel method

This is a versatile route of synthesis for the preparation of a wide range of materials e.g., ceramics and glasses [23]. It can be summarised in the following steps:

i. *Preparation of sol*

A sol is liquid colloidal solution having dissolved/dispersed metallic ions. It starts with the formation of colloid by addition of starting materials in alcoholic or aqueous solvents. It is believed that hydrolysis and condensation occur in the reaction mixture. Generally, sol is a stable solution in which small solid particles are suspended. Usually, a sol is continually stirred using magnetic stirrers for homogenization [23].

ii. *Formation of gel*

Hydrolysis generates cites for condensation for the formation of particles whereas condensation is responsible for the formation of gels. The formation of a three-dimensional network results in the formation of a visually thick gel. Most of the times, the transformation of sol into gel can be visually observed and hence this method of synthesis is known as sol-gel route of synthesis of materials [17,23,102,103].

iii. *Formation of powder*

Generally, a powder is obtained when the gel is dried. A hydrogen bond as well as van-der-Wall's force dominates the interaction between the particles present in the sol as well as gel. This reaction can be controlled by controlling temperature, pH, use of solvents, catalysts, and their rate of mixing [17,23,102,103].

iv. *Heating of powder*

The powder after further heating at high temperature at furnace produces the desired sample [17,23,102,103]. Different research groups termed this process with different names. Few of them used the term 'calcination' [10,104], whereas few of them have used the term 'annealing' [102,105]. A complete list of terms used in literature is listed in Table 2.5 and Table 2.7. Actually, the whole idea behind heating of powder is to remove the undesired volatile impurity from the sample. This can be adsorbed or absorbed water [32]. Sometimes, authors also believe that residual starting materials can be removed by heating process [95].

The general processing of the sol-gel route of synthesis is depicted in fig. 2.15 below.
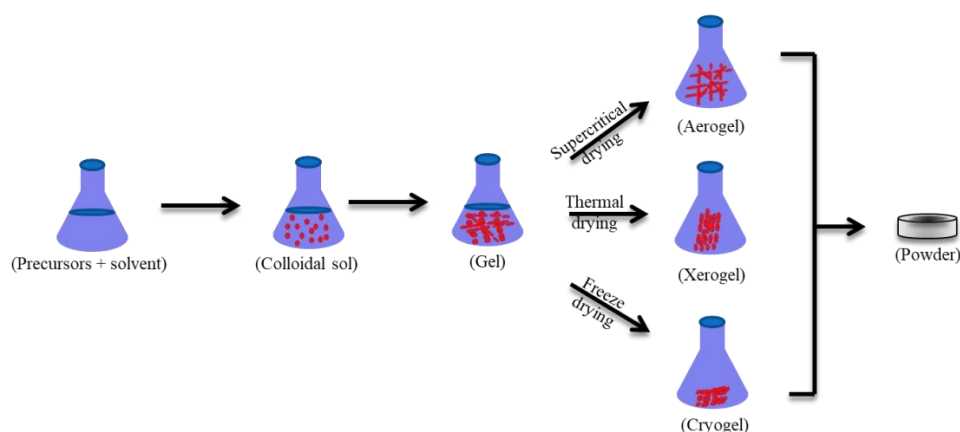
Fig.2.15 A pictorial representation of the various steps involved during sol-gel method [22].

Schematic flow of above described process is depicted in fig. 2.16 as,

Fig. 2.16 Flow chart of sol-gel route

An example of preparation of cobalt ferrite through sol-gel route is described here in brief. Gore *et al.* prepared bismuth doped cobalt ferrite using sol-gel route. They prepared a mixture of metal nitrates in deionized water. The mixture was constantly stirred using a magnetic stirrer to maintain the homogeneity of the reaction mixture.

They used citric acid and glycine as chelating agents. The gel was dried when a powder was formed. The powder was then heated at 500 ºC for four hours [81].

In this method the reaction occurs in solvent medium. This is one of the most widely used method due to its,

  (i)   simplicity,

  (ii)   can occur at room temperature as well as heat treatment can be employed if required,

  (iii)   change in precursor changes the sample which enables the researcher to produce a large variety of samples,

  (iv)   homogeneity can be achieved,

  (v)   samples with uniform grain-size can also be prepared

  (vi)   does not require sophisticated laboratory infrastructure [17,106].

Several other methods are also developed for the preparation of these materials which are briefly described in the following sub-sections (2.11.2 to 2.11.6)

2.11.2 Combustion method

This is fast and non-cumbersome method to synthesize ferrites nanoparticles. It has been reported in the literature that the quality products were excellent. The size of material particles, saturation magnetisation and their coercivity affected with rate of fuel to nitrates [4].

2.11.3 Co-precipitation route

This is a simple and cost-effective method. It is possible to control the rate of nucleation and growth of crystal by changing the reaction conditions [4].

2.11.4 Precipitation method or Stöber synthesis

This is a simple method same as co-precipitation method of synthesis. It does not require sophisticated laboratory infrastructure. The difference between co-precipitation and precipitation methods, is the length of time required in completing the reaction [4].

2.11.5 Hydrothermal method

In this route of synthesis an aqueous solution is employed in the reaction system. A special closed vessel used to create high pressure and temperature for the completion of reaction [107].

2.11.6 Plant extract mediated synthesis

The CF-NPs can be synthesised by using various parts of pants. A complete list of parts of plants used for this purpose is presented in Table 2.3. Ferrites of Ag, Co, Zn and Ni were synthesised successfully. Few doped ferrites, e.g., Ag-doped CF-NPs, Ni-doped zinc ferrite, and Zn-doped nickel ferrite were also prepared. Use of plant-parts evades the necessity of the use of expensive metal salts. The different parts of plants like flowers, leaves, and seeds act as a chelating agent, gelling agent, capping agent, and reducing agent during reactions. This is a non-toxic, eco-friendly, and cost-effective method [5].

2.12 Doping of CF-NPs with 3d-sries and 4d-series elements of Periodic Table

Various routes of synthesis used to synthesize 3d-series doped cobalt ferrites are listed in the Table 2.4 [10,15,31,76,108–113].

Table 2.4: Methods of synthesis used for 3d-series doped CF-NPs

Dopant/s	Methods of synthesis	Heating aid used/processing	Heating temp. (ºC)	Ref.
Cr	Sol-gel auto-combustion	Oven	120	[10]
Mn	Fast hydrothermal	Autoclave	200	[108]
Mn	Co-precipitation	Electric oven	150	[109]
Ni	Auto combustion	Self-propagated combustion	300	[110]
Ni	Hydrothermal	Autoclave	180	[76]
Cu	Octanoate co-precipitation	Tubular furnace	400	[31]
Zn	Auto combustion	Auto ignition	200	[111]
Zn	Chemical co-precipitation	Drying and heated at 800 ° C	100	[15]
Zn	Sol-gel auto-combustion	Oven	200	[112]
Zn	Combustion	Muffle furnace	500	[113]

The final product was obtained in the form of powder in all the above mentioned literature [18,76,109–115]. The heating process used after powder formation of 3d-series doped CF-NPs is listed in Table 2.5.

Process of powder heating	Temp. (ºC)	Time (hours)	Ref.	Process of powder heating	Temp. (ºC)	Time (hours)	Ref.
[1]S	1200	12	[7]	A	200	6	[109]
S	1200	12	[116]	A	600	6	[18]
S	1250	2	[117]	S	450	4	[110]
[2]C	500	4	[63]	D	100	3	[76]
[3]A	600	3	[60]	S	800	4	[114]
C	400, 800	2	[10]	A	800	10	[115]
S	1350	24	[118]	S	1300	12	[111]
S	1180	4	[119]	S	900	3	[112]
[4]D	80	4	[108]	C	650	5	[113]

Where, S = sintered, C = calcined, A = annealed, D = dried

The different routes of synthesis for 4d-series doped CF-NPs are listed in the Table 2.6 [19–21,62,65,104,120–128].

Table 2.6: Methods of synthesis for 4d-series doped CF-NPs

Dopant/s	Methods of synthesis	Heating aid used/processing	Heating temp. (ºC)	Ref.
Y	Citrate auto ignition	Furnace	120	[125]
Y	Citrate auto ignition	Furnace	120	[65]
Y	Sol-gel combustion	Air-furnace	200	[104]
Y	Citrate precursor	Oven	Step1: 100	[21]
		Air atmosphere	Step 2: 200	
Zr	Sol-gel using aqueous silica colloid	Dried	Step 1: 110	[126]
		Ignited	Step 2: 650	
Zr	Co-precipitation	Air-oven	110	[62]
Zr	Sol–gel based Pechini process	Oven	185	[127]
Mo	Solution combustion	Furnace	400	[128]
Ru	Conventional sol-gel	Dried	90	[120]
Ru	Pulsed laser deposition (PLD)	Deposition	600	[121]
Ag	Sol-gel auto-combustion method via chemical and green synthesis	Hot plate	300	[122]
Ag	Self-combustion and wet ferritization	Heater	Step 1: 250–300	[19]
		Suspension maintained	Step 2: 80	
Cd	Auto combustion	Heated	250	[20]
Cd	Sol-gel	Oven	Step 1: 100	[123]
		Heated	Step 2: 200	
Cd	Usual ceramic	Presintered in air	Step 1: 900	[124]
		Cooled	Step 2: Cooling	

The final product was obtained in the form of powder in all the above mentioned literature [19,105,120,121,124,129–131]. The heating process used after powder formation of 4d-series doped CF-NPs is listed in Table 2.7.

Table-2.7: Heating process after powder formation

Process of powder heating	Temp. (ºC)	Time (hours)	Ref.	Process of powder heating	Temp. (ºC)	Time (hours)	Ref.
[1]S	800	2	[125]	C	1200	20	[129]
S	800	2	[65]	C	1200	12	[130]
[2]C	*300, 600, 900, 1200	1	[104]	A	400	2	[120]
[3]A	800	2	[21]	A	450	1	[121]
A	400	2	[77]	A	800	1	[19]
S	1150	8	[132]	S	1200	3	[124]
C	700	4	[62]	S	1050	2	[131]
C	700	1	[127]	A	*400, 600, 800, 1000	2	[105]

Where, S = sintered, C = calcined, A = annealed
Samples were heated at different temperatures to study the effect of calcination and annealing temperatures.

The properties of CF-NPs can be changed by changing the method of synthesis, by changing the annealing temperature, and by doping/substitution [101]. Doping of CF-NPs with 3d-series and 4d-series elements have been widely studied because of their comparable ionic sizes [9,50,101]. Here, sub-sec. 2.12.1 describe the impact of doping in CF-NPs with 3d-series and 4d-series elements, 2.12.2 represents the Crystal structure studies using XRD, 2.12.3 FTIR analysis for various functional groups, 2.12.4 shows Vibrating Sample Magnetometer (VSM) study and 2.12.5 represents the Field Emission Scanning Electron Microscopy (FESEM) study of CF-NPs doped with 3d-series and 4d-series elements.

2.12.1 Impact of doping

The effects of doping on CF-NPs with the elements of 3d-series and 4d-series are listed in Table 2.8 [108,110,113,114,116,117,133,134].

Table 2.8: Effect of doping in CF-NPs with 3d-series and 4d-series elements

3d-series				4d-series			
Dopant	Properties	Effect of doping	Ref.	Dopant	Properties	Effect of doping	Ref.
Sc	Lattice parameter	Increases	[116]	Y	Electrical transport	Improves	[132]
V	Particle size	Improves	[133]	Zr	Coercivity and saturation magnetisation	Increases with decrease in dopant level	[127]
Ti	Curie temperature	Reduces	[117]	Nb	Magneto-electric and ferroelectric properties	Shown at doping level of 0.05	[129]
Cr	Magneto elastic, dielectric and fluorescent	Changes	[134]	Mo	Lattice parameter	Increases	[130]
Mn	Crystallite diameter	Decreases	[108]	Ru	Saturation magnetisation	Decreases	[120]

3d-series				4d-series			
Dopant	Properties	Effect of doping	Ref.	Dopant	Properties	Effect of doping	Ref.
Ni	Dielectric	Changes with the frequencies change	[110]	Ag	Antibacterial properties	Improves	[19,122]
Cu	Antibacterial	Improves	[114]	Cd	lattice parameter	Increases	[124]
Zn	Antibacterial, photocatalytic	Improves	[113]	Cd	Curie temperature	Linearly decreases	[131]

2.12.2 Crystal structure studies using X-ray Diffraction (XRD) technique

The X-ray diffraction peak obtained for CF-NPs doped with 3d-series at different º/2θ values are listed in Table 2.9 [7,108,109,114,133,135].

Table 2.9: List of crystalline peaks obtained for some 3d-series doped CF-NPs.

3d-series elements doped CoFe$_2$O$_4$							
Intensity(/º2θ)	Assign.	Dopant	Ref.	Intensity(/º2θ)	Assign.	Dopant	Ref.
31	222	Sc	[7]	30.2	220	Mn	[109]
18.389	111	V	[133]	35.5	311		[109]
30.25	220		[133]	43.2	400		[109]
35.632	311		[133]	53.1	422		[109]
37.274	222		[133]	57.1	511		[109]
43.309	400		[133]	63.17	440		[109]
53.736	422		[133]	71.39	620		[109]
57.286	511		[133]	74.82	533		[109]
62.913	440		[133]				
18.24	111	Mn	[108]	30.11	220	Zn	[135]
30.06	220		[108]	35.46	311		[135]
35.45	311		[108]	37.16	222		[135]
37.28	222		[108]	43.1	400		[135]
47.87	331		[108]	53.52	422		[135]
53.89	422		[108]	57.01	511		[135]
57.16	511		[108]	62.61	440		[135]
62.73	440		[108]	74.1	533		[135]
74	533		[108]				
79.08	444		[108]				
30.18	220	Cu	[114]	53.42	422	Cu	[114]
35.55	311		[114]	56.96	511		[114]
37.16	222		[114]	62.57	440		[114]
43.11	400		[114]				

The X-ray diffraction peak obtained for CF-NPs doped with 4d-series at different º/2θ values are listed in Table 2.10 [77,120,122,126].

4d-series doped CF-NPs					
Dopant = Y			**Dopant = Ru**		
Intensity of diffraction (/º2θ)	**Assign.**	**Ref.**	**Intensity of diffraction (/º2θ)**	**Assign.**	**Ref.**
31	220	77	30.16	220	120
36	311	77	35.59	311	120
43	400	77	43.25	400	120
57	511	77	57.16	511	120
62	440	77	62.72	440	120
Dopant = Zr			**Dopant = Ag**		
Intensity of diffraction (/º2θ)	**Assign.**	**Ref.**	**Intensity of diffraction (/º2θ)**	**Assign.**	**Ref.**
18.3	111	126	30.174	220	122
30.2	220	126	35.42	311, 222	122
35.6	311	126	43.19	400	122
37.2	222	126	53.54	422	122
43.2	400	126	57.1	511	122
53.1	422	126	62.69	440	122
57.2	511	126			
62.7	440	126			
74.2	533	126			

2.12.3 Identification of functional groups using Fourier-transform infrared (FTIR)

We have tabulated the various absorption band values obtained in FTIR analysis for various functional groups when CF-NPs doped with 3d-series elements are listed in Table 2.11 [31,60,76,113].

Table 2.11: List of absorption bands obtained in FTIR analysis for CF-NPs doped with 3d-series elements and their assignments of functional groups.

CoFe$_2$O$_4$			CoFe$_2$O$_4$		
Abs. (cm^{-1})	**Assign.**	**Ref.**	**Abs. (cm^{-1})**	**Assign.**	**Ref.**
600-500	M-O	60	586	M$_A$-O	76
430-385	M-O	60	382	M$_A$-O	76
587	Fe-O	60			
3423	OH	60	562	M$_B$-O	76
1624	H-O-H	60	375	M$_B$-O	76
2852	CH$_2$	60	540	Fe-O	31
2920	CH$_2$	60	375	Cu/Co-O	31
587-593	Fe-O	60	500-600	M-O	31
			385-450	M-O	31
3415-3428	H-O-H	113	569-582	Fe-O	113
1618-1632	C-O	113	385-403	Co-O	113

We have tabulated the various absorption band values obtained in FTIR analysis for various functional groups when CF-NPs doped with 4d-series elements are listed in Table 2.12 [20,77,104,120,122,125,127].

Table-2.12: List of absorption bands obtained in FTIR analysis for CF-NPs doped with 4d-series elements and their assignments of functional groups

4d-series elements doped CF-NPs					
Abs. (cm^{-1})	Assign.	Ref.	Abs. (cm^{-1})	Assign.	Ref.
3679-1410	O-H	[125]	600	M-O stretching vibration tetrahedral	[127]
1275	C=O stretching vibration	[125]	400	M-O stretching vibration octahedral	[127]
1060	Nitrate group	[125]	1400	C-H vibration	[127]
550	M-O vibration tetrahedral	[125]	1700	C=O	[127]
350	M-O vibration octahedral	[125]	2300	C≡N	[127]
			3100	C-H	[127]
400	M-O stretching tetrahedral	[104]	3400	H-O-H	[127]
600	M-O stretching octahedral	[104]			
590	M-O vibration tetrahedral	[77]			
410	M-O vibration octahedral	[77]	530	Intrinsic stretching vibrations of metal at the tetrahedral site	[120]
370-800, 587	Fe-O stretching vibration	[122]			
400	Fe-O stretching vibration	[122]	1052	C-O stretching vibration	[20]
579	M-O Stretching vibration tetrahedral	[20]	1365.1	O-H	[20]
415	M-O Stretching vibration octahedral	[20]			

2.12.4 Magnetic properties studies using Vibrating Sample Magnetometer (VSM)

VSM was widely used to study the magnetic behaviour of samples [50,101]. A brief paragraph on the VSM data for 3d-series doped CF-NPs obtained by various research groups is described in the following paragraph, whereas the VSM data for 4d-series doped CF-NPs obtained by various research groups is listed in Table 2.13.

Table 2.13: List of a few important magnetic properties of doped CF with 4d-series ions

Dopant	[1](M_s)	Ref.	Dopant	[2](H_c)	Ref.	Dopant	[3](H_k)	Ref.
Y	[6](D)	[125]	Y	[(D) to (I)]	[125]	Y	[(I) to (D)]	[125]
Y	(D)	[21]	Y	[7](I)	[21]	Y	(D)	[21]
Y	(D)	[77]	Y	(D)	[77]	Zr	(I)	[62]
Y	(D)	[132]	Y	(I)	[132]	Zr	(I)	[127]
Zr	(D)	[62]	Zr	(I)	[62]	Nb	(D)	[129]
Zr	(D)	[127]	Zr	[(I) to (D)]	[127]	Mo	[8](R)	[130]
Nb	(D)	[129]	Mo	(D)	[130]	Ag	[9](E)	[105]
Mo	[11][(D) to (I)]	[130]	Mo	(D)	[128]	**Dopant**	[4](M_r)	**Ref.**
Mo	[12][(I) to (D)]	[128]	Ru	(D)	[121]	Y	(D)	[125]
Ru	(D)	[120]	Ag	[13][(I) and (D)]	[105]	Zr	(D)	[62]
Ag	(D)	[105]	Cd	(D)	[19]	Zr	(D)	[127]
Cd	[(I) to (D)]	[124]	**Dopant**	[5](M_r/M_s)	**Ref.**	Mo	[10](S)	[128]
Cd	[(I) to (D)]	[131]	Y	[(D) to (I)]	[125]	Cd	(D)	[19]
-	-	-	Cd	(D)	[19]	-	-	-

Where, M_s = Saturation magnetisation, H_c = Coercivity/coercive field, H_k = Anisotropy/anisotropy field, M_r = Remnance magnetisation, M_r/M_s = Remnance ratio, D = Decreased, I = Increased, R = Reduced, E = Enhanced, S = Same, [(D) to (I)] = First decreased and then increased, [(I) to (D)] = First increased and then decreased, [(D) and (I)] = Decreased as well as increased.

The magnetic properties of 3d-series doped CF-NPs were studied by using Vibrating Sample Magnetometer (VSM). The hysteresis loop showed that the saturation

magnetisation (M_s) decreased with increasing scandium content. The coercivity (H_c) increased from 1200 G to 7194 G for r=0 to r=0.8 when CF-NPs were doped with scandium [7]. The out of plane hysteresis loop also indicated that there was some difference between CF-NPs thin films with scandium doped CF-NPs [116].The vanadium substitution changes the anisotropy field that can also effect on the coercivity value [133]. The titanium doped CF-NPs showed the reduced Curie temperatures, decreased magneto mechanical hysteresis and magnetic anisotropy [117]. The reduction in magnetocrystalline anisotropy continued for the limit (x = 0.3) at 300 K [136]. The chromium substituted CF-NPs decreased magnetic anisotropy [134]. A decrease in magnetic anisotropy was observed with increase Cr content for a constant temperature [63]. It is believed that replacement of Fe^{3+} ion with less magnetic Cr^{3+} ion at octahedral (B) site caused this decrease (i.e., decrease in magnetic anisotropy) [60]. The coercivity was also decreased due to migration of Co^{2+} ions into the tetrahedral site [10]. All the manganese doped CF-NPs samples resulted to decrease in magnetic anisotropy with increasing Cr content and increased with decreasing temparature observed at the range of 400 and 150 K [21]. The mangetostriction coefficient was monotonically decreased with increasing Mn content [137]. The wide hysteresis loop defined characteristics of hard magnetic material [108]. It also observed that all the synthesised Mn doped CF-NPs have coercivity (Hc) always greater than half the value of remanent magnetisation (Mr) [109]. The nickel substituted CF- NPs showed that the magnetic saturation (M_S) was decreased with increasing Ni^{2+} ion concentrations [18]. The hysteresis loop of nickel substituted CF-NPs for the concentration 0.4 give rise to maximum crystallite size of 44 nm [110]. The coercivity (H_c) was increased with doping of nickel ion due to many factors like size distribution, morphology of particles, magnetic domain size, micro strain and the distribution of cations at octahedral and tetrahedral sites [76]. The copper substituted CF-NPs behaved like ferromagnetic material at room temperature. The hysteresis loop of the prepared sample in the absence of magnetic field showed spontaneous magnetisation [31,114,115]. The saturation magnetisation of zinc substituted CF-NPs was increased with increasing zinc content. Magnetic measurements confirmed the ferromagnetic behaviour of Zn doped CF-NPs. The hysteresis curve confirmed that saturation magnetisation, coercivity, and remanent magnetisation decreased with increasing zinc content [15,107,112,113].

2.12.5 Study of morphology of particles using electron microscopy

FESEM was mostly used to study the   morphology of the synthesised samples [50,101].
A brief paragraph on the Field Emission Scanning Electron Microscopy/Scanning
Electron Microscopy (FESEM/SEM) for 3d-doped and 4d-doped CF-NPs obtained by
various research groups is described in the following paragraph.

Lefevre *et al.* observed the surface of the thin films using SEM [116].Imanipour reported
that doping with vanadium changed the morphology of cobalt ferrite from semi-
spherical to cubical. The EDAX analysis demonstrated the existence of secondary
phases like Fe_2O_3 were confirmed using FE-SEM in case of vanadium doped CF-NPs
[133]. Ti doped CF-NPs showed existence of greater porosities by cation substitution
than undoped CF-NPs [136]. Cr-doped CF-NPs for all the sintered samples showed
small grain size and homogeneous microstructure. It also confirmed the formation of
nanoparticles at room temperature [10,138]. Mn substituted CF-NPs showed dense and
homogeneous microstructure [118]. Ni substitution showed random distribution and
agglomeration of grains because of the ignition of fuel during course of reaction [110].
Cu substitution showed an angular morphology and irregular agglomerated particles.
The shape of particles is yeast like [31,114]. The Zn substituted CF-NPs formed spherical
shaped very fine agglomerated particles [15,89,135].

The HR-SEM (High Resolution-Scanning Electron Microscopy) study of yttrium
doped CF-NPs confirmed the cubic morphology of the particles [104]. All the zirconium
doped samples were of spherical shapes. Broad range of particle sizes were observed
[126]. Ramana *et al.* observed that an increase in molybdenum content increased the
particle size of the product. They believed that this may be due to either difference in
ionic sizes of molybdenum and iron or variable valences of molybdenum. They also
assumed that replacement of iron with larger molybdenum affected the mobility of
particles which led to the formation of larger particles [130]. It was also observed that
particles of different shapes were obtained when they were synthesised using different
methods. One example of this phenomenon was reported by Gingasu *et al.* Porous and
complex shaped particles were obtained when they prepared silver doped CF via self-

combustion method using extract of hibiscus flower whereas agglomeration of fine particles was observed when synthesised using wet-ferritization method [19].

The FE-SEM studies of yttrium doped CF-NPs confirmed the formation of homogeneously distributed agglomerated particles of uniform shape at the dopant level x = 0.5 [21]. The zirconium substitution formed highly agglomerated particles [127]. On the other hand, ruthenium doped samples were of spherical morphology. Agglomeration of particles was also observed [120]. The silver doped sample of CF-NPs showed distorted cubic morphology [122].

2.13 CF-NPs doped with rare earth elements

Cobalt ferrites is doped with rare earth elements by several research groups [9]. Jauhar *et al.* reported in their review paper that several rare earth ions doped CF-NPs, for example, "$CoLn_{0.12}Fe_{1.88}O_4$" where Ln = Sm, Ce, Eu, Dy, Gd, Er were synthesised. Doping of Sm^{3+}, Eu^{3+} and Ce^{3+} decreased saturation magnetisation values. Coercivity increased with an increase in doping levels of these ions [9]. A series of rare-earth doped CF-NPs with general formulae "$CoFe_{1.9}RE_{0.1}O_4$" where RE = La, Ce, Nd, Sm, Eu, Gd, Tb, Ho were prepared. It was reported that lattice parameters of these doped materials were larger than the un-doped CF-NPs [9]. Doping of Dy^{3+} ions increased both lattice parameter and size of crystals, whereas Curie temperature reduced unexpectedly [139]. Effect of doping in cobalt ferrite with rare earth elements is tabulated in Table 2.14.

Table 2.14: Effect of doping in CF-NPs with rare earth elements

Rare earth elements			
Dopant/s	Properties	Effect of doping	Ref.
Sm^{3+}	Saturation magnetisation	Decreases	[9]
Dy^{3+}	Lattice parameter and coercivity	Increases	[139]
Eu^{3+}	Saturation magnetisation	Decreases	[9]
Ce^{3+}	Coercivity	Increases	[9]

2.14 CF-NPs doped with representative elements

Representative elements are also used as dopants/substituents to modify the properties of cobalt ferrites [9]. Mg^{2+} ion-doped CF-NPs shows that crystallite size decreases and coercivity increases when level of doping was increased [140]. It is possible to dope

cobalt ferrite with calcium ions. It was observed that Ca^{2+} ions occupy 'A' sites of the tetrahedral ferrite sub-lattice [141] . They also observed that Al^{3+} ions doped CF-NPs showed decrease in saturation magnetisation and lattice parameter with increase in level of doping. This phenomenon was observed by Waghmare *et al.* as well [9,142]. CF-NPs were doped with tin, gallium, and bismuth. Doping with these elements increased the lattice parameter [9]. Sn-doping decreases saturation magnetisation due its non-magnetic property whereas, it increases with the doping of bismuth and gallium [9]. Gore *et al.* reported that bismuth doped ferrites can have the potential for application in magnetic recording and memory devices [81]. The effect of doping in CF-NPs with few representative elements is listed in Table 2.15 [9,142].

Table 2.15: Effect of doping in CF-NPs with representative elements

Dopant/s	Properties	Effect of doping	Ref.
Mg^{2+}	Crystallite size	Decreases	140
	Coercivity	Increases	140
Al^{3+}	Lattice parameter	Linear decrease	9,142
	Saturation magnetisation	Linear decrease	9,142
Sn^{4+}	Saturation magnetisation	Decreases	9
Bi^{3+}	Lattice parameter	Increases	9

2.15 CF-NPs doped with non-metals

The non-metal doped cobalt ferrite affected the band-gap of the crystals with the enhancement of nonmagnetic material properties [9]. Cao *et al.* doped CF-NPs with sulphur that can be used for higher chemical reactivity than the un-doped material. The doping of non-metal increases saturation magnetisation due to the cation redistribution and larger nanoparticles size [88]. They also reported in a sepearte work that the doping of CF-NPs with carbon increase its saturation magnetisation (M_s). The M_s value of nitrogen-doped CF-NPs shows no change due to the introduced non-magnetic Fe_2O_3 [143]. Effect of doping in cobalt ferrite with non-metals is presented in Table 2.16 [88,143].

Table 2.16: Effect of doping in CF-NPs with non-metals

Non-metal			
Dopant/s	Properties	Effect of doping	Ref.
S	Saturation magnetisation	Increases	88
N	Saturation magnetisation	No change	143
C	Saturation magnetisation	Increases	143

2.16 CF-NPs doped with more than one element

Few research groups synthesised CF-NPs doped with more than one element [9,144]. A brief review on co-doped CF-NPs is presented in Table 2.17.

Table 2.17: Effect of doping in CF-NPs with more than one element

S. No.	Dopants	Routes of synthesis	Remarks/Effect of doping	Ref.
1.	Cd and Cr	Standard ceramic techniques	Substitution of Cr^{3+} in CF-NPs did not influence cadmium concentration dependent properties of CF-NPs. Addition of Cr^{3+} reduced the saturation magnetisation values. CF-NPs remained paramagnetic even after co-doping.	145
2.	Mn and Cd	Sol–gel auto-combustion	Substitution of Mn^{3+} in Cd-doped CF-NPs influenced its properties significantly, e.g., lattice constant and bulk density increased whereas saturation magnetisation value decreased.	146
3.	Cr and Ce	Co-precipitation	Broad (311) reflection demonstrated that particles of smaller sizes were formed as compared to undoped materials. Ionic size of cerium influenced crystallite size of the product. Cerium having higher ionic size than iron resulted in the formation of larger crystallite sizes than doped or un-doped material. SEM result showed formation of cubic shaped particles. Agglomeration was also observed.	147
4.	Cu and Bi	Solution combustion technique	Co-doping samples demonstrated antibacterial activities against *S. aureus* and *E. coli*. They also studied the photocatalytic degradation of Congo red dye under UV and Visible light. It can be used in water treatment.	71
5.	Mn and Ni	Co-precipitation	Materials with desired band gaps can be synthesised via this method by changing the dopant. It also changed its dielectric properties.	148
6.	Cu and Ce	Combustion technique	The product was effective in photocatalytic degradation of Congo red and bisphenol A and hence can be used for water treatment.	75
7.	Ce and Mn	Facile co-precipitation technique	Co-doped samples had cubic spinel structure. A secondary phase of CeO_2 was observed. Existence of metal oxygen bond was confirmed through FTIR apart from this vibrational stretching of octahedral and tetrahedral lattice positions were also observed. CF-NPs showed spherical shapes in SEM analysis. Co-doping improved magnetic properties significantly.	149
8.	Cu and Bi	Solution combustion	Photocatalytic degradation activity of Congo red dye was found to be maximum in co-doped samples whereas it was minimum in un-doped CF-NPs. The extent of this activity of doped samples is more than un-doped samples whereas it is less than co-doped samples. They also showed antibacterial activities against *S. aureus* and *E. coli*.	144

The doping/co-doping of CF-NPs can alter their properties [9]. Hence, these materials can be used for various applications [49]. The different applications of co-doped CF-NPs are discussed in the following section (see sec. 2.17).

2.17 Applications of co-doped CF-NPs

Cobalt ferrites have various applications in scientific and industrial fields. There is need to dope cobalt ferrites for modifying and optimize its magnetic and microstructural properties. Doped/co-doped elements and their quantity is a major factor to be studied [1,71,75]. Chakrabarty *et al.* co-doped CF-NPs with manganese and nickel and observed the improved dielectric properties that can be used in device applications [148]. Shakil *et al.* observed that CF-NPs co-doped with zinc and cadmium were used in numerous applications, e.g., as sensors and actuators, data storage devices, magnetic recording devices, and in biomedical equipment's [150]. Geetha *et al.* observed that co-doped CF-NPs with Al and Ce show potential application in high-frequency memory devices [151]. Kirankumar *et al.* reported the photocatalytic degradation activities of CF-NPs co-doped with copper and cerium in Congo red and bisphenol A [75]. Sumathi *et al.* observed the enhanced antibacterial and photocatalytic activity of CF-NPs when they co-doped CF-NPs with bismuth and copper ions [71]. Similarly, the bismuth and silver-co-doped CF-NPs also show enhanced antibacterial activities as compared to un-doped CF-NPs [49]. The copper and chromium-co-doped CF-NPs show low dielectric loss, which improves their application in wireless communication and in various electronic devices [66].

The composite material shows the improved properties. Hence there is need to fabrication of composites of materials for desired properties and applications [23]. A brief discussion on composite of CF-NPs is as follows (see sec. 2.18).

2.18 Composites of CF-NPs

2.18.1 The basic concepts related to composite

Composite materials are formed with the combination of two or more than two different materials [23]. The different components of composites are insoluble in each other [152]. These properties make them an unique material [153]. Wood and bone are natural composites [152,154]. Concrete, and fibre glass are the another examples of composites [23,154]. Generally, composite material contains three components:

   i.   Matrix (continuous phase)

   ii.   Reinforcements (dispersed or discontinuous phase)

iii.   Interphase (fine interphase region)

The properties of composite materials can be tailored according to the requirements by changing the matrix, reinforcement, and the manufacturing process. Hence, they can be used in various applications (see sub-sec. 2.18.3) [152].

2.18.2 Properties of composite materials

The composite material shows several unique properties e.g., polymer composites are of lightweight, structurally stable, high strength to weight ratio and improved heat resistance activities [152,154,155]. These properties and applications depend up on matrix and reinforcement, their ratios, and manufacturing process etc. These materials can be used for several applications [152,154].

2.18.3 Applications of composites

These materials show various applications in the different fields. The composites can be used in the defence, aerospace, and transportation applications [152] . These materials can also be used in mechanical, civil, structural, and electronic engineering. They are used extensively in several biomedical applications, for example, in orthopaedics and dentistry [155]. Composites containing aramid fibres are suitable materials for protective covering like armour. Similarly, composites of Kelvar can be used for ballistic protection. They are flexible with lightweight property and hence suitable for bulletproof clothing. Several components of rocket and aircraft engines are fabricated using composites having a metal as a matrix material. Carbon containing composites are used in aerospace applications because of their temperature resistance quality [23]. The composite manufacturing technique is described in the following section (see sub-sec. 2.18.4).

2.18.4 Composite manufacturing techniques

The composite materials can be synthesised by using following methods [152];
  i.   Open contact moulding Hand
 ii.   Resin infusion processes
iii.   Compression moulding
 iv.   Injection moulding

v. Filament winding

vi. Pultrusion process

vii. Automated fibre placement

viii. Additive manufacturing

A list of composites prepared using different methods is presented in Table 2.18 [3,11,153,156–167].

Table 2.18: Different methods of preparation of composite materials

S. No.	Components of composites	Method of preparation	Impact of composite	Ref.
1.	$CoFe_2O_4$/FeOOH	One-pot hydrothermal	Flower like nanocomposite of $CoFe_2O_4$/FeOOH prepared through one-pot hydrothermal method without use of any surfactant. It shows improved super capacitive activities.	[161]
2.	SnO_2/graphite	Hydrothermal	The as prepared composite shows improved structural, dielectric, optical and electrochemical properties.	[164]
3.	$CoFe_2O_4$/PANI/Ag	Reduction chemical	The novel $CoFe_2O_4$/PANI/Ag nanocomposite shows improved antibacterial activity against gram-negative and gram-positive bacteria.	[153]
4.	Ag/ZnO	Facile Sol-Gel	The synthesised Ag/ZnO nanocomposite act as high performance photo catalyst.	[163]
5.	$CoFe_2O_4$:$BaTiO_3$ core–shell	Hydrothermal and sol-gel	The hydrothermal and sol-gel routes used to prepare the combination mixture and CoFe2O4:BaTiO3 nanocomposites with (1:1) weight ratio.	[165]
6.	Polyaniline (PANI) and montmorillonite (MMT)	Mechanochemical intercalation	The synthesised nanocomposites of polyaniline (PANI) and montmorillonite (MMT) by using the mechanochemical intercalation method show improved thermal stability of PANI with addition of MMT.	[166]
7.	CuO/ZnO	Mortar and pestle	The nanocomposite of CuO/ZnO synthesised successfully using mortar-pestle method at room temperature (weight ratio of 1:1). It was observed that the samples contained crystals (88.3% samples had crystal with crystalline size 4.18 nm).	[167]
8.	$BaTiO_3$/$CoFe_2O_4$	Structure replication	The multiferroic $BaTiO_3$/$CoFe_2O_4$ nanostructured composite material shows the improved ferrimagnetic behaviour.	[156]
9.	Fe, N co-doped TiO_2/$CoFe_2O_4$	Precipitation	The prepared nanocomposites reveal the enhanced photocatalytic performance for the degradation of methyl orange dye as compared to TiO_2.	[157]
10.	Ferrite/Multi-Walled Carbon Nano-Tubes (MWCNTs)	Reverse micelle	Ferrite/Multi-Walled Carbon Nano-Tubes (MWCNTs) composite material formation was confirmed by TEM images. The composite material shows the superparamagnetic behaviour.	[158]
11.	$CoFe_2O_4$/ Multi-wall carbon nanotubes (MWCNTs)	Electrospinning	Lamastra *et al.* studied the structural and morphological study of composite material of electrospun $CoFe_2O_4$/MWCNTs.	[11]

S. No.	Components of composites	Method of preparation	Impact of composite	Ref.
12.	$CoFe_2O_4$ and graphene	One-step hydrothermal	Fu et al. reported the formation of composites having CF with graphene. They observed that it intensely changed into highly active catalyst for degradation of rhodamine B, active black BL-G, methylene blue, active red RGB and methyl orange under visible light irradiation	[3]
13.	Chitosan/ ethylenediaminetetraacetate/ $CoFe_2O_4$	Zero-length emulsion crosslinking	Qin et al. prepared the magnetic chitosan-EDTA enwrapped CF-NPs by using the facile zero length emulsion cross-linking method.	[159]
14.	$CoFe_2O_4$/Poly vinyl alcohol (PVA)	Modified co-precipitation	Synthesised nanocomposites of cobalt ferrite with polyvinyl alcohol having magnetic properties.	[160]

We used mortar-pestle grinding method which is described briefly in the following sub-section (see sub-section 2.18.5).

2.18.5 Mortar and pestle grinding method

The grinding technique is an important aspect of mechanochemical synthesis or reactions. It can be done through mortar and pestle. The main advantage of mortar-pestle grinding method is that it does not require sophisticated laboratory infrastructure [168,169]. Details of the mortar and pestle grinding method are discussed in chapter-3 (sec. 3.5 of Materials and Methods).

The co-doped CF-NPs and composite materials are used as antimicrobial agents. These materials show the enhanced antibacterial activities [49,71,153]. Since our work is based on antibacterial behaviour of CF-NPs and its composite materials. Here, we are discussing about the antibacterial activities of magnetic materials briefly in the following section (see sec. 2.19).

2.19 Antibacterial activities

The antibacterial activity is the ability of a molecule of compound to inhibit the growth of bacteria. They also kill them. Antibacterial agents play important role in this process. The antibacterial agents can either be kill the bacteria, or inhibit the bacterial growth [170].

2.19.1 Impact of bacteria on human health

Bacteria are ubiquitous in nature. It can grow in plant animal including human body. They make colonies in various parts of our body such as gastrointestinal tract, mucosa, skin, mammary gland, urogenital tract, and the respiratory tract. They can formed the complex but discrete ecosystem to adapt in any environmental conditions. A steady relationship between the human body and its natural microbiota starts with childbirth. These exchanges are crucial for preserving overall health and wellness [171].

Earlier research on the human microbiome project has revealed that adaptations in the immunological atmosphere could be directly linked with a dysbiotic gut flora. Dysbiosis has also been linked to serious medical disorders such as cardiovascular disease, cancer, bowel inflammatory and antibiotic-resistant bacteria infections that are difficult to cure [171].

Magnetic nanoparticles show the improved antibacterial activities [172]. A brief discussion on magnetic nanoparticles as an antibacterial agent is as follows (see sub-sec. 2.19.2).

2.19.2 Nanoparticles used as antibacterial agents

Bacterial infections have become a primary cause of death in recent times. Antibiotics reduced the number of bacterial infections that caused death. Regular usage of conventional medications prevents the development of microorganisms [113]. Prolonged and uncontrolled use of antibiotic has produced a risk for antibiotic resistant ability [173]. Antibacterial agents can fight against infectious diseases, but the wide use of antibiotics generates bacterial resistance against the antibacterial agents. This will create the serious health issues. This motivates to develop a new material which can fight against infectious diseases. Nanoparticles can play an important role here to solve this problem. They can be used in different applications like in drugs, and gene delivery [170]. Among these MNPs, iron oxide nanoparticles may be used as antimicrobial agents against different bacteriae. They can easily combine with other antibacterial materials and produce the antibacterial effects [172]. Iron oxide nanoparticles show many advantages over the other NPs such as inexpensive

synthesis, biocompatibility, feasible large-scale production, and environmental safety etc. [171].

From the next paragraph we are discussing briefly about the types of bacteria in sub-sec. 2.19.3, role of bacteria *Bacillus paranthracis* and *Bacillus nitroreducens* in sub-sec. 2.19.4 and methods to test the antibacterial activities in sub-sec. 2.19.5.

2.19.3 Types of bacteria

The bacteria can be classified mainly into two types:

1. Gram positive bacteria

2. Gram negative bacteria

Magnetic nanoparticles (MNPs) like iron nanoparticles are acts as antibacterial agents against Gram positive and Gram negative bacteria. Iron oxide nanoparticles can easily combine with other antibacterial materials and produces the antibacterial effects [172].

2.19.4 Role of Bacillus paranthracis and Bacillus nitroreducens

Bacillus paranthracis belongs to Bacillus cereus group. This group has 21 species of bacteria. These species have been found in different environments, like soil, rhizosphere, as well as in the samples of human origin [174]. It is considered as an opportunistic pathogen, which is responsible for diarrhoea [174–176]. This organism was characterised in 2017 and under study now [177]. *Bacillus nitratireducens* is a newly identified bacterium. It is not widely recognized as a harmful bacterium [178,179].

2.19.5 Methods to test the antibacterial activities

Several research groups used various methods to test the antibacterial activities of the prepared samples [180]. Few different methods used for the detection of antibacterial activities of the materials are discussed briefly in following subsections (see sub-sec. 2.19.5.1 to 2.19.5.3).

2.19.5.1. Well diffusion method

In this method initially microbial inoculum is spread over the entire surface of petri plate containing fixed volume of agar medium. A hole of a diameter of 6 mm to 8 mm

is punched with a sterile cork borer or a tip on agar medium under the aseptic conditions. Fixed volume of the stock solution containing antimicrobial agent of desired concentration are injected in the well. Agar plates are then incubated using an incubator at a suitable temperature condition as per test microorganism. The diffusion of antimicrobial agent into the agar medium inhibits the growth of bacteria and creates zone of inhibitions around each well [180].

2.19.5.2 Agar dilution method

In the Agar dilution method, initially the stock solution of antibacterial agent of desired concentration is incorporated into the molten agar medium, which is inoculated with microbial inoculum under the aseptic conditions. Then petri plate is incubated into the incubator under the suitable temperature conditions. In this method the antibacterial agents of different concentrations are used by the serial two-fold dilutions. Finally, the minimum inhibitory concentration (MIC) is recorded for antimicrobial agent that inhibits the growth of bacteria [180].

2.19.5.3 Agar disk diffusion method

A microbial inoculum is spread over the entire surface of petri plate containing fixed volume of agar medium. Then, a filter paper disk of ~ 6 mm diameter is placed on the agar surface. A known volume of fixed concentration of stock solution is injected on filter paper disk. Agar plates are then incubated using an incubator at a suitable temperature condition as per test microorganism. The diffusion of antimicrobial agent into the agar medium inhibits the growth of bacteria and creates zone of inhibitions around each disk [180].

We were used the Agar disk diffusion method for antimicrobial study. Hence, the details of the Agar disk diffusion method and the mechanism of antibacterial activity are discussed in third chapter (sec. 3.6 of Materials and Methods).

2.20 Conclusion

Ferrites show a variety of characteristics, e.g., magnetic, dielectric, optical, and catalytic properties. The magnetic properties of the ferrites depend upon the variation

in saturation magnetisation and coercivity. Neel temperature and Curie temperature play an important role here. The hysteresis curve of the materials provides significant information regarding their magnetic character. It can be classified as soft and hard magnetic materials effectively. The dielectric properties of ferrite materials depend upon the polarization, dielectric constant, and ionic polarization. Dielectric materials have very high resistance. Dielectric materials are different from electrical conductors. Ferrites can show optical behaviour and be used as catalysts as well. Ferrites can be divided into 'spinel', 'garnet', 'orthoferrite', and 'hexaferrite'.

Among ferrites, spinel ferrites have unique properties. The spinel cobalt ferrite nanoparticles (CF-NPs) altered their properties when they were doped or co-doped with transition metal ions, rare earth elements, non-metals, and representative elements. These materials were synthesised by using various routes of synthesis, such as citrate auto-ignition, hydrothermal, co-precipitation, sol-gel auto-combustion methods via chemical and green synthesis, etc. The simplicity and cost-effective nature of the sol-gel method make it popular among these methods. Different uses of CF-NPs that have been doped or co-doped are caused by their altered properties. They can be used in sensors, drug delivery, magnetic resonance imaging (MRI), and other biomedical and technological applications.

The preparation of composite materials is another way to modify their properties. The composites of CF-NPs can be synthesised via different methods, e.g., one-pot hydrothermal process, modified sol-gel, hydrothermal, reduction chemical, facile sol-gel, mechanochemical intercalation, mortar and pestle, etc. The mortar-pestle grinding method was adopted due to its simplicity and the fact that it can be done in any laboratory.

The antibacterial activities of magnetic ferrites can be compared with those of antibiotics. The wide use of antibiotics generates bacterial resistance against the antibacterial agents. MNPs can play an important role in solving this problem. The magnetic nanoparticles may be used as antimicrobial agents against different bacteria. They can easily combine with other antibacterial materials and produce antibacterial

effects. The antibacterial activities of MNPs can be tested against bacteria by using different methods, e.g., the agar well diffusion method, the agar disk diffusion method, the agar dilution method, etc., to name but a few. The antibacterial activities of CF-NPs and its composite materials can be compared to those of any of these techniques.

To our knowledge, still research gap exits in co-doping of cobalt ferrite. It changes the magnetic properties of these materials which in turn will influence the antibacterial behaviour of cobalt ferrite. Still several transition metals for example, co-doping of silver with copper and zinc as well as co-doping of bismuth with silver and zinc has not been carried out. Literature says that their composites with ZnO/Ag have not been prepared. These materials will be synthesised via sol-gel route and will be characterized using Advanced Materials' Characterization Techniques. The antibacterial activities have not been explored.

Chapter 3

Materials and methods

3.1 Introduction

Magnetic materials have much importance in the field of biomedical science. These materials can be used in drug delivery, gene delivery, magnetic resonance imaging (MRI), antibacterial activities of the samples, etc. To achieve this goal, we used the sol-gel method for the synthesis of CF-NPs and co-doped CF-NPs. Mortar pestle grinding method was used for the preparation of composite material. Tests for anti-bacterial activities for as-prepared samples were performed using Agar disk diffusion. Efforts were made to reduce the impurity of the samples. All the CF-NPs samples are characterised using the various Advanced Materials' characterization techniques.

3.2 Chapter layout

The procedure for the synthesis of CF-NPs samples is discussed in sec. 3.3. The various advanced materials characterization techniques used for the characterization of CF-NPs are discussed in sec. 3.4. Method of preparation of composite is discussed in sec. 3.5, and the antibacterial activity is discussed in sec. 3.6. The chapter is summarised in sec. 3.7.

3.3 Synthesis of un-doped, doped and co-doped CF-NPs via sol-gel route
3.3.1 Equipment used for the synthesis of un-doped, doped and co-doped CF-NPs, composites as well as for antibacterial activity test

Specifications of all the apparatus including glassware used for the synthesis of un-doped, doped and co-doped CF-NPs, preparation of their composites and antibacterial activity test of all the samples are listed in Table 3.1.

Table 3.1: List of glassware and apparatus used with specifications

S. No.	Glassware/Apparatus used	Model/Make
1.	Weighing machine	NAVYUG
2.	Hot plate	NAVYUG
3.	Magnetic stirrer	IKA®C-MAG HS 7
4.	250ml Beakers	Borosilicate glass
5.	250ml conical flask	Borosilicate glass
6.	Spatula	Steel spatula
7.	Glass rod	Borosilicate glass
8.	Crucible	Silica crucible
9.	pH meter	HANNA S358236
10.	Bath sonicator	M labs ULL-15A
11.	Muffle furnace	NAVYUG
12.	100 ml Measuring cylinder	Borosilicate glass
13.	Mortar-pestle	Ceramic
14.	Watch glass	Borosilicate glass
15.	Petri plate	Borosilicate glass
16.	Incubator	NAVYUG
17.	Laminar air flow	LAMBA UDYOG
18.	Autoclave	SHIVA
19.	Micro pipette	BEXCO
20.	Forceps	Steel
21.	Sprit lamp	Steel
22.	Buds	Tulips

3.3.2 Chemicals used for the synthesis of un-doped, doped and co-doped CF- NPs

Chemicals used for the synthesis of un-doped, doped and co-doped CF-NPs are listed in Table 3.2.

Table 3.2 List of chemical used for the synthesis of co-doped CF-NPs

S. No.	Name of chemicals	Molecular formula	Source	Purity level	Mol. wt.	Purpose of use
1.	Ferric nitrate nonahydrate	$Fe(NO_3)_3.9H_2O$	Alpha Chemika	98% AR	404	Synthesis of CF-NPs
2.	Cobalt nitrate hexahydrate	$Co(NO_3)_2.6H_2O$	Molychem	97% Extra pure	291.03	Synthesis of CF-NPs
3.	Bismuth nitrate pentahydrate	$Bi(NO_3)_3.5H_2O$	Ranbaxy	98.5% Pure	485.07	Dopant
4.	Silver nitrate	$AgNO_3$	Fine	98% Pure	169.87	Dopant
5.	Zinc nitrate hexahydrate	$Zn(NO_3)_2.6H_2O$	Molychem	98%	297.48	Dopant
6.	Copper nitrate trihydrate	$Cu(NO_3)_2.3H_2O$	Alpha Chemika	98% Pure	241.60	Dopant
7.	Citric acid monohydrate	$C_6H_8O_7$	Ranbaxy	99.5% Pure	210.14	Fuel
8.	Ammonium hydroxide	NH_4OH	Molychem	25% AR	35.05	pH maintain

AR = Analytical reagent

3.3.3 Method of synthesis of co-doped CF-NPs

Stoichiometric amounts of cobalt nitrate hexahydrate and ferric nitrate nonahydrate were taken as starting materials and were dissolved in deionised water. Transition metal nitrates were used for co-doping. These metal precursors were dissolved in the deionised water to form colloidal solution. The mixture was stirred for few minutes using a magnetic stirrer. Citric acid was added as a fuel in the reaction mixture. The as-prepared sol was heated while stirring at 80 ℃ to 90 ℃ for the completion of the reaction. Ammonia solution was added during heating accompanied by stirring to maintain the pH of the reaction mixture. The sol was continuously heated under constant stirring until a gel was formed. The gel was heated strongly when a powder was formed [71,81]. Schematic of above described process is shown in fig. 3.1,
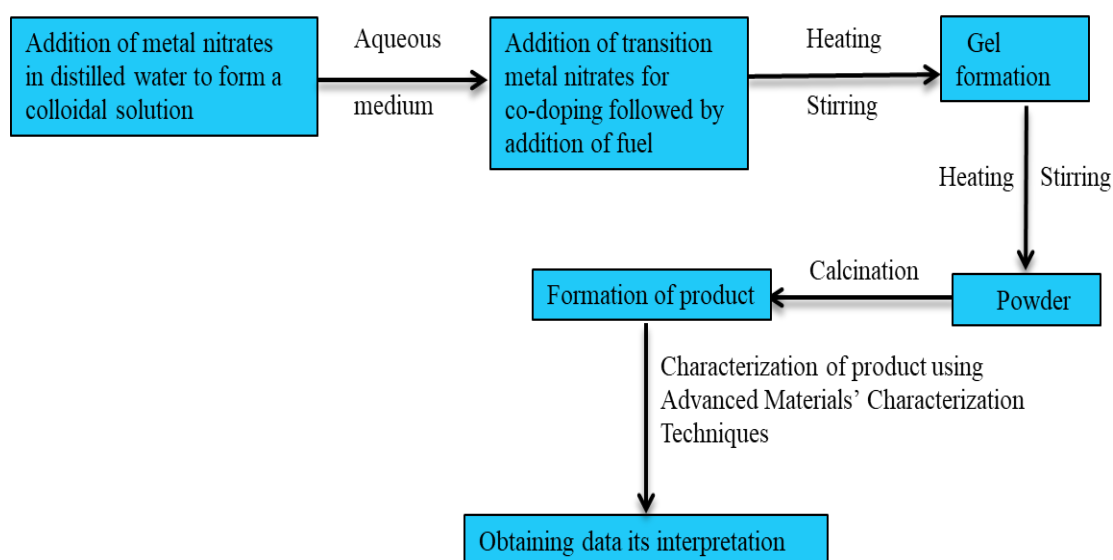
Fig. 3.1 Schematic of sol-gel route of synthesis

Various steps involved during synthesis of CF-NPs are represented in fig. 3.2.
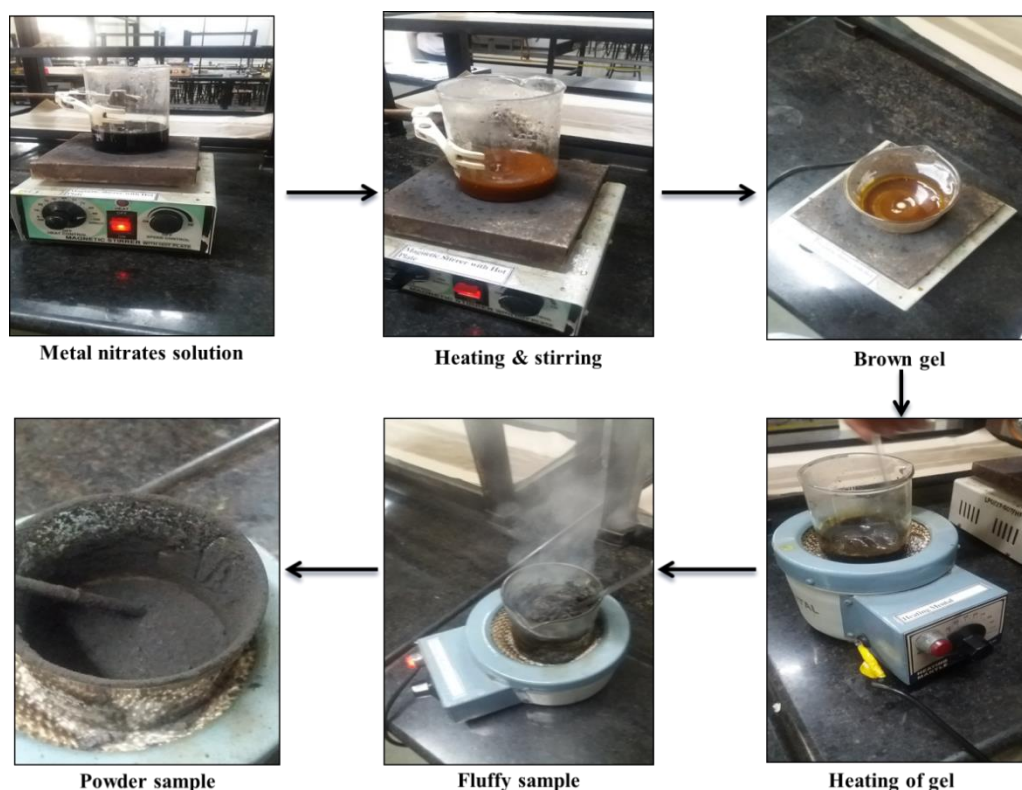
Fig. 3.2 various steps involved during the synthesis of co-doped CF-NPs via sol-gel route

It was found that metal nitrates were used as starting materials in most of the cases irrespective of the route of synthesis adopted for the purpose [19–21,62,65,77,104,105,120,122,123,125–128]. Few research groups used oxides as their starting materials e.g., doping with niobium, molybdenum, ruthenium, and cadmium was carried out using metal oxides [121,124,129,130]. In the case of doping with yttrium as well, oxide of yttrium was used as a source of yttrium. Although, in these cases (i.e., in the case of yttrium doping) nitric acid was used as one of the reactants. It was believed that Y_2O_3 reacted with nitric acid to produce nitrate of yttrium [21,65,125]. Ishaque *et al.* used ferric chloride as a source of iron, $CoO_4C_4H_6.4H_2O$ as a source of cobalt, and Y_2O_3 as a source of yttrium. They used NaOH and Na_2CO_3 to maintain the pH of the system [132]. Noor *et al.*, used polycrystalline samples of mixed ferrites as starting materials [131]. Citric acid was used as an important reactant by several research groups [20,77,105,122,126,127]. Sharma *et al.* reported that citric acid was used as a chelating agent [77] whereas Chakrabarty *et al.* used polyvinyl alcohol to reduce the process of agglomeration [104]. Here, we used metal nitrates as starting materials for the synthesis of CF-NPs.

3.3.4 List of synthesised samples of un-doped, doped and co-doped CF-NPs

Table 3.3: List of synthesised un-doped, doped and co-doped CF-NPs samples

S.No.	Sample-ids of CF-NPs	Dopant/s	Level of doping	Desired products
1.	SK-002	Ag	0.1	$CoFe_{1.9}Ag_{0.1}O_4$
2.	SK-005	Cu	0.1	$Co_{0.9}Cu_{0.1}Fe_2O_4$
3.	SK-007	Bi	0.1	$CoFe_{1.9}Bi_{0.1}O_4$
4.	SK-008	Zn	0.1	$CoFe_{1.9}Zn_{0.1}O_4$
5.	SK-006	Cu & Ag	0.1 & 0.1	$Co_{0.9}Cu_{0.1}Fe_{1.9}Ag_{0.1}O_4$
6.	SK-013	Cu & Ag	0.05 & 0.05	$Co_{0.95}Cu_{0.05}Fe_{1.95}Ag_{0.05}O_4$
7.	SK-018	Cu & Ag	0.15 & 0.15	$Co_{0.85}Cu_{0.15}Fe_{1.85}Ag_{0.15}O_4$
8.	SK-012	Zn & Ag	0.1 & 0.1	$Co_{0.9}Zn_{0.1}Fe_{1.9}Ag_{0.1}O_4$
9.	SK-014	Zn & Ag	0.05 & 0.05	$Co_{0.95}Zn_{0.05}Fe_{1.95}Ag_{0.05}O_4$
10.	SK-019	Zn & Ag	0.15 & 0.15	$Co_{0.85}Zn_{0.15}Fe_{1.85}Ag_{0.15}O_4$
11.	SK-011	Cu & Zn	0.1 & 0.1	$Co_{0.9}Cu_{0.1}Fe_{1.9}Zn_{0.1}O_4$
12.	SK-015	Cu & Zn	0.05 & 0.05	$Co_{0.95}Cu_{0.05}Fe_{1.95}Zn_{0.05}O_4$
13.	SK-020	Cu & Zn	0.15 & 0.15	$Co_{0.85}Cu_{0.15}Fe_{1.85}Zn_{0.15}O_4$
14.	SK-001	Bi & Ag	0.1 & 0.1	$Co_{0.9}Bi_{0.1}Fe_{1.9}Ag_{0.1}O_4$
15.	SK-016	Bi & Ag	0.05 & 0.05	$Co_{0.95}Bi_{0.05}Fe_{1.95}Ag_{0.05}O_4$
16.	SK-021	Bi & Ag	0.15 & 0.15	$Co_{0.85}Bi_{0.15}Fe_{1.85}Ag_{0.15}O_4$
17.	SK-010	Bi & Zn	0.1 & 0.1	$Co_{0.9}Bi_{0.1}Fe_{1.9}Zn_{0.1}O_4$
18.	SK-017	Bi & Zn	0.05 & 0.05	$Co_{0.95}Bi_{0.05}Fe_{1.95}Zn_{0.05}O_4$
19.	SK-022	Bi & Zn	0.15 & 0.15	$Co_{0.85}Bi_{0.15}Fe_{1.85}Zn_{0.15}O_4$
20.	SK-023	Un-doped	0	$CoFe_2O_4$

All the synthesised samples with their sample-ids are listed in Table 3.3.

3.4 Advanced Materials' Characterization techniques used for the characterization of CF-NPs samples

Several Advanced Materials' Characterization Techniques were used for the characterization of CF-NPs samples. X-ray diffraction (XRD) technique is used to study the crystalline structure of the sample (sub-sec. 3.4.1). We used Fourier-transform infrared (FTIR) spectroscopy (sub-sec. 3.4.2) for analysing the, functional groups present in the sample. Vibrating sample magnetometer (VSM) and Field Emission scanning electron microscopy (FESEM) are discussed in sub-sec. 3.4.3 and sec. 3.4.4 respectively. Energy dispersive X-ray analysis (EDX) technique is used for elemental analysis (sub-sec. 3.4.5). Thermal analyses of the samples were carried out using Thermogravimetric Analysis (TGA, see sub-sec 3.4.6) and Differential Scanning Calorimetry (DSC, see sub-sec. 3.4.7). The details of various analytical methods used for the characterization of CF-NPs samples are listed in Table 3.4.

Table 3.4: Instruments used to investigate the characteristics of synthesised CF-NPs

Characterisation technique	Make	Model	Location	Purpose	Ref.
XRD	Bruker	D8 ADVANCE	CIF, LPU, Phagwara	Crystalline structure studies	[171]
FTIR	PerkinElmer	ATR Two	CIF, LPU, Phagwara	Functional group identification	[171]
VSM	MicroSense	EZ-9	Sprint Testing Solution, Mumbai	Magnetic properties studies	[31]
FESEM/EDS	Carl Zeiss	SUPRA 55	Sprint Testing Solution, Mumbai	Morphological studies/Elemental identification	[171]
TGA	PerkinElmer	TGA 4000	CIF, LPU, Phagwara	Thermal properties of samples	[31]
DSC	PerkinElmer	DSC 6000	CIF, LPU, Phagwara	Thermal properties of samples	[181]

The crystal structure study of the samples was investigated by using X-ray diffraction (XRD) technique. From the next sub-sec. 3.4.1 the 'XRD' technique is discussed in detail.

3.4.1 X-ray diffraction (XRD) technique

Introduction

X-ray diffraction (XRD) technique is used to study the crystalline structure, different phases present in the sample, as well as crystal orientation. Several structural parameters, like crystallinity, strain in crystal, crystal defects, and average grain size can be studied using this technique [182].

Basic principle of XRD technique

In crystals, atoms and ions exist in regular arrangements. They form a motif or a pattern that extends in all three dimensions, making a large network. The interatomic distances in crystals are normally in angstrom units (normally 1 Å, and 1 Å = 10^{-10} m) [183]. Hence, for X-rays, crystals act as diffraction gratings. In the XRD technique, X-rays are allowed to fall on samples; these X-rays change their path after interacting with sample. The X-rays, after interaction with samples, interfere with each other. Constructive interferences occur when the X-rays interact in the same phase, which happens in the case of crystals having a regular arrangement of atoms and ions. This whole process is explained through Bragg's law. Bragg's law is given by W. L. Bragg and W. H. Bragg. Bragg's law is explained in the following paragraph.

The principle of the XRD method is based on the diffraction of X-rays by periodic atomic planes and the angle or energy-resolved detection of the diffracted signal. W. L. Bragg gave a geometrical explanation of the XRD diffraction technique. It is depicted in fig. 3.3.
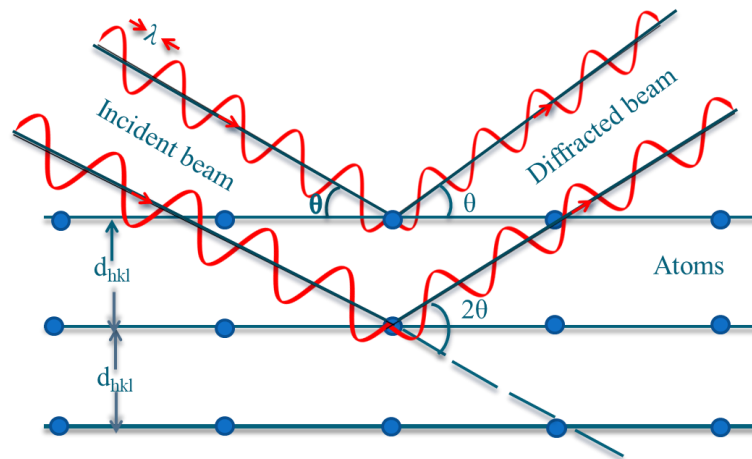
Fig. 3.3 Geometrical condition for diffraction from lattice planes [184].

Eq^n (3.1) represents the Bragg's equation [184].

$$n\lambda = 2d_{hkl}\,sin\theta \quad \dots\dots\dots\dots\dots (3.1)$$

Where,

n = Order of diffraction,

λ = Wavelength of the incident beam in nm

d_{hkl} = Lattice spacing in nm,

θ = Angle of the diffracted beam in degree

Bragg's law gives the relationship between wavelength of electromagnetic radiation, diffraction angle, and lattice space in a crystalline material. In this method, the diffracted X-rays are detected, treated, and counted. The sample was scanned at the range of 2θ degrees. All the lattice diffraction directions should be achieved due to the random orientation of powder materials. Each compound has a particular set of d-spacing. The interconversion of diffraction peaks with d-spacing's identified the compound.

Instrumentation and working

An X-ray diffractometer contains five basic elements, such as an X-ray tube, goniometer, sample holder, X-ray detector, and recorder. The brief description of these basic elements is explained in the following sub-sections.

(1) X-ray tube: The X-ray tube generates the X-rays by heating the tungsten filament in a cathode ray tube and producing the electrons. The applied voltage accelerates these electrons towards a target material and bombards it with electrons. The electrons of sufficient energy removed the inner shell electrons of the target material and produced specific X-ray spectra [182]. The schematic of a diffractometer system is presented in fig. 3.4.
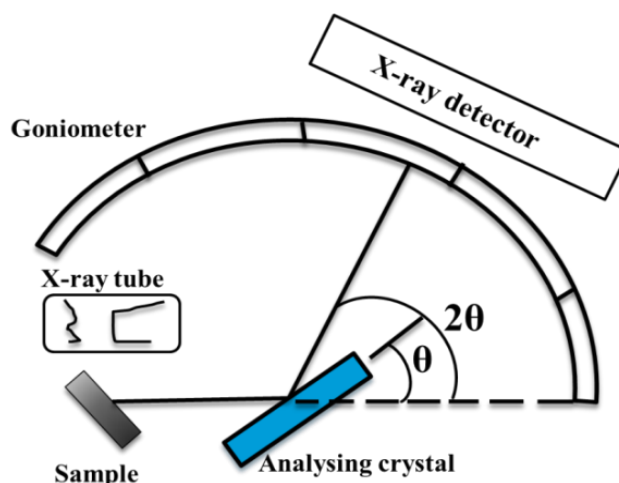
Fig. 3.4 Schematic diagram of a diffractometer [182].

(2) Goniometer: An angle is measured during X-ray diffraction via a device called a goniometer. The word goniometer is the combination of two terms named 'gonio' and 'meter'. The term 'gonio' is generated from the Greek word 'gōnia' which means 'angle', while the term 'meteron' indicates 'to measure'. It is used to rotate an object at a particular angle. The goniometer holds the incident beam optics, sample holder, and detector. The angle between the incident beam and the sample is controlled through a goniometer [185].

(3) Sample holder: The sample holder may be of glass slide or ceramic tile.

(4) X-ray detector and recorder: A detector records and processes this X-ray signal and converts the signal to a count rate, which is then output to a device such as a printer or computer monitor [184].

X-ray radiations are generated in the X-ray tube by heating the tungsten filament and producing the electrons. The voltage applied to accelerate these electrons towards a target material bombards with electrons. The electrons of sufficient energy remove the inner shell electrons of the target material and generate X-ray spectra. These X-ray spectra consist of a number of components of which $K\alpha$ and $K\beta$ are most common. The component $K\alpha$ consists $K\alpha 1$ and $K\alpha 2$, in which $K\alpha 1$ is of shorter wavelength and its intensity is twice that of $K\alpha 2$ [182]. The Schematic of atomic energy levels and emissions of characteristic X-Ray radiations is represented in fig. 3.5 [184].
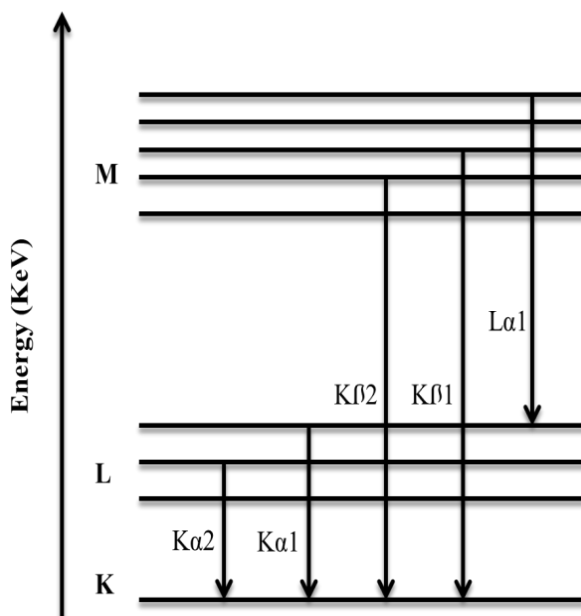
Fig. 3.5 Schematic of atomic energy levels and emissions of Characteristic X-Ray radiations [184].

The particular wavelengths of the target materials, like Cu, Fe, Mo, Cr, etc., are the main characteristic of this analytical method. The monochromatic X-rays required for the diffraction process are produced by filtering with foils or crystal monochrometers.

The wavelengths of $K\alpha1$ and $K\alpha2$ are very close to each other's so that the weight average of these two is generally used. Copper is the most commonly used target material in XRD diffraction with $CuK\alpha$ radiation of wavelength 1.54 Å. These X-rays are collimated and focused on the sample. The detector records and processes the X-ray signal and converts the signal to a count rate, which is then output to a device such as a printer or computer monitor [182,184].

XRD data analysis: Generally, the diffraction data is characterised as per the intensity distribution as a function of degree 2θ angle. The content of information that can be extracted is represented in fig. 3.6 [184].
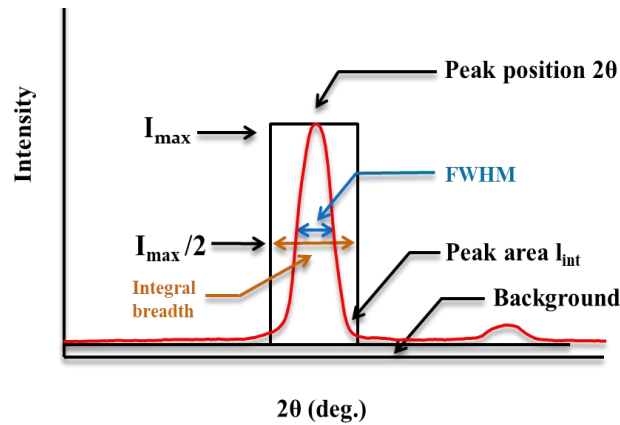
Fig. 3.6 Graphical representation of measurement of diffraction peak [184].

The maximum peak intensity (I_{max}) and integrated intensity (I_{int}) can be well-defined after the background subtractions. The peak position can be calculated by using a number of methods, such as the fit of different mathematical functions, the centre of gravity, etc. The peak width is usually considered full width at half maximum (FWHM), consistent with peak breadth at half maximum peak intensity (I_{max}) or by the integral breadth. The different parameters are used according to the purpose of the measurements [184]. The crystallite diameter (D) of the sample from the X-ray diffraction data is generally calculated by using Scherrer's eqn (3.2) [65];

$$D = \frac{K\lambda}{\beta cos\theta} \quad \text{-------------------------} \text{(3.2)}$$

Where,

D = Crystallite size,

K = 0.9 (Scherrer's constant for the cubic crystal structure)

λ = X-rays wavelength in nm (0.154 nm = 1.54 Å),

β = Radian of full width half-maximum (FWHM),

θ = Bragg's angle

The lattice parameter 'a' is calculated by using the eq^n (3.3) [65];

$$d_{(hkl)} = \frac{a}{\sqrt{h^2+k^2+l^2}} \text{ ---------------------- (3.3)}$$

Where,

a = lattice parameter

$d_{(hkl)}$ = distance between the planes

(hkl) = Miller indices

The functional group study of the samples can be done by using the Fourier-transform infrared (FTIR) spectroscopy. From the next sub-section 3.4.2 the 'FTIR' spectroscopy is described in detail.

3.4.2 Fourier-transform infrared (FTIR) spectroscopy

Introduction

Fourier-transform infrared (FTIR) spectroscopy is used to analyse the functional groups present in the sample. The position of IR absorption bands in the spectrum obtained is used for the identification of different chemical components present in the compound. Generally, IR spectroscopy is developed for quantitative and qualitative analysis [186].

Basic principle of FTIR spectroscopy

The instrument named a spectrophotometer is used to determine the absorption spectrum of a sample under investigation. The Fourier-transform spectrophotometer gives the IR spectrum as quickly as compared to the outmoded spectrophotometer [186].

Instrumentation and working

The schematic illustrates the main component of a simple FTIR spectrophotometer in fig. 3.7. A brief discussion of the components of a FTIR spectrophotometer and its working is as discussed below.
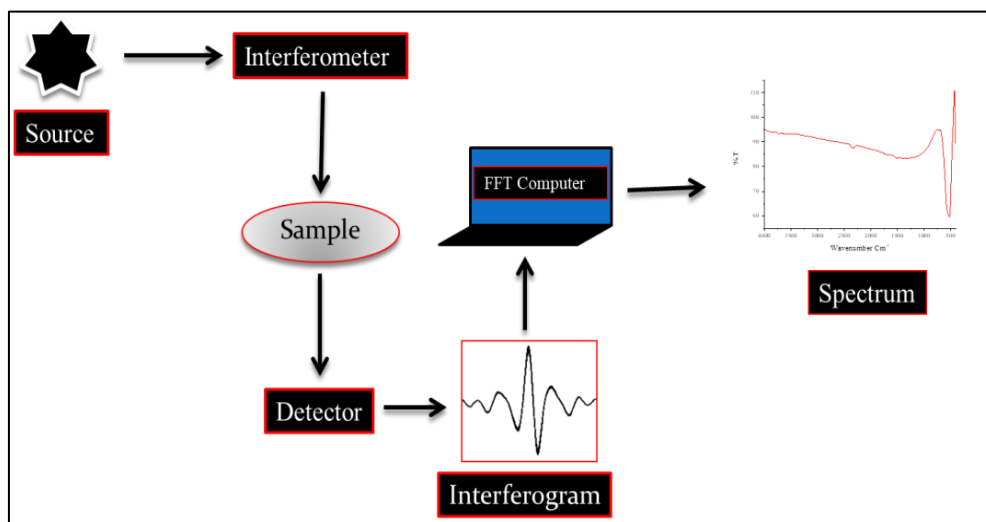
Fig. 3.7 Schematic of spectrophotometer with basic components [186].

The following components are used in FTIR spectrophotometer.

1. Source
2. Interferometer
3. Sample compartment
4. Detector
5. Recorder

The IR beam originates from a luminous black-body source in the instrument. The IR beam passes through an interferometer for spectral encoding. Beams of different path lengths recombined in an interferometer produce constructive as well as destructive interference, collectively called an interferogram. The beam now crosses the sample compartment and absorbs specific energy frequencies, which is a unique characteristic of the sample from the interferogram. The interferogram signals are detected by the detector for all the frequencies in energy versus time simultaneously. Finally, Fourier-transformation computer software recorded and displayed the required spectrum after the interferogram was subtracted from the background of the sample spectrum [186].

The magnetic behaviour of the samples can be studied by using the Vibrating sample magnetometery (VSM) technique. The detail about the 'VSM' technique is discussed in following sub-section 3.4.3.

3.4.3 Vibrating sample magnetometery (VSM)

Introduction

Vibrating sample magnetometery (VSM) is the technique used to measure the magnetic properties of the sample. It was developed by Foner in the 1950s. This technique was widely accepted due to its accuracy in data and flexibility [187].

Basic principle of vibrating sample magnetometery

The vibrating sample magnetometery (VSM) technique is based on Faraday's Law of Induction. It provides information that the change in magnetic field strength produces the electric field. After measuring the electric field, we can get the change in magnetic field. This technique is used to find out the magnetic properties of materials [188].

Instrumentation and working

Vibrating sample magnetometer used for the VSM study of the sample is illustrated in fig. 3.8.
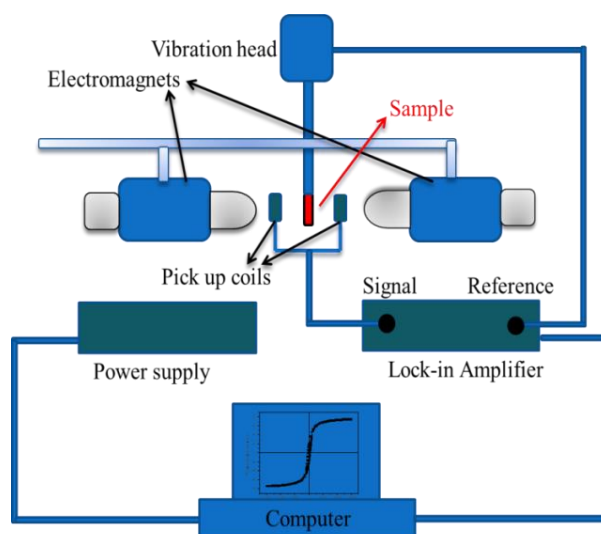
Fig. 3.8 Schematic of vibrating sample magnetometer with basic components [188].

The instrument contains basically six components. The brief discussion of the instrument and its working is conferred in the following sub-sections.

1) Vibrating head: The mechanical vibration of suitable range of frequencies can be generated by vibrating head. It is basically a loudspeaker. A rod is attached with vibrating element and lower end of rod is used to fill the sample. Generally, it is made up of diamagnetic, stiff, and insulating material [187,189].

2) Source of magnetic field: The magnetic field should have following two characteristics: It should be uniform throughout the space of the sample and, should be able to saturate the sample under analysis [187,189].

3) Electromagnet: The standard electromagnet which produces the uniform magnetic field can be used for this purpose [187,189].

4) Coils: Coils create lesser fields as compared to electromagnets but it can provide better uniform field [187,189].

5) Pick-up coils: The pick-up coils are situated among the poles of electromagnet and sample [187,189].

6) Calibration: The magnetic moment calibration can be done with saturation magnetisation value of the sample [187,189].

During the working process of the instrument, the sample is placed at the lower end of the vibrating head of the machine, and a strong magnetic field is applied to saturate the sample. The lock-in amplifier measured the signal, and a calibration factor was attained. It is necessary to saturate the sample in both directions with magnetic fields and get the average value of the signal to avoid off-set signals [187,189].

The morphology of the samples was studied with Field Emission scanning electron microscopy (FESEM). Detail of the 'FESEM' technique is discussed in following sub-section 3.4.4.

3.4.4 Field Emission scanning electron microscopy (FESEM)
Introduction

Field Emission scanning electron microscopy (FESEM) is an advanced electron microscopic technique used to find out the images of the surface of the sample. It is performed in the high vacuum conditions due to the tendency of the molecules to disrupt the electron beam and emitted secondary and backscattered electrons which are used for imaging [190].

Basic principle of FESEM technique

The FESEM technique is based on the principle of SEM analysis. The basic difference between SEM and FESEM is that the former technique used the thermionic electron source, while the later technique used the field emission electron source [190,191]. In this technique, the interaction between the electrons and sample materials generates the images. Due to its higher magnification as compared to a light microscope, it provides better results for researchers. The electron source is an important component in scanning electron microscopy. FESEM provides better resolution and higher magnification results as compared to SEM [191].

Instrumentation and working

The basic components required for the FESEM instrumentation technique are as listed below.

1) Electron optical system: The electron optical system is required to create an electron probe.

2) Specimen leg: The specimen leg is used to place the specimen in it.

3) Secondary electron detector: The secondary electron detector is used for the collection of secondary electrons.

4) Image display unit: The image display unit generated the images which are displayed on the screen.

5) Operating system: This system is used to carry out a number of operations. The schematic for the instrument used in the FESEM analysis technique is illustrated in fig. 3.9.
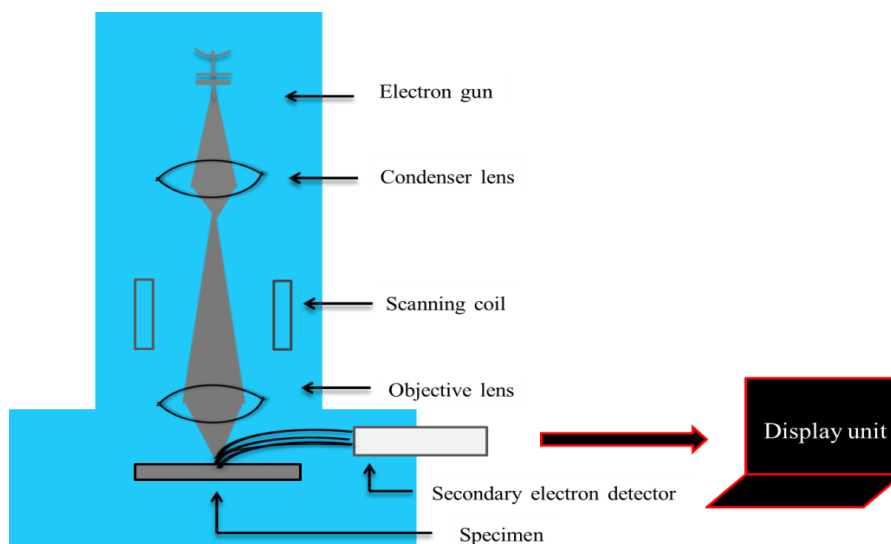
Fig. 3.9 Schematic of FESEM with basic components [192].

An electron beam is generated by an electron gun in which the cathode is made up of a tungsten wire with a diameter less than 1 mm. This wire is heated up to a temperature range of 2800 °C. Due to heating at high temperatures, the ejection of electrons takes place from the tungsten wire. These ejected electrons are called thermoelectrons. It is noted that lanthanum hexaboride (LaB6) can also be used as a cathode for the production of thermoelectrons. The positively charged metal anode collects the thermoelectrons. A small hole at the centre of the anode allows a beam of thermoelectrons to pass. The size of the beam can be controlled by a negatively charged electrode, which is fixed between the cathode and anode. The thinnest point of an electron beam is called the crossover. Generally, electron beams with crossover diameters in the range of 15 µm to 20 µm are used. [190]. The electron beams of requisite diameter are produced by magnetic lenses named condenser lens and objective lens. These lenses are located inside the electron gun. A hole is created of a thin metal plate and placed between the condenser lens and the objective lens. The condenser lens is used to narrow down the beam of electrons. The hole allows the narrow beam of electron passes through the objective lens which is focused in the

electron probe towards the sample material. These electrons are called primary electrons. The specimen leg of the instrument can move in all the directions. It can also be sloped and rotated [192].

When the primary electron beam strikes the sample, there are possibilities of several types of phenomena to occur. They are as follows:

i. Secondary electrons are generated due to inelastic collision between the primary electrons and sample. These secondary electrons are detected by secondary electron detectors.

ii. Backscattered electrons are generated due to elastic collision between primary electrons and the nucleus of the atoms present in the sample. The BSE detectors detect these electrons.

iii. The Auger electrons may also be produced due to collision between primary electrons and the sample due to the production of excess energy during the transition of electrons from a higher level of energy to a lower level and consumed to eject the electrons of other atoms of the sample.

iv. The characteristic X-rays are also produced due to the releases of a certain amount of energy during the transition of an electron from a higher state to a lower state.

v. X-ray fluorescence is created because of the interaction of highly excited primary electrons with samples. This has a minor probe [192].

The elemental detection of the samples can be studied by using the Energy dispersive X-ray analysis (EDX). From the next sub-section 3.4.5 we are discussing the 'EDX' technique.

3.4.5 Energy dispersive X-ray analysis (EDX)

Introduction

Energy dispersive X-ray (EDX) spectroscopy is used to detect the elemental composition of the sample by using scanning electron microscope (SEM) [190].

Basic principle and working of EDX

The characteristic X-rays are generated after the collision between the electron beam and sample in a typical SEM. The X-ray emission spectrum is different for the different elements so they can be discriminated and measured for their concentration in the sample. The characteristic X-ray is produced by the interaction of the primary electron beam with the atom of the sample. A primary electron beam excites the electrons of an atom, and ejects them to create an electron hole. An outer, higher energy shell electron of the atom replaces the missing ejected electron and releases the additional X-ray [190].

When primary electrons hit the sample, the possibility of generation of two types of X-rays:

1. Characteristic X-rays: During the inelastic collisions between the primary electrons beam and sample, the primary electron may impart some of its energy to the electrons of the atoms of the sample. The electrons of the atoms of the sample material receive this energy and get kicked-out of the shell and create a hole or an empty shell. Electrons of higher energy levels fall to lower energy empty shells and release a certain amount of energy in the form of characteristic X-ray. This whole process is shown as in fig. 3.10. The characteristic X-rays analysis provides the elemental composition of the sample.
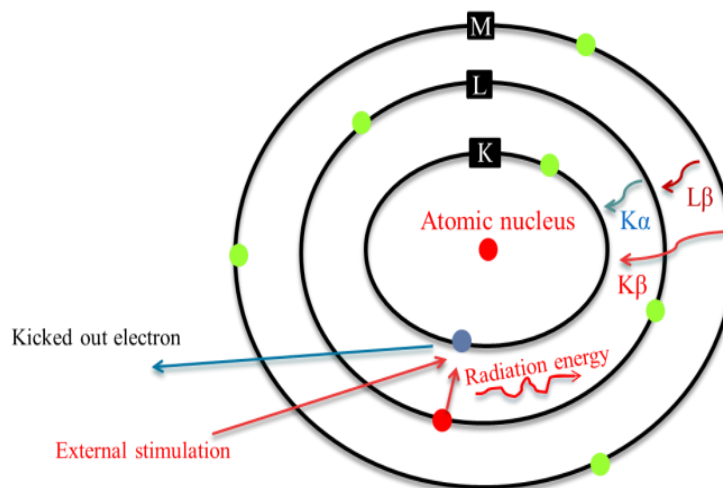
Fig. 3.10 Process of generation of characteristic X-Ray [190].

The characteristic X-ray lines are named on the basis of the shell in which the vacancy is created and the shell from which an electron drops to fill that vacancy. For example, the $K\alpha$ radiation is emitted when the ejection of an electron takes place from the K-shell and the electron of adjacent L-shell jump down into the K-shell. If an electron jumps down from M-shell to K-shell then the emitted radiations are known as $K\beta$ radiations. Similarly, when a hole is created in L-shell and an electron jumps down from M-shell, it is named as $L\alpha$-radiation and if the electron jumps down from N-shell to L-shell the radiation is called $L\beta$ radiation [190].

2. Continuum (Bremsstrahlung) X-rays: The X-rays produced by the interaction between the primary electron beam and the nucleus of the atoms present in the sample. These X-ray characterise the background at which characteristic X-rays peaks are imposed. Due to the difference in intensities between the continuum X-ray and the characteristic X-ray, the continuum X-rays must be removed as background during data analysis [190].

The thermal properties of the samples were investigated using the Thermogravimetric analysis (TGA) and Differential Scanning Calorimetry (DSC) techniques. TGA and DSC are discussed in sub-sections 3.4.6 and 3.4.7 respectively.

3.4.6 Thermogravimetric Analysis (TGA)

Introduction

Thermogravimetric Analysis (TGA) is a powerful technique for the measurement of the thermal stability of materials, including polymers [193].

Basic principle of Thermogravimetric Analysis

In this method, changes in the weight of a specimen are measured while its temperature is increased. Moisture and volatile contents of a sample can be measured by TGA [193].

Instrumentation and working

The schematic of TGA instrumentation is as shown below (see fig. 3.11) [193].
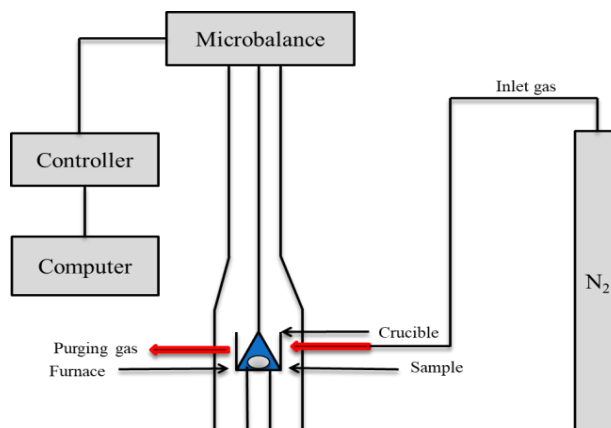
Fig. 3.11 Schematic of instrument used in thermogravimetric analysis (TGA) [193].

The TGA apparatus is equipped with the following components,

1. Furnace
2. Sample pan
3. A in-built weighing scale (balance)
4. A computer to display the data

A highly sensitive scale is used for the measurement of weight change of the sample under the control of the heat using a furnace. The balance is placed above the furnace and thermally isolated from the heat. A high precision hang-down wire is used for the suspension of balance into the furnace. A sample pan is placed at the end portion of the hang-down wire. A thermostatic chamber is used to protect the balance from the thermal effects [193,194].

3.4.7 Differential Scanning Calorimetry (DSC)

Introduction

Differential scanning calorimetry (DSC) is the analytical technique that is used for the thermal analysis of the samples [194,195].

Basic principle of Differential Scanning Calorimetry

DSC measured the heat flow change in materials as a function of temperature. This technique analyses the temperature at which a sample changes its phase. Change in phase of a material involves exchange of energy with surrounding. When energy is

absorbed by the sample during phase change, it is called an endothermic process whereas when a sample releases energy during phase change, it is called exothermic reaction. DSC machine tells us the temperature at which an extra amount of energy is either absorbed or released by the sample which suggests that the phase of the sample has been changed at this characteristic temperature. There are several events that can be studied using DSC, e.g., melting point, temperature of crystallisation, and temperature of degradation. The temperature range of the machine that we used was -70 °C to 450 °C [194,196]. The measurement was performed under controlled conditions [195].

Instrumentation and working

The schematic of DSC instrumentation is represented in fig. 3.12. The instrument runs isothermally with constant temperature change under an atmosphere of nitrogen. The enthalpy change (heat flow) is plotted against time under these conditions [194,196]. In this technique, the output of the signal produced is directly related to the thermal power difference between the sample and the inert reference [195].
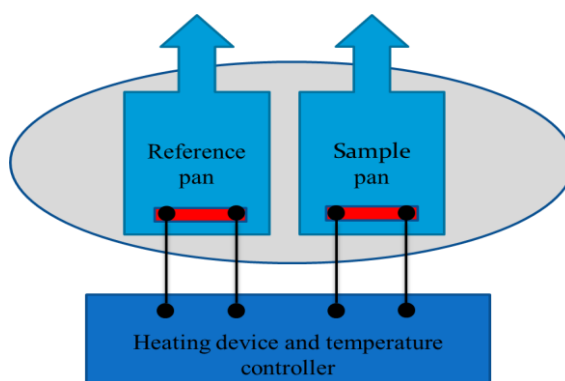
Fig. 3.12 Schematic of differential scanning calorimetry (DSC) instrument

From, the next section we will discuss about the synthesis of composites. The ZnO/Ag composites of the CF-NPs were prepared by using the mortar-pestle grinding technique. From the next following sec. 3.5, the synthesis of ZnO/Ag composites using the mortar-pestle grinding method is discussed in detail.

3.5 Synthesis of ZnO/Ag composite/s via mortar-pestle grinding method

3.5.1 Equipment's used for the preparation of ZnO/Ag composite of CF-NPs

The details of equipment's used for the preparation of composite materials are discussed in sub-sec. 3.3.1 (see Table 3.1).

3.5.2 Chemical used for the preparation of ZnO/Ag composite of CF-NPs

Table 3.5: List of chemical used for the preparation of ZnO/Ag composite of doped/co-doped CF-NPs

S. No.	Name of chemicals	Molecular formula	Source	Purity level	Mol. Wt.	Purpose of use
1.	CF-NPs samples	-	As prepared	-	-	Matrix
2.	Silver nitrate	$AgNO_3$	Fine	98%	169.87	Additive
2.	Zinc Oxide	ZnO	Molychem	99% AR	81.41	Filler
3.	Starch	$(C_6H_{10}O_5)_n$	Molychem	-	162.14	Binder

AR = Analytical reagent

3.5.3 Method of preparation of ZnO/Ag composite of CF-NPs

The stoichiometric amount of co-doped cobalt ferrite (CF-NPs) with transition metal ions was used as a starting material. The powder sample of CF-NPs, zinc oxide, silver nitrate and binder were taken in the fixed molar ratios of 1:3:3:7 respectively. Starch was used as a binder in the composite formation. The mixture was transferred in the mortar and pestle (ceramic). It was grounded thoroughly manually using a pastel for ~ 10 minutes. The prepared sample was ZnO/Ag composite of CF-NPs [169,197]. The schematic for the preparation of composite materials is represented in fig. 3.13.
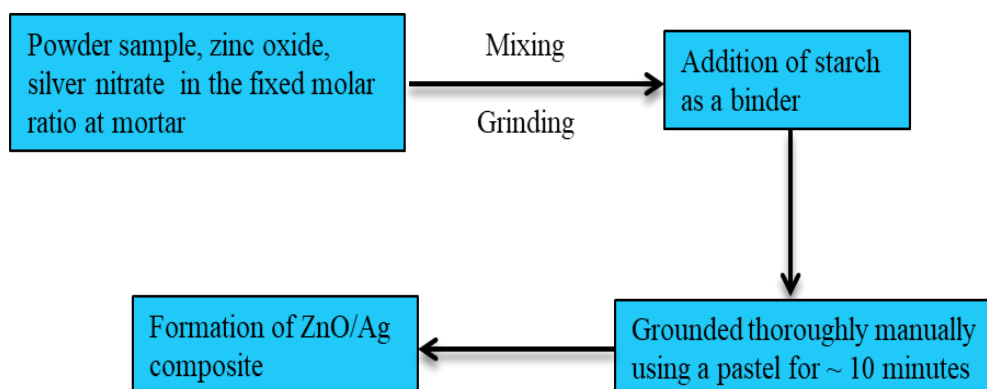
Fig. 3.13 Schematic flow of composite preparation via mortar-pestle grinding method

Various steps involved during the process of composite formation are depicted in fig. 3.14 as shown below.

<div align="center">

Mixing of starting   Addition of binder   Grinding of mixture   Composites
materials
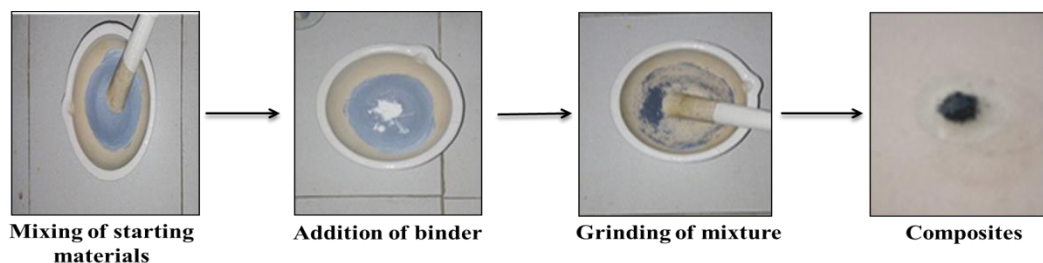
Fig. 3.14 various steps involved in the formation of composite

</div>

3.5.4 Detail of composite samples of synthesised CF-NPs

A complete list of composite materials of all the synthesised CF-NP samples is listed in Table 3.6 as shown below.

Table 3.6: List of various composite samples of un-doped, doped and co-doped CF-NPs

S.No.	Sample-id of composite	CF-NPs used as matrix	Dopant/s	Level of doping
1.	SKC-002	SK-002	Ag	0.1
2.	SKC-005	SK-005	Cu	0.1
3.	SKC-007	SK-007	Bi	0.1
4.	SKC-008	SK-008	Zn	0.1
5.	SKC-006	SK-006	Cu & Ag	0.1 & 0.1
6.	SKC-013	SK-013	Cu & Ag	0.05 & 0.05
7.	SKC-018	SK-018	Cu & Ag	0.15 & 0.15
8.	SKC-012	SK-012	Zn & Ag	0.1 & 0.1
9.	SKC-014	SK-014	Zn & Ag	0.05 & 0.05
10.	SKC-019	SK-019	Zn & Ag	0.15 & 0.15
11.	SKC-011	SK-011	Cu & Zn	0.1 & 0.1
12.	SKC-015	SK-015	Cu & Zn	0.05 & 0.05
13.	SKC-020	SK-020	Cu & Zn	0.15 & 0.15
14.	SKC-001	SK-001	Bi & Ag	0.1 & 0.1
15.	SKC-016	SK-016	Bi & Ag	0.05 & 0.05
16.	SKC-021	SK-021	Bi & Ag	0.15 & 0.15
17.	SKC-010	SK-010	Bi & Zn	0.1 & 0.1
18.	SKC-017	SK-017	Bi & Zn	0.05 & 0.05
19.	SKC-022	SK-022	Bi & Zn	0.15 & 0.15
20.	SKC-023	SK-023	Un-doped	0

The antibacterial activities of the samples were examined via Agar disk diffusion test. Agar disk diffusion test is discussed in the next section (see sec. 3.6).

3.6 Agar disk diffusion test for antibacterial activity

3.6.1 Introduction

The Agar disk diffusion method is a widely used method to detect the antibacterial activities of the prepared samples. The detail of Agar disk diffusion method is described in the following paragraph.

3.6.2 Equipment used for the antibacterial activity test

The details of equipment used for the antibacterial activity test of all the prepared samples are discussed in sub-sec. 3.3.1 (see Table 3.1).

3.6.3 Chemicals used for antibacterial activity test

Table 3.7: List of chemical used for the antibacterial study of doped/co-doped CF-NPs

S. No.	Name of chemicals	Molecular formula	Source	Purity level	Mol. Wt.	Purpose of use
1.	Stock solutions	-	Prepared samples	-	-	Antibacterial study
2.	Amoxicillin	-	500 mg tablet	-	-	Positive control
3.	Liquid paraffin	C_nH_{2n+2}	Rankem	99%	436.84	Negative control
4.	Nutrient Agar	Basal media	Himedia	-	-	Agar medium
5.	Filter paper disk	-	Whatmann paper	-	-	Zone formation

3.6.4 Test for antibacterial activity of samples using Agar disk diffusion method

In this well-known procedure, agar plates are inoculated with a standardised inoculum of the test microorganism. Filter paper disks (about 6 mm in diameter), are loaded with the desired concentrations of the samples. These disks are then placed on the agar surface. The Petri plates are incubated under suitable conditions. Generally, an antimicrobial agent diffuses into the agar and inhibits germination and growth of the test microorganism, and then the diameters of inhibition growth zones are measured using a Vernier scale [180]. Fig. 3.15 shows the formation of zones of inhibition to test the antibacterial activities of various samples of CF-NPs and their composite materials against *Bacillus paranthracis* and *Bacillus nitroreducens* using Agar disk diffusion test.
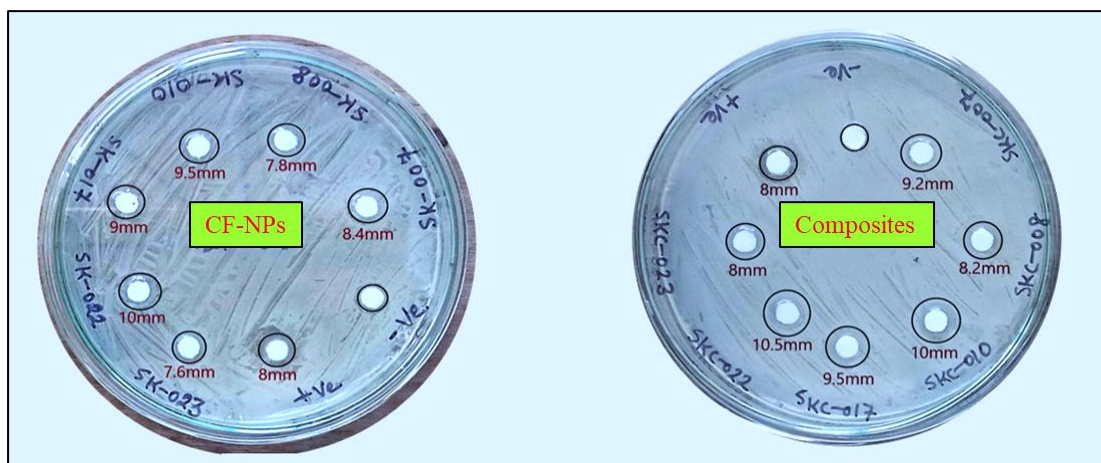
Fig. 3.15 Pictorial representation of antibacterial activity results of various samples of CF-NPs and their composite materials against Bacillus paranthracis and Bacillus nitroreducens using agar disk diffusion test

3.6.5 Mechanism of antibacterial activity of magnetic material

The antibacterial mechanism of magnetic CF-NPs as well as their nanocomposites is explained schematically in fig. 3.16 [171].
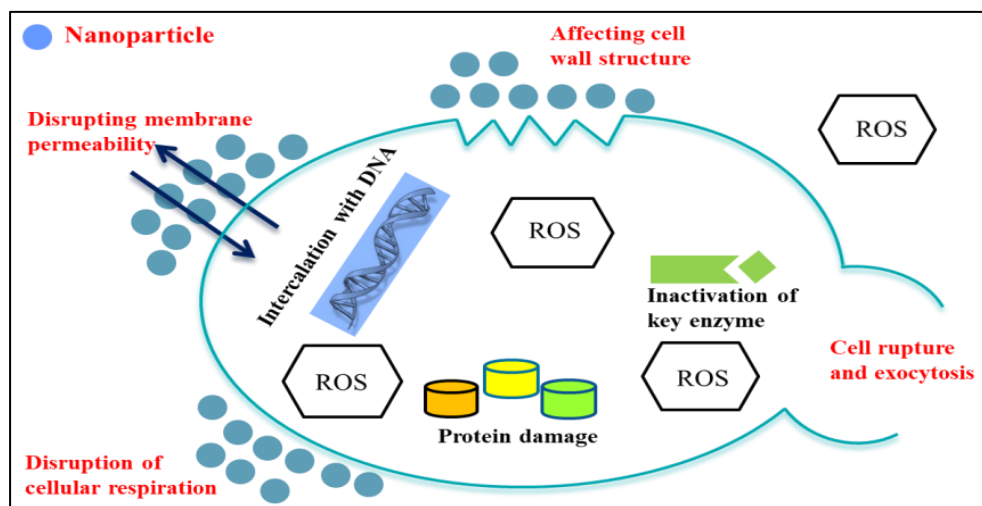
Fig. 3.16 Antibacterial mechanism of magnetic CF-NPs

It is assumed that the electrostatic forces of attraction between the magnetic nanoparticles (MNPs) and the bacterial cell walls are responsible for their attachment with each other. The metabolic function of the cell membrane gets disturbed due to the electrostatic forces of attraction and damaged the cell membrane [171]. The

intracellular components release the genetic materials, including lipids and proteins, after the damage of cell membrane and destroyed the bacterial cells. It is believed that the MNPs, when catalysed, produce reactive oxygen species (ROS) and play a significant role in killing the bacterial cell. The destruction of the cell membrane may be due to the sharp edges and vertices on the nanostructure [70,171,198].

3.7 Conclusion

Here, we synthesised the various co-doped CF-NPs with transition metal ions via the sol-gel method. Various Advanced Materials' characterisation techniques were used to characterise the prepared samples.

XRD used to study the crystalline structure of the samples. FTIR detected the functional groups present in the samples. Magnetic character studied via VSM. The morphology and elemental detection were carried out using FESEM/EDS analysis. The thermal properties of the samples were examined by TGA and DSC. The composite materials of the samples were prepared by using the mortar-pestle grinding method. Antibacterial activities of all the prepared samples and their composites were examined by using the Agar disk diffusion method.

Chapter 4
Objectives and research gap

4.1 Objectives

1. Synthesis of cobalt ferrite co-doped with (a) silver (I) and copper (II) (b) zinc (II) and silver (I) (c) copper (II) and zinc (II), via sol-gel route and fabrication of their composites with ZnO/Ag.

2. Synthesis of cobalt ferrite co-doped with (a) silver (I) and bismuth (III) (b) zinc (II) and bismuth (III), via sol-gel route and fabrication of their composites with ZnO/Ag.

3. Characterization of the above-mentioned materials using Advanced Materials' Characterization Techniques.

4. Study of antibacterial activity of the above said materials.

4.2 Research gap

Synthesis and characterisation of ferrite nanoparticles have been done by several research groups all over the world. These materials have numerous applications in various fields. For example, they are used in fabricating memory devices, as inductors, in biomedical applications, as high-frequency microwave absorbers, and in telecommunication and radar systems, to name but a few. Several routes of synthesis have been employed for the preparation of these materials, for example, the sol-gel route, co-precipitation methods, Stöber's synthesis or precipitation method, hydrothermal method, solid state reactions, and from natural products as well, for example, china rose and egg white, have been used by several research groups. The sol-gel method is widely used because of its several strong points. For example, it does not require very sophisticate laboratory infrastructure, monodisperse grain sizes can be prepared, and a variety of starting materials can be chosen to synthesise a range of products. To our knowledge, still research gap exits in co-doping of cobalt ferrite. It changes the magnetic properties of these materials, which in turn will influence the antibacterial behaviour of cobalt ferrite. Still several transition metals, for example, co-doping of silver with copper and zinc as well as co-doping of bismuth

with silver and zinc has not been carried out. Literature says that their composites with ZnO/Ag have not been prepared. These materials will be synthesised via the sol-gel route and will be characterised using Advanced Materials' characterisation techniques. The antibacterial activities have not been explored. Research on novel and effective antibacterial drugs will be prompted by the growing awareness of antibiotic-resistant bacteria as a health risk.

Chapter 5

Antibacterial activities of co-doped cobalt ferrite with Cu-Ag and their composite/s with ZnO/Ag

5.1 Introduction

This chapter deals with the synthesised co-doped CF-NPs with Cu-Ag and its ZnO/Ag composite materials. The various Advanced Materials' characterisation techniques were used to characterise these CF-NPs. The antibacterial activities of all the samples were tested by using Agar disk diffusion test. The various results obtained are discussed in the following sec. 5.2 to 5.7.

5.2 Crystalline structure studies using XRD
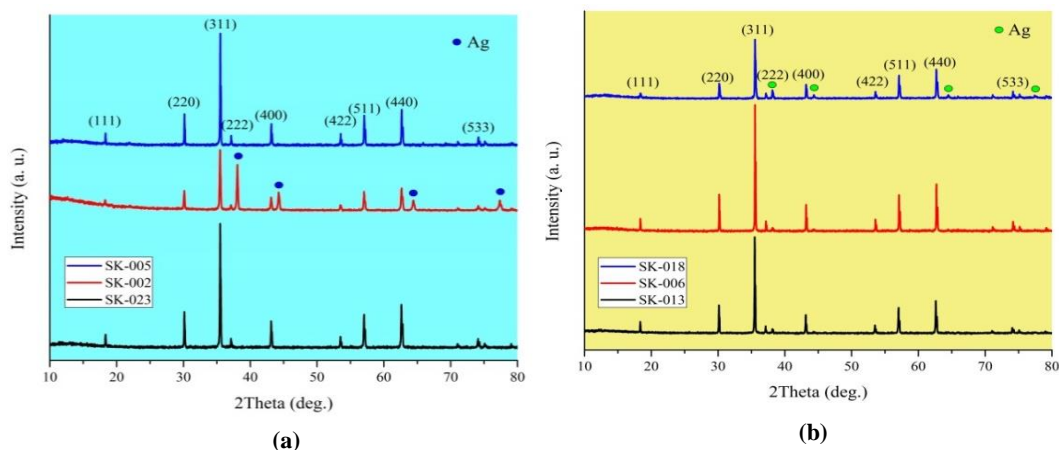
Fig. 5.1 Powder XRD pattern of:
(a)un-doped and doped CF-NPs with sample-ids: SK-023, SK-002 and SK-005;
(b)co-doped CF-NPs with sample-ids: SK-013, SK-006 and SK-018.

Here, fig 5.1 (a) represents the XRD pattern of un-doped CF-NPs (SK-023), silver doped CF-NPs (SK-002), and copper doped CF-NPs (SK-005), while fig. 5.1(b) represents the XRD pattern of Cu-Ag co-doped CF-NPs (sample-ids: SK-013, SK-006, and SK-018). The CuKα radiation of wavelength 1.54 Å was used as a source of X-rays. It was studied at º/2θ between the range of 10º to 80º. The list of samples with their levels of doping is tabulated in Table 5.1.

Table 5.1: List of un-doped, doped and co-doped CF-NPs with their level of doping

S.No.	Sample-ids	Dopant/s	Level of doping	Desired products
1.	SK-002	Ag	0.1	$CoFe_{1.9}Ag_{0.1}O_4$
2.	SK-005	Cu	0.1	$CoFe_{1.9}Cu_{0.1}O_4$
3.	SK-013	Cu &Ag	0.05 & 0.05	$Co_{0.95}Cu_{0.05}Fe_{1.95}Ag_{0.05}O_4$
4.	SK-006	Cu &Ag	0.10 & 0.10	$Co_{0.9}Cu_{0.1}Fe_{1.9}Ag_{0.1}O_4$
5.	SK-018	Cu &Ag	0.15 & 0.15	$Co_{0.85}Cu_{0.15}Fe_{1.85}Ag_{0.15}O_4$
6.	SK-023	Un-doped	0	$CoFe_2O_4$

The angle º/2θ of diffraction of using JCPDS (01-083-3116) is listed in Table 5.2.

Table 5.2: List of diffraction angles (º/2θ) with their respective diffraction plane

Diffraction angle (º/2θ)	Diffraction plane	Diffraction angle (º/2θ)	Diffraction plane	Diffraction angle (º/2θ)	Diffraction plane
18.37°	(111)	37.21°	(222)	57.11°	(333)
30.11°	(220)	43.14°	(400)	62.80°	(440)
35.49°	(311)	53.50°	(422)	74.11°	(533)

All the peaks confirmed the cubic inverse spinel structure of CF-NPs with space group fd-3m [4]. The presence of a secondary phase of silver is observed in the silver doped sample (SK-002), same as reported in the earlier studies marked as (●) (see fig. 5.1a). The presence of an additional phase of silver might be due to the ionic size difference between Ag^+ ions (~1.29 Å) and Fe^{3+} ions (~0.67Å). Therefore, the possibility of its occupancy at the tetrahedral or octahedral sites becomes easy. Similarly, a secondary phase of silver marked as (●) was also noticed at co-doped samples (SK-013, SK-006, and SK-018). Ionic size differences between dopant ions and host ions may be accountable for this type of behaviour [49,122,144]. No additional phase is observed in the sample of copper doped CF [115]. It was also observed the minor shifting in high intense peaks at the plane 311 as compared to the un-doped sample. It might be due to the doping and co-doping of CF-NPs [49]. The crystallite sizes and lattice parameters of un-doped, doped, and co-doped CF-NPs are tabulated in Table 5.3.

Table 5.3: The crystallite sizes and lattice parameters of un-doped, Cu and Ag doped, and Cu-Ag co-doped CF-NPs

Sample-ids	Dopant/s	Doping level	2θ	FWHM	D (nm)	Lattice parameter (Å)
SK-002	Ag	0.1	35.48	0.180	~ 47.0	8.381
SK-005	Cu	0.1	35.52	0.143	~ 58.6	8.378
SK-013	Cu-Ag	0.05 & 0.05	35.51	0.141	~ 58.4	8.385
SK-006	Cu-Ag	0.10 & 0.10	35.55	0.138	~ 60.8	8.373
SK-018	Cu-Ag	0.15 & 0.15	35.57	0.167	~ 50.3	8.373
SK-023	Un-doped	0	35.51	0.150	~ 54.0	8.385

The lattice parameter of the cubic crystal structure was calculated by using the eq^n. (3.3) [66]. The lattice parameter in Ag-doped sample (SK-002) and Cu-doped sample (SK-005) decreases as compared to un-doped sample (SK-023) (see Table 5.3). The decrease in lattice parameter in sample-id: SK-002 is due to the ionic size difference between the larger Ag^+ ion (1.29 Å) and the smaller Fe^{3+} ion (0.67 Å) [49], whereas in sample-id: SK-005 the decrease is due to the ionic size difference between the smaller Cu^{2+} ion (0.73 Å) and the larger Co^{2+} ion (0.745 Å) [75,199]. These results are in good agreement with earlier reported results [19,200].

The lattice parameter of co-doped samples also decreases as compared to the un-doped sample (SK-023) with increases in their level of doping. The lattice parameters of co-doped samples SK-006 and SK-018 were perceived nearly the same. This anomalous behaviour might be due to the ionic size difference of host and guest ions [75,199].

The crystallite sizes of samples were calculated by using Scherrer's eq^n. (see eq^n. 3.2). The crystallite size in Ag-doped sample (SK-002) decreases [49201], while in Cu-doped sample (SK-005) it increases [200] (see Table 5.3). These results are in good agreement with earlier reported results. Although Kirankumar *et al.* observed the decrease in crystallite size in Cu-doped CF-NPs when synthesised via combustion route and sintered at 700 ℃ and 900 ℃ for 2 hours [75].

The co-doped samples with dopants levels 0.05 (sample id: SK-013) and 0.10 (sample id: SK-006) show an increase in crystallite size while the co-doped sample with dopant level 0.15 (sample id: SK-018) shows a decrease in crystallite size as compared to un-doped CF-NPs (sample id: SK-023) (see Table 5.3). The anomaly in crystallite size of co-doped samples might be due to the difference in ionic radius of dopants (Cu^{2+} and Ag^+) ions and host (Co^{2+} and Fe^{3+}) ions [142,202]. The trends of variation of lattice parameters and crystallite sizes of un-doped, Cu, and Ag-doped/ co-doped CF-NPs are represented in fig. 5.2.

83
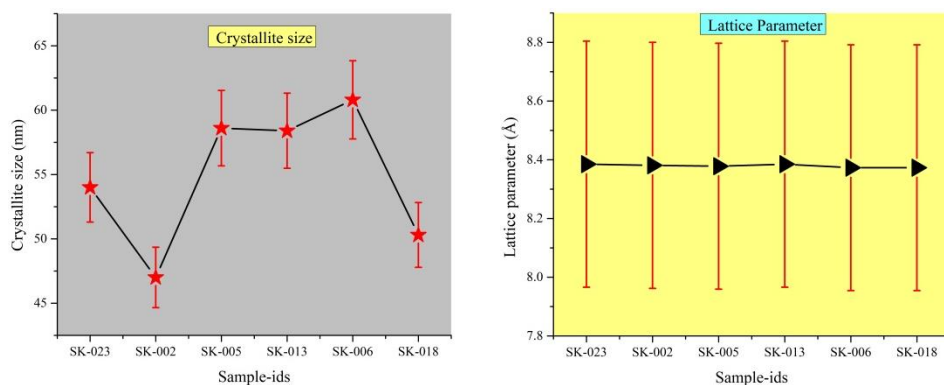
Fig 5.2 Variation of crystallite size and lattice parameter of un-doped CF-NPs, Cu and Ag doped/ co-doped CF-NPs

5.3 Compositional analysis of samples using FTIR

(a)

(b)

(c)
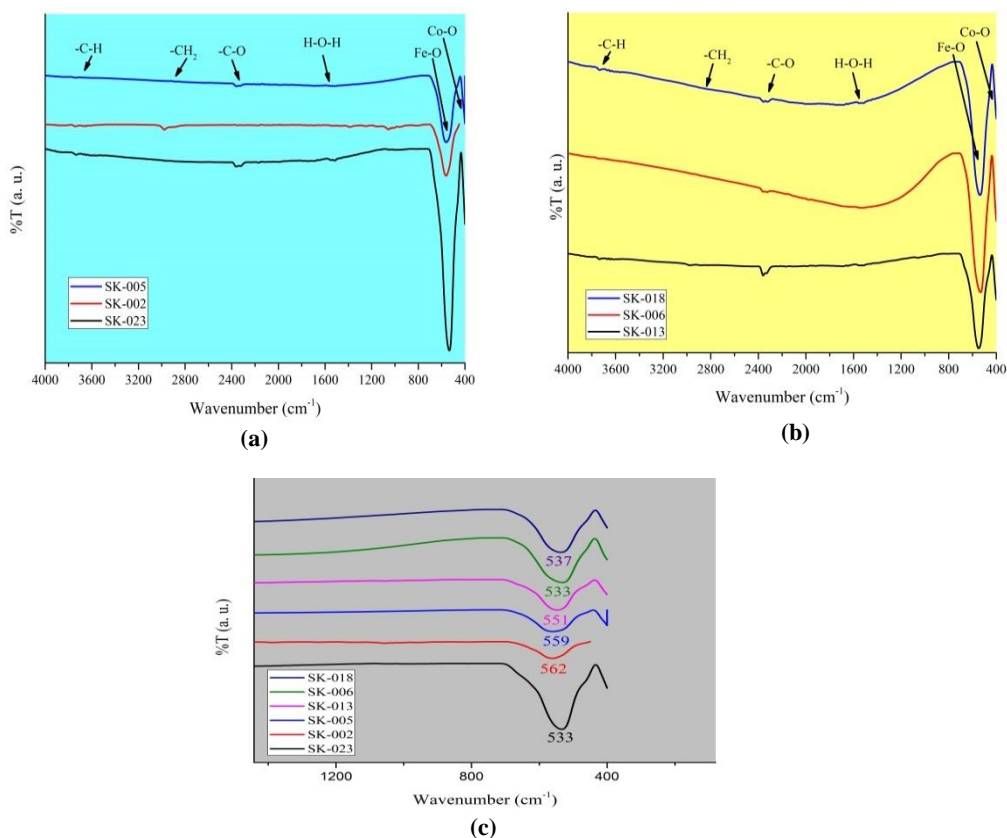
Fig. 5.3 FTIR pattern of sample-ids:
(a) SK-023, SK-002 and SK-005;
(b) SK-013, SK-006 and SK-018.
(c) narrow scan view of all the samples at the frequency range of 400-600 cm^{-1}.

The FTIR spectra of un-doped, Cu and Ag doped, and Cu-Ag co-doped CF-NPs are illustrated in figs. 5.3 (a) and 5.3 (b), while fig. 5.3 (c) represents the narrow scan

view of all the samples of CF-NPs in the range of 400 cm^{-1} to 800 cm^{-1}. The sharp absorption band at ~ 400 cm^{-1} to ~ 600 cm^{-1} specified the metal-oxygen bonds [101]. The absorption bands at the range of ~ 535 cm^{-1} to ~ 523 cm^{-1} indicated about Fe-O intrinsic stretch tetrahedral, while the band at the range of 404 cm^{-1} to 408 cm^{-1} indicated about Co-O intrinsic stretch octahedral sites [71,144]. The Ag-doped CF-NPs (SK-002), Cu-doped CF-NPs (SK-005), and co-doped CF-NPs (SK-013, SK-006, and SK-018) show few minor frequency changes as compared to the un-doped sample (SK-023) [71]. The absorption bands at the frequency range of ~ 1500 cm^{-1} to ~ 1600 cm^{-1} indicated H–O–H group, band at ~ 2853 cm^{-1} for CH$_2$ symmetric, and the band at ~ 2344 cm^{-1} for C–O mode, while the band at the range of ~ 3670 cm^{-1} indicates C–H bending mode [47]. These absorption bands are also listed in Table 5.4.

Table 5.4: List of absorption bands in un-doped, Cu and Ag doped, and Cu-Ag co-doped CF-NPs

SK-023 (CoFe$_2$O$_4$)			SK-002 (CoFe$_{1.9}$Ag$_{0.1}$O$_4$)		
Observed abs. band	Assign.	Ref.	Observed abs. band	Assign.	Ref.
~ 3740	(-C-H) bending	[5]	~ 3736	(-C-H) bending	[5]
~ 2348	(-C-O) mode	[47]	~ 2960	(-CH$_2$) symmetric	[47]
~ 1536	(H-O-H)	[47]	~ 1590	(H-O-H)	[47]
~ 540	(Fe–O) stretch tetrahedral	[144]	~ 560	(Fe–O) stretch tetrahedral	[144]
~ 402	(Co–O) stretch octahedral	[144]	~ 448	(Co–O) stretch octahedral	[144]
SK-005 (CoFe$_{1.9}$Cu$_{0.1}$O$_4$)			SK-013 (Co$_{0.95}$Cu$_{0.05}$Fe$_{1.95}$Ag$_{0.05}$O$_4$)		
Observed abs. band	Assign.	Ref.	Observed abs. band	Assign.	Ref.
~ 3735	(-C-H) bending	[5]	~ 3736	(-C-H) bending	[5]
~ 2347	(-C-O) mode	[47]	~ 2341	(-C-O) mode	[47]
~ 1552	(H-O-H)	[47]	~ 1537	(H-O-H)	[47]
~ 560	(Fe–O) stretch tetrahedral	[144]	~ 547	(Fe–O) stretch tetrahedral	[144]
~ 402	(Co–O) stretch octahedral	[144]	~ 404	(Co–O) stretch octahedral	[144]
SK-006 (Co$_{0.9}$Cu$_{0.1}$Fe$_{1.9}$Ag$_{0.1}$O$_4$)			SK-018 (Co$_{0.85}$Cu$_{0.15}$Fe$_{1.85}$Ag$_{0.15}$O$_4$)		
Observed abs. band	Assign.	Ref.	Observed abs. band	Assign.	Ref.
~ 3736	(-C-H) bending	[5]	~ 3736	(-C-H) bending	[5]
~ 2338	(-C-O) mode	[47]	~ 2338	(-C-O) mode	[47]
~ 1560	(H-O-H)	[47]	~ 1563	(H-O-H)	[47]
~ 534	(Fe–O) stretch tetrahedral	[144]	~ 537	(Fe–O) stretch tetrahedral	[144]
~ 404	(Co–O) stretch octahedral	[144]	~ 404	(Co–O) stretch octahedral	[144]

5.4 Vibrating-sample magnetometer (VSM) analysis

The VSM was used to analyse the magnetic properties of co-doped CF-NPs with copper and silver at the dopants concentrations of 0.15. Fig. 5.4 illustrates the hysteresis loop of co-doped CF-NPs with copper and silver (sample id: SK-018).
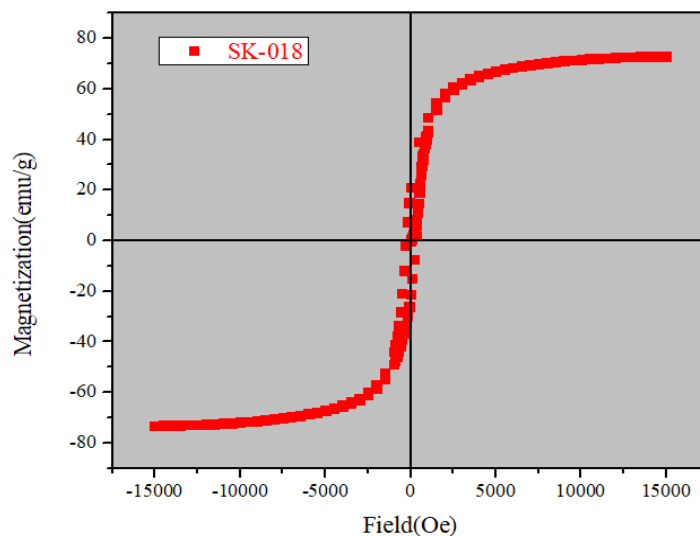
Fig. 5.4 Magnetic hysteresis curve of sample SK-018

Here, the saturation magnetisation (M_s) was recorded at 72.79 emu/g. The hysteresis curve showed low or negligible coercivity (H_c) and indicates that the materials became superparamagnetic. The superparamagnetic materials do not retain magnetism even after the removal of the applied magnetic field. The high saturation magnetisation and superparamagnetic character show that these materials can be suitable for various biomedical applications [9,146,203].

5.5 Morphological studies and elemental analysis of samples using FESEM and EDS
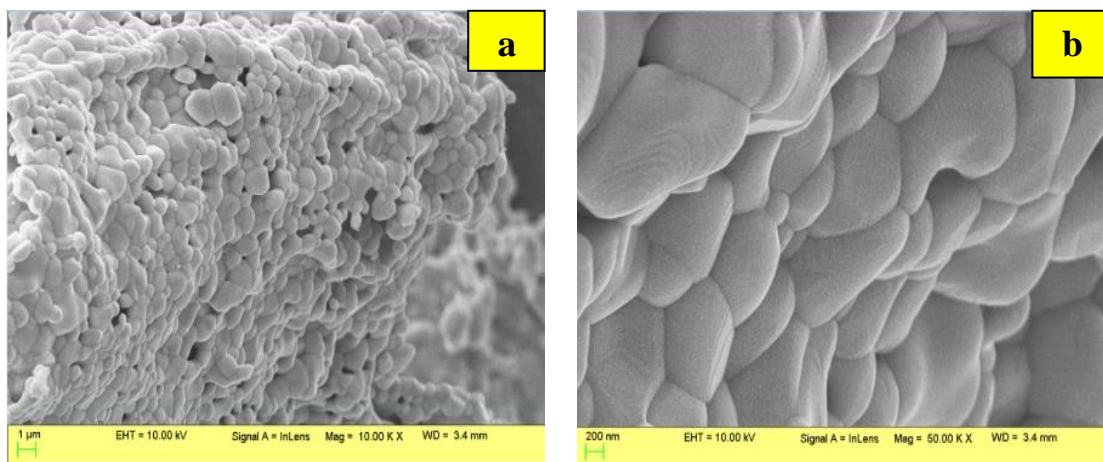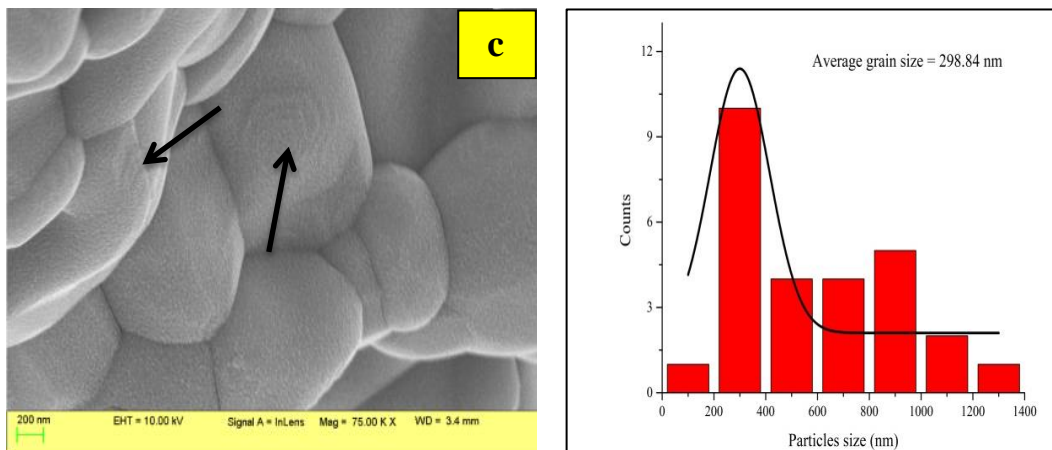
Fig. 5.5 FESEM pictures of co-doped sample SK-018

The FESEM pictures of co-doped CF-NPs (sample-id: SK-018) are reproduced in fig. 5.5. The agglomeration and stacking of the particles can be observed (see fig. 5.5a) [132]. In figs. 5.5b and 5.5c, the pentognal shaped particles with clear edges and surfaces can be seen. A few wrinkles can also be observed at the surface of the particles pointed out with arrows in fig. 5.5c [114,204–206]. The measured value of the average grain size was 298.84 nm. It was measured by using the Image J software.
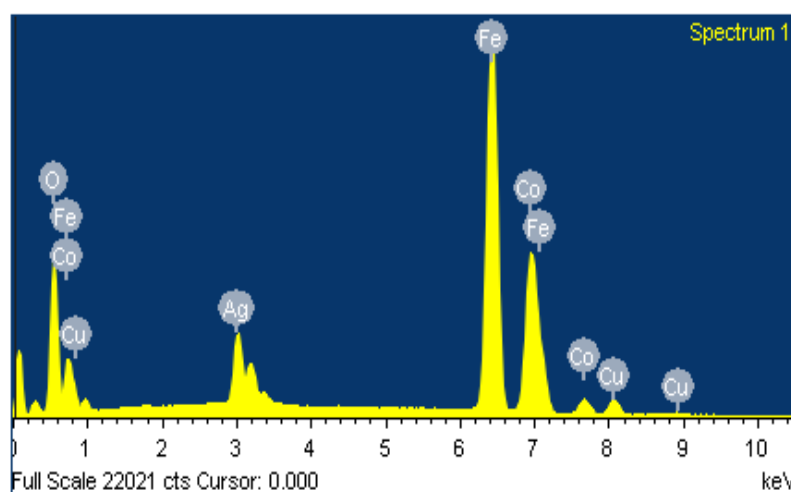
Fig. 5.6 EDS mapping of co-doped sample SK-018

The Energy Dispersive X-ray spectroscopy (EDS) result of one of the co-doped CF-NPs (sample id: SK-018) is presented in fig. 5.6. The presence of elements in the

87

prepared sample can be identified with elemental mapping. Here, the microscopist has chosen the K-lines and L-lines for the quantitative analysis of the sample. The weight percentages and atomic percentages of the elements present in the sample were calculated quantitatively. Table 5.5 lists the quantitative result of the sample SK-018 and indicates the existence of their consitutent elements. It was confirmed the presence of Ag, Cu, Fe, Co, and O in sample-id: SK-018 [71,75,104].

Table 5.5: List of elements in $Co_{0.85}Cu_{0.15}Fe_{1.85}Ag_{0.15}O_4$ (SK-018)

Elements	Weight %	Atomic %
O K	16.89	43.11
Fe K	48.20	35.25
Co K	23.55	16.32
Cu K	3.88	2.50
Ag L	7.47	2.83

The observed values are different from the expected value of atomic percentage because the EDS is a semi-quantitative and semi-qualitative method of analysis [207,208].

5.6 Thermal analysis of samples

The thermal properties and stabilities of the synthesised samples were examined via Thermogravimetric analyser (TGA) and Differential scanning calorimeter (DSC).
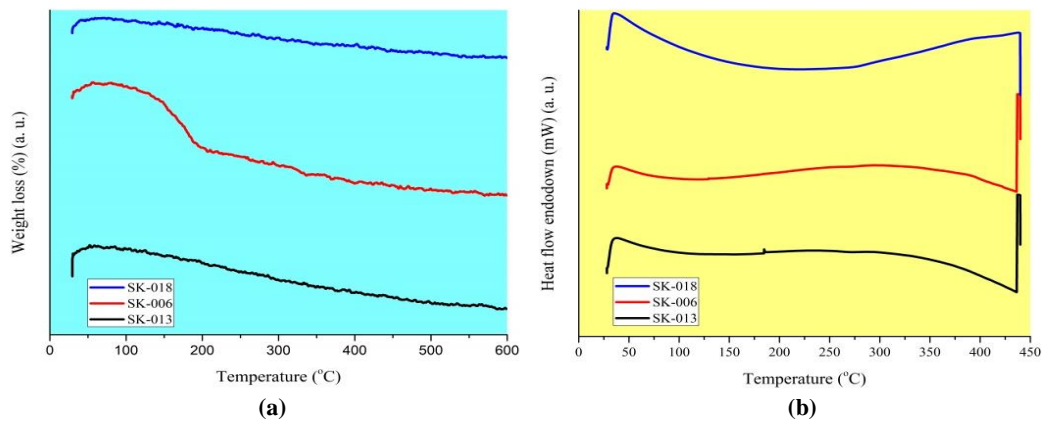
Fig. 5.7 Thermal properties of co-doped CF-NPs through:
(a) TGA of SK-013, SK-006 and SK-018;
(b) DSC of SK-013, SK-006 and SK-018.

Fig. 5.7(a) illustrates the TGA curves of co-doped samples (sample-ids: SK-013, SK-006, and SK-018). Here the insignificant weight loss can be seen up to 600 ºC. It may

be due to the loss in adsorbed/absorbed content of water at the surface of the samples. This indicates the thermal stability of these materials in the specified range of the temperature [207,209,210].

Fig. 5.7(b) illustrates the DSC curves of co-doped samples (sample-ids: SK-013, SK-006, and SK-018). A minor thermal event can be seen in all three samples. The co-doped sample SK-013 showed a minor exothermic event at 186 ºC. The co-doped sample SK-006 showed a slight exothermic change at 260 ºC while the sample SK-018 decomposed in the endothermic region at 230 ºC [207,209,210]. The data of the thermal analysis of all the samples are also listed in Table 5.6.

Table 5.6: The data obtained after thermal analysis of the co-doped CF-NPs

TGA		DSC	
Sample-ids	Weight loss (%)	Sample-ids	Temperature at which minute thermal event observed
SK-013	0.02	SK-013	~186 ˚C
SK-006	0.06	SK-006	~260 ˚C
SK-018	0.02	SK-018	~230 ˚C

5.7 Antibacterial activities

The various zones of inhibition created by the different samples of CF-NPs and their ZnO/Ag composites can be seen in the figs. 5.8 (a) to 5.8 (b) respectively.
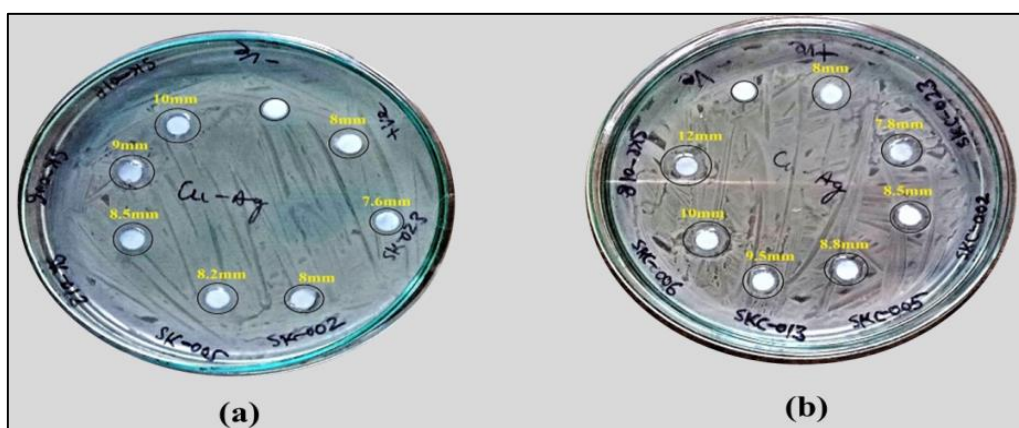
Fig. 5.8 Photographs of zone of inhibitions of:
(a) SK-023, SK-002, SK-005, SK-013, SK-006, SK-018;
(b) SKC-023, SKC-002, SKC-005, SKC-013, SKC-006, SKC-018.

A list of diameter of zone of inhibitions in all the samples of CF-NPs and their composites is tabulated in Table 5.7.

Table 5.7: Measurment of zone of inhibitions in all the samples of CF-NPs and its composites

Sample-ids	Zone of inhibitions (mm)	Sample-ids	Zone of inhibitions (mm)
SK-023	7.6	SKC-023	7.8
SK-002	8.0	SKC-002	8.5
SK-005	8.2	SKC-005	8.8
SK-013	8.5	SKC-013	9.5
SK-006	9.0	SKC-006	10.0
SK-018	10.0	SKC-018	12.0

The measured diameter of zones of inhibition shows that the antibacterial activities of the silver doped sample (SK-002) and the copper doped sample (SK-005) were higher than the un-doped sample (SK-023). These results are in good agreement with earlier reported values [19,71]. The antibacterial zones of inhibition in co-doped samples increase in a steady way. It increases in the co-doped sample of dopant level 0.05 (SK-013) to the co-doped sample of dopant level 0.15 (SK-018). Here, the sample SK-018 shows enhanced antibacterial activity among all the co-doped CF-NPs.

Similarly, the ZnO/Ag composites of CF-NPs follow the same trend. The composite of un-doped CF-NPs (SKC-023) created the smallest zone, while the composite of co-doped CF-NPs (SKC-018) of dopant level 0.15 generated the largest zone. The zones of inhibition in the composite of CF-NPs increase in a steady way from SKC-002 to SKC-018. This trend of increase in zones of inhibition is also represented by using the bar graph diagram (see fig. 5.9).

(a)   **(b)**
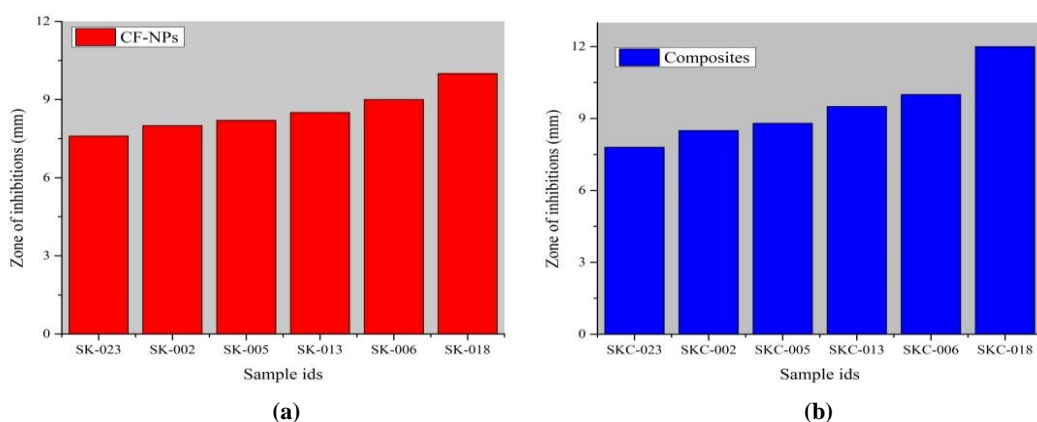
Fig. 5.9 Bar graph pictures of inhibition zone of:
(a) SK-023, SK-002, SK-005, SK-013, SK-006, SK-018;
(b) SKC-023, SKC-002, SKC-005, SKC-013, SKC-006, SKC-018.

Therefore, it can be concluded that the composite samples of CF-NPs show enhanced antibacterial activities compared to their respective samples of CF-NPs [153,211].
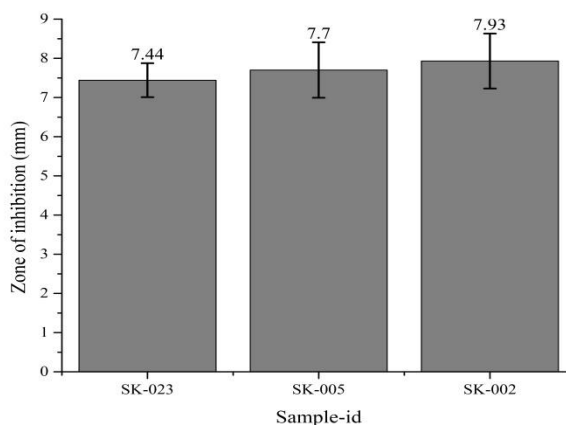
Fig. 5.10 Bar graph picture presenting the reproducibility of the sample-ids: SK-023, SK-005 and SK-002.

The reproducibility of antibacterial activities of the sample-ids: SK-023, SK-002, and SK-005 is shown in fig. 5.10. Here, the trend of variation and reproducibility of the samples follow the same order as it has been found in the antibacterial activities of silver doped CF and copper doped CF. The CF-NPs doped with silver and copper showed enhanced antibacterial activities than un-doped samples [14,19,71]. Silver doped CF-NPs showed higher antibacterial activity than copper doped CF-NPs. As reported in literature as well, the copper doped CF-NPs showed greater antibacterial activities than un-doped samples [14,71]. We also observed that the CF-NPs co-doped with copper and silver showed better antibacterial activities than the singly doped CF-NPs as well as un-doped samples.

5.8 Conclusions

Here, we have successfully synthesised un-doped, Cu and Ag-doped, and Cu-Ag co-doped CF-NPs via the sol-gel method, as well as its ZnO/Ag composites, by using the mortar-pestle grinding method. Samples were analysed using the various Advanced Materials' characteriasation techniques. XRD examined the crystalline structure of the samples and its variation in crystallite size and lattice parameters. FTIR confirmed the existence of a metal-oxygen bond. The level of doping was accountable for the shift

in absorption bands. The superparamagnetic behaviour of co-doped sample SK-018 was detected via VSM. The superparamagnetic material is suitable for various biomedical applications. A FESEM micrograph confirmed the presence of agglomerated particles with a pentagonal shape. The EDS result examined the elemental detection in co-doped sample SK-018. It indicated the presence of Ag, Cu, Fe, Co, and O elements with atomic percentages and confirmed the co-doping in CF-NPs. TGA shows the absence of impurity in co-doped samples of CF-NPs, while DSC analysis shows an insignificant thermal event. All the synthesised samples of CF-NPs and their ZnO/Ag composites effectively show their antibacterial activities against *Bacillus paranthracis* and *Bacillus nitratireducens*. The composite samples show enhanced antibacterial activities than samples of CF-NPs. All the as-prepared samples showed antibacterial activities.

Chapter 6

Antibacterial activities of co-doped cobalt ferrite with Ag-Zn and their composite/s with ZnO/Ag

6.1 Introduction

This chapter deals with the prepared co-doped CF-NPs with Ag-Zn and its ZnO/Ag composite materials. The various Advanced Materials' characterisation techniques were used to characterise these CF-NPs. The antibacterial activities of all the samples were tested by using Agar disk diffusion test. The various results obtained are discussed in the following sections (see sections 6.2 to 6.7).

6.2 Crystalline structure studies using XRD
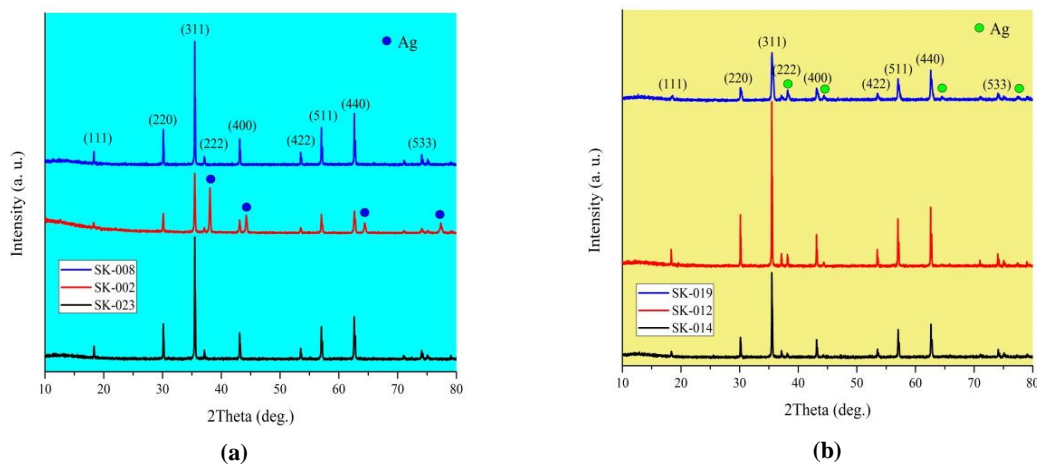
Fig. 6.1 XRD pattern of:
(a) $CoFe_2O_4$, $CoFe_{1.9}Ag_{0.1}O_4$, $CoFe_{1.9}Zn_{0.1}O_4$;
(b) $Co_{0.95}Ag_{0.05}Fe_{1.95}Zn_{0.05}O_4$, $Co_{0.9}Ag_{0.1}Fe_{1.9}Zn_{0.1}O_4$, $Co_{0.85}Ag_{0.15}Fe_{1.85}Zn_{0.15}O_4$.

Fig. 6.1 (a) illustrates the powder XRD patterns of un-doped CF-NPs, Ag-doped and Zn-doped CF-NPs, while the fig. 6.1 (b) represents the co-doped CF-NPs with Ag and Zn. The level of doping of all the samples is also listed in Table 6.1.

Table 6.1: Un-doped, Ag and Zn doped, and Ag-Zn co-doped CF-NPs with their sample-ids at different concentrations

S.No.	Sample-id	Dopants	Level of Doping	Desired product
1.	SK-002	Ag	0.1	$CoFe_{1.9}Ag_{0.1}O_4$
2.	SK-008	Zn	0.1	$CoFe_{1.9}Zn_{0.1}O_4$
3.	SK-014	Ag & Zn	0.05 & 0.05	$Co_{0.95}Ag_{0.05}Fe_{1.95}Zn_{0.05}O_4$
4.	SK-012	Ag & Zn	0.10 & 0.10	$Co_{0.9}Ag_{0.1}Fe_{1.9}Zn_{0.1}O_4$
5.	SK-019	Ag & Zn	0.15 & 0.15	$Co_{0.85}Ag_{0.15}Fe_{1.85}Zn_{0.15}O_4$
6.	SK-023	Un-doped	0	$CoFe_2O_4$

The diffraction angles at different planes with JCPDS no. 01-083-3116 are summarised in Table 6.2.

Table 6.2: List of diffraction planes concerning diffraction angles (º/2θ)

Diffraction angle (º/2θ)	Diffraction plane	Diffraction angle (º/2θ)	Diffraction plane	Diffraction angle (º/2θ)	Diffraction plane
18.37°	(111)	37.21°	(222)	57.11°	(333)
30.11°	(220)	43.14°	(400)	62.80°	(440)
35.49°	(311)	53.50°	(422)	74.11°	(533)

These results confirmed the cubic crystal structure of samples. It was also observed the minor change in diffraction angle (º/2θ) towards higher angles after doping and co-doping [77]. An additional phase of silver (Ag) was noticed in the silver-doped sample (SK-002). The ionic size differences between guest ions Ag^+ (~1.29 Å) and host ions Co^{2+} (~0.72 Å) are responsible for this type of behaviour, same as reported earlier [49,122]. No additional phase was observed in the zinc-doped sample (SK-008) [113]. Similarly, in fig. 2(b) an additional phase of silver (Ag) was also noticed in co-doped samples (SK-014, SK-012, and SK-019). It might be due to the ionic size difference between dopants (Ag^+ and Zn^{2+}) and host ions (Co^{2+} and Fe^{3+}) [122,144]. The lattice parameters for cubic spinel structure were calculated by using equation (3.3), whereas the crystallite size was calculated using Debye Scherrer's equation (3.2) (see chapter no. 3) [212,213]. It was observed the decrease in crystallite size of the Ag-doped CF-NPs (SK-002) [49,201], whereas it increases in Zn-doped CF-NPs (SK-008) as compared to un-doped CF-NPs. Sastry *et al.* [201] and Das *et al.* [202] noticed similar types of behaviour in Zn-doped CF-NPs. The co-doping level also affected the crystallite size of the samples. It was observed that the crystallite size decreased after co-doping, followed by an increase, and then further decreased as compared to the un-doped sample (see Table 6.3). Similar behaviour was also observed in the lattice parameter, as listed in Table 6.3. This behaviour might be due to the ionic sizes difference

between dopants ions and host ions [71,75]. The trend of change in crystallite size is graphically shown in fig. 6.2. It may be noted that the ionic size of Ag^+ (~1.29 Å) is greater than Co^{2+} (~0.72 Å) [71,122], while Zn^{2+} (~0.82 Å) is greater than Fe^{3+} (~0.645 Å) ion [199].

Table 6.3: Variation of crystallite size and lattice parameter of prepared samples of un-doped, Ag and Zn doped, and Ag-Zn co-doped CF-NPs

Sample-ids	Dopant/s	Level of Doping	°/2θ	FWHM	D (nm)	Lattice parameter (Å)
SK-002	Ag	0.1	35.48	0.180	~ 47	8.381
SK-008	Zn	0.1	35.54	0.143	~ 57	8.409
SK-014	Ag & Zn	0.05 & 0.05	35.53	0.159	~ 52	8.385
SK-012	Ag & Zn	0.10 & 0.10	35.50	0.134	~ 63	8.388
SK-019	Ag & Zn	0.15 & 0.15	35.59	0.350	~ 23	8.366
SK-023	Un-doped	0	35.51	0.150	~ 54	8.385

(a)   (b)
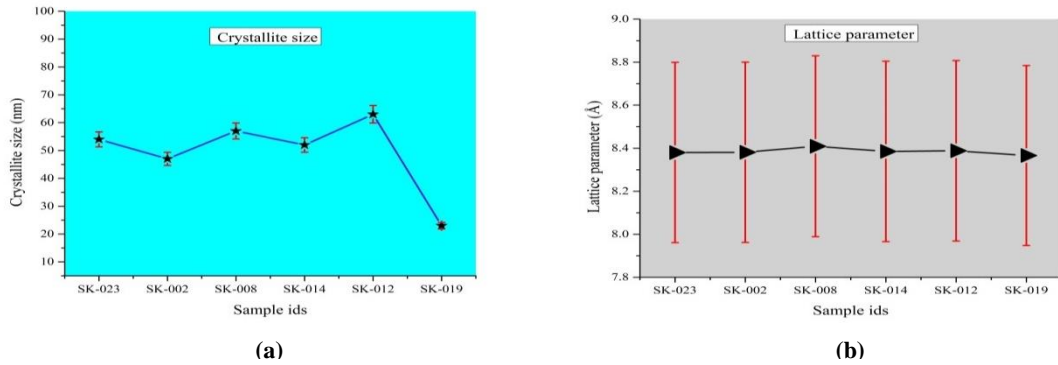
Fig. 6.2 Trends of change in:
(a) Crystallite size of sample-ids SK-023, SK-002, SK-008, SK-014, SK-012, and SK-019;
(b) Lattice parameter of sample-ids SK-023, SK-002, SK-008, SK-014, SK-012, and SK-019.

6.3 Compositional analysis of samples using FTIR

The FTIR pattern of un-doped, Ag and Zn doped CF-NPs, and Ag-Zn co-doped CF-NPs is illustrated in figs. 6.3 (a) to 6.3 (b). It was observed the two strong absorption bands at 400 cm^{-1} to 600 cm^{-1}. The absorption band at ~ 400 cm^{-1} is due to the Co-O stretching vibrations at octahedral sites, while the band at 500 cm^{-1} to 600 cm^{-1} is due to the Fe-O stretching vibrations at the tetrahedral sites [144]. These bands show the spinel structure of CF-NPs, which reveals that the spinel structure of CF-NPs remained intact after the co-doping. The absorption band at 1500 cm^{-1} to 1600 cm^{-1} is of H-O-H while the band at ~ 2344 cm^{-1} is due to C–O mode. The band at ~ 3670 cm^{-1} is due to the the C–H bending mode. The band at ~ 2960 cm^{-1} was due to the CH_2

95

symmetric. It was seen only in the silver doped sample (SK-002) [32,47,101,144]. All the absorption bands obtained in different samples of CF-NPs are listed in Table 6.4.
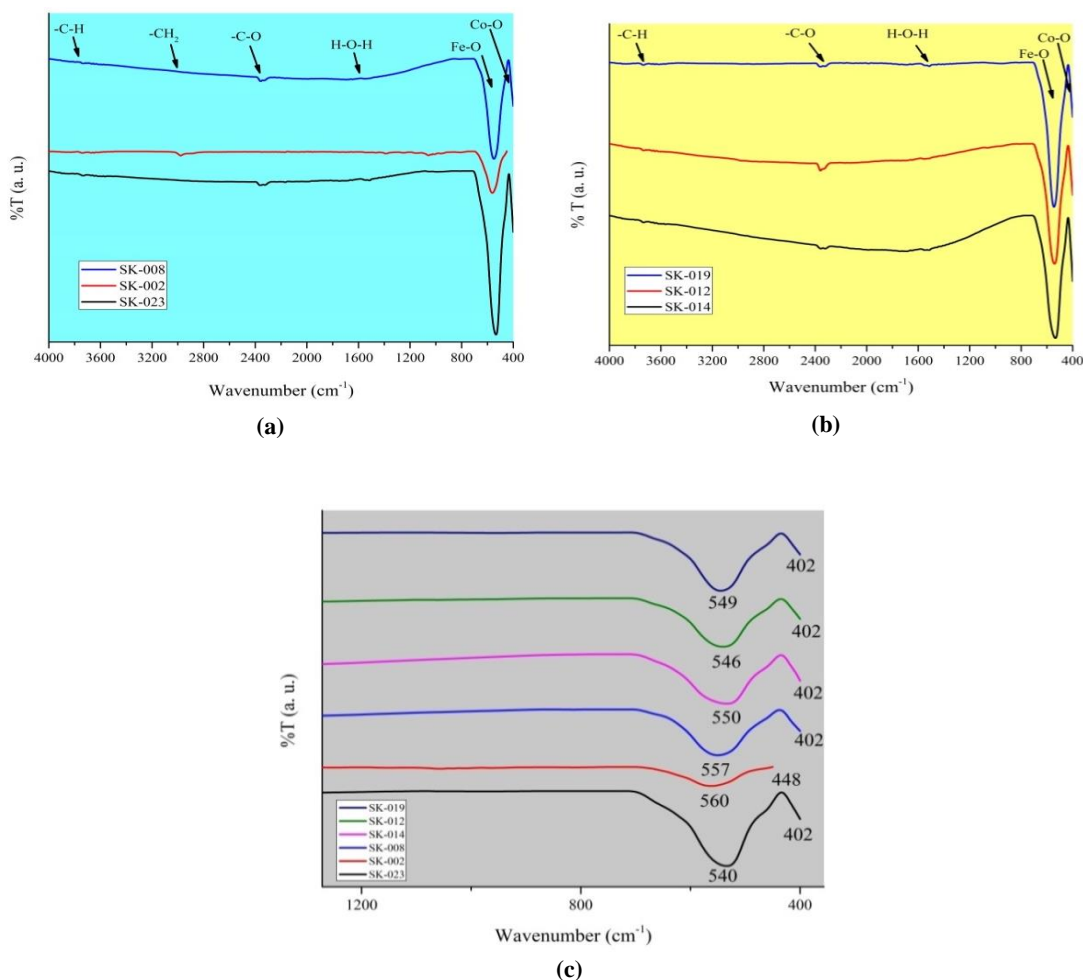
Fig. 6.3 FTIR pattern of:
(a) $CoFe_2O_4$, $CoFe_{1.9}Ag_{0.1}O_4$, $CoFe_{1.9}Zn_{0.1}O_4$;
(b) $Co_{0.95}Ag_{0.05}Fe_{1.95}Zn_{0.05}O_4$, $Co_{0.9}Ag_{0.1}Fe_{1.9}Zn_{0.1}O_4$, $Co_{0.85}Ag_{0.15}Fe_{1.85}Zn_{0.15}O_4$;
(c) Narrow scan view at 400-600 cm^{-1} of all the CF-NPs samples.

In the narrow scan view at the 400 cm^{-1} to 800 cm^{-1} for metal-oxygen (M-O) bond was observed that the absorption band of the Fe-O bond slightly shifted at a smaller wavelength or higher wavenumber when we compared with the un-doped sample (SK-023), whereas Co-O stretching vibration remains un-effected (see Table 6.4). In fig. 6.3 (c), it can be seen that the absorption band of the Fe-O bond at the tetrahedral site shifted at a higher wavenumber in both the silver-doped sample (SK-002) and the zinc-doped sample (SK-008), the same as reported earlier in the liturature [14,82].

Table 6.4: List of a few important absorption bands at various frequency and wavelength ranges obtained in FTIR analysis.

SK-023 ($CoFe_2O_4$)			SK-002 ($CoFe_{1.9}Ag_{0.1}O_4$)		
Observed abs. band	Assign.	Ref.	Observed abs. band	Assign.	Ref.
~ 3740	-C-H bending	[5]	~ 3736	-C-H bending	[5]
~ 2348	-C-O mode	[47]	~ 2960	-CH_2 symmetric	[47]
~ 1536	H-O-H	[47]	~ 1590	H-O-H	[47]
~ 540	Fe–O stretch tetrahedral	[75]	~ 560	Fe–O stretch tetrahedral	[75]
~ 402	Co–O stretch octahedral	[75]	~ 448	Co–O stretch octahedral	[75]
SK-008 ($CoFe_{1.9}Zn_{0.1}O_4$)			SK-014 ($Co_{0.95}Ag_{0.05}Fe_{1.95}Zn_{0.05}O_4$)		
Observed abs. band	Assign.	Ref.	Observed abs. band	Assign.	Ref.
~ 3749	-C-H bending	[5]	~ 3755	-C-H bending	[5]
~ 2344	-C-O mode	[47]	~ 2337	-C-O mode	[47]
~ 1543	H-O-H	[47]	~ 1533	H-O-H	[47]
~ 557	Fe–O stretch tetrahedral	[75]	~ 550	Fe–O stretch tetrahedral	[75]
~ 402	Co–O stretch octahedral	[75]	~ 402	Co–O stretch octahedral	[75]
SK-012 ($Co_{0.9}Ag_{0.1}Fe_{1.9}Zn_{0.1}O_4$)			SK-019 ($Co_{0.85}Ag_{0.15}Fe_{1.85}Zn_{0.15}O_4$)		
Observed abs. band	Assign.	Ref.	Observed abs. band	Assign.	Ref.
~ 3755	-C-H bending	[5]	~ 3733	-C-H bending	[5]
~ 2350	-C-O mode	[47]	~ 2357	-C-O mode	[47]
~ 1552	H-O-H	[47]	~ 1533	H-O-H	[47]
~ 546	Fe–O stretch tetrahedral	[75]	~ 549	Fe–O stretch tetrahedral	[75]
~ 402	Co–O stretch octahedral	[75]	~ 402	Co–O stretch octahedral	[75]

*Note that here all the identified absorption bands are given in wavenumber (cm⁻¹).

Co-doped samples (SK-014, SK-012, SK-019) also show shifting in the absorption band towards a higher wavenumber, but it remains less than the doped samples (see fig. 6.3 (c)). This frequency change at the Fe-O bond might be due to the redistribution of cations (Fe, Co, Zn, and Ag) at both sites when we changed the concentration of dopant/s (Ag^+ and Zn^{2+}) ions [82].

6.4 Vibrating-sample magnetometer (VSM) analysis
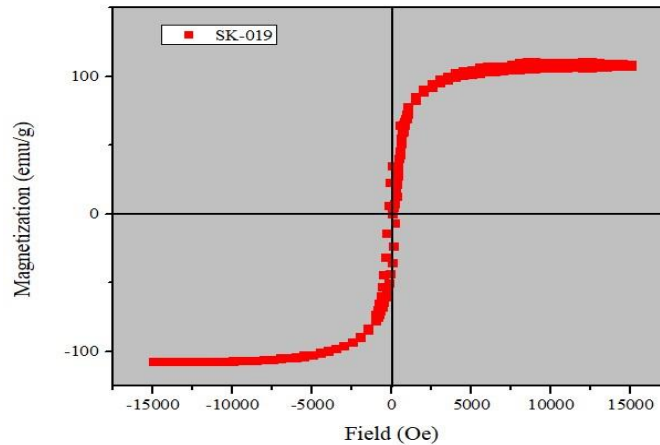
Fig. 6.4 Hysteresis loop of sample-id SK-019

Fig. 6.4 represents the hysteresis loop of the sample-id SK-019 ($Co_{0.85}Ag_{0.15}Fe_{1.85}Zn_{0.15}O_4$). The hysteresis curve of the sample measured the saturation magnetisation (M_s) and coercivity (H_c) values. The saturation magnetisation (M_s) was measured up to 150 emu/g. The recorded value of the saturation magnetisation was found to be 110.11 emu/g. The low or zero coercivity with higher saturation magnetisation exhibits the development of superparamagnetic material. The superparamagnetic sample does not show magnetic behaviour even in the absence of an applied magnetic field [214]. These materials are suitable for various biomedical applications, e.g. drug delivery, Magnetic Resonance Imaging (MRI), gene delivery, and identification of different bacteria, viruses, and proteins [9,146,203,214].

6.5 Morphological studies and elemental analysis of samples using FESEM and EDS
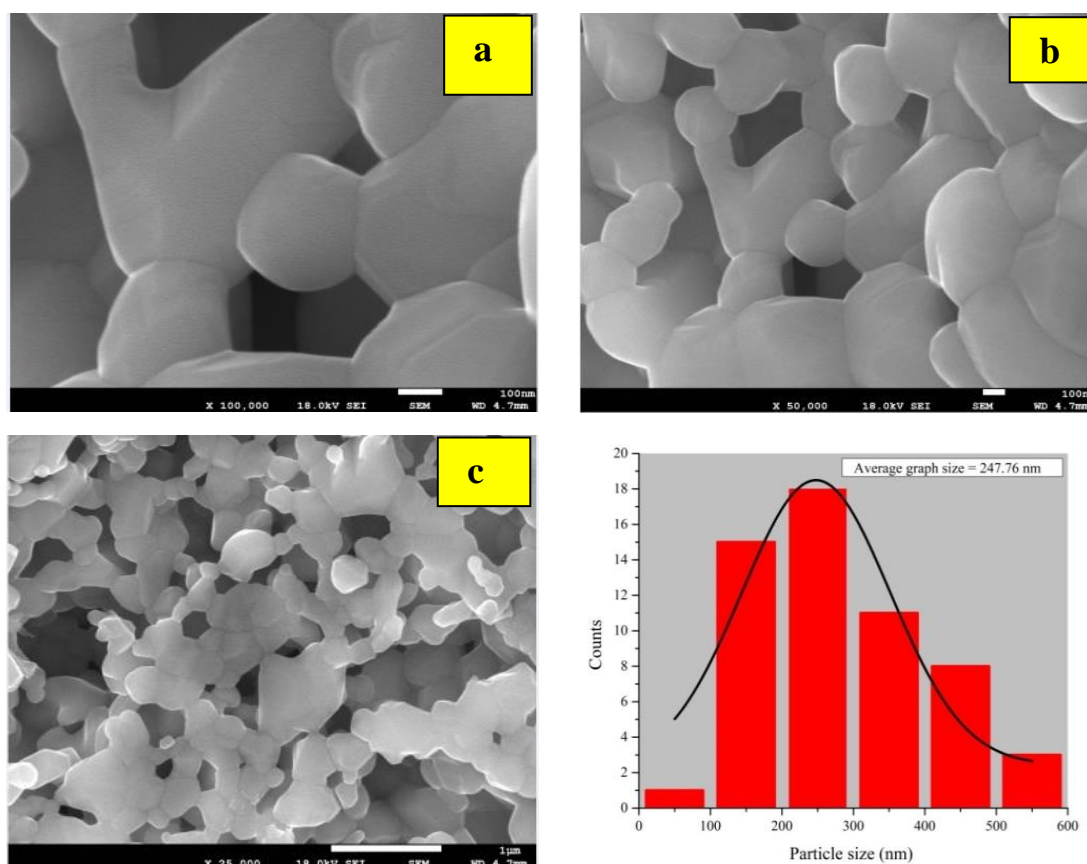
Fig. 6.5 FESEM pictures of the sample-id SK-019

Fig. 6.5 illustrates the FESEM pictures of sample-id SK-019 ($Co_{0.85}Ag_{0.15}Fe_{1.85}Zn_{0.15}O_4$). The particles of clear and rounded edges with angular morphology can be easily seen in figs. 6.5 (a) and 6.5 (b). The agglomerated particles are clearly perceived at fig. 6.5 (c). The average grain size of the particles was measured 247.76 nm. It was calculated by using the Image J software [114,204,209].
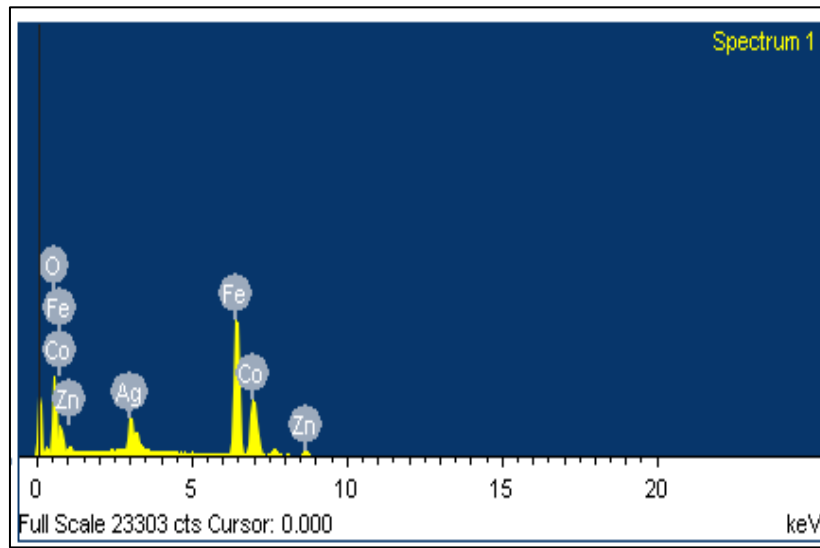
Fig. 6.6 EDS mapping of sample id: SK-019

The elemental detection of sample-id SK-019 ($Co_{0.85}Ag_{0.15}Fe_{1.85}Zn_{0.15}O_4$) was performed with EDS analysis (see fig. 6.6). The atomic percent and weight percent of the elements present in the samples as attained in this study are also listed in Table 6.5. Here, the microscopist picked up K-lines and L-lines.

Table 6.5: Atomic percent and weight percent as attained in EDS spectra of sample-id SK-019
($Co_{0.85}Ag_{0.15}Fe_{1.85}Zn_{0.15}O_4$)

Elements	Weight %	Atomic %
O K	21.60	50.98
Fe K	44.63	30.18
Co K	21.32	13.66
Zn K	3.60	2.08
Ag L	8.85	3.10

The result indicated that the co-doped sample of CF-NPs contained silver and zinc apart from the other constituent elements. This suggests that CF was successfully co-doped with silver and zinc [71,75,207].

6.6 Thermal analysis of samples
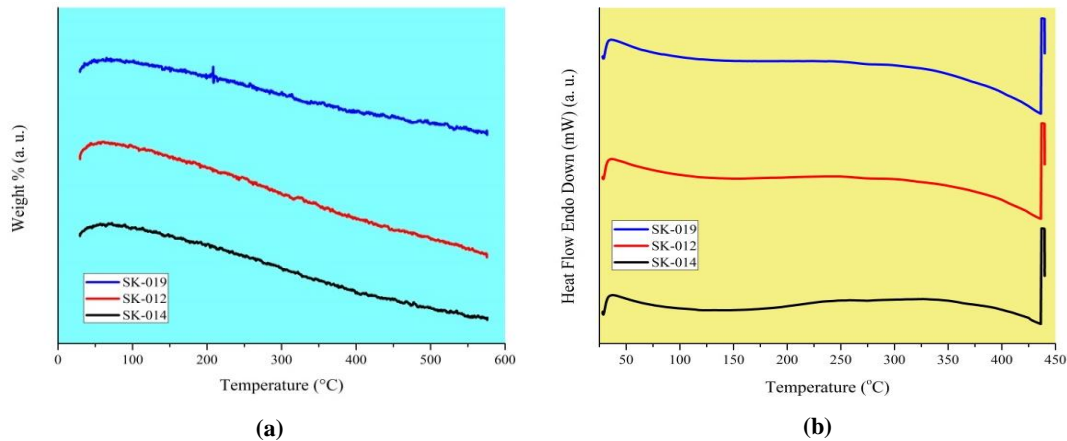
Fig. 6.7 Thermal analysis results obtained via:
(a) TGA of the sample-ids: SK-014, SK-012 and SK-019;
(b) DSC of the sample-ids: SK-014, SK-012 and SK-019.

Fig. 6.7 (a) represents the TGA curves of the co-doped samples of CF-NPs with sample-ids: SK-014, SK-012, and SK-019. The insignificant weight loss was observed when we heated the samples up to 600 ºC. It is attributed to structural water loss. No impurity is present in the samples. These are thermally stable up to 600 ºC [207,209,210].

Fig 6.7 (b) represents the DSC curves of the co-doped samples of CF-NPs with sample-ids: SK-014, SK-012, and SK-019. Here, all three co-doped CF-NPs slightly decomposed. It has been observed that the sample-id: SK-014 decomposed thermally at 146 ºC in one endothermic region. The sample-id: SK-012 decomposed thermally at 140 ºC in one endothermic region, and the sample-id: SK-019 decomposed thermally at 151 ºC in one endothermic region. No endothermic peak was noticed after 450 ºC, indicating the formation phase is stable after the heat treatment [207,209,210]. The data of the thermal analysis of all the samples are also listed in Table 6.6.

Table 6.6: The data obtained after thermal analysis of the co-doped CF-NPs

TGA		DSC	
Sample-ids	Weight loss (%)	Sample-ids	Temperature at which minute thermal event observed
SK-014	0.05	SK-014	~146 ˚C
SK-012	0.06	SK-012	~140 ˚C
SK-019	0.04	SK-019	~151 ˚C

100

6.7 Antibacterial activities

The different zones of inhibition created by the samples of CF-NPs and their ZnO/Ag composites are represented in figs. 6.8 (a) and 6.8 (b), respectively. A list of the diameter of the zones of inhibition in all the samples of CF-NPs and their composite materials is also tabulated in Table 6.7.
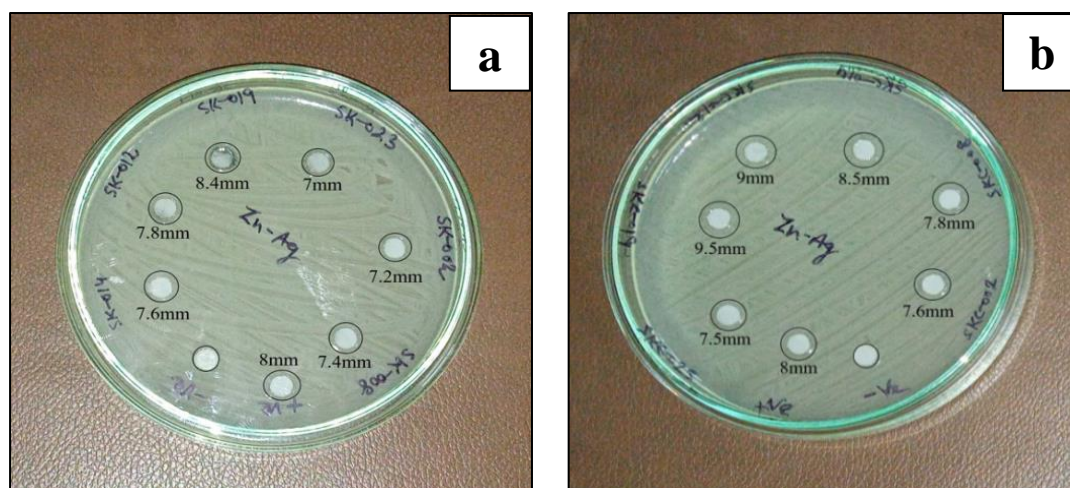
Fig. 6.8 Pictures of zone of inhibitions formed by sample ids:
(a) SK-023, SK-002, SK-008, SK-014, SK-012, SK-019, C +ve and C –ve;
(b) SKC-023, SKC-002, SKC-008, SKC-014, SKC-012, SKC-019, C +ve and C –ve.

Table 6.7: Measured diameter of zone of inhibitions in un-doped, doped and co-doped samples of CF-NPs and its ZnO/Ag composites

Sample-ids	Zone of inhibition (mm)	Sample-ids	Zone of inhibition (mm)
SK-023	7	SKC-023	7.5
SK-002	7.2	SKC-002	7.6
SK-008	7.4	SKC-008	7.8
SK-014	7.6	SKC-014	8.5
SK-012	7.8	SKC-012	9.0
SK-019	8.4	SKC-019	9.5
C+ve	8	C+ve	8

The diameter of the zone of inhibition reveals that the silver-doped CF-NPs (SK-002) and zinc-doped CF-NPs (SK-008) create a larger zone as compared to the un-doped CF-NPs (SK-023). These results are in good agreement with earlier reported results [14]. The zone of inhibition was also found to be larger in co-doped CF-NPs than in the undoped sample. It was observed that the diameter of the zone of inhibition increases in a regular manner in co-doped samples SK-014 to SK-019 with an increase in their

level of doping. Although the zone of inhibition in co-doped samples was found to be larger than that in doped samples [71,113]. Therefore, co-doping enhanced the antibacterial activities of the samples. The level of doping plays an important role in enhancing the antibacterial activities of the co-doped samples [71].

Similarly, the ZnO/Ag composites of CF-NPs also follow the same trend. The diameter of the zone of inhibition of composite materials was found to be larger than their respective CF-NPs. Hence, it can be concluded that the ZnO/Ag composite showed improved antibacterial activities as compared to CF-NPs [153,211]. Fig. 6.9 (a) and 6.9 (b) graphically represent the trends of variation in zones of inhibition in CF-NPs and their ZnO/Ag composites.

(a) (b)
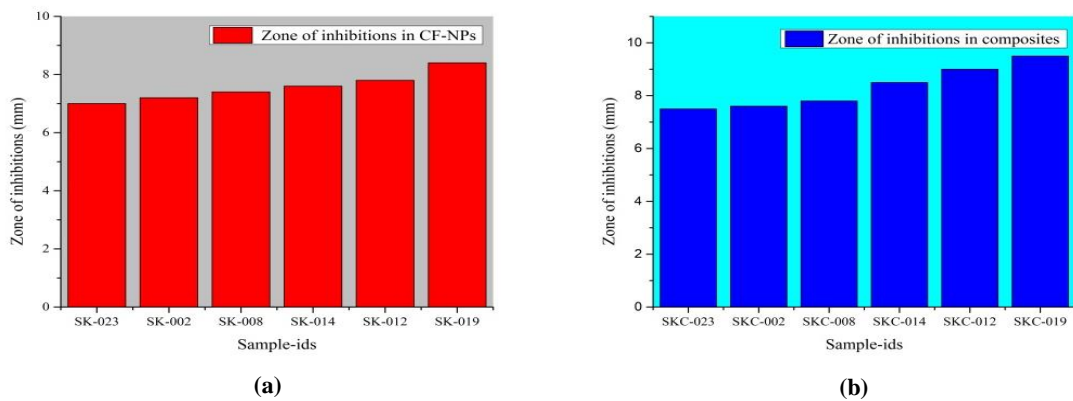
Fig. 6.9 Bar graph of antibacterial zone of inhibitions in:
(a) Un-doped CF-NPs, Ag and Zn doped/ co-doped CF-NPs;
(b) Composites of un-doped CF-NPs, Ag and Zn doped/ co-doped CF-NPs.
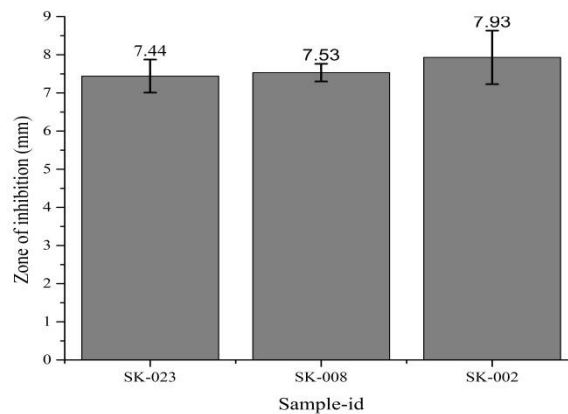
Fig. 6.10 Bar graph picture showing the reproducibility of the sample-ids: SK-023, SK-008 and SK-002.

The reproducibility of antibacterial activities of the sample-ids: SK-023, SK-008, and SK-002 is shown in fig. 6.10. Here, the trend of variation and reproducibility of the samples follow the same order as it has been found in the antibacterial activities of silver doped CF-NPs and zinc doped CF-NPs. As reported in literature as well, the zinc doped CF-NPs showed greater antibacterial activities than un-doped samples [14]. Silver-doped CF likewise exhibits higher antibacterial activity than the un-doped CF-NPs [14,19]. We also observed that the CF-NPs co-doped with silver and zinc showed enhanced antibacterial activities than the singly doped CF-NPs as well as the un-doped samples.

6.8 Conclusion

Here, we successfully synthesised the doped and co-doped CF-NPs with silver and zinc via the sol-gel auto-combustion route. The composite materials of CF-NPs with ZnO/Ag were also prepared by the mortar-pestle grinding method. The level of doping changes the size of the crystals. Initially, the size of crystals decreased with co-doping, followed by an increase, and finally, it again decreased. The lattice parameter also slightly changes with the concentrations of dopants. The FTIR was used for the identification of functional groups present in the samples. The different absorption bands proved the presence of metal-oxygen bonds. The VSM of sample-id: SK-019 identified the superparamagnetic character, which can be used in different biomedical applications, e.g., gene delivery, drug delivery, MRI, etc. FESEM shows the presence of agglomerated particles with rounded edges. EDS analysis of sample-id: SK-019 confirmed the co-doping. Thermal analysis via TGA showed insignificant weight loss in all the co-doped samples, whereas DSC revealed that all three co-doped CF-NPs samples insignificantly decomposed. The antibacterial activities of all the samples of CF-NPs were enhanced regularly with the level of co-doping against Bacillus paranthracis and Bacillus nitratireducens. The same trend was also observed in their composite of ZnO/Ag. The composites of all the CF-NPs showed enhanced antibacterial activities as compared to their respective samples of CF-NPs.

Chapter 7

Antibacterial activities of co-doped cobalt ferrite with Cu-Zn and their composite/s with ZnO/Ag

7.1 Introduction

This chapter deals with the prepared co-doped CF-NPs with Cu-Zn and its ZnO/Ag composite materials. The various Advanced Materials' characterisation techniques were used to characterise these CF-NPs. The antibacterial activities of all the samples were tested by using Agar disk diffusion test. The various results obtained are discussed in the following sections (see sections 7.2 to 7.7).

7.2 Crystalline structure studies using XRD

The powder XRD patterns of various samples of CF-NPs with sample-ids: SK-023, SK-005, SK-008, SK-015, SK-011, and SK-020 are represented in figs. 7.1 (a) to 7.1 (b).
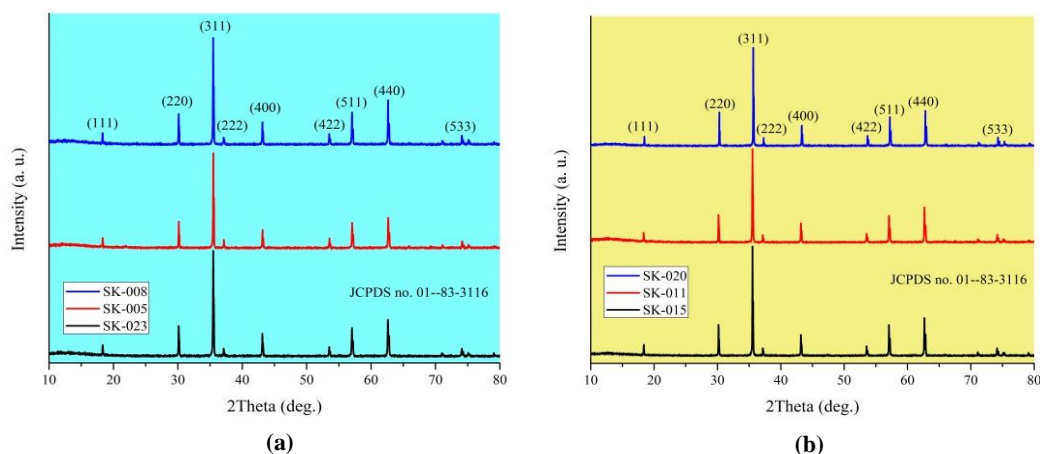
Fig. 7.1 Powder XRD patterns of:
(a) SK-023, SK-005 and SK-008;
(b) SK-015, SK-011 and SK-020.

These results revealed the cubic crystal structure of the samples. The angles of diffraction ($^\circ/2\theta$) of different planes as obtained according to JCPDS card no. 01-083-3116, are listed in Table 7.1.

Table 7.1: List of diffraction angles (°/2θ) with their respective diffraction plane

Diffraction angle (°/2θ)	Diffraction plane	Diffraction angle (°/2θ)	Diffraction plane	Diffraction angle (°/2θ)	Diffraction plane
18.37°	(111)	37.21°	(222)	57.11°	(333)
30.11°	(220)	43.14°	(400)	62.80°	(440)
35.49°	(311)	53.50°	(422)	74.11°	(533)

The XRD was performed at °/2θ between 10° to 80°, when CuKα radiations of wavelength 1.54 Å were used. The levels of doping are also listed in Table 7.2.

Table 7.2: List of sample-ids of CF-NPs along with doping levels

S.No.	Sample-ids	Dopant/s	Level of doping	Desired products
1.	SK-005	Cu^{2+}	0.1	$CoFe_{1.9}Cu_{0.1}O_4$
2.	SK-008	Zn^{2+}	0.1	$CoFe_{1.9}Zn_{0.1}O_4$
3.	SK-015	Cu^{2+} & Zn^{2+}	0.05 & 0.05	$Co_{0.95}Cu_{0.05}Fe_{1.95}Zn_{0.05}O_4$
4.	SK-011	Cu^{2+} & Zn^{2+}	0.1 & 0.1	$Co_{0.9}Cu_{0.1}Fe_{1.9}Zn_{0.1}O_4$
5.	SK-020	Cu^{2+} & Zn^{2+}	0.15 & 0.15	$Co_{0.85}Cu_{0.15}Fe_{1.85}Zn_{0.15}O_4$
6.	SK-023	Un-doped	0	$CoFe_2O_4$

The highly intense peak at plane (311) can be clearly detected in all the samples. However, the diffraction angle (°/2θ) is shifted slightly after doping and co-doping [77]. The lattice parameters of cubic crystal are calculated using the eq^n. (3.3) [66,142,202]. It can be observed that the lattice parameter in copper doped sample (SK-005) decreases while in zinc doped sample (SK-008) it increases (see Table 7.2). These results are in good agreement with earlier report values. The size of host ions and guest ions are accountable for these changes [199]. Here, it has been pointed out that the diameter of Cu^{2+} (~ 0.73 Å) ion smaller than the diameter of Co^{2+} (~ 0.745 Å) ion [75] whereas, the diameter of Zn^{2+} (~ 0.82 Å) ion [199] is larger than the diameter of Fe^{3+} (~ 0.645 Å) ion [75].

The co-doped samples (SK-015, SK-011, and SK-020) show a linear increase in lattice parameters with an increase in concentration of the dopants. Although, it was seen the minor change in lattice parameter values in the co-doped samples. Perhaps, the overall effect of co-doping of Cu^{2+} and Zn^{2+} ions is reflected in the form of only a minor increase in the lattice parameters, as one of the dopants (Cu^{2+} ions) is reducing the lattice parameter whereas the other dopant (Zn^{2+} ions) increased it [71,75,199].

Crystallite sizes of the CF-NPs samples were calculated by using Scherrer's eq[n]. 3.2 [66,202]. The crystallite sizes and lattice parameters obtained using eq[n]. 3.2 and eq[n]. 3.3 are listed in Table 7.3.

Table 7.3: List of crystallite sizes and lattice parameters of different samples

Sample-ids	Dopant/s	Level of doping	º/2θ	FWHM	D (nm)	Lattice parameter (Å)
SK-005	Cu	0.1	35.52	0.143	~ 58.6	8.378
SK-008	Zn	0.1	35.54	0.143	~ 57.6	8.409
SK-015	Cu & Zn	0.05 & 0.05	35.54	0.144	~ 58.4	8.378
SK-011	Cu & Zn	0.1 & 0.1	35.67	0.148	~ 56.1	8.380
SK-020	Cu & Zn	0.15 & 0.15	35.66	0.130	~ 63.4	8.390
SK-023	Un-doped	0	35.51	0.150	~ 54.0	8.385

It was observed the increase in crystallite size of the Cu-doped CF-NPs (SK-005) as well as in Zn-doped CF-NPs (SK-008) as compared to un-doped CF-NPs. These results were the same as reported earlier in the literature [82,142,200]. Co-doped CF-NPs also show an increase in the crystallite size than un-doped CF. The crystallite size of co-doped samples first decreases up to the dopant concentrations of 0.1, then it further increases. The ionic size of the dopant ions as compared to host ions (Co^{2+} and Fe^{3+}) might be responsible for these changes [71,75]. All the data on crystallite size is tabulated in Table 7.3.

The trends of variation of lattice parameters and crystallite sizes of the un-doped CF-NPs, Cu and Zn doped/ co-doped CF-NPs are represented in fig. 7.2.
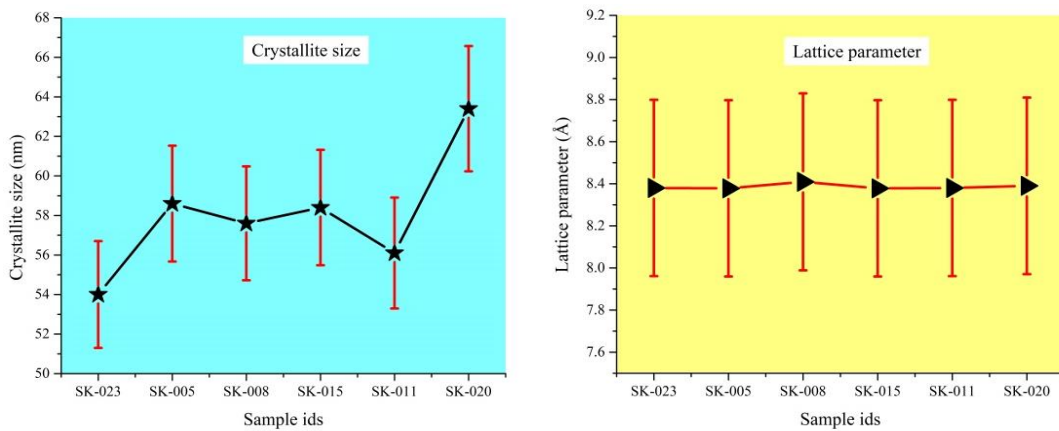
Fig. 7.2 Trends of variation of lattice parameters and crystallite sizes of un-doped CF-NPs, Cu and Zn doped/co-doped CF-NPs.

7.3 Compositional analysis of samples using FTIR

FTIR analysis studied the chemical compositions of all the samples. The analysed results obtained during this practice are represented in fig. 7.3(a) and fig. 7.3(b).
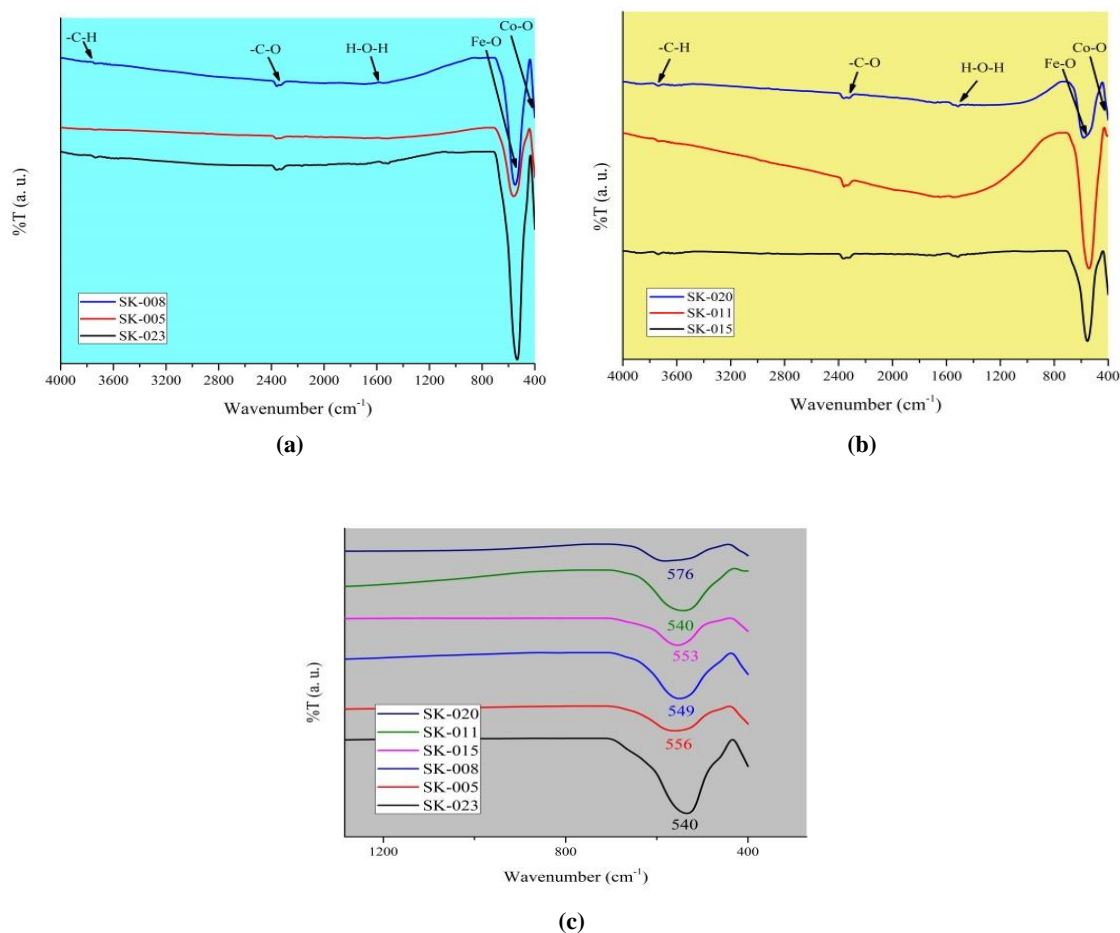
Fig. 7.3 FTIR results of:
(a) Un-doped and Cu and Zn doped CF-NPs with sample-ids: SK-023, SK-005 and SK-008;
(b) Cu and Zn co-doped CF-NPs with sample-ids: SK-015, SK-011 and SK-020;
(c) Narrow scan view of all the samples at the range of 400-600 cm⁻¹.

All the samples exhibited a sharp absorption band in the range of ~ 405 cm^{-1}. A strong absorption band in the range of ~ 500 cm^{-1} to ~ 600 cm^{-1} is also seen in all the samples. These bands are recognise the spinel ferrite structure of the samples. The band at ~ 405 cm^{-1} is due to the Co-O stretching vibration at octahedral sites, while the bands at ~ 500 cm^{-1} to ~ 600 cm^{-1} are characterised by the Fe-O stretching vibration at tetrahedral sites. These results are in good agreement with reported values [71,113,144]. The narrow scan view of all the samples shows that the increase in level of doping slightly shifted the Fe-O stretching band of tetrahedral sites towards lower

wavelength or higher wavenumber when compared with the un-doped sample (see Table 7.4). However, the co-doped samples (SK-011) with dopant concentartions of 0.10 revealed the same behaviour as the un-doped sample (SK-023), i.e., the absorption band was attained at ~ 540 cm^{-1} in both cases [32,47,66,71]. A few minor absorption bands are also observed in the FTIR spectra, which are listed in Table 7.4.

Table 7.4: List of absorption bands obtained in FTIR analysis

SK-023 ($CoFe_2O_4$)			SK-005 ($CoFe_{1.9}Cu_{0.1}O_4$)		
Observed abs. band	**Assign.**	**Ref.**	**Observed abs. band**	**Assign.**	**Ref.**
~ 3740	-C-H bending	[5]	~ 3735	-C-H bending	[5]
~ 2348	-C-O mode	[47]	~ 2347	-C-O mode	[47]
~ 1546	H-O-H	[47]	~ 1552	H-O-H	[47]
~ 540	Fe–O stretch tetrahedral	[144]	~ 560	Fe–O stretch tetrahedral	[144]
~ 402	Co–O stretch octahedral	[144]	~ 402	Co–O stretch octahedral	[144]
SK-008 ($CoFe_{1.9}Zn_{0.1}O_4$)			**SK-015 ($Co_{0.95}Cu_{0.05}Fe_{1.95}Zn_{0.05}O_4$)**		
Observed abs. band	**Assign.**	**Ref.**	**Observed abs. band**	**Assign.**	**Ref.**
~3749	-C-H bending	[5]	~ 3742	-C-H bending	[5]
~ 2344	-C-O mode	[47]	~ 2344	-C-O mode	[47]
~ 1543	H-O-H	[47]	~ 1523	H-O-H	[47]
~ 552	Fe–O stretch tetrahedral	[144]	~ 554	Fe–O stretch tetrahedral	[144]
~ 402	Co–O stretch octahedral	[144]	~ 402	Co–O stretch octahedral	[144]
SK-011 ($Co_{0.9}Cu_{0.1}Fe_{1.9}Zn_{0.1}O_4$)			**SK-020 ($Co_{0.85}Cu_{0.15}Fe_{1.85}Zn_{0.15}O_4$)**		
Observed abs. band	**Assign.**	**Ref.**	**Observed abs. band**	**Assign.**	**Ref.**
~ 3742	-C-H bending	[5]	~ 3742	-C-H bending	[5]
~ 2344	-C-O mode	[47]	~ 2344	-C-O mode	[47]
~ 1550	H-O-H	[47]	~ 1526	H-O-H	[47]
~ 540	Fe–O stretch tetrahedral	[144]	~ 578	Fe–O stretch tetrahedral	[144]
~ 402	Co–O stretch octahedral	[144]	~ 402	Co–O stretch octahedral	[144]

7.4 Vibrating-sample magnetometer (VSM) analysis

The magnetic properties of the co-doped sample SK-020 ($Co_{0.85}Cu_{0.15}Fe_{1.85}Zn_{0.15}O_4$) was analysed via VSM. Fig. 7.4 represents the hysteresis curve of the sample SK-020. Godara *et al.* examined the decrease in saturation magnetisation (M_s) and coercivity (H_c) values when CF-NPs were doped with chromium. These changes were observed with an increase in dopant concentrations [215]. Here, the hysteresis loop shows low or negligible value of coercivity [203]. Although, the saturation magnetisation was found to be higher, its recorded value was 105.88 emu/g. The nearly zero or low value of coercivity (H_c) indicated the change of ferromagnetic material into superparamagnetic material [158].
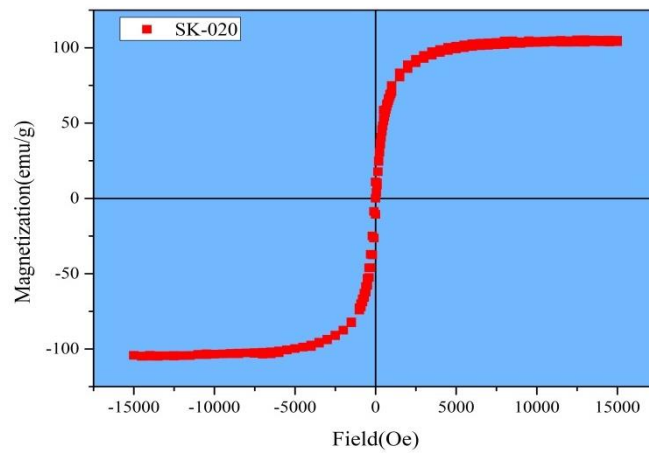
Fig. 7.4 Magnetic hysteresis loop of sample-id SK-020

These superparamagnetic materials can be used in different biomedical applications [9,214].

7.5 Morphological studies and elemental analysis of samples using FESEM and EDS
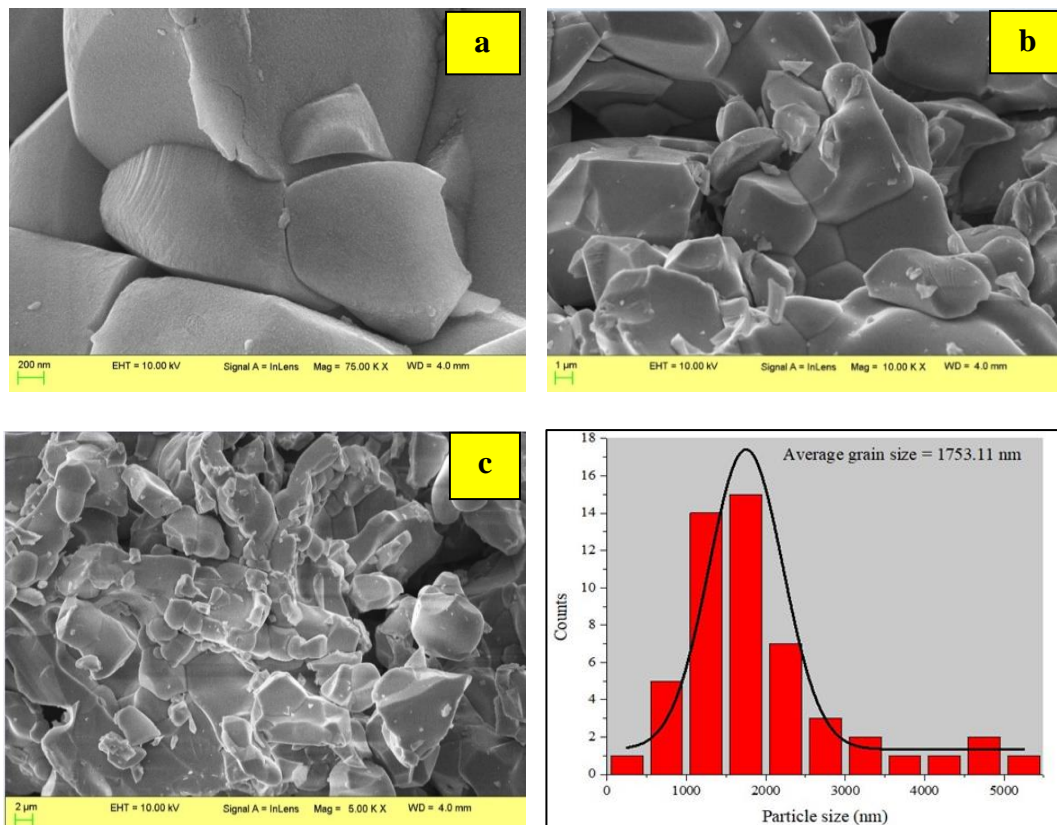
Fig. 7.5 FESEM pictures of co-doped sample SK-020.

Fig. 7.5 illustrates the different FESEM pictures of sample-id: SK-020. It was seen the irregular particles with clear and rounded edges in fig 7.5a [114]. These agglomerated particles also show clean surfaces [206]. The fig. 7.5b shows brick-like shapes with rounded edges and angular morphology. The micrograph shows the agglomerated particles in a large clusters (see fig. 7.5c) [204,205]. The average grain size of the particles was measured at 1753.11 nm by using Image J software.

Energy dispersive X-ray spectroscopy analysis (EDS) with FESEM is used to find the presence of elements and their quantities in the given sample. Fig. 7.6 represents the EDS mapping of the sample-id: SK-020 ($Co_{0.85}Cu_{0.15}Fe_{1.85}Zn_{0.15}O_4$).
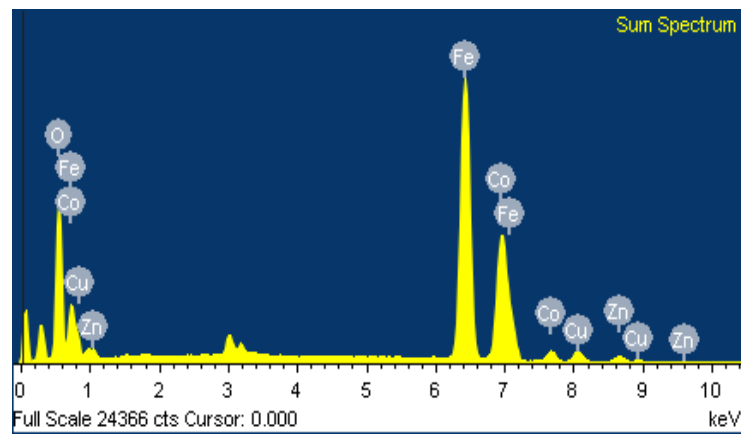
Fig. 7.6 EDS mapping of the co-doped CF-NPs with sample-id SK-020

The quantitative analysis was performed to examine the weight percent and atomic percent of the elements in the sample. Here, it was noted that the only K-lines were picked up by the microscopist. Table 7.5 listed that the sample contained Cu and Zn apart from other constituent elements present in the CF-NPs sample. This recommends the successful co-doping of copper and zinc in the CF-NPs sample [71,75,104]. These obtained results are also summarised in Table 7.5.

Table 7.5: List of elements obtained in EDS analysis with weight percent and atomic percent (Sample-id: SK-020)

Elements	Weight %	Atomic %
O K	17.89	43.83
Fe K	51.03	35.82
Co K	25.08	16.69
Cu K	3.55	2.19
Zn K	2.45	1.47

It should be noted that EDS analysis is a semi-qualitative as well as semi-quantitative method of detection of the elements [207,208].

7.6 Particle size and morphology studies using TEM

The TEM analysis was used to study the morphology and sizes of the particles of Cu-Zn co-doped CF-NPs. Figs. 7.7 (a) to 7.7 (b) represent the TEM images of co-doped CF-NPs with a doping level of 0.15 (sample-id: SK-020). Agglomerated crystalline particles with sharp edges can be seen in these images [49,216]. The average particle size measured by using Image J software was 98.35 nm.
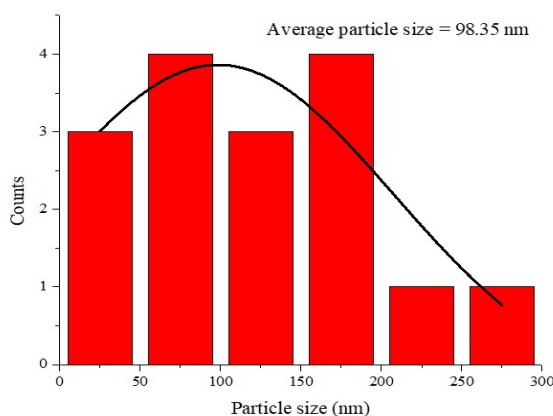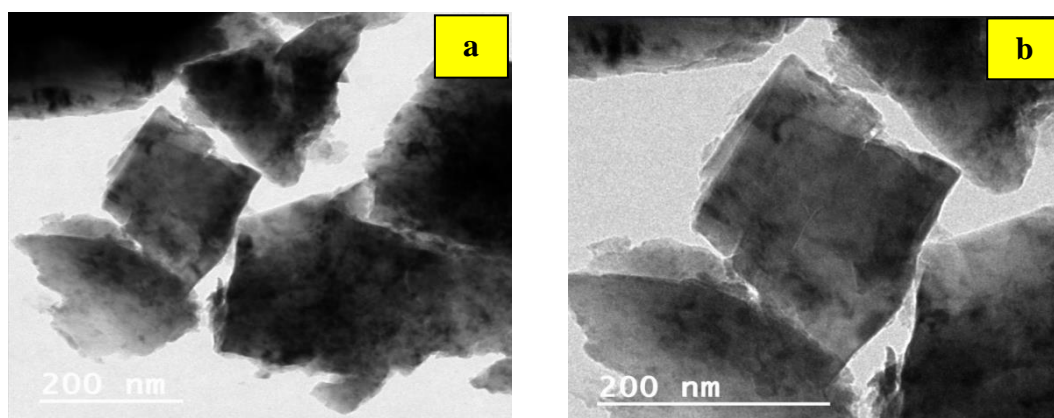
Fig. 7.7 (a) to (c) TEM images of the sample-id: SK-020

7.7 Thermal Analysis of samples

TGA and DSC were used to analyse the thermal properties of the sample. Here, the samples were heated in the range of 30 ℃ (room temperature) to 450 ℃ with a

heating rate of 10 ºC/min. The thermal stability, i.e. degradation of the samples with temperature, was studied by the TGA technique. The phase change after heating the sample was studied via DSC. The results obtained are presented in figs. 7.8a and 7.8b.
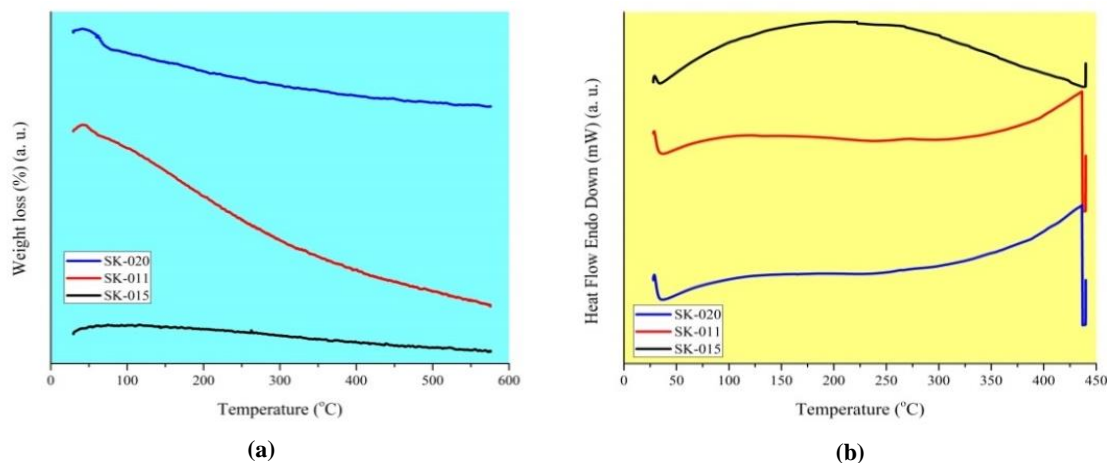
Fig.7.8 Thermal analysis via:
(a) TGA of all the co-doped samples with sample-ids: SK-015, SK-011 and SK-020;
(b) DSC of all the co-doped samples with sample-ids: SK-015, SK-011, and SK-020.

Fig. 7.8a illustrates the TGA analysis results of co-doped samples (SK-015, SK-011, and SK-020). It was noticed that no significant weight loss was observed in the specific temperature range. It confirms the thermal stability of the samples. Although, a small, gradual weight loss was observed in the samples, that might be due to the loss of water. It is believed that molecules of water that get adsorbed/absorbed at the surface of the samples were lost after the TGA treatment [109,147,181,209,210,217,218].

Similarly, DSC analysis did not show again any distinct thermal event (see fig. 7.8b). This result also shows the thermal stability of the samples at a particular temperature range. However, sample-id: SK-015 exhibits very small exothermic behaviour in the range of ~200 ºC. Although the sample-ids: SK-011 and SK-020 revealed very small endothermic events in the range of ~270 ºC and ~ 224 ºC respectively. It is believed that these properties of samples are attributed to the presence of residual nitrates and hydroxyl groups in the co-doped CF-NPs [109,147,181,209,210,217,218]. The data of the thermal analysis of all the samples are also listed in Table 7.6.

112

Table 7.6: The data obtained after thermal analysis of the co-doped CF-NPs

TGA		DSC	
Sample-ids	Weight loss (%)	Sample-ids	Temperature at which minute thermal event observed
SK-015	0.03	SK-015	~200 °C
SK-011	0.24	SK-011	~270 °C
SK-020	0.10	SK-020	~224 °C

7.8 Antibacterial activities

The antibacterial activities of all the samples were studied using the Agar disk diffusion method. It was examined against the bacteria *Bacillus paranthracis* and *Bacillus nitratireducens*. *Bacillus paranthracis* belongs to the *Bacillus* cereus group and is one of the 21 species in this group. It was found in different environments, including samples of human origin, the rhizosphere, and soil [174]. It was characterised in 2017 and is under study now [177]. *Bacillus nitratireducens* is a newly identified bacterium. It is not widely recognised as a harmful bacterium [178,179].
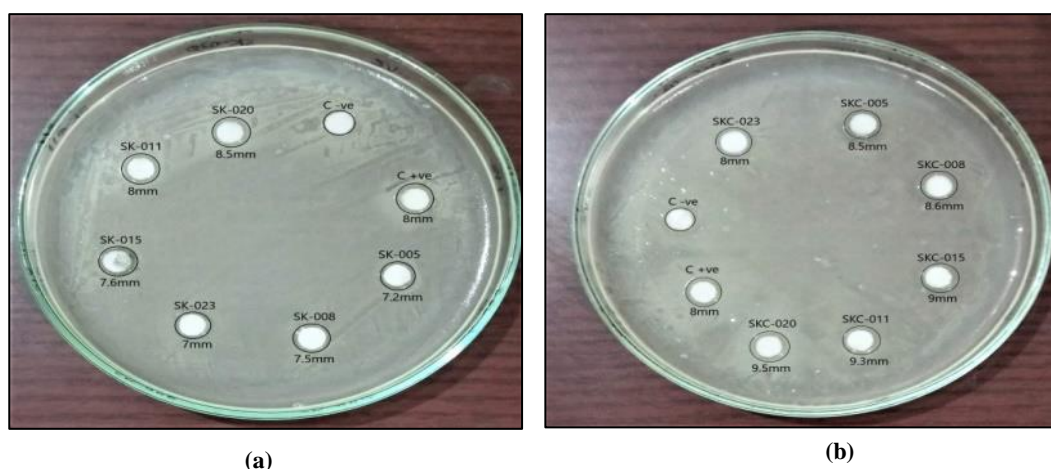
Fig. 7.9 Antibacterial zone of inhibitions created by:
(a) sample-ids: SK-023, SK-005, SK-008, SK-015, SK-011, SK-020;
(b) sample-ids: SKC-023, SKC-005, SKC-008, SKC-015, SKC-011, SKC-020.

Figs. 7.9 (a) and 7.9 (b) represent the different zones of inhibition created by CF-NPs and their ZnO/Ag composites, respectively. The diameter of zones of inhibition created by different samples of CF-NPs and their ZnO/Ag composites is tabulated in Table 7.7.

Sample-ids	Zone of inhibitions (mm)	Sample-ids	Zone of inhibitions (mm)
SK-023	7	SKC-023	7.5
SK-005	7.2	SKC-005	8.5
SK-008	7.4	SKC-008	8.6
SK-015	7.5	SKC-015	9
SK-011	8	SKC-011	9.3
SK-020	8.5	SKC-020	9.5

It was found that the co-doped CF-NPs of higher dopant concentrations (sample-id: SK-020) created the largest zone of inhibition among the samples of CF-NPs. It shows enhanced antibacterial activity as compared to the rest of the co-doped CF-NPs. The composite of the co-doped sample with higher dopant concentrations (sample–id: SKC-020) also created the biggest zone of inhibition as compared to other composite samples. Although all the samples created a substantial zone of inhibition, demonstrating that all these samples possessed antibacterial activities. The zone of inhibitions is illustrated by using the bar diagrams in figs. 7.10 (a) and 7.10 (b).
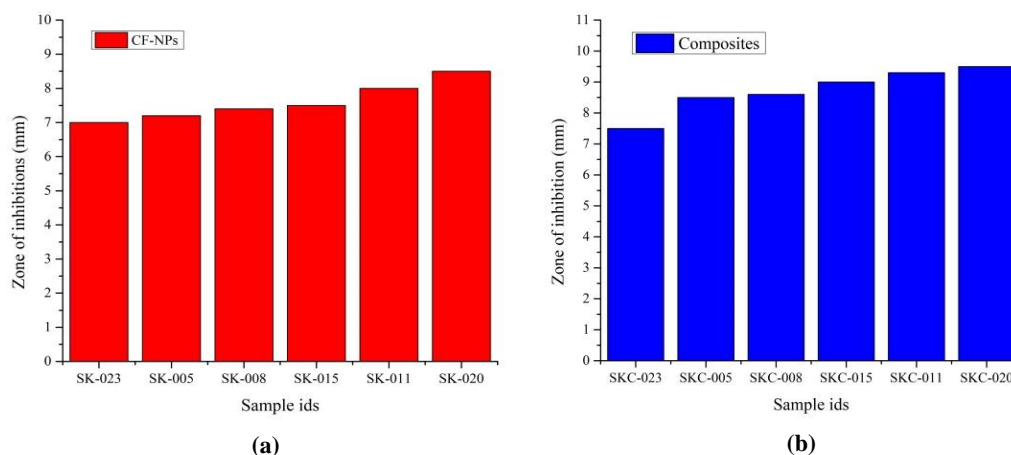
Fig. 7.10 Bar diagrams of antibacterial activities of CF-NPs and their composites of:
(a) sample-ids: SK-023, SK-005, SK-008, SK-0115, SK-011 and SK-020;
(b) sample-ids: SKC-023, SKC-005, SKC-008, SKC-015, SKC-011 and SKC-020.

The copper doped CF-NPs (SK-005) and zinc doped CF-NPs (SK-008) generated a bigger zone of inhibition than the un-doped CF-NPs (SK-023), same as reported earlier in the literature [71,113]. This trend was also maintained in co-doped CF-NPs. The co-doped CF-NPs created a bigger zone of inhibition compared to doped CF-NPs. It

increases in a regular manner in all the co-doped CF-NPs as the level of doping increases (see Table 7.7).

The composite samples of all the co-doped CF-NPs (sample ids: SKC-015, SKC-011, and SKC-020) also followed the same trend. The zones of inhibition in all the composite samples of co-doped CF-NPs increased as the level of doping increased. Hence, it can be concluded that the composites of all the samples showed enhanced antibacterial activities compared with their respective un-doped, doped/ co-doped CF-NPs [153,211].
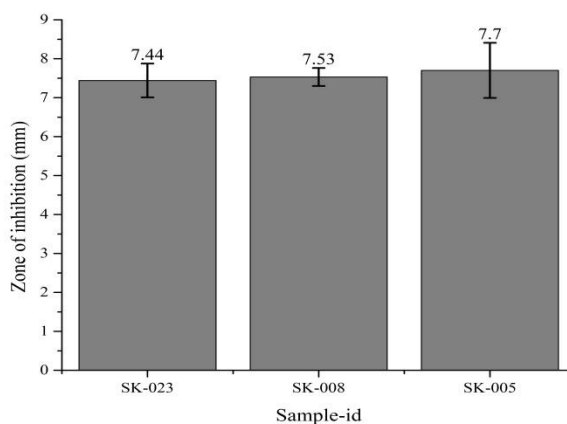
Fig. 7.11 Bar graph picture showing the reproducibility of the sample-ids: SK-023, SK-008 and SK-002.

The reproducibility of antibacterial activities of the sample-ids: SK-023, SK-008, and SK-005 is revealed in fig. 7.11. Here, the trend of variation and reproducibility of the samples follow the same order as it has been found in the antibacterial activities of copper doped CF and zinc doped CF. The zinc doped CF-NPs and copper doped CF-NPs showed greater antibacterial activities than un-doped samples, as reported in the earlier studies [14,71]. We also noticed that the CF-NPs co-doped with copper and zinc showed better antibacterial activities than the singly doped CF-NPs as well as the un-doped samples.

7.9 Conclusion

Here, we successfully synthesised the doped/ co-doped CF-NPs with Cu-Zn via the sol-gel auto-combustion route and its ZnO/Ag composites with the mortar-pestle

grinding technique. The crystalline structure of co-doped samples was studied through XRD analysis. The doping level also affects the crystallite size and lattice parameter. FTIR results suggested that the octahedral and the tetrahedral shapes remained intact in the doped/co-doped samples. The VSM examined the magnetic properties of all the doped and co-doped samples. The co-doped sample was found to be superparamagnetic. Superparamagnetic materials can be used in biomedical applications such as drug delivery, gene delivery, MRI, etc. The FESEM micrographs show the angular morphologies of the agglomerated particles with clear edges and surfaces. TEM shows the formation of nanosized particles. EDS mapping confirmed the co-doping of CF-NPs with copper and zinc. All the samples of CF and its ZnO/Ag composites effectively revealed the antibacterial activities. The obtained results exposed the higher antibacterial activities against the *Bacillus paranthracis* and *Bacillus nitratireducens* with composites of CF-NPs as compared to doped/co-doped CF-NPs.

Chapter 8

Antibacterial activities of co-doped cobalt ferrite with Bi-Ag and their composite/s with ZnO/Ag

8.1 Introduction

This chapter deals with the prepared co-doped CF-NPs with Bi-Ag and its ZnO/Ag composite materials. The various Advanced Materials' characterization techniques were used to characterize these CF-NPs. The antibacterial activities of all the samples were tested by using Agar disk diffusion test. The various results obtained are discussed in the following sections (see sections 8.2 to 8.7).

8.2 Crystalline structure studies using XRD
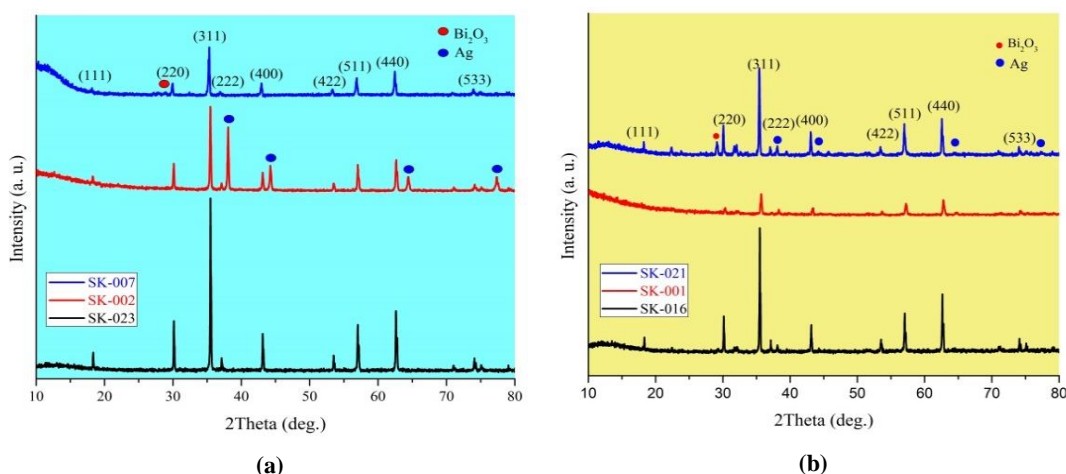
Fig. 8.1 XRD pattern of:
(a) Un-doped CF-NPs (SK-023), Bi and Ag doped CF-NPs (SK-007 and SK-002) respectively;
(b) Bi-Ag co-doped CF-NPs (SK-016, SK-001 and SK-021).

Fig. 8.1 (a) represents the XRD patterns of sample-ids: SK-023, SK-002, and SK-007, while fig. 8.1 (b) represents the XRD pattern of co-doped samples with sample-ids: SK-001, SK-016, and SK-021. These peaks confirmed the cubic crystal structure of the samples with JCPDS card no. 01-083-3116 [14,81]. The diffraction angles at different planes with JCPDS no. 01-083-3116 [14,81] are summarised in Table 8.1.

Table 8.1: List of diffraction planes concerning diffraction angles (°/2θ)

Diffraction angle (°/2θ)	Diffraction plane	Diffraction angle (°/2θ)	Diffraction plane	Diffraction angle (°/2θ)	Diffraction plane
18.37°	(111)	37.21°	(222)	57.11°	(333)
30.11°	(220)	43.14°	(400)	62.80°	(440)
35.49°	(311)	53.50°	(422)	74.11°	(533)

The level of doping of all the samples is also listed in Table 8.2.

Table 8.2: Un-doped, Bi and Ag doped, and Bi-Ag co-doped CF-NPs with their sample-ids at different concentrations

S.No.	Sample-ids	Dopant/s	Level of Doping	Desired product
1.	SK-002	Ag	0.1	$CoFe_{1.9}Ag_{0.1}O_4$
2.	SK-007	Bi	0.1	$CoFe_{1.9}Bi_{0.1}O_4$
3.	SK-016	Bi & Ag	0.05 & 0.05	$Co_{0.95}Bi_{0.05}Fe_{1.95}Ag_{0.05}O_4$
4.	SK-001	Bi & Ag	0.10 & 0.10	$Co_{0.9}Bi_{0.1}Fe_{1.9}Ag_{0.1}O_4$
5.	SK-021	Bi & Ag	0.15 & 0.15	$Co_{0.85}Bi_{0.15}Fe_{1.85}Ag_{0.15}O_4$
6.	SK-023	Un-doped	0	$CoFe_2O_4$

Here, all the peaks confirmed the cubic inverse spinel structure of CF-NPs with space group fd-3m [4]. A secondary phase of silver was seen in the silver doped CF-NPs (SK-002) in fig. 8.1 (a) marked as (●) same as reported in the literature. The presence of an additional phase of silver might be due to the ionic size difference between Ag^+ ions (~1.29 Å) as compared to Fe^{3+} ions (~ 0.67 Å). Similarly, a secondary phase of silver marked as (●) was also observed in all the co-doped samples (SK-016, SK-001, and SK-021). Ionic size difference may be responsible for this type of behaviour [49,122,144]. An additional phase of Bi_2O_3 was also noticed in the bismuth doped CF-NPs (SK-007) marked as (●) same as reported in the literature. It may also be due to the ionic radii difference between Bi^{3+} ions and Co^{2+} ions. Note that the ionic radii of the Bi^{3+} ion are ~1.03 Å [81], while the ionic radii of the Co^{2+} ion are ~0.72Å [81]. It is believed that Bi^{3+} ions occupied octahedral or tetrahedral sites. Same behaviour was observed in Bi-Ag co-doped CF-NPs (SK-021) where an additional phase of bismuth oxide (Bi_2O_3) can be seen in fig. 8.1 (b).

The lattice parameter of the cubic crystal structure was calculated by using the equation (3.3) [66]. The lattice parameter increased in Bi-doped CF-NPs (SK-007) whereas it decreased in Ag-doped CF-NPs (SK-002). It also increases in the Bi-Ag co-doped CF-NPs (SK-016, SK-001, and SK-021) as the doping level increases in the samples. It might be due to the ionic size difference of dopants (Bi^{3+} and Co^{2+}) and

host ions (Co^{2+} and Fe^{3+}) [71]. It can be observed that the minor shift in the highly intense peak of the plane (311) in all the samples may be due to the doping/co-doping [77]. The ionic size of the Fe^{3+} ion (~ 0.67 Å) [81] is lesser than the Ag^+ ion (~ 1.29 Å) [122]. Thus, the lattice parameter increases after co-doping of bismuth and silver ions because of smaller ionic radii of host ions (Co^{2+} and Fe^{3+}) than the guest ions (Bi^{3+} and Ag^+). The crystallite size of samples can be calculated using Scherrer's equation (3.2) [142,202,219]. It is noticed that the calculated value of crystallite size decreases in the silver doped sample (SK-002) [201] and in the bismuth doped sample (SK-007) [8]. These results are in good agreement with earlier reported values, whereas in all the co-doped samples (SK-016, SK-001, and SK-021) the crystallite size first decreased and then increased with an increase in level of doping (see Table 8.3).

The results obtained are listed in Table 8.3.

Table 8.3: Trends of crystallite size and lattice parameter of different Bi-Ag doped and co-doped samples of CF-NPs as calculated using Scherrer's equation

Sample-ids	Dopant/s	Level of doping	°/2θ	FWHM	D nm	Lattice parameter Å
SK-002	Ag	0.1	35.48	0.18	~ 47	8.381
SK-007	Bi	0.1	35.28	0.22	~ 38	8.420
SK-016	Bi & Ag	0.05 & 0.05	35.50	0.15	~ 55	8.385
SK-001	Bi & Ag	0.10 & 0.10	35.67	0.22	~ 37	8.390
SK-021	Bi & Ag	0.15 & 0.15	35.43	0.17	~ 49	8.392
SK-023	Un doped	0	35.51	0.15	~ 54	8.385

The trends of variation of lattice parameters and crystallite sizes of un-doped, Bi, and Ag-doped/co-doped CF-NPs are represented in fig. 8.2. Agrawal *et al.* also reported the behaviour of CF-NPs doped with zinc in similar ways [219] (see fig. 8.2).
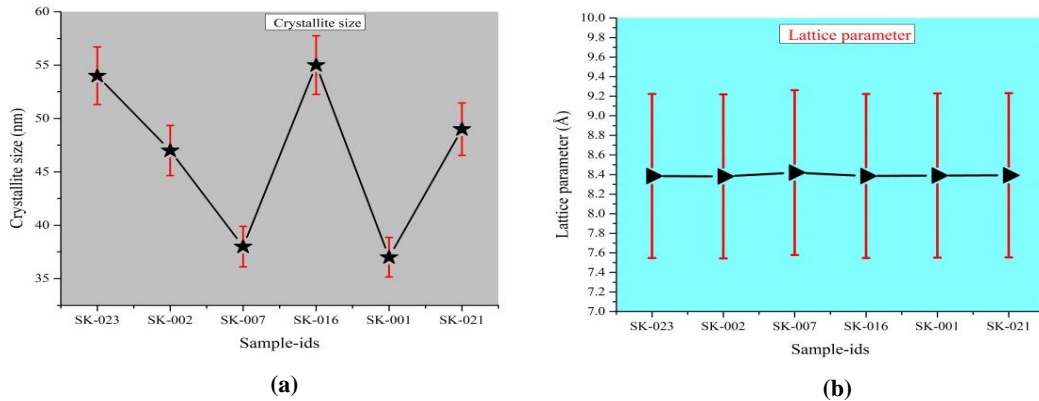
Fig. 8.2 The trends of variation of:
(a) Lattice parameter of un-doped, Bi and Ag doped/ co-doped CF-NPs;
(b) Crystallite size of un-doped, Bi and Ag doped/ co-doped CF-NPs.

8.3 Compositional analysis of samples using FTIR

(a)   (b)

(c)
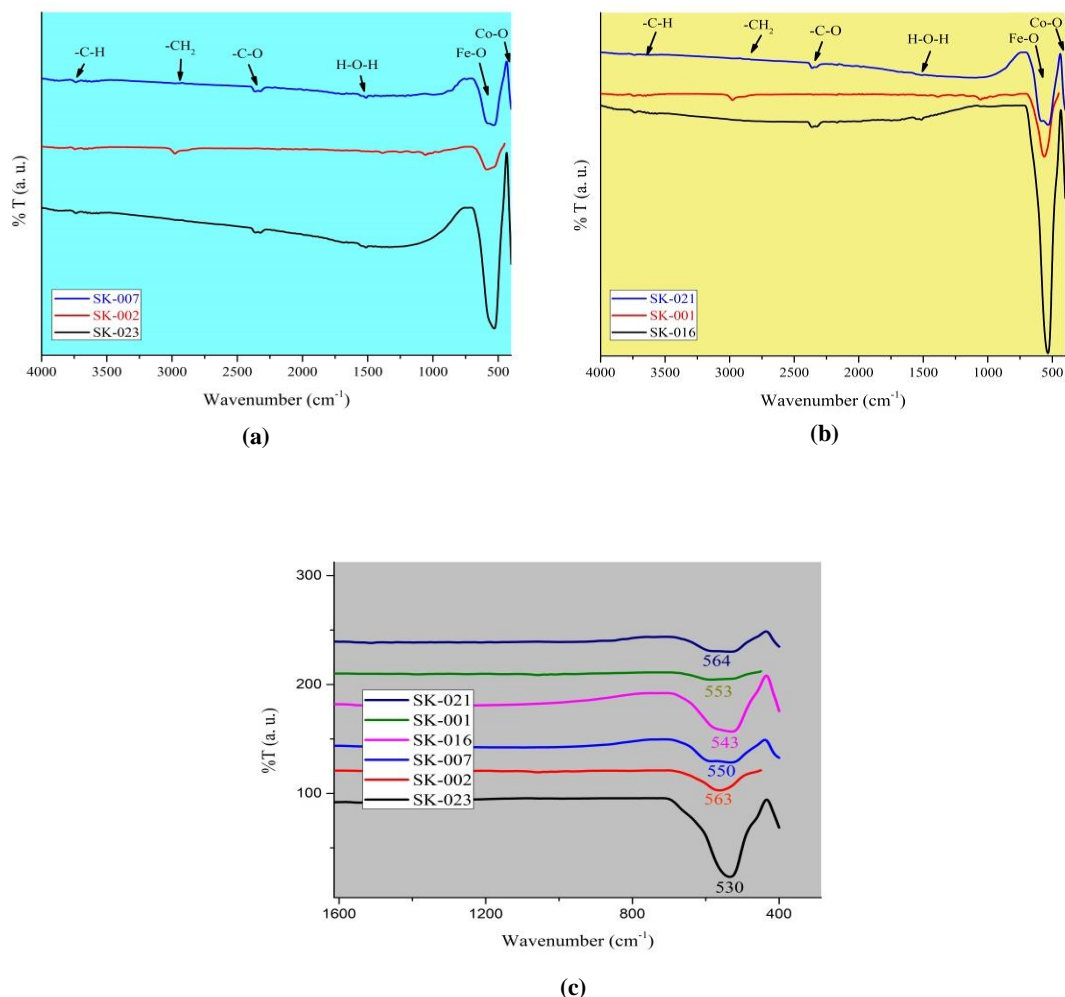
Fig. 8.3 FTIR spectra of sample-ids:
(a) SK-023, SK-002, and SK-007;
(b) SK-016, SK-001, and SK-021;
(c) Narrow scans view of all the samples at the range of 400-600 cm^{-1}

Figs 8.3(a) and 8.3(b) illustrate the FTIR spectra of un-doped CF-NPs (SK-023), silver doped CF-NPs (SK-002), bismuth doped CF-NPs (SK-007), and Bi-Ag co-doped CF-NPs (SK-016, SK-001, and SK-021) at different dopant/s concentartions, respectively. The doping/co-doping level of each of these CF-NPs samples is also listed in the Table 8.4. These CF-NPs were analysed by using FTIR analysis within the range of wavenumbers 400 cm^{-1} to 4000 cm^{-1}. It was observed that the absoption bands of all the CF-NPs for different functional groups are of nearly the same range

120

as can be seen in figs. 8.3 (a) and 8.3 (b). These absorption bands with assignments and appropriate references are listed in Table 8.4.

Table 8.4: List of absorption bands obtained in FTIR analysis

SK-023 ($CoFe_2O_4$)			SK-002 ($CoFe_{1.9}Ag_{0.1}O_4$)		
Observed abs. band	Assign.	Ref.	Observed abs. band	Assign.	Ref.
~ 3742	-C-H bending	[47]	~ 3738	-C-H bending	[47]
~ 2338	-C-O mode	[47]	~ 2320	-C-O mode	[47]
~ 1517	H-O-H	[47]	~ 1524	H-O-H	[47]
~ 538	Fe–O stretch tetrahedral	[71]	~ 565	Fe–O stretch tetrahedral	[71]
~ 402	Co–O stretch octahedral	[71]	~ 402	Co–O stretch octahedral	[71]
SK-007 ($CoFe_{1.9}Bi_{0.1}O_4$)			SK-016 ($Co_{0.95}Bi_{0.05}Fe_{1.95}Ag_{0.05}O_4$)		
Observed abs. band	Assign.	Ref.	Observed abs. band	Assign.	Ref.
~3742	-C-H bending	[47]	~ 3742	-C-H bending	[47]
~ 2345	-C-O mode	[47]	~ 2338	-C-O mode	[47]
~ 1557	H-O-H	[47]	~ 1517	H-O-H	[47]
~ 551	Fe–O stretch tetrahedral	[71]	~ 531	Fe–O stretch tetrahedral	[71]
~ 402	Co–O stretch octahedral	[71]	~ 402	Co–O stretch octahedral	[71]
SK-001 ($Co_{0.9}Bi_{0.1}Fe_{1.9}Ag_{0.1}O_4$)			SK-021 ($Co_{0.85}Bi_{0.15}Fe_{1.85}Ag_{0.15}O_4$)		
Observed abs. band	Assign.	Ref.	Observed abs. band	Assign.	Ref.
~ 3742	-C-H bending	[47]	~ 3742	-C-H bending	[47]
~ 2324	-C-O mode	[47]	~ 2352	-C-O mode	[47]
~ 1540	H-O-H	[47]	~ 1510	H-O-H	[47]
~ 551	Fe–O stretch tetrahedral	[71]	~ 561	Fe–O stretch tetrahedral	[71]
~ 402	Co–O stretch octahedral	[71]	~ 402	Co–O stretch octahedral	[71]

A sharp absorption was observed band at ~ 402 cm^{-1} in un-doped CF-NPs (SK-023), Bi and Ag doped CF-NPs (SK-002 and SK007), as well as in Bi-Ag co-doped CF-NPs (SK-016, SK-001, SK-021). This absorption band indicated the presence of Co-O stretching vibration at the octahedral sites. The bands at the range of ~ 500 cm^{-1} to ~ 600 cm^{-1} are characterised by the Fe-O stretching vibration at the tetrahedral sites. These results are in good agreement with reported values [71,113,144]. Shanmugam *et al.* also noticed the same behaviour in the FTIR when they examined the broadening and shifting of the absorption band in this region [71].

8.4 Study of the magnetic behaviour of the sample using VSM

The magnetic behaviour of the Bi-Ag co-doped CF-NPs with sample-id: SK-021 ($Co_{0.85}Bi_{0.15}Fe_{1.85}Ag_{0.15}O_4$) was examined by VSM technique. The hysteresis loop of the sample SK-021 can be presented in fig.8.4.
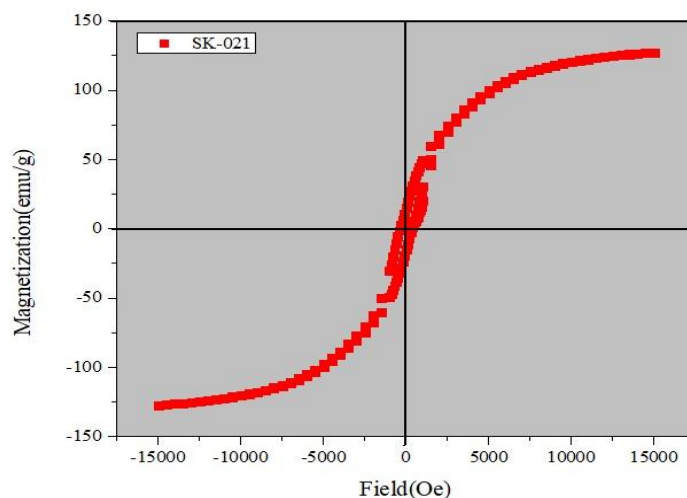
Fig. 8.4 Hysteresis loop of co-doped CF-NPs with sample-id: SK-021

In the hysteresis loop, the saturation magentisation (M_s) was found to be higher when observed up to 150 emu/g. The recorded value was 129.26 emu/g. The coercivity (H_c) was found low or nearly zero [203]. The low value of coercivity is responsible for the change of ferromagnetic material into superparamagnetic material [158]. These superparamagnetic materials are suitable for various biomedical applications [9,214].

8.5 Morphological studies and elemental analysis of samples using FESEM and EDS

Figs. 8.5 (a) to 8.5 (d) present the different FESEM images of Bi-Ag co-doped CF-NPs (SK-021) at the 0.15 concentration. It was observed the hexogonal shaped particles with sharp and clear edges in these images (see figs. 8.5 (b) to (d)). The agglomerated particles with a clear surface can be seen in fig. 8.5 (a). The average grain size of the particles was measured at 873.33 nm. It was calculated by using Image J software [114,204–206].
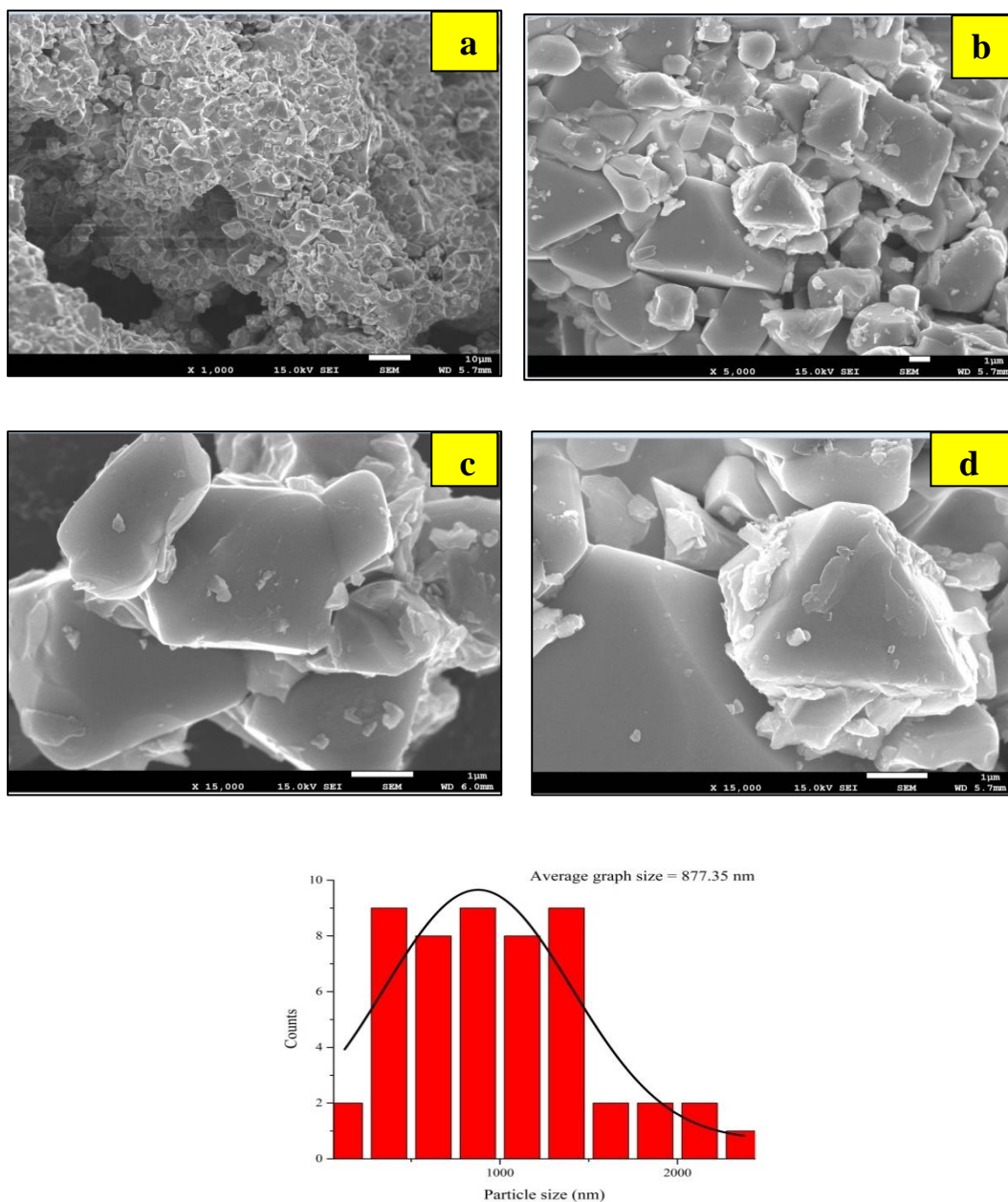
Fig. 8.5 Different FESEM pictures of sample-id: SK-021

Energy dispersive X-ray spectroscopy analysis (EDS) with FESEM is used to find the presence of elements and their quantities in the given sample. Fig. 8.6 represents the EDS mapping of the sample-id: SK-021 ($Co_{0.85}Bi_{0.15}Fe_{1.85}Ag_{0.15}O_4$). The quantitative analysis was performed to study the atomic percent and weight percent of the elements in the sample of CF-NPs.
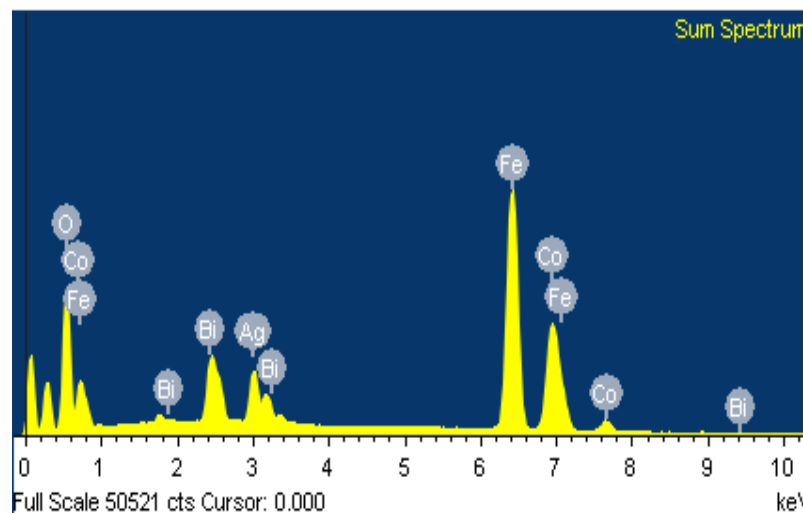
Fig. 8.6 EDS mapping of the co-doped CF-NPs with sample-id SK-021

Here, the microscopist picked the K-lines, L-lines, and M-lines. Table 8.5 listed that the sample contained Bi and Ag apart from other constituent elements present in the CF-NPs sample. This recommends the successful co-doping of bismuth and silver in the co-doped CF-NPs with 0.15 dopant concentrations [71,75,104]. These obtained results are also summarised in the Table 8.5.

Table 8.5: List of elements obtained in EDS analysis with weight percent and atomic percent (Sample-id: SK-021)

Elements	Weight %	Atomic %
O K	21.63	53.46
Fe K	40.02	28.33
Co K	20.07	13.46
Ag L	7.25	2.66
Bi M	11.03	2.09

It should be noted that EDS analysis is a semi-qualitative as well as semi-quantitative method of detection of the elements [207,208].

8.6 Particle size and morphology studies using TEM

Further, TEM was used to study the sizes of particles of CF-NPs co-doped with bismuth and silver. Figs. 8.7 (a) to 8.7 (c) represent the images of particles. Shrap edges of crystals can be clearly seen here as well. Particles of a range of sizes can be observed. Although Image J was used to analyse the particles' size, particles with diameters in the range of ~24.42 nm can be observed. Sumathi *et al.* studied CF-NPs

co-doped with copper and cerium. They reported the particles' sizes in the range of ~ 27 nm to ~ 38 nm [75].

(a)   (b)   (C)
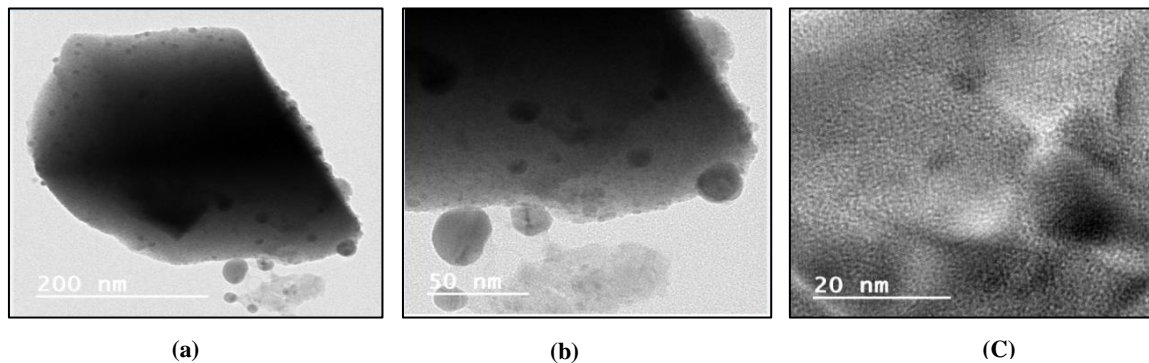
Fig. 8.7 (a) to (c) Different TEM images of the sample-id SK-021

8.7 Thermal Analysis of samples

Thermogravimetric analysis (TGA) and Differential scanning calorimetry (DSC) techniques were used to study the thermal properties of the samples. Here, the samples were heated in the range of 30 ℃ to 450 ℃ at the heating rate of 10 ℃/min. The thermal stability, i.e., degradation of the samples with temperature was studied by the Thermogravimetric analysis. The phase change after heating the sample was studied via Differential scanning calorimetry. The results of TGA and DSC are illustrated in figs. 8.8 (a) and 8.8 (b), respectively.

(a)   (b)
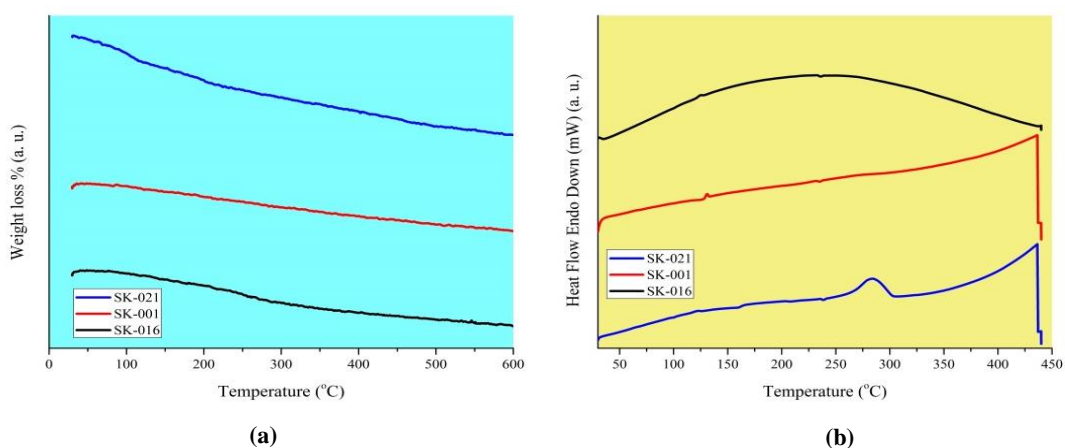
Fig. 8.8 The thermal analysis of the CF-NPs through:
(a) TGA of all the co-doped samples with sample-ids: SK-016, SK-001 and SK-021;
(b) DSC of all the co-doped samples with sample-ids: SK-016, SK-001, and SK-021.

Fig. 8.8 (a) illustrates the TGA results of co-doped samples (SK-015, SK-011, and SK-021). There is no significant weight loss observed in the co-doped samples at the specific temperature range. These results confirme the thermal stability of the co-doped samples. Although a small, gradual weight loss was observed in the samples that might be due to the loss of water. It is believed that molecules of water that get adsorbed/absorbed at the surface of the samples was lost after the TGA treatment [109,147,181,209,210,217,218].

Similarly, no thermal event was observed in the DSC analysis of co-doped CF-NPs (see fig. 8.8 (b)). The DSC results confirmed the thermal stability of the samples at a particular temperature range. However, sample-Id: SK-016 exhibits very small exothermic behaviour at the range of ~ 280 ℃. Although the sample-Id: SK-001 revealed insignificant exothermic events at the range of ~ 130 ℃ and the sample-Id: SK-021 showed very small exothermic events at the range of ~ 225 ℃. It is believed that these properties of samples are attributed to the presence of residual nitrates and hydroxyl groups in the co-doped CF-NPs [109,147,181,209,210,217,218].

The data of the thermal analysis of all the samples are also listed in Table 8.6.

Table 8.6: The data obtained after thermal analysis of the co-doped CF-NPs

TGA		DSC	
Sample-ids	**Weight loss (%)**	**Sample-ids**	**Temperature at which minute thermal event observed**
SK-016	0.08	SK-016	~ 280 ˚C
SK-001	0.06	SK-001	~ 130 ˚C
SK-021	0.14	SK-021	~ 225 ˚C

8.8 Antibacterial activities

The antibacterial activities were examined via Agar disk diffusion method. The microsopic study of the permanent slide confirmed the presence of bacteria of *Bacillus* family. Amoxicillin as a positive control and liquid paraffin as a negative control were used during the process of the antibacterial activity test. All the CF-NPs successfully generated different zones of inhibitions and obtained their antibacterial

126

activities (see figs. 8.9 (a) and 8.9 (b)), while the composites of all the CF-NPs are represented in fig. 8.9 (c).
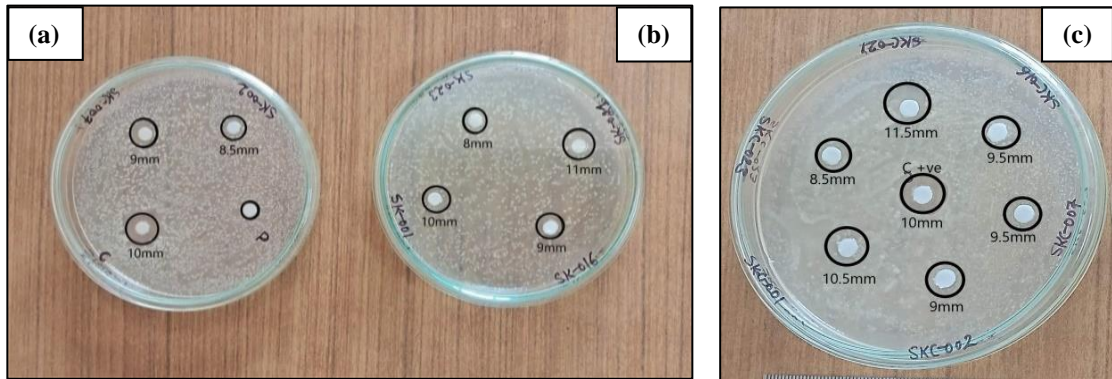
Fig. 8.9 The antibacterial zone of inhibitions of:
(a) SK-002, SK-007, C (+ve) i.e. Amoxicillin, and C (-ve) i.e., Paraffin;
(b) SK-023, SK-016, SK-001, and SK-021;
(c) SKC-002, SKC-007, SKC-016, SKC-001, SKC-021, SKC-023, and C (+ve) i.e., Amoxicillin.

The zone of inhibitions was calculated with Image J software. It was observed that the co-doping of higher dopant concentrations (SK-021) created the bigger zone of inhibitions. Similarly, the composite of the CF-NPs of higher dopant concentration (sample id: SKC-021) also formed the largest zone of inhibitions. The diameters of the zone of inhibitions of the CF-NPs are also listed in Table 8.7.

Table 8.7: Diameter of the zone of inhibitions of different CF-NPs and its ZnO/Ag composites

Sample-ids	Zone of inhibitions (mm)	Sample-ids	Zone of inhibitions (mm)
SK-023	8.0	SKC-023	8.5
SK-002	8.5	SKC-002	9.0
SK-007	9.0	SKC-007	9.5
SK-016	9.0	SKC-016	9.5
SK-001	10	SKC-001	10.5
SK-021	11	SKC-021	11.5

It can be seen that the diameter of the zone of inhibitions of Bi-doped CF-NPs (SK-007) and Ag-doped CF-NPs (SK-002) created the largest zones than the un-doped CF-NPs (SK-023), as reported in the literature [19,71]. It was found that the co-doped CF-NPs created the larger zone of inhibitions than un-doped and doped CF-NPs. Antibacterial activites of co-doped samples increased as the level of co-doping increased. Here, the sample-id SK-021 created the largest zone of inhibitions. The composite samples of CF-NPs also revealed the same trend. Sample-id SKC-021

generated the largest zone of inhibitions [153,211]. Hence, it can be concluded that the ZnO/Ag composites of CF-NPs show enhanced antibacterial activities as compared to their respective samples of CF-NPs. Graphically, the trend of antibacterial activities of CF-NPs and its composites is represented in the figs. 8.10 (a) and 8.10 (b) respectively.
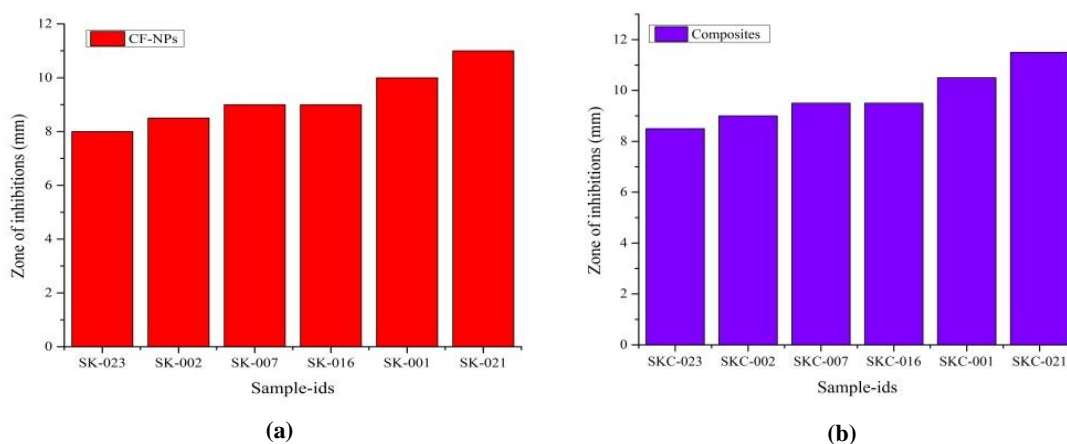
Fig. 8.10 Graphical representation of zone of inhibition of:
(a) Un-doped CF-NPs, Bi and Ag doped/ co-doped CF-NPs;
(b) Composites of un-doped CF-NPs, Bi and Ag doped/ co-doped CF-NPs.
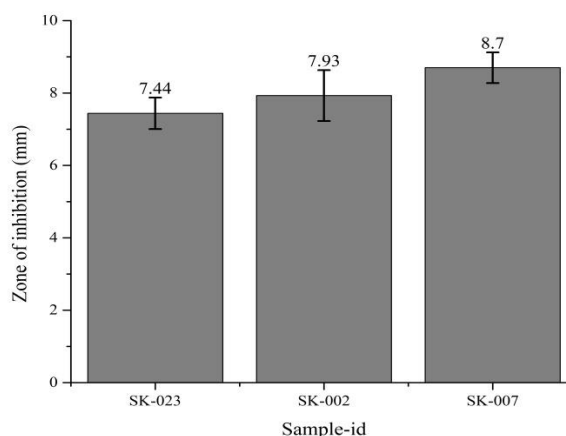
Fig. 8.11 Bar graph picture showing the reproducibility of the sample-ids: SK-023, SK-002 and SK-007.

The reproducibility of antibacterial activities of the sample-ids: SK-023, SK-002, and SK-007 is shown in fig. 8.11. Here, the trend of variation and reproducibility of the samples follow the same order as it has been found in the antibacterial activities of

bismuth doped CF-NPs and silver doped CF-NPs. It has been observed that the antibacterial activities of silver doped CF-NPs remain higher than those of un-doped CF-NPs [14,19,122]. Similarly, bismuth doped CF-NPs also show higher antibacterial activity than un-doped CF-NPs, as reported in the earlier studies [71]. We also observed that the CF-NPs co-doped with bismuth and silver showed enhanced antibacterial activities than the singly doped CF-NPs as well as the un-doped samples.

8.9 Conclusion

Here, the co-doped cobalt ferrite nanoparticles (CF-NPs) with bismuth and silver were successfully synthesised by using the sol-gel auto-combustion method. The ZnO/Ag composites of these CF-NPs were also prepared by mortar-pestle grinding method. The presence of Bi and Ag was confirmed through XRD analysis in all the doped and co-doped samples. The crystallite size and lattice parameter were changed with the level of doping. The FTIR study shows the minor shift in the absorption bands in doped/co-doped CF-NPs as compared to un-doped CF-NPs. The VSM result of the co-doped sample showed the change of ferromagnetic material into superparamagnetic material. The superparamagnetic materials can be used in the different biomedical applications. FESEM shows the agglomeration of the particles, while EDS confirmed the co-doping in the CF-NPs. TEM shows the formation of nanosized particles' in the range of ~27 nm to ~38 nm. The thermal analysis of the samples indicated that these samples were thermally stable at the specific range of the temperature. All the synthesised CF-NPs and their ZnO/Ag composites effectively showed the antibacterial activities. The composites of all the samples show enhanced antibacterial activities than CF-NPs against the bacteria of *Bacillus* family, named *Bacillus paranthracis* and *Bacillus nitratireducens*.

Chapter 9

Antibacterial activities of co-doped cobalt ferrite with Bi-Zn and their composite/s with ZnO/Ag

9.1 Introduction

This chapter deals with the synthesised co-doped CF-NPs with Bi-Zn and its ZnO/Ag nanocomposites. The various Advanced Materials' characterization techniques were used to characterise these CF-NPs. The antibacterial activities of all the samples were tested by using Agar disk diffusion test. The various results obtained are discussed in the following sections (see sections 9.2 to 9.7).

9.2 Crystalline structure studies using XRD
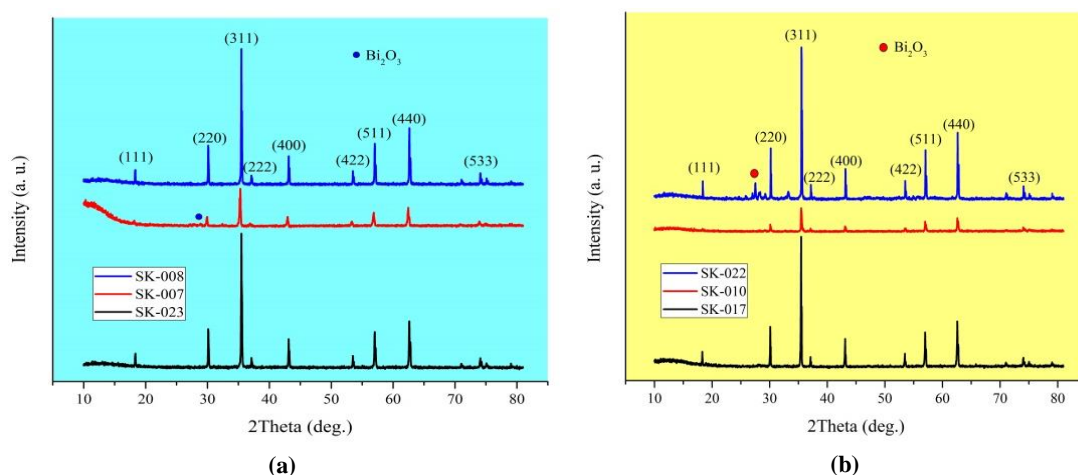
Fig. 9.1 Powder XRD pattern of:
(a) Un-doped CF-NPs (SK-023), Bi and Zn doped CF-NPs (SK-007 and SK-008);
(b) Bi-Zn co-doped CF-NPs (SK-017, SK-010 and SK-022).

Figs. 9.1 (a) and 9.1 (b) represent the XRD spectra of un-doped CF-NPs (SK-023), Bi and Zn-doped CF-NPs (SK-007 and SK-008), and Bi-Zn co-doped CF-NPs (SK-017, SK-010, and SK-022) respectively. It was performed at the diffraction angle (º/2θ) between 10º to 80º. The CuKα radiations of wavelength 1.54 Ǻ were used throughout the practice. All the diffraction peaks confirmed the cubic spinel structure of CF-NPs with JCPDS card no. 01-083-3116 (see Table 9.1) [14,81].

Table 9.1: List of angle of diffraction (°/2θ) with respect to diffraction planes

Angle of diffraction (°/2θ)	Diffraction plane	Angle of diffraction (°/2θ)	Diffraction plane	Angle of diffraction (°/2θ)	Diffraction plane
18.37°	(111)	37.21°	(222)	57.11°	(511)
30.11°	(220)	43.14°	(400)	62.80°	(440)
35.49°	(311)	53.50°	(422)	74.11°	(533)

The level of doping of all the samples is also listed in Table 9.2.

Table 9.2: Un-doped, Bi and Zn doped, and Bi-Zn co-doped CF-NPs with their sample-ids at different concentrations

S. No.	Sample-ids	Dopant/s	Level of Doping	Desired product
1.	SK-007	Bi	0.1	$CoFe_{1.9}Bi_{0.1}O_4$
2.	SK-008	Zn	0.1	$CoFe_{1.9}Zn_{0.1}O_4$
3.	SK-017	Bi & Zn	0.05 & 0.05	$Co_{0.95}Bi_{0.05}Fe_{1.95}Zn_{0.05}O_4$
4.	SK-010	Bi & Zn	0.10 & 0.10	$Co_{0.9}Bi_{0.1}Fe_{1.9}Zn_{0.1}O_4$
5.	SK-022	Bi & Zn	0.15 & 0.15	$Co_{0.85}Bi_{0.15}Fe_{1.85}Zn_{0.15}O_4$
6.	SK-023	Un-doped	0	$CoFe_2O_4$

Fig. 9.1(a) showed the XRD spectra of un-doped CF-NPs (SK-023), Bi and Zn doped CF-NPs (SK-007 and SK-008). It was observed the presence of a secondary phase of Bi_2O_3 in bismuth doped CF-NPs (SK-007). This result is in good agreement with the earlier reported value [49]. Note that the ionic radius of the Bi^{3+} ion (~1.03 Å) is greater than the Co^{2+} ion (~ 0.72Å). Therefore, it can occupy the tetrahedral or octahedral sites easily. No impurities were seen in un-doped and doped samples [14,81]. Similarly, in fig. 9.1 (b), a secondary phase of bismuth oxide (Bi_2O_3) was also seen in Bi-Zn co-doped CF-NPs of higher dopant concentrations (sample-id: SK-022). The presence of a secondary phase might be due to the ionic size difference between dopant ions and host ions after co-doping [71].

The lattice parameter of the cubic crystal structure was calculated by using the equation (3.3) [66,81,112]. The bismuth doped CF-NPs (SK-007) and zinc doped CF-NPs (SK-008) showed increase in lattice parameter than the un-doped CF-NPs (SK-023). It might be due to the larger ionic radius of Bi^{3+} (1.03 Å) ion than Co^{2+} (0.72 Å) ion and Zn^{2+} (0.74 Å) ion than Fe^{3+} (0.67 Å) ion [81,112]. However, the simultaneous co-doping of Bi^{3+} ions and Zn^{2+} ions at various concentrations shows an increase in the lattice parameter in SK-017 to SK-010 when the level of doping increased from 0.05 to 0.10. Although at the dopant level of 0.15 (sample id: SK-022), it decreases. This anomalous behaviour might be due to the ionic size difference of dopant ions (Bi^{3+}

and Zn^{2+}) and host ions (Co^{2+} and Fe^{3+}) ions [71]. The minor shift in the highly intense peak at the plane (311) can be seen in the entire samples as compared to the un-doped sample. Doping/co-doping may be responsible for this kind of observation [77].

The crystallite size of samples can be calculated using Scherrer's equation (3.2) [142,202,219]. It was observed the reduction in the crystallite size of the bismuth doped CF-NPs (SK-007) [8] however, it increased in zinc doped CF-NPs (SK-008) [209]. These results are the same as reported earlier in the literature. In the co-doped CF-NPs the crystallite size of the sample SK-017 increases first, then decreases in SK-010. After that, it further increases in sample SK-022 (see Table 9.3). The variation in the crystallite size is dependent upon the level of co-doping. The ionic size difference between dopant ions and Co^{2+} and Fe^{3+} might be responsible for this type of behaviour [49,71,75]. The trends of variation of lattice parameters and crystallite sizes of un-doped, Bi, and Zn doped/co-doped CF-NPs are represented in fig. 9.2.

Table 9.3: Trends of crystallite size and lattice parameter of different Bi and Zn doped/ co-doped CF-NPs as calculated using Scherrer's equation

Sample-id	Dopant/s	Level of doping	°/2θ	FWHM	D (nm)	Lattice parameter (Å)
SK-007	Bi	0.1	35.28	0.220	~ 38	8.420
SK-008	Zn	0.1	35.50	0.145	~ 57	8.409
SK-017	Bi & Zn	0.05 & 0.05	35.48	0.146	~ 58	8.388
SK-010	Bi & Zn	0.10 & 0.10	35.51	0.190	~ 44	8.409
SK-022	Bi & Zn	0.15 & 0.15	35.56	0.138	~ 60	8.381
SK-023	Un-doped	0	35.51	0.150	~ 54	8.385
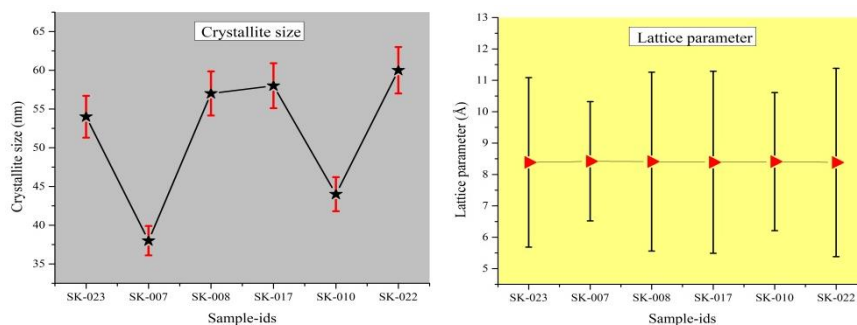
Fig. 9.2 Variation of crystallite size and lattice parameter of un-doped, Bi and Zn doped/ co-doped CF-NPs.

9.3 Compositional analysis of samples using FTIR

(a)

(b)

(c)
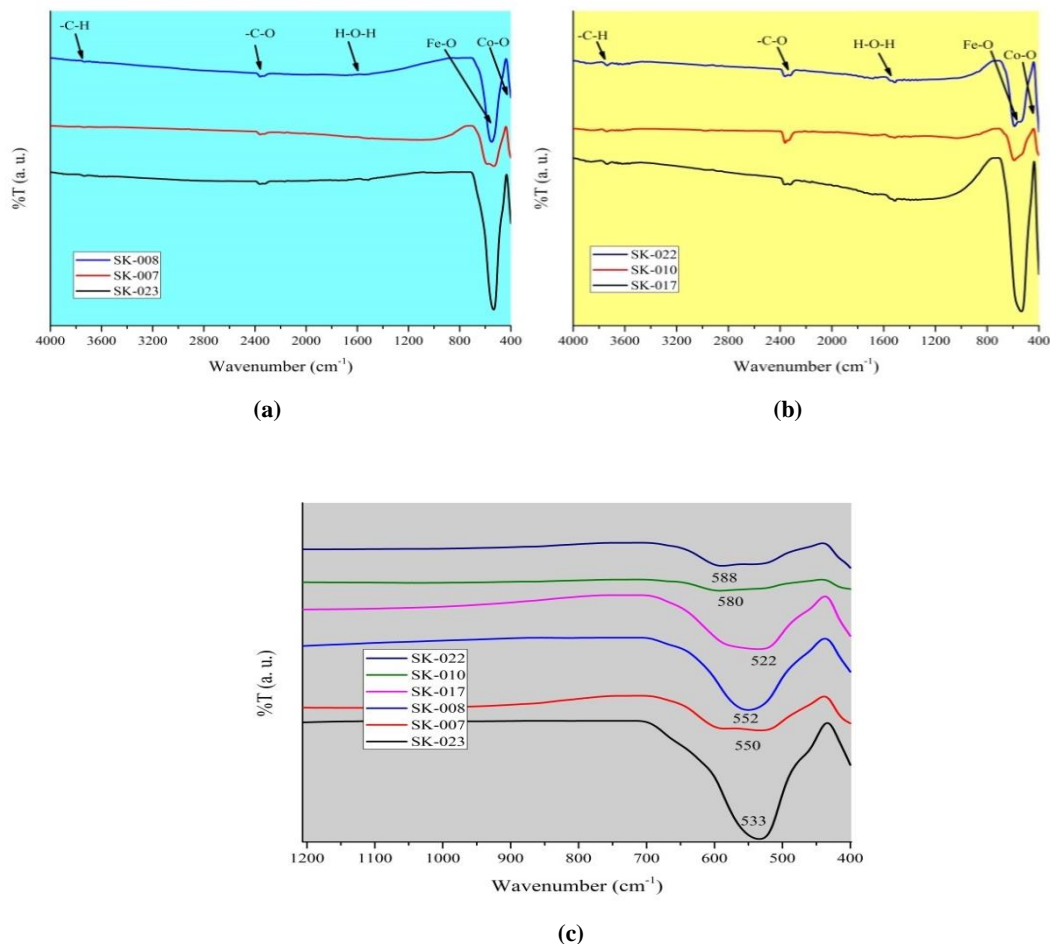
Fig. 9.3 FTIR pattern of:
(a) Un-doped CF-NPs (SK-023), Bi and Zn doped CF-NPs (SK-007 and SK-008);
(b) Bi-Zn co-doped CF-NPs (SK-017, SK-010 and SK-022).
(c) Narrow scan view of all the CF-NPs at the range of 400-600 cm^{-1}.

Various functional groups present in synthesised samples of CF-NPs were identified using FTIR studies. Here, fig. 9.3 illustrates the FTIR spectra of un-doped CF-NPs, Bi and Zn doped/co-doped CF-NPs at the different levels of doping. The absorption bands observed at ~ 400 cm^{-1} to ~ 600 cm^{-1} is indicate the metal-oxygen bonds at the tetrahedral sites and octahedral sites. The sharp absorption band in the range of ~ 402 cm^{-1} was seen in all the CF-NPs samples. These bands identified the presence of Co-O bond at the octahedral sites whereas the band at ~ 540 cm^{-1} to 590 cm^{-1} shows the presence of Fe-O bonds at the tetrahedral sites. The narrow scan view of the band at 400 to 600 cm^{-1} shows a minor change in absorption bands towards a higher

133

wavenumber or lower wavelength in all the doped/co-doped CF-NPs than un-doped CF-NPs [71]. A few more absorption bands were also seen in the FTIR spectra. A list of various absorbtion bands obtained as per assignments is presented in Table 9.4.

Table 9.4: List of FTIR absorption bands in un-doped, doped and co-doped samples of CF-NPs

SK-023 ($CoFe_2O_4$)			SK-017 ($Co_{0.95}Bi_{0.05}Fe_{1.95}Zn_{0.05}O_4$)		
Observed abs. band	Assign.	Ref.	Observed abs. band	Assign.	Ref.
~ 3740	-C-H bending	5	~ 3742	-C-H bending	5
~ 2348	-C-O mode	47	~ 2351	-C-O mode	47
~ 1536	H-O-H	47	~ 1513	H-O-H	47
~ 540	Fe–O stretch tetrahedral	144	~ 547	Fe–O stretch tetrahedral	144
~ 402	Co–O stretch octahedral	144	~ 404	Co–O stretch octahedral	144
SK-007 ($CoFe_{1.9}Bi_{0.1}O_4$)			SK-010 ($Co_{0.9}Bi_{0.1}Fe_{1.9}Zn_{0.1}O_4$)		
Observed abs. band	Assign.	Ref.	Observed abs. band	Assign.	Ref.
~ 3670	-C-H bending	5	~ 3742	-C-H bending	5
~ 2344	-C-O mode	47	~ 2358	-C-O mode	47
~ 1590	H-O-H	47	~ 1523	H-O-H	47
~ 544	Fe–O stretch tetrahedral	144	~ 580	Fe–O stretch tetrahedral	144
~ 402	Co–O stretch octahedral	144	~ 404	Co–O stretch octahedral	144
SK-008 ($CoFe_{1.9}Zn_{0.1}O_4$)			SK-022 ($Co_{0.85}Bi_{0.15}Fe_{1.85}Zn_{0.15}O_4$)		
Observed abs. band	Assign.	Ref.	Observed abs. band	Assign.	Ref.
~ 3735	-C-H bending	5	~ 3742	-C-H bending	5
~ 2347	-C-O mode	47	~ 2364	-C-O mode	47
~ 1552	H-O-H	47	~ 1527	H-O-H	47
~ 552	Fe–O stretch tetrahedral	144	~ 587	Fe–O stretch tetrahedral	144
~ 402	Co–O stretch octahedral	144	~ 404	Co–O stretch octahedral	144

9.4 Study of the magnetic behaviour of the sample using VSM
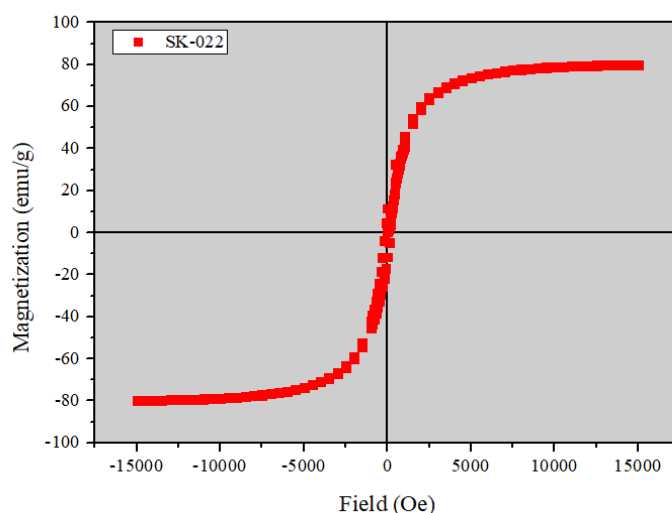
Fig. 9.4 Hysteresis loop of co-doped CF-NPs (sample-id: SK-022)

134

The magnetic character of bismuth and zinc co-doped CF-NPs studied by using VSM (Vibrating Sample Magnetometer). The hysteresis loop of a co-doped sample of dopant level 0.15 (sample-id: SK-022) is illustrated in fig. 9.4. It was measured up to 100 emu/g. The recorded value of saturation magnetisation (M_s) was 80 emu/g. The high value of saturation magnetisation and low or negligible coercivity (H_c) revealed the superparamagnetic character of the co-doped sample SK-022. The superparamagnetic behaviour shows that the material does not retain magnetism even in the absence of an applied magnetic field. This type of behaviour is suitable for different biomedical applications [9,146,203].

9.5 Morphological studies and elemental analysis of samples using FESEM and EDS
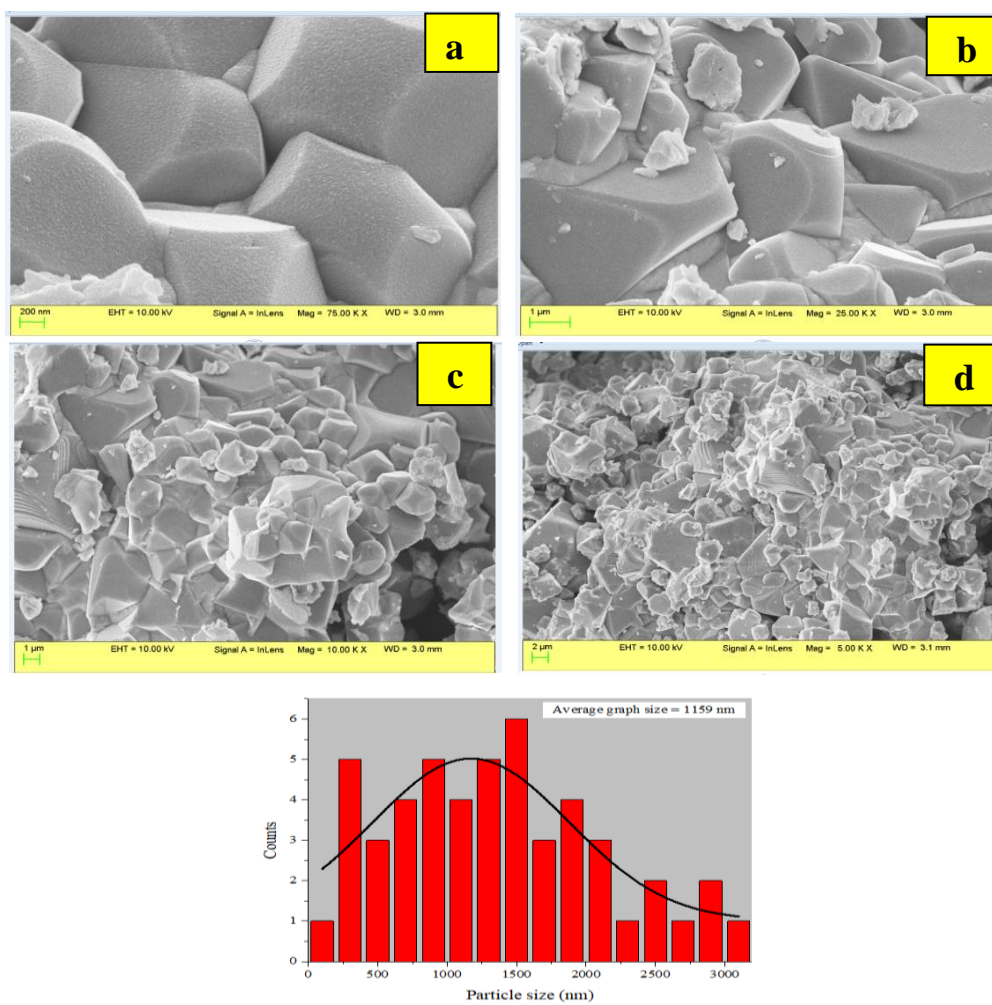
Fig. 9.5 FESEM images of co-doped CF-NPs (sample-id: SK-022)

135

Fig. 9.5 displays various FESEM pictures of sample-id: SK-022. The particles of rounded and clear edges can be seen in fig 9.5a. Agglomerated particles with clean surfaces were also seen in fig. 9.5b to fig. 9.5d. These images show that the particles have rounded and angular edges, and these were arranged in large clusters. The average grain size of the sample id: SK-022 was measured 1159 nm. It was calculated with Image J software [114,204–206].

EDS analysis is used for elemental analysis (both qualitative and quantitative). Here, the co-doped sample $Co_{0.85}Bi_{0.15}Fe_{1.85}Zn_{0.15}O_4$ (sample-id: SK-022) was examined. The mapping of elements in this sample is presented in fig. 9.6.
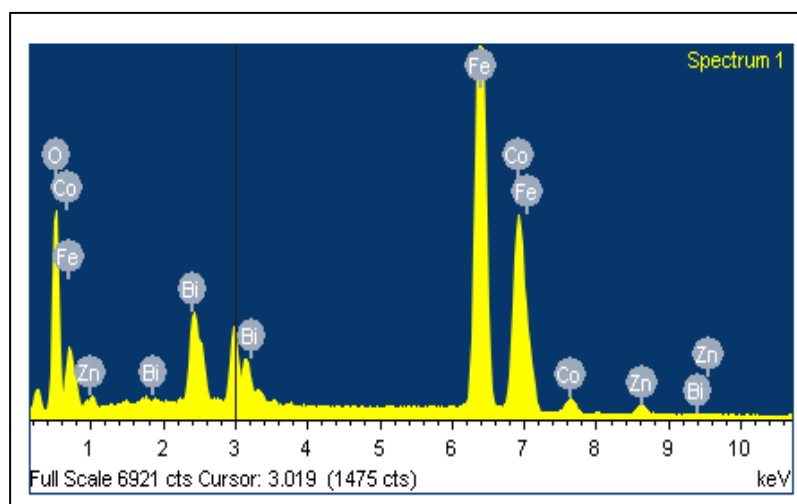
Fig. 9.6 EDS mapping of the elements in sample id: SK-022

It can be noted that the microscopist selected the K-lines and M-lines only. Table 9.5 summarises the results obtained during quantitative analysis with weight percent and atomic percent of elements in the sample SK-022. These results confirmed the effective co-doping of CF-NPs with bismuth and zinc ions [71,75].

Table 9.5: List of weight percent and atomic percent of the elements in sample-id: SK-022.

Elements	Weight %	Atomic %
O K	16.34	43.43
Fe K	46.55	35.43
Co K	23.99	17.31
Zn K	2.60	1.69
Bi M	10.52	2.14

It is clear from the data in Table 9.4; the atomic percent of the observed value and expected value are different from each other. It should be pointed out that it is a semi-qualitative and semi-quantitative method of analysis [207,208]. These results show the deviance due to mode of analysis and control of the machine.

9.6 Thermal analysis of samples
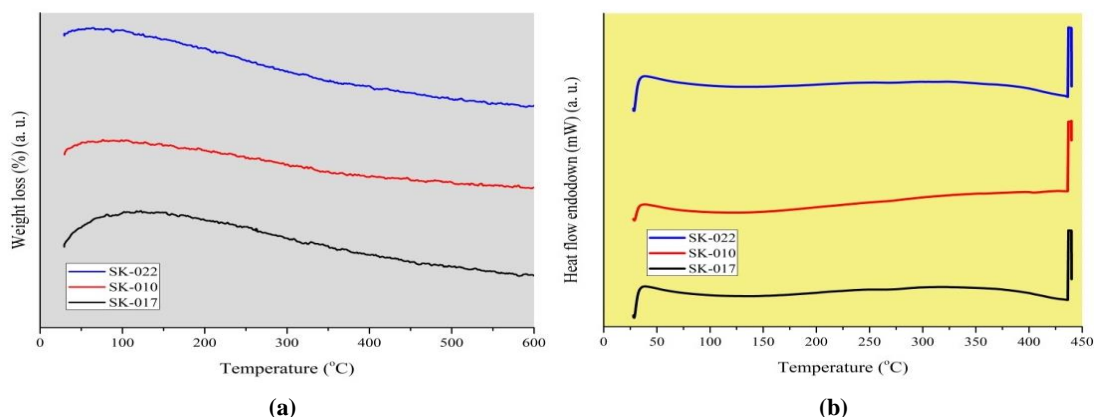
Fig. 9.7 Thermal analysis of co-doped CF-NPs via:
(a) TGA of co-doped samples SK-017, SK-010 and SK-022;
(b) DSC of co-doped samples SK-017, SK-010, and SK-022.

Fig. 9.7 (a) represents the TGA results of co-doped CF-NPs (SK-017, SK-010, and SK-022). No significant weight loss was observed in all the co-doped samples at a particular range of temperature. The TGA results confirmed the thermal stability of the Bi-Zn co-doped CF-NPs samples. Although a minor, gradual weight loss was observed, it might be due to the loss of water. It is believed that molecules of water that get adsorbed/absorbed at the surface of the samples were lost after the TGA treatment [21,82,109,147,181,209,210,217,218].

Similarly, during the DSC study, no thermal event was noticed (see fig. 9.7(b)). DSC analysis of the samples confirmed their thermal stabilities at a specific range of temperature. However, the sample-id SK-017 showed a minute endothermic event at ~125 ˚C, whereas a minor exothermic event can be observed at ~322 ˚C. Similar behaviour can be observed in the other two samples as well [109,147,181,209,210,217,218].
All the data obtained in the thermal analysis of the samples are listed in Table 9.6.

Table 9.6: The thermal analysis results of the Bi-Zn co-doped CF-NPs

TGA		DSC	
Sample-ids	Weight loss (%)	Sample-ids	Temperature at which minute thermal event observed
SK-017	0.02 %	SK-017	~325 °C
SK-010	0.03 %	SK-010	~336 °C
SK-022	0.06 %	SK-022	~300 °C

9.7 Antibacterial activities

Fig. 9.8 represents the results of the antibacterial activities of un-doped CF-NPs, Bi and Zn doped/co-doped CF-NPs. It was performed by using the Agar disk diffusion test. The measured zone of inhibitions showing the antibacterial activities of all samples of CF-NPs and their ZnO/Ag nanocomposites are also listed in Table 9.7. It was found that the diameter of the zone of inhibition was higher in the bismuth doped CF-NPs (SK-007) and zinc doped CF-NPs (SK-008) than un-doped CF-NPs (SK-023). These results are in good agreement with earlier reported values [14,71]. The diameter of the zone of inhibitions in co-doped samples increases in a regular manner from SK-017 to SK-022 as the level of doping increases [153,211].

Similarly, the composites of the doped samples created the bigger zone of inhibitions as compared to the composite of the un-doped sample. The zone of inhibitions in composites of co-doped samples also increases in a regular manner from SKC-017 to SKC-022. Although, the composites of all the samples created the bigger zone of inhibitions than their respective samples of CF-NPs [49].

Fig. 9.8 Measurement of antibacterial zone of inhibitions in:
(a) SK-023, SK-007, SK-008, SK-017, SK-010, SK-022, C +ve and C –ve;
(b) SKC-023, SKC-007, SKC-008, SKC-017, SKC-010, SKC-022, C +ve and C –ve.

Table 9.7: list of measured diameters of zone of inhibitions in un-doped, doped and co-doped CF-NPs

Sample-id	Zone of inhibitions (mm)	Sample-id	Zones of inhibitions (mm)
SK-023	7.6	SKC-023	8.0
SK-007	8.4	SKC-007	9.2
SK-008	7.8	SKC-008	8.2
SK-017	9.0	SKC-017	9.5
SK-010	9.5	SKC-010	10.0
SK-022	10.0	SKC-022	10.5

Graphically, the trend of antibacterial activities of CF-NPs and its ZnO/Ag composites is represented in figs. 9.9 (a) and 9.9 (b) respectively.

(a)   **(b)**
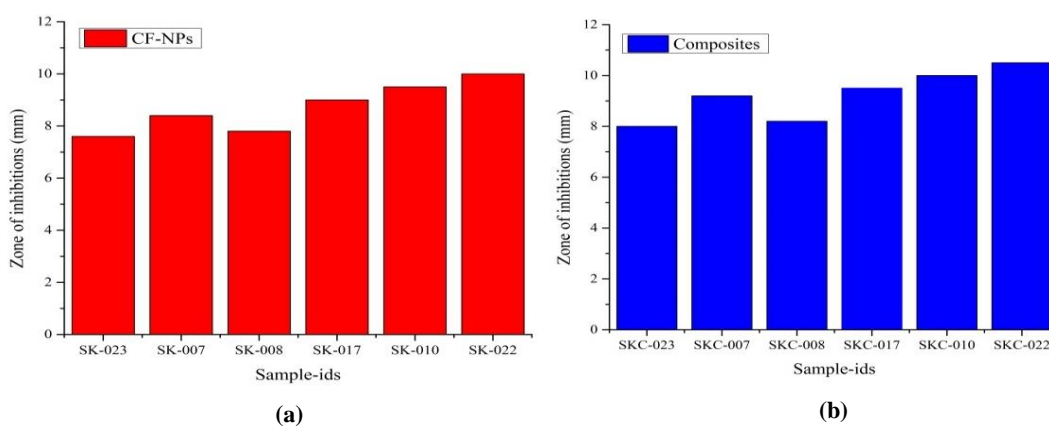
Fig. 9.9 Graphical representation of zone of inhibition of:
(a) Un-doped CF-NPs, Bi and Zn doped/co-doped CF-NPs;
(b) Composites of un-doped CF-NPs, Bi and Zn doped/co-doped CF-NPs.
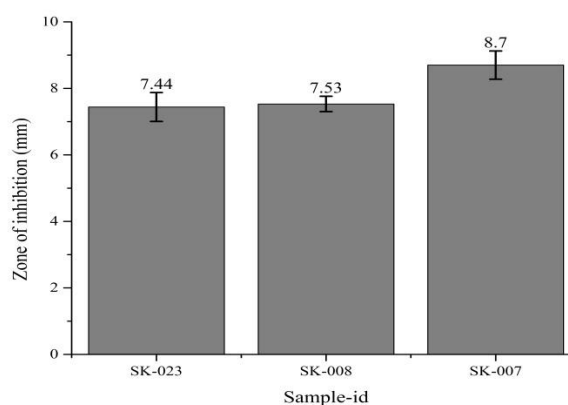
Fig. 9.10 Bar graph pictures presenting the reproducibility of the sample-ids: SK-023, SK-008 and SK-007.

The reproducibility of antibacterial activities of the sample-ids: SK-023, SK-008, and SK-007 is shown in fig. 9.10. Here, the trend of variation and reproducibility of the samples follow the same order as it has been found in the antibacterial activities of bismuth doped CF-NPs and zinc doped CF-NPs. It has been found that the antibacterial activities of zinc doped CF-NPs remain higher than those of un-doped CF-NPs [14]. The bismuth doped CF-NPs also show higher antibacterial activity than the un-doped sample, as reported earlier in the literature [71]. We also observed that the CF-NPs co-doped with bismuth and zinc showed better antibacterial activities than the singly doped CF-NPs as well as the un-doped samples.

9.8 Conclusion

Here, we synthesised the bismuth-zinc co-doped CF-NPs via the sol-gel auto-combustion route. The ZnO/Ag composites of CF-NPs were also prepared by mortar-pestle grinding method.

Powder XRD analysis confirmed the presence of Bi and Zn in all the doped and co-doped CF-NPs. The level of doping in CF-NPs changes their crystallite sizes and lattice parameters. The FTIR pattern shows the slight shifting of the absorption bands in doped and co-doped CF-NPs compared to un-doped CF-NPs. The magnetic properties of the samples were studied using VSM. The hysteresis loop of the co-doped sample (SK-022) showed the change of ferromagnetic material into a superparamagnetic material. The superparamagnetic materials are suitable for different biomedical applications such as gene delivery, drug delivery, and MRI. FESEM images showed the presence of agglomerated particles of rounded and clear edges, whereas EDS confirmed the presence of elements such as Bi, Zn, Co, Fe, and O. The thermal properties of all the co-doped CF-NPs showed that these CF-NPs were thermally stable at the specific range of temperature.

The synthesised CF-NPs and their ZnO/Ag composites successfully revealed the antibacterial activities. The composite samples showed enhanced antibacterial activities as compared to samples of CF against the *Bacillus paranthracis* and *Bacillus nitratireducens*.

Chapter 10

Summary and Conclusion

Cobalt ferrite has a spinel structure with the general formula AB_2O_4. They exhibit several exceptional properties because of their unique molecular structure. They can be used in several technological applications, e.g., in the fabrication of sensors, electronic devices, and optical devices. They can also be used in several biomedical applications, e.g., in Magnetic Resonance Imaging (MRI), drug delivery, and gene delivery.

Here, we synthesised a series of cobalt ferrite samples doped/co-doped with various ions successfully. A complete list of samples synthesised in this work is provided in Chapter 3. We used several pairs of ions, e.g., 'silver (I) and copper (II)', 'zinc (II) and silver (I)', 'copper (II) and zinc (II)', 'silver (I) and bismuth (III)', and 'zinc (II) and bismuth (III)' as dopants. The sol-gel method was used for this purpose. This route of synthesis offers a method of material synthesis where reactions can be carried out under mild conditions, e.g., low temperatures (room temperature), and the requirement of simple laboratory infrastructure, to name but a few. Changes in precursors and reagents result in the formation of entirely different products, which enables us to prepare a wide variety of materials with desired properties. We used metal nitrates as sources of cobalt and iron. Similarly, nitrates of respective ions were used as source metal ions that were used as dopants. Citric acid was used as fuel, whereas ammonium hydroxide was used to control the pH of the reaction system. The temperature was maintained below 100 ℃ throughout the reaction. The sol was turned into a gel, which, on further heating, resulted in the formation of a black, fine powder. The powder was calcined at 1000 ℃ for four hours in an electric furnace under restricted air supply.

The as-prepared un-doped/doped/co-doped CF-NPs was further modified, and composites were prepared through the mortar-pestle grinding method. We used ZnO/Ag for this purpose. Starch was used as binder. This was also a very simple

procedure that was carried out under ambient conditions. We mixed these materials manually.

The antibacterial activities of all the samples (undoped/doped/co-doped CF-NPs and their composites) were studied using Agar disk diffusion method against *Bacillus paranthracis* and *Bacillus nitratireducens*.

We obtained few results almost similar in all the samples, irrespective of dopants. The XRD result showed that the crystals of all the samples were of cubic spinel structure. Hence, while calculating crystallite size using Debye Scherrer's equation, we used the numeric value for Scherrer's constant as 0.9. Also, we used the same XRD machine for this study, which used *CuKα* radiation, and hence the numeric value for wavelength was taken as 1.54 Å. The $º/2\theta$ value for this measurement was also kept the same in all our measurements (10º to 80º). We obtained a sharp XRD peak in all the samples for the (311) plane with minor variations. The minor variation can be attributed to different levels of doping in different samples. The variations are discussed further in the following paragraphs, where we discussed results separately according to dopant ions. Similarly, the FTIR results demonstrated that co-doping did not impact the octahedral structure of the molecule. We believe that these part molecules were at least thermodynamically stable enough that co-doping could not disturb their structure. All the samples showed an absorption band within the wavenumber range of~400 cm^{-1} to~ 600 cm^{-1}, suggesting the presence of a metal-oxygen bond in the molecules.

All the samples were analysed for thermal analysis using both TGA and DSC. TGA was used to find out the thermal degradation or thermal stability of the samples within the temperature range of analysis. We performed the TGA analysis from room temperature (RT, i.e., 30 ºC) to 600 ºC, whereas in DSC thermal analysis was carried from (RT, i.e., 30 ºC) to 440 ºC. It was observed that these samples did not show any significant thermal events, which demonstrates that the samples were thermally stable. A very slight loss in weight in TGA analysis was observed in all the co-doped samples. This can be attributed to a loss of moisture from the sample as the samples were

prepared in water medium. It is also possible that that those absorbed and adsorbed water molecules were expelled when heated, which is reflected in the slight loss of weight in TGA results. Perhaps, organic impurities present in the sample may also be responsible for this loss, as citric acid was used as fuel to complete the reaction. Thermal stability can be useful for a few applications, for example, in the fabrication of medicine where, the medicine has to be transported geographically from one point to another. Many times it has to be transported through severe climatic conditions. These samples can be proved useful for those applications. Although, few minor variations have been observed, which we have discussed separately where we discussed results separately according to dopant ions in the following paragraphs.

Similarly, co-doping influenced the magnetic properties of CF-NPs severely. The ferromagnetic material was changed into superparamagnetic materials as obtained from VSM results. These results demonstrate that the material can be potentially used for drug delivery as well as gene delivery applications. In the micrographs, almost all the samples showed agglomeration. The EDX analysis confirmed the presence of expected ions. TEM results of a few samples show the formation of nanosized particles. All the variations are discussed separately in the following paragraphs. Hereafter, we have summarised the variations obtained (pairwise) according to the co-doping of ions.

Doping of CF-NPs with Cu (II) and Ag (I) ions (Pair 1)

The lattice parameters of co-doped samples decreased when the doping levels were 0.05 and 0.1, whereas the value of this parameter remained the same when we increased the doping level from 0.1 to 0.15. The crystallite size varied a lot. When we compare its value with an un-doped sample, the crystallite size increased with an increase in doping level, but this trend changed with a further increase in doping levels. The crystallite size was less in the case of samples with doping level 0.15 than the crystallite size of the samples with dopant level 0.1. Although a minor shift was observed with the change in doping level. VSM showed the superparamagnetic character of the co-doped sample (sample-id: SK-018). The micrographs obtained

from Field emission scanning electron microscopy confirmed the pentagonal shape of the particles in the sample (sample-id: SK-018). Elemental analysis was studied using EDS. It confirmed the presence of Cu, Ag, Fe, Co, and oxygen, confirming that the molecules were successfully co-doped. The DSC curves of co-doped samples (sample-ids: SK-013, SK-006, and SK-018) showed a minor thermal event. The samples SK-013 and SK-006 showed a minor exothermic event at 186 ºC and 260 ºC, respectively, whereas the sample SK-018 decomposed in the endothermic region at 230 ºC. All the samples of CF-NPs and their composites successfully showed antibacterial activities. The antibacterial zone of inhibition in Cu-Ag co-doped CF-NPs increased linearly with the level of doping. ZnO/Ag composites of these CF-NPs also followed the same trend. The composites of CF-NPs showed enhanced antibacterial activities compared to CF-NPs.

Doping of CF-NPs with Ag (I) and Zn (II) ions (Pair 2)

The XRD pattern of the un-doped, Ag-Zn doped/co-doped CF-NPs showed the change in size of the crystals with the dopant's level. Initially, the size of crystals decreased with co-doping, followed by an increase, and finally, it again decreased. The lattice parameters of co-doped samples increased when the doping levels were 0.05 and 0.1, whereas the value of this parameter decreased when we increased the doping level from 0.1 to 0.15. VSM of co-doped sample SK-019 confirmed its superparamagnetic character. The presence of agglomerated particles with rounded edges was confirmed in SK-019 with FESEM micrographs. EDS analysis of the co-doped sample SK-019 confirmed the co-doping. DSC curves illustrated that all the co-doped samples slightly decomposed. The antibacterial activities of all the Ag-Zn co-doped CF-NPs increased in a regular manner with an increase in dopant concentrations. Similarly, the antibacterial activities of their composites also increased in a regular manner. Composites showed better antibacterial activity than CF-NPs.

Doping of CF-NPs with Cu (II) and Zn (II) ions (Pair 3)

The powder XRD pattern of Cu-Zn un-doped and doped/co-doped CF-NPs showed the variation of crystallite size and lattice parameters. The crystallite size of co-doped samples initially decreased from the dopant concentrations of 0.05 to 0.1; after that, it

144

further increased. The ionic size difference between dopant ions and host ions (Co^{2+} and Fe^{3+}) might be responsible for these changes. The co-doped samples (SK-015, SK-011, and SK-020) showed a slightly linear increase in the lattice parameter with an increase in the level of doping. A minor shift in the absorption band was observed with the change in concentrations of dopant. The VSM result of co-doped sample SK-020 suggested that the sample was superparamagnetic. FESEM images of the sample SK-020 showed the presence of agglomerated particles of angular morphology with clear edges and surfaces. EDS confirmed the presence of Cu, Zn, Fe, Co, and O in SK-020. The TEM result of sample-id SK-020 shows the formation of nanosized particles of the range of 98.35 nm. DSC did not exhibit any distinct thermal events in all the co-doped samples. The antibacterial activity of the as-prepared CF-NPs increased with an increase in the dopant concentrations. The ZnO/Ag composites also followed the same trend. The composite samples showed better antibacterial activities than CF-NPs.

Doping of CF-NPs with Bi (III) and Ag (I) ions (Pair 4)

The XRD pattern of un-doped, Bi-Ag doped/co-doped CF-NPs showed the change in the crystallite sizes and lattice parameters. The crystallite size of co-doped samples initially decreased from the dopant concentrations of 0.05 to 0.1; then it further increased in the sample at dopant concentrations of 0.15. The ionic size difference between dopant ions and host ions (Co^{2+} and Fe^{3+}) might be responsible for these changes. The co-doped samples (SK-016, SK-001, and SK-021) showed a slightly linear increase in the lattice parameter with an increase in dopant concentrations. It showed a minor shift in the absorption bands in doped/co-doped CF-NPs compared to un-doped CF-NPs. The VSM result of co-doped sample SK-021 shows the superparamagnetic character. It can be used in different biomedical applications. FESEM micrographs of SK-021 showed agglomerated particles of hexagonal shapes with sharp and clear edges, while EDS confirmed the presence of Bi, Ag, Fe, Co, and O in the sample SK-021. The TEM result of sample-id SK-021 shows the presence of nanosized particles in the range of ~27 nm to ~38 nm. No distinct thermal event was observed in DSC. All the synthesised Bi-Ag doped/co-doped CF-NPs and their ZnO/Ag composite samples successfully showed antibacterial activities. The antibacterial activity of Bi-Ag co-doped CF-NPs increases in a regular manner with an

145

increase in the level of doping. The composite of these samples also followed the same trend. All the composite samples created larger zones of inhibition than CF-NPs and showed improved antibacterial activities.

Doping of CF-NPs with Bi (III) and Zn (II) ions (Pair 5)

Powder XRD patterns of Bi-Zn doped/co-doped CF-NPs confirmed the change in crystallite sizes and lattice parameters with dopant concentrations. It was observed that the crystallite size decreased after co-doping, followed by an increase, and then further decreased. The lattice parameter of co-doped CF-NPs increased from the dopant level of 0.05 to 0.1, and then decreased at the dopant level of 0.15. FTIR showed a minor shift in the absorption bands in doped/co-doped CF-NPs compared to un-doped CF-NPs. The VSM showed the magnetic properties of the co-doped sample SK-022. The hysteresis loop of SK-022 confirmed the formation of superparamagnetic material. FESEM images of the sample SK-022 showed the presence of agglomerated particles with rounded and clear edges. EDS confirmed the presence of elements such as Bi, Zn, Co, Fe, and O in co-doped sample SK-022. The synthesised CF-NPs and their ZnO/Ag composites successfully revealed their antibacterial activities. The composite of all the CF-NPs shows improved antibacterial activities as compared to CF-NPs.

Co-doping enhanced the antibacterial activity of CF-NPs as compared to un-doped CF. The antibacterial activity in each pair of co-doped CF-NPs increased with an increase in the level of doping. The largest antibacterial zone of inhibition was observed in BiAg co-doped CF-NPs (SK-021), whereas the Cu-Zn co-doped CF-NPs (SK-015) created the lowest zone of inhibition. It might be due to the ionic size difference of dopant ions and host ions. The composite of Cu-Ag co-doped CF-NPs (SKC-018) created the largest zone of inhibition, while the composite of Zn-Ag co-doped CF-NPs (SKC-014) created the smallest zone of inhibition. It is believed that the formation of reactive oxygen species (ROS) and the electrostatic interaction of MNPs with the cell wall might be responsible for these types of activities. However, the exact process by which NPs enter bacteria is still unknown. In the future, the different trends of particle size on the antibacterial activity of co-doped samples can be explored.

146

References

(1)   Karimi, Z.; Mohammadifar, Y.; Shokrollahi, H.; Asl, S. K.; Yousefi, G.; Karimi, L. Magnetic and Structural Properties of Nano Sized Dy-Doped Cobalt Ferrite Synthesized by Co-Precipitation. *J. Magn. Magn. Mater.* **2014**, *361*, 150–156. https://doi.org/10.1016/j.jmmm.2014.01.016.

(2)   Srinivasan, S. Y.; Paknikar, K. M.; Bodas, D.; Gajbhiye, V. Applications of Cobalt Ferrite Nanoparticles in Biomedical Nanotechnology. *Nanomedicine* **2018**, *13* (10), 1221–1238. https://doi.org/10.2217/nnm-2017-0379.

(3)   Fu, Y.; Chen, H.; Sun, X.; Wang, X. Combination of Cobalt Ferrite and Graphene: High-Performance and Recyclable Visible-Light Photocatalysis. *Appl. Catal. B Environ.* **2012**, *111–112*, 280–287. https://doi.org/10.1016/j.apcatb.2011.10.009.

(4)   Houshiar, M.; Zebhi, F.; Razi, Z. J.; Alidoust, A.; Askari, Z. Synthesis of Cobalt Ferrite (CoFe2O4) Nanoparticles Using Combustion, Coprecipitation, and Precipitation Methods: A Comparison Study of Size, Structural, and Magnetic Properties. *J. Magn. Magn. Mater.* **2014**, *371*, 43–48. https://doi.org/10.1016/j.jmmm.2014.06.059.

(5)   Kalia, S.; Kumar, A.; Munjal, N.; Prasad, N. Synthesis of Ferrites Using Various Parts of Plants: A Mini Review. *J. Phys. Conf. Ser.* **2021**, *1964* (3). https://doi.org/10.1088/1742-6596/1964/3/032003.

(6)   Melo, R. S.; Silva, F. C.; Moura, K. R. M.; De Menezes, A. S.; Sinfrônio, F. S. M. Magnetic Ferrites Synthesised Using the Microwave-Hydrothermal Method. *J. Magn. Magn. Mater.* **2015**, *381*, 109–115. https://doi.org/10.1016/j.jmmm.2014.12.040.

(7)   Lefevre, C.; Roulland, F.; Viart, N.; Greneche, J. M.; Pourroy, G. Magnetic Dilution of the Iron Sublattice in CoFe2-XSc XO4 (0≤x≤1). *J. Solid State Chem.* **2010**, *183* (11), 2623–2630. https://doi.org/10.1016/j.jssc.2010.09.004.

(8)   Kumar, N. S.; Kumar, K. V. Synthesis and Structural Properties of Bismuth Doped Cobalt Nanoferrites Prepared by Sol-Gel Combustion Method. **2015**, No. December, 140–151.

(9)   Jauhar, S.; Kaur, J.; Goyal, A.; Singhal, S. *Tuning the Properties of Cobalt Ferrite: A Road towards Diverse Applications*; 2016; Vol. 6. https://doi.org/10.1039/c6ra21224g.

(10)   Lin, J.; Zhang, J.; Sun, H.; Lin, Q.; Guo, Z.; Yang, H.; He, Y. Structural and Magnetic Property of Cr3+ Substituted Cobalt Ferrite Nanomaterials Prepared by the Sol-Gel Method. *Materials (Basel).* **2018**, *11* (11). https://doi.org/10.3390/ma11112095.

(11)   Lamastra, F. R.; Nanni, F.; Camilli, L.; Matassa, R.; Carbone, M.; Gusmano, G. Morphology and Structure of Electrospun CoFe2O4/Multi-Wall Carbon Nanotubes Composite Nanofibers. *Chem. Eng. J.* **2010**, *162* (1), 430–435. https://doi.org/10.1016/j.cej.2010.05.025.

(12)   Turtelli, R. S.; Kriegisch, M.; Atif, M.; Grössinger, R. Co-Ferrite-A Material with Interesting Magnetic Properties. *IOP Conf. Ser. Mater. Sci. Eng.* **2014**, *60* (1). https://doi.org/10.1088/1757-899X/60/1/012020.

(13)   Tanbir, K.; Ghosh, M. P.; Singh, R. K.; Kar, M.; Mukherjee, S. Effect of Doping Different Rare Earth Ions on Microstructural, Optical, and Magnetic Properties of Nickel–Cobalt Ferrite Nanoparticles. *J. Mater. Sci. Mater. Electron.* **2020**, *31* (1), 435–443. https://doi.org/10.1007/s10854-019-02546-9.

(14)   Prabagar, C. J.; Anand, S.; Janifer, M. A.; Pauline, S.; Theoder, P. A. S. Effect of Metal Substitution (Zn, Cu and Ag) in Cobalt Ferrite Nanocrystallites for Antibacterial Activities. *Mater. Today Proc.* **2021**, *47* (xxxx), 1999–2006. https://doi.org/10.1016/j.matpr.2021.04.150.

(15)   Tatarchuk, T.; Bououdina, M.; Macyk, W.; Shyichuk, O.; Paliychuk, N.; Yaremiy, I.; Al-Najar, B.; Pacia, M. Structural, Optical, and Magnetic Properties of Zn-Doped CoFe2O4 Nanoparticles. *Nanoscale Res. Lett.* **2017**, *12* (1). https://doi.org/10.1186/s11671-017-1899-x.

(16)   Kombaiah, K.; Vijaya, J. J.; Kennedy, L. J.; Bououdina, M.; Al-Najar, B. Conventional and Microwave Combustion Synthesis of Optomagnetic CuFe2O4 Nanoparticles for Hyperthermia Studies. *J. Phys. Chem. Solids* **2018**, *115*, 162–171. https://doi.org/10.1016/j.jpcs.2017.12.024.

(17)   Sajjia, M.; Oubaha, M.; Hasanuzzaman, M.; Olabi, A. G. Developments of Cobalt Ferrite Nanoparticles Prepared by the Sol-Gel Process. *Ceram. Int.*

2014, *40* (1 PART A), 1147–1154.
https://doi.org/10.1016/j.ceramint.2013.06.116.

(18) Maaz, K.; Karim, S.; Mashiatullah, A.; Liu, J.; Hou, M. D.; Sun, Y. M.; Duan, J. L.; Yao, H. J.; Mo, D.; Chen, Y. F. Structural Analysis of Nickel Doped Cobalt Ferrite Nanoparticles Prepared by Coprecipitation Route. *Phys. B Condens. Matter* **2009**, *404* (21), 3947–3951.
https://doi.org/10.1016/j.physb.2009.07.134.

(19) Gingasu, D.; Mindru, I.; Patron, L.; Calderon-Moreno, J. M.; Mocioiu, O. C.; Preda, S.; Stanica, N.; Nita, S.; Dobre, N.; Popa, M.; Gradisteanu, G.; Chifiriuc, M. C. Green Synthesis Methods of CoFe2O4 and Ag-CoFe2O4 Nanoparticles Using Hibiscus Extracts and Their Antimicrobial Potential. *J. Nanomater.* **2016**, *2016*. https://doi.org/10.1155/2016/2106756.

(20) Kaur, H.; Singh, A.; Kumar, V.; Ahlawat, D. S. Structural, Thermal and Magnetic Investigations of Cobalt Ferrite Doped with Zn2+ and Cd2+ Synthesized by Ustion Methodauto Comb. *J. Magn. Magn. Mater.* **2019**, *474* (March 2018), 505–511. https://doi.org/10.1016/j.jmmm.2018.11.010.

(21) Kumari, S.; Kumar, V.; Kumar, P.; Kar, M.; Kumar, L. Structural and Magnetic Properties of Nanocrystalline Yttrium Substituted Cobalt Ferrite Synthesized by the Citrate Precursor Technique. *Adv. Powder Technol.* **2015**, *26* (1), 213–223. https://doi.org/10.1016/j.apt.2014.10.002.

(22) Bokov, D.; Turki Jalil, A.; Chupradit, S.; Suksatan, W.; Javed Ansari, M.; Shewael, I. H.; Valiev, G. H.; Kianfar, E. Nanomaterial by Sol-Gel Method: Synthesis and Application. *Adv. Mater. Sci. Eng.* **2021**, *2021*.
https://doi.org/10.1155/2021/5102014.

(23) Askeland, D. R. *The Science and Engineering of Materials*, 3rd ed.; Springer US: Boston, MA, 1996. https://doi.org/10.1007/978-1-4613-0443-2.

(24) Fu, Y.; Chen, H.; Sun, X.; Wang, X. Applied Catalysis B : Environmental Combination of Cobalt Ferrite and Graphene : High-Performance and Recyclable Visible-Light Photocatalysis. *"Applied Catal. B, Environ.* **2012**, *111–112*, 280–287. https://doi.org/10.1016/j.apcatb.2011.10.009.

(25) Benčina, M.; Mavrič, T.; Junkar, I.; Bajt, A.; Krajnović, A.; Lakota, K.; Žigon, P.; Sodin-Šemrl, S.; Kralj-Iglič, V.; Iglič, A. The Importance of Antibacterial

Surfaces in Biomedical Applications. *Adv. Biomembr. Lipid Self-Assembly* **2018**, *28*, 115–165. https://doi.org/10.1016/bs.abl.2018.05.001.

(26) Nasrollahzadeh, M.; Sajadi, S. M.; Sajjadi, M.; Issaabadi, Z. *An Introduction to Nanotechnology*, 1st ed.; Elsevier Ltd., 2019; Vol. 28. https://doi.org/10.1016/B978-0-12-813586-0.00001-8.

(27) Subramani, K.; Elhissi, A.; Subbiah, U.; Ahmed, W. *Introduction to Nanotechnology*; Elsevier Inc., 2019. https://doi.org/10.1016/B978-0-12-815886-9.00001-2.

(28) Dinadayalane, T. C.; Leszczynski, J. Remarkable Diversity of Carbon-Carbon Bonds: Structures and Properties of Fullerenes, Carbon Nanotubes, and Graphene. *Struct. Chem.* **2010**, *21* (6), 1155–1169. https://doi.org/10.1007/s11224-010-9670-2.

(29) Paras; Yadav, K.; Kumar, P.; Teja, D. R.; Chakraborty, S.; Chakraborty, M.; Mohapatra, S. S.; Sahoo, A.; Chou, M. M. C.; Liang, C. Te; Hang, D. R. A Review on Low-Dimensional Nanomaterials: Nanofabrication, Characterization and Applications. *Nanomaterials* **2023**, *13* (1), 1–44. https://doi.org/10.3390/nano13010160.

(30) Srivastava, R.; Yadav, B. C. Ferrite Materials: Introduction, Synthesis Techniques, and Applications as Sensors. *Int. J. Green Nanotechnol. Biomed.* **2012**, *4* (2), 141–154. https://doi.org/10.1080/19430892.2012.676918.

(31) Kamta Tedjieukeng, H. M.; Tsobnang, P. K.; Fomekong, R. L.; Etape, E. P.; Joy, P. A.; Delcorte, A.; Lambi, J. N. Structural Characterization and Magnetic Properties of Undoped and Copper-Doped Cobalt Ferrite Nanoparticles Prepared by the Octanoate Coprecipitation Route at Very Low Dopant Concentrations. *RSC Adv.* **2018**, *8* (67), 38621–38630. https://doi.org/10.1039/c8ra08532c.

(32) Laokul, P.; Amornkitbamrung, V.; Seraphin, S.; Maensiri, S. Characterization and Magnetic Properties of Nanocrystalline CuFe 2O4, NiFe2O4, ZnFe2O 4 Powders Prepared by the Aloe Vera Extract Solution. *Curr. Appl. Phys.* **2011**, *11* (1), 101–108. https://doi.org/10.1016/j.cap.2010.06.027.

(33) Kharisov, B. I.; Dias, H. V. R.; Kharissova, O. V. Mini-Review: Ferrite Nanoparticles in the Catalysis. *Arab. J. Chem.* **2019**, *12* (7), 1234–1246.

https://doi.org/10.1016/j.arabjc.2014.10.049.

(34) Phenomena, M.; Intermetallic, N.; Physique, J. De; Materials, M. Magnetism in Solids : General. **2000**, 1–15.

(35) K.L. Watson. TOPIC 34 MAGNETIC BEHAVIOUR OF MATERIALS. **1998**, 333–337.

(36) Kotnala, R. K.; Shah, J. *Ferrite Materials: Nano ToSpintronics Regime*; Elsevier, 2015; Vol. 23. https://doi.org/10.1016/B978-0-444-63528-0.00004-8.

(37) Wieser, M. E.; Coplen, T. B. *Atomic Weights of the Elements 2009 (IUPAC Technical Report)*; 2011; Vol. 83. https://doi.org/10.1351/PAC-REP-10-09-14.

(38) Sechovský, V. Magnetism in Solids: General Introduction. *Encycl. Mater. Sci. Technol.* **2001**, 5018–5032. https://doi.org/10.1016/b0-08-043152-6/00872-x.

(39) Harris, F. E. Molecular Orbital Theory. *Adv. Quantum Chem.* **1967**, *3* (C), 61–127. https://doi.org/10.1016/S0065-3276(08)60087-8.

(40) Hospital, C. C. May 7, 1927. **1927**, *119* (3001), 3001.

(41) Zheng, X. G.; Xu, C. N.; Nishikubo, K.; Nishiyama, K.; Higemoto, W.; Moon, W. J.; Tanaka, E.; Otabe, E. S. Finite-Size Effect on Néel Temperature in Antiferromagnetic Nanoparticles. *Phys. Rev. B - Condens. Matter Mater. Phys.* **2005**, *72* (1), 1–8. https://doi.org/10.1103/PhysRevB.72.014464.

(42) Oitmaa, J.; Zheng, W. Curie and Néel Temperatures of Quantum Magnets. *J. Phys. Condens. Matter* **2004**, *16* (47), 8653–8660. https://doi.org/10.1088/0953-8984/16/47/016.

(43) Fabian, K.; Shcherbakov, V. P.; McEnroe, S. A. Measuring the Curie Temperature. *Geochemistry, Geophys. Geosystems* **2013**, *14* (4), 947–961. https://doi.org/10.1029/2012GC004440.

(44) Theodoridis, T.; Kraemer, J. Obituary James Alfred Ewing, 1855 - 1935. *R. Soc.* **1935**, *1* (4), 475–492. https://doi.org/https://doi.org/10.1098/rsbm.1935.0011.

(45) Walz, F. The Verwey Transition - A Topical Review. *J. Phys. Condens. Matter* **2002**, *14* (12). https://doi.org/10.1088/0953-8984/14/12/203.

(46) Mathew, D. S.; Juang, R. S. An Overview of the Structure and Magnetism of Spinel Ferrite Nanoparticles and Their Synthesis in Microemulsions. *Chem. Eng. J.* **2007**, *129* (1–3), 51–65. https://doi.org/10.1016/j.cej.2006.11.001.

151

(47) Vats, S.; Kumar, A.; Kalia, S.; Mohammad, J.; Prasad, N. Synthesis of Bismuth Doped Cobalt Ferrite and Its Composite with Polyaniline. *Mater. Today Proc.* **2021**, No. xxxx, 7–10. https://doi.org/10.1016/j.matpr.2021.07.448.

(48) Jadhav, V. V.; Shirsat, S. D.; Tumberphale, U. B.; Mane, R. S. *Properties of Ferrites*; Elsevier Inc., 2020. https://doi.org/10.1016/b978-0-12-819237-5.00003-1.

(49) Kalia, S.; Dhiman, V.; Tekou Carol T., T.; Basandrai, D.; Prasad, N. Antibacterial Activities of Bi-Ag Co-Doped Cobalt Ferrite and Their ZnO/Ag Nanocomposite/S. *Inorg. Chem. Commun.* **2023**, *150*, 110382. https://doi.org/10.1016/J.INOCHE.2022.110382.

(50) Kalia, S.; Kumar, A.; Sharma, S.; Prasad, N. Properties, Applications, and Synthesis of First Transition Series Substituted Cobalt Ferrite: A Mini Review. *J. Phys. Conf. Ser.* **2022**, *2267* (1), 012133. https://doi.org/10.1088/1742-6596/2267/1/012133.

(51) Dedi; Idayanti, N.; Kristiantoro, T.; Alam, G. F. N.; Sudrajat, N. Magnetic Properties of Cobalt Ferrite Synthesized by Mechanical Alloying. *AIP Conf. Proc.* **2018**, *1964* (February 2016). https://doi.org/10.1063/1.5038285.

(52) Nur-E-Alam, M.; Vasiliev, M.; Belotelov, V.; Alameh, K. Properties of Ferrite Garnet (Bi, Lu, Y)3(Fe, Ga)5O12 Thin Film Materials Prepared by RF Magnetron Sputtering. *Nanomaterials* **2018**, *8* (5), 1–19. https://doi.org/10.3390/nano8050355.

(53) Pullar, R. C. Hexagonal Ferrites: A Review of the Synthesis, Properties and Applications of Hexaferrite Ceramics. *Prog. Mater. Sci.* **2012**, *57* (7), 1191–1334. https://doi.org/10.1016/j.pmatsci.2012.04.001.

(54) Coutinho, P. V.; Cunha, F.; Barrozo, P. Structural, Vibrational and Magnetic Properties of the Orthoferrites LaFeO3 and YFeO3: A Comparative Study. *Solid State Commun.* **2017**, *252*, 59–63. https://doi.org/10.1016/j.ssc.2017.01.019.

(55) Hosni, N.; Zehani, K.; Bartoli, T.; Bessais, L.; Maghraoui-Meherzi, H. Semi-Hard Magnetic Properties of Nanoparticles of Cobalt Ferrite Synthesized by the Co-Precipitation Process. *J. Alloys Compd.* **2017**, *694*, 1295–1301. https://doi.org/10.1016/j.jallcom.2016.09.252.

(56) Albers-Schoenberg. Journal of The American Ceramic Society-. *J. Am. Ceram. Soc.* **1958**, *41* (11).

(57) Constantinides, S. Semi-Hard Magnets: The Important Role of Materials with Intermediate Coercivity. *Magn. 2011* **2011**.

(58) Durance, T.; Yaghmaee, P. *Microwave Dehydration of Food and Food Ingredients*, Second Edi.; Elsevier B.V., 2011; Vol. 4. https://doi.org/10.1016/B978-0-08-088504-9.00306-8.

(59) Kaur, S.; Sandhu, M.; Kaur, J. Dielectric Theory and Its Properties. *Int. J. Emerg. Technol. Eng. Res.* **2016**, *4* (3), 145–150.

(60) Vadivel, M.; Ramesh Babu, R.; Sethuraman, K.; Ramamurthi, K.; Arivanandhan, M. Synthesis, Structural, Dielectric, Magnetic and Optical Properties of Cr Substituted CoFe2O4 Nanoparticles by Co-Precipitation Method. *J. Magn. Magn. Mater.* **2014**, *362*, 122–129. https://doi.org/10.1016/j.jmmm.2014.03.016.

(61) Quinn, J. J.; Yi, K.-S. *Dielectric Properties of Solids*; 2009; Vol. 3. https://doi.org/10.1007/978-3-540-92231-5_8.

(62) Kavitha, S.; Kurian, M. Effect of Zirconium Doping in the Microstructure, Magnetic and Dielectric Properties of Cobalt Ferrite Nanoparticles. *J. Alloys Compd.* **2019**, *799*, 147–159. https://doi.org/10.1016/j.jallcom.2019.05.183.

(63) Raghasudha, M.; Ravinder, D.; Veerasomaiah, P. FTIR Studies and Dielectric Properties of Cr Substituted Cobalt Nano Ferrites Synthesized by Citrate-Gel Method. *Nanosci. Nanotechnol.* **2013**, *3* (5), 105–114. https://doi.org/10.5923/j.nn.20130305.01.

(64) Kadam, A. B.; Mande, V. K.; Kadam, S. B.; Kadam, R. H.; Shirsath, S. E.; Borade, R. B. Influence of Gadolinium (Gd3+) Ion Substitution on Structural, Magnetic and Electrical Properties of Cobalt Ferrites. *J. Alloys Compd.* **2020**, *840*, 155669. https://doi.org/10.1016/j.jallcom.2020.155669.

(65) Chakrabarty, S.; Pal, M.; Dutta, A. Yttrium Doped Cobalt Ferrite Nanoparticles: Study of Dielectric Relaxation and Charge Carrier Dynamics. *Ceram. Int.* **2018**, *44* (12), 14652–14659. https://doi.org/10.1016/j.ceramint.2018.05.091.

(66) Getso, R. S.; Mohammed, J.; Tchouank Tekou Carol, T.; Mukhtar, G.; Halilu,

N.; Sharma, S.; Srivastava, A. K.; Prasad, N.; Ahmad, M.; Basandrai, D. Structural and Dielectric Properties of Cr3+-Cu2+ Substituted Cobalt Ferrites. *J. Phys. Conf. Ser.* **2020**, *1531* (1). https://doi.org/10.1088/1742-6596/1531/1/012029.

(67) Wells, P. B. Catalysis. In *Encyclopedia of Materials: Science and Technology*; Elsevier, 2001; pp 1020–1025. https://doi.org/10.1016/B0-08-043152-6/00189-3.

(68) Albuquerque, A. S.; Tolentino, M. V. C.; Ardisson, J. D.; Moura, F. C. C.; De Mendona, R.; MacEdo, W. A. A. Nanostructured Ferrites: Structural Analysis and Catalytic Activity. *Ceram. Int.* **2012**, *38* (3), 2225–2231. https://doi.org/10.1016/j.ceramint.2011.10.071.

(69) Roduner, E. Understanding Catalysis. *Chem. Soc. Rev.* **2014**, *43* (24), 8226–8239. https://doi.org/10.1039/c4cs00210e.

(70) Jasrotia, R.; Verma, A.; Verma, R.; Kumar, S.; Ahmed, J.; Krishan, B.; Kumari, S.; Tamboli, A. M.; Sharma, S.; Kalia, S. Nickel Ions Modified Co[Sbnd]Mg Nanophotocatalysts for Solar Light-Driven Degradation of Antimicrobial Pharmaceutical Effluents. *J. Water Process Eng.* **2022**, *47* (April), 102785. https://doi.org/10.1016/j.jwpe.2022.102785.

(71) Savunthari, V.; Shanmugam, K. Photocatalytic and Antibacterial Activity of Bismuth and Copper Co- Doped Cobalt Ferrite Nanoparticles. *J. Mater. Sci. Mater. Electron.* **2018**, *0* (0), 0. https://doi.org/10.1007/s10854-018-8890-x.

(72) Tebyetekerwa, M.; Zhang, J.; Xu, Z.; Truong, T. N.; Yin, Z.; Lu, Y.; Ramakrishna, S.; Macdonald, D.; Nguyen, H. T. Mechanisms and Applications of Steady-State Photoluminescence Spectroscopy in Two-Dimensional Transition-Metal Dichalcogenides. *ACS Nano* **2020**, *14* (11), 14579–14604. https://doi.org/10.1021/acsnano.0c08668.

(73) Zhu, X.; Gao, T. *Spectrometry*; Elsevier Inc., 2018. https://doi.org/10.1016/B978-0-12-815053-5.00010-6.

(74) Chiarotti, G. Optical Properties of Solids. *Electron. Mater.* **1973**, 199–237. https://doi.org/10.1007/978-1-4615-6890-2_9.

(75) Kirankumar, V. S.; Sumathi, S. Copper and Cerium Co-Doped Cobalt Ferrite Nanoparticles: Structural, Morphological, Optical, Magnetic, and

Photocatalytic Properties. *Environ. Sci. Pollut. Res.* **2019**, *26* (19), 19189–19206. https://doi.org/10.1007/s11356-019-05286-9.

(76)   Melo, R. S.; Banerjee, P.; Franco, A. Hydrothermal Synthesis of Nickel Doped Cobalt Ferrite Nanoparticles: Optical and Magnetic Properties. *J. Mater. Sci. Mater. Electron.* **2018**, *29* (17), 14657–14667. https://doi.org/10.1007/s10854-018-9602-2.

(77)   Sharma, R.; Komal; Kumar, V.; Bansal, S.; Singhal, S. Boosting the Catalytic Performance of Pristine CoFe2O4 with Yttrium (Y3+) Inclusion in the Spinel Structure. *Mater. Res. Bull.* **2017**, *90*, 94–103. https://doi.org/10.1016/j.materresbull.2017.01.049.

(78)   Of, H.; Applications, F. 8 Applications and Functions Of.

(79)   Valenzuela, R. Novel Applications of Ferrites. *Phys. Res. Int.* **2012**, *2012*. https://doi.org/10.1155/2012/591839.

(80)   Chang, T.-H. Ferrite Materials and Applications. *Electromagn. Mater. Devices* **2020**, 1–14. https://doi.org/10.5772/intechopen.84623.

(81)   Gore, S. K.; Mane, R. S.; Naushad, M.; Jadhav, S. S.; Zate, M. K.; Alothman, Z. A.; Hui, B. K. N. Influence of Bi3+-Doping on the Magnetic and Mössbauer Properties of Spinel Cobalt Ferrite. *Dalt. Trans.* **2015**, *44* (14), 6384–6390. https://doi.org/10.1039/c5dt00156k.

(82)   Andhare, D. D.; Patade, S. R.; Kounsalye, J. S.; Jadhav, K. M. Effect of Zn Doping on Structural, Magnetic and Optical Properties of Cobalt Ferrite Nanoparticles Synthesized via. Co-Precipitation Method. *Phys. B Condens. Matter* **2020**, *583*. https://doi.org/10.1016/j.physb.2020.412051.

(83)   Manchanda, S. Nanotechnology Reviews ' Just Accepted ' Papers. *Nanotechnol. Rev.* **2011**.

(84)   Kooti, M.; Afshari, M. Magnetic Cobalt Ferrite Nanoparticles as an Efficient Catalyst for Oxidation of Alkenes. *Sci. Iran.* **2012**, *19* (6), 1991–1995. https://doi.org/10.1016/j.scient.2012.05.005.

(85)   Maier, J. Doping Strategies in Inorganic and Organic Materials. *Zeitschrift fur Anorg. und Allg. Chemie* **2017**, *643* (23), 2083–2087. https://doi.org/10.1002/zaac.201700317.

(86)   Sharifianjazi, F.; Moradi, M.; Parvin, N.; Nemati, A.; Jafari Rad, A.; Sheysi,

N.; Abouchenari, A.; Mohammadi, A.; Karbasi, S.; Ahmadi, Z.; Esmaeilkhanian, A.; Irani, M.; Pakseresht, A.; Sahmani, S.; Shahedi Asl, M. Magnetic CoFe2O4 Nanoparticles Doped with Metal Ions: A Review. *Ceram. Int.* **2020**, *46* (11), 18391–18412. https://doi.org/10.1016/j.ceramint.2020.04.202.

(87) Ran, F. Y.; Tsunemaru, Y.; Hasegawa, T.; Takeichi, Y.; Harasawa, A.; Yaji, K.; Kim, S.; Kakizaki, A. Valence Band Structure and Magnetic Properties of Co-Doped Fe 3O4(100) Films. *J. Appl. Phys.* **2011**, *109* (12). https://doi.org/10.1063/1.3597825.

(88) Cao, D.; Wang, X.; Pan, L.; Li, H.; Jing, P.; Wang, J.; Liu, Q. Nonmetal Sulfur-Doped Coral-like Cobalt Ferrite Nanoparticles with Enhanced Magnetic Properties. *J. Mater. Chem. C* **2016**, *4* (5), 951–957. https://doi.org/10.1039/c5tc02931g.

(89) Madhukara Naik, M.; Bhojya Naik, H. S.; Nagaraju, G.; Vinuth, M.; Raja Naika, H.; Vinu, K. Green Synthesis of Zinc Ferrite Nanoparticles in Limonia Acidissima Juice: Characterization and Their Application as Photocatalytic and Antibacterial Activities. *Microchem. J.* **2019**, *146* (December 2018), 1227–1235. https://doi.org/10.1016/j.microc.2019.02.059.

(90) Ghoran, S. H.; Dashti, M. F.; Maroofi, A.; Shafiee, M.; Zare-Hoseinabadi, A.; Behzad, F.; Mehrabi, M.; Jangjou, A.; Jamali, K. Biosynthesis of Zinc Ferrite Nanoparticles Using Polyphenol-Rich Extract of Citrus Aurantium Flowers. *Nanomedicine Res. J.* **2020**, *5* (1), 20–28. https://doi.org/10.22034/NMRJ.2020.01.003.

(91) Sriramulu, M.; Shukla, D.; Sumathi, S. Aegle Marmelos Leaves Extract Mediated Synthesis of Zinc Ferrite: Antibacterial Activity and Drug Delivery. *Mater. Res. Express* **2018**, *5* (11), 1–9. https://doi.org/10.1088/2053-1591/aadd88.

(92) Manikandan, A.; Durka, M.; Antony, S. A. Hibiscus Rosa-Sinensis Leaf Extracted Green Methods, Magneto-Optical and Catalytic Properties of Spinel CuFe2O4 Nano- and Microstructures. *J. Inorg. Organomet. Polym. Mater.* **2015**, *25* (5), 1019–1031. https://doi.org/10.1007/s10904-015-0203-8.

(93) Muthukumar, H.; Palanirajan, S. K.; Shanmugam, M. K.; Gummadi, S. N.

Plant Extract Mediated Synthesis Enhanced the Functional Properties of Silver Ferrite Nanoparticles over Chemical Mediated Synthesis. *Biotechnol. Reports* **2020**, *26*, e00469. https://doi.org/10.1016/j.btre.2020.e00469.

(94) Chen, D. H.; He, X. R. Synthesis of Nickel Ferrite Nanoparticles by Sol-Gel Method. *Mater. Res. Bull.* **2001**, *36* (7–8), 1369–1377. https://doi.org/10.1016/S0025-5408(01)00620-1.

(95) Naseri, M. G.; Saion, E. B.; Hashim, M.; Shaari, A. H.; Ahangar, H. A. Synthesis and Characterization of Zinc Ferrite Nanoparticles by a Thermal Treatment Method. *Solid State Commun.* **2011**, *151* (14–15), 1031–1035. https://doi.org/10.1016/j.ssc.2011.04.018.

(96) Farley, K. E.; Marschilok, A. C.; Takeuchi, E. S.; Takeuchi, K. J. Synthesis and Electrochemistry of Silver Ferrite. *Electrochem. Solid-State Lett.* **2012**, *15* (2), 2–6. https://doi.org/10.1149/2.010202esl.

(97) Kuznetsov, M. V.; Morozov, Y. G.; Belousova, O. V. Synthesis of Copper Ferrite Nanoparticles. *Inorg. Mater.* **2013**, *49* (6), 606–615. https://doi.org/10.1134/S0020168513050063.

(98) Gingasu, D.; Mindru, I.; Preda, S.; Calderon-Moreno, J. M.; Culi, D. C.; Patron, L.; Diamandescu, L. Green Synthesis of Cobalt Ferrite Nanoparticles Using Plant Extracts. *Rev. Roum. Chim.* **2017**, *62* (8–9), 645–653.

(99) Karunakaran, G.; Jagathambal, M.; Van Minh, N.; Kolesnikov, E.; Kuznetsov, D. Green Synthesis of NiFe2O4 Spinel-Structured Nanoparticles Using Hydrangea Paniculata Flower Extract with Excellent Magnetic Property. *Jom* **2018**, *70* (7), 1337–1343. https://doi.org/10.1007/s11837-018-2871-7.

(100) Alijani, H. Q.; Pourseyedi, S.; Torkzadeh-Mahani, M.; Seifalian, A.; Khatami, M. Bimetallic Nickel-Ferrite Nanorod Particles: Greener Synthesis Using Rosemary and Its Biomedical Efficiency. *Artif. Cells, Nanomedicine Biotechnol.* **2020**, *48* (1), 242–251. https://doi.org/10.1080/21691401.2019.1699830.

(101) Kalia, S.; Prasad, N. Overview of Properties, Applications, and Synthesis of 4d-Series Doped/Substituted Cobalt Ferrite. *Inorg. Chem. Commun.* **2023**, *147* (October 2022), 110201. https://doi.org/10.1016/j.inoche.2022.110201.

(102) Jauhar, S.; Goyal, A.; Lakshmi, N.; Chandra, K.; Singhal, S. Doping Effect of

Cr3+ Ions on the Structural, Magnetic and Electrical Properties of Co-Cd Ferrites: A Study on the Redistribution of Cations in CoCd0.4CrxFe1.6-XO4 (0.1 ≤ x ≤ 0.6) Ferrites. *Mater. Chem. Phys.* **2013**, *139* (2–3), 836–843. https://doi.org/10.1016/j.matchemphys.2013.02.041.

(103) Lončarević, D.; Čupić, Ž. *The Perspective of Using Nanocatalysts in the Environmental Requirements and Energy Needs of Industry*; 2019. https://doi.org/10.1016/B978-0-12-815749-7.00004-9.

(104) Shobana, M. K.; Kwon, H.; Choe, H. Structural Studies on the Yttrium-Doped Cobalt Ferrite Powders Synthesized by Sol-Gel Combustion Method. *J. Magn. Magn. Mater.* **2012**, *324* (14), 2245–2248. https://doi.org/10.1016/j.jmmm.2012.02.110.

(105) Singhal, S.; Jauhar, S.; Chandra, K.; Bansal, S. Spin Canting Phenomenon in Cadmium Doped Cobalt Ferrites, CoCd XFe2-XO4 (x = 0•0, 0•2, 0•4, 0•6, 0•8 and 1•0), Synthesized Using Sol-Gel Auto Combustion Method. *Bull. Mater. Sci.* **2013**, *36* (1), 107–114. https://doi.org/10.1007/s12034-013-0439-2.

(106) Mund, H. S.; Ahuja, B. L. Structural and Magnetic Properties of Mg Doped Cobalt Ferrite Nano Particles Prepared by Sol-Gel Method. *Mater. Res. Bull.* **2017**, *85*, 228–233. https://doi.org/10.1016/j.materresbull.2016.09.027.

(107) Yang, G.; Park, S. J. Conventional and Microwave Hydrothermal Synthesis and Application of Functional Materials: A Review. *Materials (Basel).* **2019**, *12* (7). https://doi.org/10.3390/ma12071177.

(108) Vlazan, P.; Miron, I.; Sfirloaga, P. Cobalt Ferrite Substituted with Mn: Synthesis Method, Characterization and Magnetic Properties. *Ceram. Int.* **2015**, *41* (3), 3760–3765. https://doi.org/10.1016/j.ceramint.2014.11.051.

(109) Ati, A. A.; Abdalsalam, A. H.; Hasan, A. S. Thermal, Microstructural and Magnetic Properties of Manganese Substitution Cobalt Ferrite Prepared via Co-Precipitation Method. *J. Mater. Sci. Mater. Electron.* **2021**, *32* (3), 3019–3037. https://doi.org/10.1007/s10854-020-05053-4.

(110) Velhal, N. B.; Patil, N. D.; Shelke, A. R.; Deshpande, N. G.; Puri, V. R. Structural, Dielectric and Magnetic Properties of Nickel Substituted Cobalt Ferrite Nanoparticles: Effect of Nickel Concentration. *AIP Adv.* **2015**, *5* (9). https://doi.org/10.1063/1.4931908.

(111) Reddy, M. V.; Paul, J. P.; Das, D. Effect of Zinc Doping on Magnetic and Magnetoelastic Properties of Cobalt Ferrite Synthesized by Autocombustion Process. *AIP Conf. Proc.* **2013**, *1536*, 1015–1016. https://doi.org/10.1063/1.4810577.

(112) Hossain, M. S.; Alam, M. B.; Shahjahan, M.; Begum, M. H. A.; Hossain, M. M.; Islam, S.; Khatun, N.; Hossain, M.; Alam, M. S.; Al-Mamun, M. Synthesis, Structural Investigation, Dielectric and Magnetic Properties of Zn2+-Doped Cobalt Ferrite by the Sol-Gel Technique. *J. Adv. Dielectr.* **2018**, *8* (4), 2–7. https://doi.org/10.1142/S2010135X18500303.

(113) Madhukara Naik, M.; Bhojya Naik, H. S.; Nagaraju, G.; Vinuth, M.; Vinu, K.; Viswanath, R. Green Synthesis of Zinc Doped Cobalt Ferrite Nanoparticles: Structural, Optical, Photocatalytic and Antibacterial Studies. *Nano-Structures and Nano-Objects* **2019**, *19*, 100322. https://doi.org/10.1016/j.nanoso.2019.100322.

(114) Sanpo, N.; Wang, J.; Berndt, C. C. Sol-Gel Synthesized Copper-Substituted Cobalt Ferrite Nanoparticles for Biomedical Applications. *J. Nano Res.* **2013**, *22*, 95–106. https://doi.org/10.4028/www.scientific.net/JNanoR.22.95.

(115) Samavati, A.; Mustafa, M. K.; Ismail, A. F.; Othman, M. H. D.; Rahman, M. A. Copper-Substituted Cobalt Ferrite Nanoparticles: Structural, Optical and Antibacterial Properties. *Mater. Express* **2016**, *6* (6), 473–482. https://doi.org/10.1166/mex.2016.1338.

(116) Lefevre, C.; Roulland, F.; Thomasson, A.; Autissier, E.; Leuvrey, C.; Barre, S.; Versini, G.; Viart, N.; Pourroy, G. Stabilization of Scandium Rich Spinel Ferrite CoFe2-XScxO4 (X≤1) in Thin Films. *J. Solid State Chem.* **2015**, *232*, 118–122. https://doi.org/10.1016/j.jssc.2015.09.012.

(117) Rao, K. S.; Kumar, A. M.; Varma, M. C.; Choudary, G. S. V. R. K.; Rao, K. H. Cation Distribution of Titanium Substituted Cobalt Ferrites. *J. Alloys Compd.* **2009**, *488* (1), 6–9. https://doi.org/10.1016/j.jallcom.2009.08.086.

(118) Melikhov, Y.; Snyder, J. E.; Jiles, D. C.; Ring, A. P.; Paulsen, J. A.; Lo, C. C. H.; Dennis, K. W. Temperature Dependence of Magnetic Anisotropy in Mn-Substituted Cobalt Ferrite. *J. Appl. Phys.* **2006**, *99* (8). https://doi.org/10.1063/1.2151793.

(119) Caltun, O.; Rao, G. S. N.; Rao, K. H.; Rao, B. P.; Dumitru, I.; Kim, C.; Kim, C. The Influence of Mn Doping Level on Magnetostriction Coefficient of Cobalt Ferrite. **2007**, *316*, 618–620. https://doi.org/10.1016/j.jmmm.2007.03.045.

(120) Singh, S.; Singhal, S. Transition Metal Doped Cobalt Ferrite Nanoparticles: Efficient Photocatalyst for Photodegradation of Textile Dye. *Mater. Today Proc.* **2019**, *14*, 453–460. https://doi.org/10.1016/j.matpr.2019.04.168.

(121) Peda, M.; Kumar, P. S. A. Magnetic and Electrical Transport Properties of Ru Doped Cobalt Ferrite Thin Films with Perpendicular Magnetic Anisotropy. *AIP Adv.* **2021**, *11* (1). https://doi.org/10.1063/9.0000169.

(122) Mahajan, P.; Sharma, A.; Kaur, B.; Goyal, N.; Gautam, S. Green Synthesized (Ocimum Sanctum and Allium Sativum) Ag-Doped Cobalt Ferrite Nanoparticles for Antibacterial Application. *Vacuum* **2019**, *161* (July 2018), 389–397. https://doi.org/10.1016/j.vacuum.2018.12.021.

(123) Kumar, S.; Farea, A. M. M.; Batoo, K. M.; Lee, C. G.; Koo, B. H.; Yousef, A.; Alimuddin. Mössbauer Studies of Co0.5CdxFe 2.5-XO4 (0.0≤×≤0.5) Ferrite. *Phys. B Condens. Matter* **2008**, *403* (19–20), 3604–3607. https://doi.org/10.1016/j.physb.2008.06.001.

(124) Ghani, A. A.; Sattar, A. A.; Pierre, J. Composition Dependence of Magnetization in Co1-XCdxFe2O4 Ferrites. *J. Magn. Magn. Mater.* **1991**, *97* (1–3), 141–146. https://doi.org/10.1016/0304-8853(91)90173-8.

(125) Chakrabarty, S.; Dutta, A.; Pal, M. Effect of Yttrium Doping on Structure, Magnetic and Electrical Properties of Nanocrystalline Cobalt Ferrite. *J. Magn. Magn. Mater.* **2018**, *461*, 69–75. https://doi.org/10.1016/j.jmmm.2018.04.051.

(126) Tong, J.; Jiang, Q.; Chen, Z.; Jiang, Z.; Li, C. Two-Step Thermochemical Cycles for CO2 Splitting on Zr-Doped Cobalt Ferrite Supported on Silica. *Sol. Energy* **2015**, *116*, 133–143. https://doi.org/10.1016/j.solener.2015.04.007.

(127) Motavallian, P.; Abasht, B.; Abdollah-Pour, H. Zr Doping Dependence of Structural and Magnetic Properties of Cobalt Ferrite Synthesized by Sol–Gel Based Pechini Method. *J. Magn. Magn. Mater.* **2018**, *451*, 577–586. https://doi.org/10.1016/j.jmmm.2017.11.112.

(128) Heiba, Z. K.; Mostafa, N. Y.; Abd-Elkader, O. H. Structural and Magnetic Properties Correlated with Cation Distribution of Mo-Substituted Cobalt Ferrite

Nanoparticles. *J. Magn. Magn. Mater.* **2014**, *368*, 246–251.
https://doi.org/10.1016/j.jmmm.2014.05.036.

(129) Ramchandra Kiran, R.; Mondal, R. A.; Dwevedi, S.; Markandeyulu, G.
Structural, Magnetic and Magnetoelectric Properties of Nb Substituted Cobalt
Ferrite. *J. Alloys Compd.* **2014**, *610*, 517–521.
https://doi.org/10.1016/j.jallcom.2014.05.051.

(130) Orozco, C.; Melendez, A.; Manadhar, S.; Singamaneni, S. R.; Reddy, K. M.;
Gandha, K.; Niebedim, I. C.; Ramana, C. V. Effect of Molybdenum
Incorporation on the Structure and Magnetic Properties of Cobalt Ferrite. *J.
Phys. Chem. C* **2017**, *121* (45), 25463–25471.
https://doi.org/10.1021/acs.jpcc.7b08162.

(131) Noor, S.; Hakim, M. A.; Sikder, S. S.; Manjura Hoque, S.; Maria, K. H.;
Nordblad, P. Magnetic Behavior of Cd2 Substituted Cobalt Ferrites. *J. Phys.
Chem. Solids* **2012**, *73* (2), 227–231.
https://doi.org/10.1016/j.jpcs.2011.10.038.

(132) Ishaque, M.; Azhar Khan, M.; Ali, I.; Khan, H. M.; Asif Iqbal, M.; Islam, M.
U.; Warsi, M. F. Study on the Electromagnetic Behavior Evaluation of Y3+
Doped Cobalt Nanocrystals Synthesized via Co-Precipitation Route. *J. Magn.
Magn. Mater.* **2014**, *372*, 68–73. https://doi.org/10.1016/j.jmmm.2014.07.043.

(133) Imanipour, P.; Hasani, S.; Seifoddini, A.; Farnia, A.; Karimabadi, F.;
Jahanbani-Ardakani, K.; Davar, F. The Possibility of Vanadium Substitution on
Co Lattice Sites in CoFe2O4 Synthesized by Sol–Gel Autocombustion
Method. *J. Sol-Gel Sci. Technol.* **2020**, *95* (1), 157–167.
https://doi.org/10.1007/s10971-020-05316-w.

(134) Lee, S. J.; Lo, C. C.; Matlage, P. N.; Song, S. H.; Melikhov, Y. Magnetic and
Magnetoelastic Properties of Cr-Substituted Cobalt Ferrite. **2012**, *073910*
(2007). https://doi.org/10.1063/1.2794711.

(135) Chunfeng, B.; Tegus, O.; Ochirkhyag, T.; Odkhuu, D.; Tsogbadrakh, N.;
Sangaa, D.; Davaasambuu, J. Study of Structural and Magnetic Properties of
Spinel Zn Doped Cobalt Ferrites. *Solid State Phenom.* **2020**, *310 SSP*, 124–
133. https://doi.org/10.4028/www.scientific.net/SSP.310.124.

(136) Nlebedim, I. C.; Jiles, D. C. Thermal Effects on the Magnetic Properties of

Titanium Modified Cobalt Ferrite. *J. Appl. Phys.* **2015**, *117* (17), 1–5. https://doi.org/10.1063/1.4919229.

(137) Caltun, O.; Rao, G. S. N.; Rao, K. H.; Parvatheeswara Rao, B.; Dumitru, I.; Kim, C. O.; Kim, C. G. The Influence of Mn Doping Level on Magnetostriction Coefficient of Cobalt Ferrite. *J. Magn. Magn. Mater.* **2007**, *316* (2 SPEC. ISS.), 618–620. https://doi.org/10.1016/j.jmmm.2007.03.045.

(138) Lee, S. J.; Lo, C. C. H.; Matlage, P. N.; Song, S. H.; Melikhov, Y.; Snyder, J. E.; Jiles, D. C. Magnetic and Magnetoelastic Properties of Cr-Substituted Cobalt Ferrite. *J. Appl. Phys.* **2007**, *102* (7). https://doi.org/10.1063/1.2794711.

(139) Mohammadifar, Y.; Shokrollahi, H.; Karimi, Z.; Karimi, L. The Synthesis of Co1-XDyxFe2O4 Nanoparticles and Thin Films as Well as Investigating Their Magnetic and Magneto-Optical Properties. *J. Magn. Magn. Mater.* **2014**, *366*, 44–49. https://doi.org/10.1016/j.jmmm.2014.04.017.

(140) Dlamini, W. B.; Msomi, J. Z.; Moyo, T. XRD, Mössbauer and Magnetic Properties of MgxCo1-XFe2O4 Nanoferrites. *J. Magn. Magn. Mater.* **2015**, *373*, 78–82. https://doi.org/10.1016/j.jmmm.2014.01.066.

(141) Bouhas, A.; Amzal, M.; Zouranen, B. Mössbauer Study of the Calcium Substituted Cobalt Ferrite. *Mater. Chem. Phys.* **1993**, *33* (1–2), 80–84. https://doi.org/10.1016/0254-0584(93)90094-3.

(142) Waghmare, S. P.; Borikar, D. M.; Rewatkar, K. G. Impact of Al Doping on Structural and Magnetic Properties of Co-Ferrite. *Mater. Today Proc.* **2017**, *4* (11), 11866–11872. https://doi.org/10.1016/j.matpr.2017.09.105.

(143) Cao, D.; Pan, L.; Li, J.; Cheng, X.; Zhao, Z.; Xu, J.; Li, Q.; Wang, X.; Li, S.; Wang, J.; Liu, Q. Investigation on the Structures and Magnetic Properties of Carbon or Nitrogen Doped Cobalt Ferrite Nanoparticles. *Sci. Rep.* **2018**, *8* (1), 1–9. https://doi.org/10.1038/s41598-018-26341-4.

(144) Sumathi, S.; Lakshmipriya, V. Structural, Magnetic, Electrical and Catalytic Activity of Copper and Bismuth Co-Substituted Cobalt Ferrite Nanoparticles. *J. Mater. Sci. Mater. Electron.* **2017**, *28* (3), 2795–2802. https://doi.org/10.1007/s10854-016-5860-z.

(145) Vasambekar, P. N.; Kolekar, C. B.; Vaingankar, A. S. Magnetic Behaviour of Cd2+ and Cr3+ Substituted Cobalt Ferrites. *Mater. Chem. Phys.* **1999**, *60* (3),

282–285. https://doi.org/10.1016/S0254-0584(99)00062-0.

(146) Singhal, S.; Jauhar, S.; Lakshmi, N.; Bansal, S. Mn3+ Substituted Co-Cd Ferrites, CoCd0.4Mn XFe1.6-XO4 (0.1 ≤ x ≤ 0.6): Cation Distribution, Structural, Magnetic and Electrical Properties. *J. Mol. Struct.* **2013**, *1038*, 45–51. https://doi.org/10.1016/j.molstruc.2013.01.020.

(147) Mustafa, G.; Islam, M. U.; Zhang, W.; Jamil, Y.; Anwar, A. W.; Hussain, M.; Ahmad, M. Investigation of Structural and Magnetic Properties of Ce3+-Substituted Nanosized Co-Cr Ferrites for a Variety of Applications. *J. Alloys Compd.* **2015**, *618*, 428–436. https://doi.org/10.1016/j.jallcom.2014.07.132.

(148) Chakrabarty, S.; Dutta, A.; Pal, M. Effect of Mn and Ni Codoping on Ion Dynamics of Nanocrystalline Cobalt Ferrite: A Structure Property Correlation Study. *Electrochim. Acta* **2015**, *184*, 70–79. https://doi.org/10.1016/j.electacta.2015.10.027.

(149) Qin, X.; Zhang, T.; Wang, J.; Zhao, R.; Ma, Y.; Wang, F.; Xu, X. Influence of Ce-Mn Co-Doping on the Structure and Magnetic Properties of Cobalt Ferrites. *J. Alloys Compd.* **2022**, *929*. https://doi.org/10.1016/j.jallcom.2022.167256.

(150) Shakil, M.; Inayat, U.; Arshad, M. I.; Nabi, G.; Khalid, N. R.; Tariq, N. H.; Shah, A.; Iqbal, M. Z. Influence of Zinc and Cadmium Co-Doping on Optical and Magnetic Properties of Cobalt Ferrites. *Ceram. Int.* **2020**, *46* (6), 7767–7773. https://doi.org/10.1016/j.ceramint.2019.11.280.

(151) Priya, A. S.; Geetha, D.; Kavitha, N. Evaluation of Structural and Dielectric Properties of Al, Ce Co-Doped Cobalt Ferrites. *Mater. Res. Express* **2018**, *5* (6). https://doi.org/10.1088/2053-1591/aacd1e.

(152) Ngo, T. Composite and Nanocomposite Materials - From Knowledge to Industrial Applications. *Compos. Nanocomposite Mater. - From Knowl. to Ind. Appl.* **2020**. https://doi.org/10.5772/intechopen.80186.

(153) Kooti, M.; Kharazi, P.; Motamedi, H. Preparation, Characterization, and Antibacterial Activity of CoFe2O4/Polyaniline/Ag Nanocomposite. *J. Taiwan Inst. Chem. Eng.* **2014**, *45* (5), 2698–2704. https://doi.org/10.1016/j.jtice.2014.04.006.

(154) Abramovich, H. Introduction to Composite Materials. *Stab. Vib. Thin-Walled Compos. Struct.* **2017**, 1–47. https://doi.org/10.1016/B978-0-08-100410-

4.00001-6.

(155) Kar, K. K. *Composite Materials: Processing, Applications, Characterizations*; 2016. https://doi.org/10.1007/978-3-662-49514-8.

(156) Haffer, S.; Lüder, C.; Walther, T.; Köferstein, R.; Ebbinghaus, S. G.; Tiemann, M. A Synthesis Concept for a Nanostructured CoFe2O 4/BaTiO3 Composite: Towards Multiferroics. *Microporous Mesoporous Mater.* **2014**, *196*, 300–304. https://doi.org/10.1016/j.micromeso.2014.05.023.

(157) Gaikwad, P. N.; Hankare, P. P.; Wandre, T. M.; Garadkar, K. M.; Sasikala, R. Photocatalytic Performance of Magnetically Separable Fe, N Co-Doped TiO2-Cobalt Ferrite Nanocomposite. *Mater. Sci. Eng. B Solid-State Mater. Adv. Technol.* **2016**, *205*, 40–45. https://doi.org/10.1016/j.mseb.2015.12.006.

(158) Singh, C.; Bansal, S.; Singhal, S. Synthesis of Zn1-XCoxFe2O 4/MWCNTs Nanocomposites Using Reverse Micelle Method: Investigation of Their Structural, Magnetic, Electrical, Optical and Photocatalytic Properties. *Phys. B Condens. Matter* **2014**, *444*, 70–76. https://doi.org/10.1016/j.physb.2014.03.033.

(159) Qin, R.; Li, F.; Chen, M.; Jiang, W. Preparation of Chitosan-Ethylenediaminetetraacetate-Enwrapped Magnetic CoFe 2 O 4 Nanoparticles via Zero-Length Emulsion Crosslinking Method. *Appl. Surf. Sci.* **2009**, *256* (1), 27–32. https://doi.org/10.1016/j.apsusc.2009.07.032.

(160) Mirzaee, S.; Farjami Shayesteh, S.; Mahdavifar, S. Anisotropy Investigation of Cobalt Ferrite Nanoparticles Embedded in Polyvinyl Alcohol Matrix: A Monte Carlo Study. *Polymer (Guildf).* **2014**, *55* (16), 3713–3719. https://doi.org/10.1016/j.polymer.2014.06.039.

(161) Zhang, Y. X.; Hao, X. D.; Diao, Z. P.; Li, J.; Guan, Y. M. One-Pot Controllable Synthesis of Flower-like CoFe2O 4/FeOOH Nanocomposites for High-Performance Supercapacitors. *Mater. Lett.* **2014**, *123*, 229–234. https://doi.org/10.1016/j.matlet.2014.02.103.

(162) Levei, E. A.; Cadar, O.; Goga, F.; Borodi, G.; Barbu-tudoran, L. Nanocomposites Obtained by a Modified Sol – Gel Method. **2022**, 1–37.

(163) Sun, L.; Shao, R.; Tang, L. Q.; Chen, Z. D. Synthesis of Ag/ZnO Nanocomposite with Excellent Photocatalytic Performance via a Facile Sol-Gel

Method. *Adv. Mater. Res.* **2014**, *875–877*, 251–256.
https://doi.org/10.4028/www.scientific.net/AMR.875-877.251.

(164) Khan, S. A.; Rahman, N.; Khan, T.; Khan, R. Oxygen Vacancies Induced Variations in Structural , Optical and Dielectric Properties of SnO 2 / Graphite Nanocomposite. *J. Mater. Sci. Mater. Electron.* **2021**, *32* (2), 1402–1412. https://doi.org/10.1007/s10854-020-04912-4.

(165) Chaudhuri, A.; Mandal, K. Journal of Magnetism and Magnetic Materials Large Magnetoelectric Properties in CoFe 2 O 4 : BaTiO 3 Core – Shell Nanocomposites. *J. Magn. Magn. Mater.* **2015**, *377*, 441–445. https://doi.org/10.1016/j.jmmm.2014.10.142.

(166) Yoshimoto, S.; Ohashi, F.; Ohnishi, Y.; Nonami, T. Synthesis of Polyaniline-Montmorillonite Nanocomposites by the Mechanochemical Intercalation Method. *Synth. Met.* **2004**, *145* (2–3), 265–270. https://doi.org/10.1016/j.synthmet.2004.05.011.

(167) Gopinath, G. P.; Sayyad, S. B. Study the Synthesis of CuO/ZnO Nanocomposite by Mortar and Pestle and Its Characterization. *Int. J. Emerg. Technol. Innov. Res.* **2017**, *4* (11), 543–546.

(168) Rezayati, S.; Dinmohammadi, G.; Ramazani, A.; Sajjadifar, S. Mortar–Pestle Grinding Technique as an Efficient and Green Method Accelerates the Tandem Knoevenagel–Michael Cyclocondensation Reaction in the Presence of Ethylenediamine Immobilized on the Magnetite Nanoparticles. *Polycycl. Aromat. Compd.* **2022**, *0* (0), 1–23. https://doi.org/10.1080/10406638.2022.2110506.

(169) Zhang, P.; Liu, C.; Yu, L.; Hou, H.; Sun, W.; Ke, F. Synthesis of Benzimidazole by Mortar–Pestle Grinding Method. *Green Chem. Lett. Rev.* **2021**, *14* (4), 610–617. https://doi.org/10.1080/17518253.2021.1991483.

(170) Singh, K.; Mishra, A.; Sharma, D.; Singh, K. *Antiviral and Antimicrobial Potentiality of Nano Drugs*; Elsevier Inc., 2018. https://doi.org/10.1016/B978-0-12-814029-1.00013-2.

(171) Allafchian, A.; Hosseini, S. S. Antibacterial Magnetic Nanoparticles for Therapeutics: A Review. *IET Nanobiotechnology* **2019**, *13* (8), 786–799. https://doi.org/10.1049/iet-nbt.2019.0146.

(172) Nehra, P.; Chauhan, R. P. Antimicrobial Activity of Magnetic Nanostructures. *Nanotechnol. Life Sci.* **2019**, 301–318. https://doi.org/10.1007/978-3-030-16439-3_16.

(173) Mohan, P.; Mala, R. Comparative Antibacterial Activity of Magnetic Iron Oxide Nanoparticles Synthesized by Biological and Chemical Methods against Poultry Feed Pathogens. *Mater. Res. Express* **2019**, *6* (11). https://doi.org/10.1088/2053-1591/ab4964.

(174) Bukharin, O. V; Chainikova, I. N.; Perunova, N. B.; Andryuschenko, S. V; Ivanova, E. V; Bondarenko, T. A. Crossm. No. 9, 43–44.

(175) Carroll, L. M.; Wiedmann, M.; Mukherjee, M.; Nicholas, D. C.; Mingle, L. A.; Dumas, N. B.; Cole, J. A.; Kovac, J. Characterization of Emetic and Diarrheal Bacillus Cereus Strains from a 2016 Foodborne Outbreak Using Whole-Genome Sequencing: Addressing the Microbiological, Epidemiological, and Bioinformatic Challenges. *Front. Microbiol.* **2019**, *10* (FEB). https://doi.org/10.3389/fmicb.2019.00144.

(176) de Sousa, L. P. Genomic and Pathogenicity of a Bacillus Paranthracis Isolated from Book Page Surface. *Infect. Genet. Evol.* **2021**, *92* (February), 9–11. https://doi.org/10.1016/j.meegid.2021.104867.

(177) Liu, Y.; Du, J.; Lai, Q.; Zeng, R.; Ye, D.; Xu, J.; Shao, Z. Corrigendum: Proposal of Nine Novel Species of the Bacillus Cereus Group. *Int. J. Syst. Evol. Microbiol.* **2018**, *68* (8), 2706. https://doi.org/10.1099/ijsem.0.002902.

(178) Prasath, B. B.; Wang, Y.; Su, Y.; Zheng, W.; Lin, H.; Yang, H. Coagulant plus Bacillus Nitratireducens Fermentation Broth Technique Provides a Rapid Algicidal Effect of Toxic Red Tide Dinoflagellate. *J. Mar. Sci. Eng.* **2021**, *9* (4). https://doi.org/10.3390/jmse9040395.

(179) Guo, J.; Wang, Y. qiang; Yang, G.; Chen, Y.; Zhou, S.; Zhao, Y.; Zhuang, L. Bacillus Nitroreducens Sp. Nov., a Humus-Reducing Bacterium Isolated from a Compost. *Arch. Microbiol.* **2016**, *198* (4), 347–352. https://doi.org/10.1007/s00203-016-1193-9.

(180) Balouiri, M.; Sadiki, M.; Ibnsouda, S. K. Methods for in Vitro Evaluating Antimicrobial Activity: A Review. *J. Pharm. Anal.* **2016**, *6* (2), 71–79. https://doi.org/10.1016/j.jpha.2015.11.005.

(181) Kulkarni, A. B.; Mathad, S. N. Variation in Structural and Mechanical Properties of Cd-Doped Co-Zn Ferrites. *Mater. Sci. Energy Technol.* **2019**, *2* (3), 455–462. https://doi.org/10.1016/j.mset.2019.03.003.

(182) Bunaciu, A. A.; Udriştioiu, E. gabriela; Aboul-Enein, H. Y. X-Ray Diffraction: Instrumentation and Applications. *Crit. Rev. Anal. Chem.* **2015**, *45* (4), 289–299. https://doi.org/10.1080/10408347.2014.949616.

(183) Harold Rawson. Properties and Applications of Glass. *Elsevier Sci. Publ. Co.* **1980**, *3*, 318.

(184) Epp, J. *X-Ray Diffraction (XRD) Techniques for Materials Characterization*; 2016.

(185) Goniometer, T. C.; Goniometer, T. R. 1911 Encyclopædia Britannica / Goniometer. **1911**.

(186) Mohamed, M. A.; Jaafar, J.; Ismail, A. F.; Othman, M. H. D.; Rahman, M. A. *Fourier Transform Infrared (FTIR) Spectroscopy*; Elsevier B.V., 2017. https://doi.org/10.1016/B978-0-444-63776-5.00001-2.

(187) Thomson, T. *Magnetic Properties of Metallic Thin Films*; 2013. https://doi.org/10.1533/9780857096296.2.454.

(188) First, S.; Principles, V. S. M. Vsm Principles. *Water* **2006**, 1–5.

(189) Lopez-Dominguez, V.; Quesada, A.; Guzmán-Mínguez, J. C.; Moreno, L.; Lere, M.; Spottorno, J.; Giacomone, F.; Fernández, J. F.; Hernando, A.; García, M. A. A Simple Vibrating Sample Magnetometer for Macroscopic Samples. *Rev. Sci. Instrum.* **2018**, *89* (3). https://doi.org/10.1063/1.5017708.

(190) Abd Mutalib, M.; Rahman, M. A.; Othman, M. H. D.; Ismail, A. F.; Jaafar, J. *Scanning Electron Microscopy (SEM) and Energy-Dispersive X-Ray (EDX) Spectroscopy*; Elsevier B.V., 2017. https://doi.org/10.1016/B978-0-444-63776-5.00009-7.

(191) Akhtar, K.; Khan, S. A.; Khan, S. B.; Asiri, A. M. *Scanning Electron Microscopy: Principle and Applications in Nanomaterials Characterization*; 2018. https://doi.org/10.1007/978-3-319-92955-2_4.

(192) Weiss, A. D. Scanning Electron Microscopes. *Semicond. Int.* **1983**, *6* (10), 90–94. https://doi.org/10.1016/s0026-0576(03)90123-1.

(193) Joardder, M. U. H.; Karim, A.; Kumar, C.; Brown, R. J. Determination of

Effective Moisture Diffusivity of Banana Using Thermogravimetric Analysis. *Procedia Eng.* **2014**, *90*, 538–543. https://doi.org/10.1016/j.proeng.2014.11.769.

(194) 4 Surface and Material Characterization Techniques. https://doi.org/10.1016/B978-0-8155-1523-4.50006-7.

(195) Reading, F. Temperature-Modulated Techniques. *Thermochim. Acta* **2001**, 22–29.

(196) Kreuzer, M. Solid-Supported Lipid Membranes and Their Response to Varied Environmental Conditions. **2011**, No. April.

(197) Andreev, V. G.; Letyuk, L. M.; Maiorov, V. R.; Podgornaya, S. V.; Strygin, A. A. Binders in the Manufacture of Magnetic Ceramics (Ferrites). *Steel Transl.* **2007**, *37* (7), 589–592. https://doi.org/10.3103/S0967091207070078.

(198) Jasrotia, R.; Prakash, J.; Kumar, G.; Verma, R.; Kumari, S.; Kumar, S.; Singh, V. P.; Nadda, A. K.; Kalia, S. Robust and Sustainable Mg1-XCexNiyFe2-YO4 Magnetic Nanophotocatalysts with Improved Photocatalytic Performance towards Photodegradation of Crystal Violet and Rhodamine B Pollutants. *Chemosphere* **2022**, *294* (January), 133706. https://doi.org/10.1016/j.chemosphere.2022.133706.

(199) Iqbal, S.; Fakhar-e-Alam, M.; Atif, M.; Amin, N.; Alimgeer, K. S.; Ali, A.; Aqrab-ul-Ahmad; Hanif, A.; Aslam Farooq, W. Structural, Morphological, Antimicrobial, and in Vitro Photodynamic Therapeutic Assessments of Novel Zn+2-Substituted Cobalt Ferrite Nanoparticles. *Results Phys.* **2019**, *15* (May), 102529. https://doi.org/10.1016/j.rinp.2019.102529.

(200) Ghosh, M. P.; Mukherjee, S. Microstructural, Magnetic, and Hyperfine Characterizations of Cu-Doped Cobalt Ferrite Nanoparticles. *J. Am. Ceram. Soc.* **2019**, *102* (12), 7509–7520. https://doi.org/10.1111/jace.16687.

(201) Satheeshkumar, M. K.; Kumar, E. R.; Srinivas, C.; Suriyanarayanan, N.; Deepty, M.; Prajapat, C. L.; Rao, T. V. C.; Sastry, D. L. Study of Structural, Morphological and Magnetic Properties of Ag Substituted Cobalt Ferrite Nanoparticles Prepared by Honey Assisted Combustion Method and Evaluation of Their Antibacterial Activity. *J. Magn. Magn. Mater.* **2019**, *469*, 691–697. https://doi.org/10.1016/j.jmmm.2018.09.039.

(202) Somaiah, N.; Jayaraman, T. V.; Joy, P. A.; Das, D. Magnetic and Magnetoelastic Properties of Zn-Doped Cobalt-Ferrites - CoFe 2-XZn XO 4 (X=0, 0.1, 0.2, and 0.3). *J. Magn. Magn. Mater.* **2012**, *324* (14), 2286–2291. https://doi.org/10.1016/j.jmmm.2012.02.116.

(203) Tran, N.; Mir, A.; Mallik, D.; Sinha, A.; Nayar, S.; Webster, T. J. Bactericidal Effect of Iron Oxide Nanoparticles on Staphylococcus Aureus. *Int. J. Nanomedicine* **2010**, *5* (1), 277–283. https://doi.org/10.2147/ijn.s9220.

(204) Sagayaraj, R.; Dhineshkumar, T.; Prakash, A.; Aravazhi, S.; Chandrasekaran, G.; Jayarajan, D.; Sebastian, S. Fabrication, Microstructure, Morphological and Magnetic Properties of W-Type Ferrite by Co-Precipitation Method: Antibacterial Activity. *Chem. Phys. Lett.* **2020**, *759* (August), 137944. https://doi.org/10.1016/j.cplett.2020.137944.

(205) Sanpo, N.; Tharajak, J.; Li, Y.; Berndt, C. C.; Wen, C.; Wang, J. Biocompatibility of Transition Metal-Substituted Cobalt Ferrite Nanoparticles. *J. Nanoparticle Res.* **2014**, *16* (7). https://doi.org/10.1007/s11051-014-2510-3.

(206) Sanpo, N.; Berndt, C. C.; Wen, C.; Wang, J. Transition Metal-Substituted Cobalt Ferrite Nanoparticles for Biomedical Applications. *Acta Biomater.* **2013**, *9* (3), 5830–5837. https://doi.org/10.1016/j.actbio.2012.10.037.

(207) Nasrazadani, S.; Hassani, S. Modern Analytical Techniques in Failure Analysis of Aerospace, Chemical, and Oil and Gas Industries. *Handb. Mater. Fail. Anal. with Case Stud. from Oil Gas Ind.* **2016**, 39–54. https://doi.org/10.1016/B978-0-08-100117-2.00010-8.

(208) Wolfgong, W. J. *Chemical Analysis Techniques for Failure Analysis: Part 1, Common Instrumental Methods*; Elsevier Ltd., 2016. https://doi.org/10.1016/B978-0-12-800950-5.00014-4.

(209) Sanpo, N.; Berndt, C. C.; Wang, J. Microstructural and Antibacterial Properties of Zinc-Substituted Cobalt Ferrite Nanopowders Synthesized by Sol-Gel Methods. *J. Appl. Phys.* **2012**, *112* (8), 1–7. https://doi.org/10.1063/1.4761987.

(210) Rhaman, M. M.; Matin, M. A.; Hossain, M. N.; Mozahid, F. A.; Hakim, M. A.; Islam, M. F. Bandgap Engineering of Cobalt-Doped Bismuth Ferrite Nanoparticles for Photovoltaic Applications. *Bull. Mater. Sci.* **2019**, *42* (4). https://doi.org/10.1007/s12034-019-1871-8.

(211) Kooti, M.; Gharineh, S.; Mehrkhah, M.; Shaker, A.; Motamedi, H. Preparation and Antibacterial Activity of CoFe2O4/SiO2/Ag Composite Impregnated with Streptomycin. *Chem. Eng. J.* **2015**, *259*, 34–42. https://doi.org/10.1016/j.cej.2014.07.139.

(212) Dippong, T.; Levei, E. A.; Goga, F.; Petean, I.; Avram, A.; Cadar, O. The Impact of Polyol Structure on the Formation of Zn0.6Co0.4Fe2O4 Spinel-Based Pigments. *J. Sol-Gel Sci. Technol.* **2019**, *92* (3), 736–744. https://doi.org/10.1007/s10971-019-05140-x.

(213) Dippong, T.; Levei, E. A.; Cadar, O.; Goga, F.; Barbu-Tudoran, L.; Borodi, G. Size and Shape-Controlled Synthesis and Characterization of CoFe2O4 Nanoparticles Embedded in a PVA-SiO2 Hybrid Matrix. *J. Anal. Appl. Pyrolysis* **2017**, *128* (October), 121–130. https://doi.org/10.1016/j.jaap.2017.10.018.

(214) Xiao, Y.; Du, J. Superparamagnetic Nanoparticles for Biomedical Applications. *J. Mater. Chem. B* **2020**, *8* (3), 354–367. https://doi.org/10.1039/c9tb01955c.

(215) Kaur, S.; Kumar, V.; Jasrotia, R.; Bhasin, V. Spinel Nanoferrite (CoFe 2 O 4): The Impact of Cr Doping on Its Structural , Surface Morphology , Magnetic , and Antibacterial Activity Traits Spinel Nanoferrite (CoFe 2 O 4): The Impact of Cr Doping on Its Structural , Surface Morphology , Magnetic ,. *Opt. Mater. (Amst).* **2022**, *133* (October), 113026. https://doi.org/10.1016/j.optmat.2022.113026.

(216) Desai, S. S.; Shirsath, S. E.; Mujasam Batoo, K.; Adil, S. F.; Khan, M.; Patange, S. M. Influence of Zn-Zr Substitution on the Crystal Chemistry and Magnetic Properties of CoFe2O4 Nanoparticles Synthesized by Sol-Gel Method. *Phys. B Condens. Matter* **2020**, *596* (July), 412400. https://doi.org/10.1016/j.physb.2020.412400.

(217) Mariosi, F. R.; Venturini, J.; da Cas Viegas, A.; Bergmann, C. P. Lanthanum-Doped Spinel Cobalt Ferrite (CoFe2O4) Nanoparticles for Environmental Applications. *Ceram. Int.* **2020**, *46* (3), 2772–2779. https://doi.org/10.1016/j.ceramint.2019.09.266.

(218) Dippong, T.; Levei, E. A.; Deac, I. G.; Neag, E.; Cadar, O. Influence of CU2+,

NI2+, and ZN2+ Ions Doping on the Structure, Morphology, and Magnetic Properties of Co-Ferrite Embedded in SiO2 Matrix Obtained by an Innovative Sol-Gel Route. *Nanomaterials* **2020**, *10* (3). https://doi.org/10.3390/nano10030580.

(219) Agrawal, S.; Parveen, A.; Azam, A. Journal of Magnetism and Magnetic Materials Structural , Electrical , and Optomagnetic Tweaking of Zn Doped CoFe 2 À x Zn x O 4 À δ Nanoparticles. **2016**, *414* (3), 144–152. https://doi.org/10.1016/j.jmmm.2016.04.059.

List of publications

S. No.	Title of the Paper	Published Date	Volume & Issue Number	Name of journal	Publication house	ISSN/ISBN Number
1.	Synthesis of ferrites using various parts of plants: a mini review	1st July 2021	1964 & 3	Journal of Physics: Conference Series	IOP Science	1742-6588
2.	Synthesis of bismuth doped cobalt ferrite and its composite with polyaniline	1st Jan 2022	48 & 3	Materials Today: Proceedings	Elsevier	2214-7853
3.	Properties, applications, and synthesis of first transition series substituted cobalt ferrite: a mini review	1st May 2022	2267 & 1	Journal of Physics: Conference Series	IOP Science	1742-6588
4.	Overview of properties, applications, and synthesis of 4d-series doped/substituted cobalt ferrite	28th Nov 2022	147	Inorganic Chemistry Communications	Elsevier	1387-7003
5.	Antibacterial activities of Bi-Ag co-doped cobalt ferrite and their ZnO/Ag nanocomposite/s	1st April 2023	150	Inorganic Chemistry Communications	Elsevier	1387-7003

1.

Synthesis of ferrites using various parts of plants: a mini review

Shyam Kalia, Abhishek Kumar, Neha Munjal and Nupur Prasad*

Lovely Professional University, Jalandhar, Punjab, 144411.

*Corresponding author: nupur.20362@lpu.co.in

Abstract. Ferrite nanoparticles are magnetic. They also show photocatalytic and antibacterial activities. These unique properties make them extremely useful for various applications e.g., they can potentially be used for electronic equipment, telecommunication systems, radar, sensing material, catalytic and photocatalytic applications, and several biomedical applications. Several methods have been developed to synthesise these materials. These include sol-gel, co-precipitation, ball-milling, combustion, hydrothermal heating, and microwave hydrothermal procedure. Recently, these materials have been using various parts of plants. *Hibiscus rosa-sinensis*, *Hydrangea paniculata*, rosemary, nyctanthes arbor-tristis, sesame seed, aegle marmelos, *Limonia acidissima* juice, aloe vera, amaranthus blitum, ginger and cardamom, were used for this purpose. Ferrites of silver, cobalt, zinc, and nickel were prepared successfully. Few doped ferrites, e.g., silver doped cobalt ferrite, nickel doped zinc ferrite, and zinc doped nickel ferrite were also synthesised. Use of plant-parts evades the necessity of the use of expensive metal salts. Various parts of plants, e.g., flowers, leaves, and seeds act as a gelling agent, chelating agent, reducing agent, and capping agent during reactions. This is a non-toxic, eco-friendly, and cost-effective method. The samples were characterized using various Advance Materials Characterisation Techniques. The results were very much in agreement with the desired values. In a few cases, better antibacterial activities have been observed with ferrites obtained via this method. Left-over parts of food and fruits can be used for this method which may help in waste management. Still, the tremendous scope is left in this area that can be exploited which may include scaling-up of the product.

Keywords: nanoparticles, magnetic materials, chemical and biosynthesis, antibacterial activities

2.

Synthesis of bismuth doped cobalt ferrite and its composite with polyaniline

Shilpa Vats [a], Abhishek Kumar [a], Shyam Kalia [a], Jibrin Mohammad [b], Nupur Prasad [a,*]

[a] Lovely Professional University, Phagwara, Punjab 144411, India
[b] Federal University, Dutse, Jigwa, Nigeria

ARTICLE INFO

ABSTRACT

Ferrites are ceramics having Fe (III) ions. Cobalt ferrite was doped with bismuth via sol–gel method. The doped samples were mixed with polyaniline to form the composites. Polyaniline was chosen as it was a cheap material. Sol–gel method is a time saving and simple method. It also brings about the homogeneity in the reaction. The synthesized material was calcinated at 900 °C for 6 h. Preparation of polyaniline was done by oxidative polymerization method. Here ammonium persulphate act as an oxidative agent. The polyaniline was washed with methanol and dried for 24 h in an oven. The composite of bismuth doped cobalt ferrite and polyaniline were studied through X-ray diffraction (XRD), FTIR, UV, VSM and FESEM. It was observed that magnetic and optical properties changed with change in amount of dopant.

1. Introduction

as MRI (magnetic resonance imaging) [3–6]. Based on crystal structure ferrites can be classified into several groups. These groups are

3.

Properties, applications, and synthesis of first transition series substituted cobalt ferrite: a mini review

S Kalia[1, 3], A Kumar[2, 3], S Sharma[3] and N Prasad[3*]
[1.] Government P. G. College, Dhaliara (Kangra), Himachal Pradesh. 177103
[2.] Intertek India Pvt. Ltd., Plot no. 68, 69, Udyog Vihar Phase-I, Dundahera village, Sector 20, Gurugram, Haryana. 122001
[3.] Central Instrumentation Facility, Division of Research and Development, Lovely Professional University, Phagwara, Punjab. 144411
*Email address: nupur.20362@lpu.co.in

Abstract. Spinel, orthoferrite, garnet, and hexagonal are the various forms of ferrites. They exhibit different properties due to their different molecular structures. Cobalt ferrite (CF) is a spinel ferrite. They show magnetic, dielectric, optical, catalytical, and antibacterial properties. The CF nanoparticles (NPs) are extensively used in various field e.g., electronics and telecommunication, environmental sciences, biomedical applications, and catalysis, to name but a few. These materials can be doped to modify their properties so that they can be used for desired applications. Several methods have been developed for the doping of these materials e.g., sol-gel, co-precipitation, hydrothermal heating, microwave hydrothermal heating, auto-combustion, ball milling, and microemulsion. Sol-gel method is widely used for this purpose as this does not require complex laboratory infrastructure and hence cost effective. Particles of narrow size distribution can also be synthesised under ambient or at lower temperatures. Here, the doping of CF-NPs with first transition series has been reviewed. The comparable ionic sizes of cobalt and iron, and ions of first transition series, help the process of doping. Doping of CF-NPs with first transition series changes their properties in several ways e.g., the size of crystals and Curie temperature can be altered by doping with scandium, titanium, and chromium. Values of coercivity and saturation magnetization can also be modified by doping this material with zinc, nickel, and copper. Anisotropy also changes when CF-NPs are doped with the above said elements. CF-NPs with altered properties have significant applications e.g., zinc-doped can be used for stress sensor applications.

1. Introduction

Metal oxide nanoparticles (NPs) show exceptional magnetic, optical, and dielectric properties. Various metal oxides were synthesised. Cobalt ferrite (CF) NPs are one of them. Substitution and doping of

4.

Overview of properties, applications, and synthesis of 4d-series doped/ substituted cobalt ferrite

S. Kalia [a, c], N. Prasad [b, *]

[a] Government College, Dhaliara (Kangra), Himachal Pradesh 177103, India
[b] Central Instrumentation Facility, Division of Research and Development, Lovely Professional University, Phagwara, Punjab 144411, India
[c] School of Chemical Engineering and Physical Sciences, Lovely Professional University, Phagwara, Punjab 144411, India

ARTICLE INFO

ABSTRACT

Ferrites have great importance in the field of material science. Cobalt ferrite is one of them which have immense scientific interest due to its unique properties and applications. This material exhibits numerous remarkable properties e.g., magnetic, dielectric, optical, photocatalytic, and catalytic, to name but a few. They also show antibacterial activities. Properties of CF can be tailored by several ways. This provides an opportunity to create materials of desired properties. Several methods have been used to synthesise this material. Although, it has been observed that sol–gel route and its modifications are widely used. The method of synthesis, heat treatment and effect of doping strongly influenced the particle size of samples, morphology, and structure, and hence their properties like electrical, optical, magnetic, and catalytic properties. Biomedical applications also depend upon these properties of the material. Their properties can also be tailored by doping with transition metals and rare earth element. It is possible to prepare nanocomposites of this material, which opens a new area that can be utilized by scientists and technocrats for the enhancement of knowledge and cutting edge technology. In this age, when the human civilisation is going for digitization, magnetic materials of this quality that can be used for storage and transportation of data, makes its own prominent place in the world of technology. Here, we have reviewed properties, applications, and routes of synthesis of CF doped with elements of 4d-series. To our knowledge this has not be done in the recent years.

5.

Short communication

Antibacterial activities of Bi-Ag co-doped cobalt ferrite and their ZnO/ Ag nanocomposite/s

S Kalia [a,b], Vikas Dhiman [c], Tchouank Tekou Carol T. [a], Deepak Basandrai [a], N Prasad [a,d,*]

[a] School of Chemical Engineering and Physical Sciences, Lovely Professional University, G. T. Road, Phagwara, Punjab 144411, India
[b] Department of Chemistry, Government College, Dhaliara (Kangra), HP 177103, India
[c] Department of Physics, Government College, Dhaliara (Kangra), HP 177103, India
[d] Central Instrumentation Facility, Division of Research and Development, Lovely Professional University, G. T. Road, Phagwara, Punjab 144411, India

ARTICLE INFO

ABSTRACT

Cobalt ferrite was co-doped with bismuth and silver of different concentrations via sol–gel combustion method. Citric acid was used as fuel. The powder product was calcined using an electric furnace at 1000 °C for 4 hrs. X-ray diffraction pattern of co-doped cobalt ferrite nanoparticles (CF-NPs) showed the formation of cubic crystalline structure. Few very small absorption bands were also observed. The crystallite sizes of these materials were ~ 40 nm to ~ 60 nm. As calculated using Scherrer's equation it has been observed that the crystallite size changed with change in doping and co-doping levels. This is a very pertinent observation showing that crystallite size can be controlled through doping and co-doping. Since properties of particles largely depend on the sizes of the particles this also imply that particles of desired properties can be synthesised using this method. The results obtained through X-ray diffraction were further deeply analysed using Rietveld Refinement using FullProf suite. Fourier Transform Infrared (FTIR) Spectroscopic studies confirmed the formation of spinel structures. Few very small absorption bands were also observed in FTIR. Particle sizes as observed using Zeta potential and Particle Size Analyser (ZS) was approximately 675 nm. Field Emission Scanning Electron Microscope (FESEM), Transmission Electron Microscope (TEM) showed that the particles were agglomerated. Composites of co-doped CF-NPs with ZnO/Ag were prepared manually by grinding them in a mortar and pestle. Starch was used as a binder. All these samples including composites showed antibacterial activities. The results revealed that co-doped cobalt ferrite nanoparticles of higher dopant concentration exhibit higher antibacterial activity. These materials can be used in various biomedical applications.

List of conferences

S.No.	Name of conference proceeding	Date	Organizer
1.	"Recent Advances in Fundamental and Applied Sciences" (RAFAS 2021)	25th to 26th June 2021	Lovely Professional University Punjab
2.	International Conference on Advances in Computational Science and Engineering (ICACSE 2020)	25 & 26th, December 2020	Live4Research Institute of Research and Development, India.
3.	International Conference on Advances in Nanomaterials and Devices for Energy and Environment (ICAN-2019)	27th to 29th January 2019	ABV-Indian Institute of Information Technology and Management, Gwalior

List of workshops

S.No.	Name of workshop	Date	Organizer
1.	Molecular Spectroscopy and Thermal Analysis for Innovation and Industrial Applications	27th Nov. to 1st Dec. 2020	PerkinElmer-LPU Centre of Excellence in Materials' Characterization, in association with Central Instrumentation Facility, Division of Research and Development at Lovely Professional University, Punjab.
2.	Use of LATEX in typesetting technical documents	31st Aug. to 4th Sept. 2020	Department of Physics, Dr. B. R. Ambedkar National Institute of Technology, Jalandhar, Punjab

Annexure 1

Table: The diameter of zone of inhibitions of all the synthesized samples presenting their antibacterial activities

Pair 1 (Cu-Ag)				Pair 2 (Ag-Zn)			
Sample-ids	Zone of inhibitions (mm)	Sample-ids	Zone of inhibitions (mm)	Sample-ids	Zone of inhibition (mm)	Sample-ids	Zone of inhibition (mm)
SK-023	7.6	SKC-023	7.8	SK-023	7	SKC-023	7.5
SK-002	8.0	SKC-002	8.5	SK-002	7.2	SKC-002	7.6
SK-005	8.2	SKC-005	8.8	SK-008	7.4	SKC-008	7.8
SK-013	8.5	SKC-013	9.5	SK-014	7.6	SKC-014	8.5
SK-006	9.0	SKC-006	10.0	SK-012	7.8	SKC-012	9.0
SK-018	10.0	SKC-018	12.0	SK-019	8.4	SKC-019	9.5
Pair 3 (Cu-Zn)				**Pair 4 (Bi-Ag)**			
Sample-ids	Zone of inhibitions (mm)	Sample-ids	Zone of inhibitions (mm)	Sample-ids	Zone of inhibition (mm)	Sample-ids	Zone of inhibition (mm)
SK-023	7	SKC-023	7.5	SK-023	8.0	SKC-023	8.5
SK-005	7.2	SKC-005	8.5	SK-002	8.5	SKC-002	9.0
SK-008	7.4	SKC-008	8.6	SK-007	9.0	SKC-007	9.5
SK-015	7.5	SKC-015	9	SK-016	9.0	SKC-016	9.5
SK-011	8	SKC-011	9.3	SK-001	10	SKC-001	10.5
SK-020	8.5	SKC-020	9.5	SK-021	11	SKC-021	11.5
Pair 5 (Bi-Zn)							
Sample-ids	Zone of inhibitions (mm)	Sample-ids	Zone of inhibitions (mm)	Sample-ids	Zone of inhibition (mm)	Sample-ids	Zone of inhibition (mm)
SK-023	7.6	SKC-023	8.0	SK-017	9.0	SKC-017	9.5
SK-007	8.4	SKC-007	9.2	SK-010	9.5	SKC-010	10.0
SK-008	7.8	SKC-008	8.2	SK-022	10.0	SKC-022	10.5